Title
Acuity, Crowding, Feature Detection, and Fixation in Normal and Amblyopic Vision

Author
Song, Shuang

Publication Date
2009

Peer reviewed|Thesis/dissertation

Acuity, Crowding, Feature Detection, and Fixation in Normal and Amblyopic Vision

by

Shuang Song

A dissertation submitted in partial satisfaction of the

requirements for the degree of

Doctor of Philosophy

in

Vision Science

in the

Graduate Division

of the

University of California, Berkeley

Committee in charge:

Professor Dennis M. Levi, Chair
Professor Susana Chung
Professor David R. Brillinger

Fall 2009

Acuity, Crowding, Feature Detection, and Fixation
in Normal and Amblyopic Vision

by Shuang Song

To my parents, sister, and husband

whose love gives me confidence.

CONTENTS

ACKNOWLEDGEMENTS

I would like to thank all my dissertation committee members, Dennis Levi, Susana Chung, and David Brillinger, for their guidance and support throughout my dissertation work. My advisor and the chairman, Dennis Levi, has admirable scientific intuition and knowledge in vision research; his insightful interpretation of an experimental result often opens another door for my research; his superb efficiency at work is the goal I might never be able to achieve; his mentorship grants me freedom while wisely curbing my sometimes unrealistic imaginations and has led my graduate study in the right direction. Susana Chung has supported my study in many ways; her interesting lab meetings, sharp comments on my manuscripts, and generous sharing of her academic experiences are not only important for my completion of the dissertation, but also makes this journey more enjoyable. David Brillinger has given me the idea of fixational eye movements modeling and offered crucial statistical / mathematical advices as well as encouragements that made this chapter come true.

I would also like to thank Austin Roorda, Denis Pelli, Stan Klein, and Sourav Chatterjee. Austin Roorda has developed the adaptive optics scanning laser ophthalmoscope (AOSLO) and has been actively applying the apparatus and technique to vision research, including the fixational eye movements recording that is the basis of a significant part of my dissertation. Denis Pelli is a collaborator of the first half of my dissertation; his substantial intellectual input to the chapters on visual acuity is greatly appreciated. Stan Klein's advices on psychophysical experimental design and data analysis have been very helpful to me, and I also appreciate his always being accessible and willing to teach. Sourav Chatterjee introduced me to mathematics / statistics and I truly admire his talent and dedication to science.

I would like to thank all my lab members, my classmates, and those who have kindly offered me help and support during my dissertation work. My life at Berkeley is memorable because of all these people. I would like to specially thank Roger Li who has given me many kinds of advices I need – from basic computerized stimulus generation to career choices, Ethan Rossi who helped me collect the fixational eye movement data and suggested some important methods, Charlotte Wickham who helped me on the fixational eye movement modeling, and Susan Kim who helped me on the image processing of the fixational eye movement recordings.

I would also like to thank all the observers of my study, especially the amblyopes. I could not have done anything without their hours and hours performing repeated tedious visual tasks. I hope our vision research will benefit people with amblyopia in the near future.

Lastly, I would like to thank my parents, sister, and husband for their love and trust in me. Knowing that they are always behind me, I have nothing to fear.

ABSTRACT

Acuity, Crowding, Feature Detection, and Fixation
in Normal and Amblyopic Vision

by

Shuang Song

Doctor of Philosophy in Vision Science

University of California, Berkeley

Professor Dennis M. Levi, Chair

Both functional and physical properties related to vision are known to be abnormal in amblyopia. The former include spatial and temporal visual deficits such as reduced letter acuity and temporal sensitivity, crowding, and decreased position acuity; the latter refers to eccentric and unstable fixational eye movements in strabismic amblyopia. This dissertation represents parallel studies that aim to characterize amblyopic vision from these angles using different approaches.

In the first series of experiments, we systematically explored the size and spacing requirements for identifying a letter among other letters by measuring flanked and unflanked letter acuities in normals and amblyopes, centrally and peripherally, while fixing the medium contrast and brief presentation duration. At fixation, for normals and non-strabismic amblyopes, no crowding has been found: legibility of a flanked letter is limited by overlap masking or acuity depending on the letter spacing. In normal peripheral vision and strabismic amblyopia, legibility is limited by crowding unless the letter spacing is very loose. We show that strabismic and non-strabismic amblyopia are much like normal vision at increased eccentricity or with added blur, respectively, as characterized by the crowding-acuity ratio. For clinical screening tests for strabismic and non-strabismic amblyopia, we recommend measuring both unflanked letter acuity and flanked letter acuity with tight spacing.

In the second series of experiments, we explored the effects of various factors on both flanked and unflanked visual acuities in normal observers. Specifically, we varied polarity, contrast, and duration of the letter stimuli, as well as the pupil size of the observer by adding a pinhole. We find that the critical spacing for crowding in the fovea is 0.09 ~ 0.1 deg. The main effects of and interactions between the above factors provide the context and supplement to the

results from the above experiments, based on which we extend the letter legibility model developed from the above experiments by parameterization of each legibility limit to account for a wide range of conditions.

In the third series of experiments, the first experiment estimated the spatiotemporal mechanism for detecting a luminance increment of a bright bar embedded in spatiotemporal noise for normal and amblyopic observers. The normal template is characterized by a temporal summation zone surrounded by symmetric spatial inhibition zones and followed by a temporal inhibition zone. The abnormal amblyopic template lacks inhibition but with normal temporal summation. Neither blurring the stimuli in space and time nor varying the signal-to-noise ratio caused any significant change in the normal or amblyopic template. However, decreasing the fundamental frequency of the stimuli restored the normal template in the amblyopic eye. Furthermore, the normal periphery shares spatial properties with amblyopia but the temporal properties may be different. The second experiment mapped the dynamic of spatiotemporal interactions of crowded stimulus orientations in normal and amblyopic eyes. For normal eyes, crowding occurs at locations adjacent to the target in space and around or before the target presentation in time. Different types of cues may affect the spatiotemporal interaction map differently, but the strongest crowding never coincides with the target presentation. The amblyopic spatiotemporal interaction map is not substantially different from that of the normal eyes, except that in general the spatiotemporal interaction is more widely distributed around and after the target presentation. “Anti-crowding” – repulsion of perceived orientation that is induced by farther flankers is documented in both normal and amblyopic eyes.

In the fourth series of experiments, an adaptive optics scanning laser ophthalmoscope (AOSLO) was used to record fixational eye movements, allowing direct viewing of retinal movements and fixation locations. Fixational eye movements were modeled as a stochastic process governed by a potential function assumed to have the form of a quadratic polynomial for both normal and strabismic amblyopic observers. Our results confirm that microsaccades, on average, correct for fixation inaccuracy. Microsaccades occur more frequently and tend to move faster towards the target at relatively large displacements. Drift is modeled as a Brownian motion with constant rate over time plus an error-correcting component initially following a microsaccade. The unstable eccentric fixational eye movements in strabismic amblyopia are characterized by frequent intrusive saccades with large amplitudes and high speeds. The strabismic amblyopic fixation pattern on multiple loci is task dependent, with less eccentric but unstable fixation induced by challenging tasks, and relatively stable fixation by small highly visible static targets.

INTRODUCTION

Human visual functions, such as resolution, binocular vision, position acuity, and other higher-level visual functions, mature with post-natal visual experience at different stages. An arrest of the normal visual development caused by strabismus, anisometropia, etc. early in life will result in unbalanced binocular competition and the subsequent pathological vision in the weaker eye. This developmental visual disorder is called amblyopia (1991; Levi, 1991; Levi & Carkeet, 1993). Since the fine tuning for different visual functions during post-natal development is not yet understood, the range and depth of amblyopic visual deficits are still unclear. Studying normal and amblyopic vision together will provide insights into each other and facilitate our understanding of both.

Previous studies have shown evidence that strabismic amblyopia is like the normal peripheral vision, whereas anisometropic amblyopia is like the degraded normal foveal vision (Ciuffreda et al., 1991; Levi, 1991; Levi & Carkeet, 1993). Although screened by the same criteria, these two subtypes of amblyopia behave quite differently in many visual tasks. The visual loss in anisometropic amblyopia is often a direct consequence of the reduced contrast sensitivity and can be compensated by equalizing the stimulus visibility for the amblyopic and the nonamblyopic eyes. However, like normal peripheral vision, strabismic amblyopia is characterized by "extra loss" that cannot be accounted for by the reduced contrast sensitivity alone. The limits of strabismic amblyopia as well as those of peripheral vision seem to reside at higher cortical levels. One such perceptual bottleneck shared by both strabismic amblyopia and the normal peripheral vision is crowding – the impaired visibility of a target embedded in similar distracters in the vicinity, which may be related to cortical magnification physiologically or feature integration semantically (Levi & Klein, 1985). Position acuity that probably also requires higher-level processing is similarly more severely worsened in strabismic amblyopia and in the normal peripheral vision, compared to the grating acuity that is solely determined by the contrast sensitivity function (Levi & Klein, 1982; Levi & Klein, 1985). These qualitative characteristics of visual functions suggest the similarity between strabismic amblyopia and the normal peripheral vision. However, a quantitative comparison (i.e. functions that characterize all conditions) would serve as an even stronger argument, and a more general task would add significant weight to the hypothesis, both of which are the goals of the first and second series of experiments. In this series of studies, we applied a modified letter acuity task commonly used in a clinical setting and quantitatively characterized the unflanked and flanked letter identification limits in both the strabismic and anisometropic amblyopic fovea, as well as both in the normal fovea with different amounts of optical blur and at different eccentricities. The relationship between unflanked and flanked acuities should be the same for strabismic amblyopia and the normal periphery, and for anisometropic amblyopia and the normal blurred fovea, respectively, if the hypothesis stated at the beginning of this paragraph is correct.

Visual perception is a multi-dimensional and multiscale process. The familiar letter identification task in the first series of experiments involves a large amount of visual information processing whose exact mechanism is still beyond our understanding. More basic problems include mechanisms for detecting simple features such as contrast and orientation of a complex image (e.g. a letter or a face), under uncrowded or crowded conditions. These perceptual mechanisms are dynamic, acting in space and time. Previous studies on temporal or contrast sensitivity functions have shown that the visual system prefers stimuli that vary in space and time, which is reflected by the on/off structure in both spatial and temporal response profiles (Hubel & Wiesel, 1959; Kelly, 1971a, 1971b; Kelly & Savoie, 1978; Watson, 1986). However, the spatiotemporal interaction of perceptual mechanisms has rarely been studied in amblyopia (Levi & Harwerth, 1977).

In the first of the third series of experiments, we applied the method of classification images to estimate the human spatiotemporal template for detecting a simple image feature embedded in independent spatiotemporal noise (Ahumada, 1996). Using this method, much more freedom than in earlier studies was allowed for both normal and amblyopic observers to apply their strategies to perform this task, and we expected to obtain more natural and better defined human templates under normal or pathological conditions. The temporal mechanisms for detecting a crowded feature are largely unknown (but see Westheimer & Hauske, 1975). In the second of the third series of experiments, the same method of classification images was used to characterize the spatiotemporal interactions of the crowded stimuli in the strabismic amblyopic fovea and the normal periphery. Given that crowding exists in both strabismic amblyopic central vision and normal peripheral vision, the purpose of this experiment is to investigate the dynamic in more detail.

Visual functions such as letter identification or simpler image feature detection described above are built upon physical foundations that include the anatomical structures of the eye and beyond, the physiological properties of neurons, the saccadic eye movements that bring objects of interest to the fovea, and the fixational eye movements that prevent perceptual fading caused by neural adaptation. The fourth series of experiments and analysis focus on the quantitative modeling of the oculomotor mechanisms of fixational eye movements in normal and strabismic amblyopic eyes, which is the basis of understanding the fixational eye movements' importance in visual perception and development (Martinez-Conde, 2006; Martinez-Conde, Macknik, & Hubel, 2004). An adaptive optics scanning laser ophthalmoscope (AOSLO) was used in this study as a novel eye tracker, which allows direct observation of the target image on the retina and hence the fixation location relative to the fovea (Roorda, Romero-Borja, Donnelly III, Queener et al., 2002). The two components of the fixational eye movements, namely drifts and microsaccades, are modeled as stochastic processes constrained by the potential functions (Brillinger, 2007a), which capture both the randomness and the non-random error-correcting property of the fixational eye movements in a natural way. Strabismic amblyopic fixational eye movements are known to be abnormally erratic with frequent intrusive saccades (Ciuffreda,

Kenyon, & Stark, 1979a). In this study, we also quantitatively characterized the fixational eye movements of both eyes of a strabismic amblyopic observer who had large unstable eccentric fixation in the amblyopic eye, in an attempt to answer questions such as “what components are abnormal, what are normal?” or “does the fixation pattern depend on task?”. We believe the systematic modeling of fixational eye movements in normal and amblyopic eyes will build important basis for future studies on their possible physiological roles in visual perception.

THREE LIMITS ON LETTER IDENTIFICATION

BY NORMAL AND AMBLYOPIC OBSERVERS

1 Introduction

Identifying letters is essential to full participation in literate society. Since Snellen (1866), it has been the most popular test of vision. The conventional acuity chart is intended to measure the threshold size for identifying an isolated letter. The discovery of "crowding" revealed that, in the central vision of amblyopes and the peripheral vision of normals, the measured acuity is affected by the presence of other letters in the vicinity of the target letter (Bouma, 1970; Korte, 1923; Stuart & Burian, 1962). When objects are closer together than the "critical spacing of crowding", the visual system combines features from them all, producing a jumbled percept. Acuity is a size limit: the smallest readable letter size. Crowding is a spacing limit: What matters is center-to-center spacing, not size. Critical spacing has been measured under a wide range of conditions, but there is no systematic study of how size and spacing together limit legibility of a letter among flankers (neighboring letters).

Knowing that some amblyopes, unlike normals, have crowding in central vision, and that this abnormal crowding accounts for their reading deficit (Levi, Song, & Pelli, 2007), has raised interest in clinical testing for crowding. Furthermore, the childhood development of crowding and reading may be linked (Pelli & Tillman, 2008). Here we present systematic measurements of the size and spacing requirements for legibility of a flanked letter, which led us to develop a simple model for how legibility is limited by acuity, crowding, and "overlap masking". This model helps us interpret our amblyopic results and optimize a flanked acuity test (to be used in conjunction with standard acuity) as a clinical test for crowding.

Amblyopia is a developmental disorder of vision. It is most often associated with strabismus or anisometropia during early life, and these amblyogenic factors are associated with different psychophysical losses (McKee, Levi, & Movshon, 2003). Both strabismic and anisometropic amblyopes have reduced contrast sensitivity. Other visual dysfunctions such as reduced Snellen acuity and Vernier acuity, abnormal spatial interaction, and spatial distortions have also been observed (Ciuffreda et al., 1991; McKee et al., 2003). Normal peripheral vision shows many characteristics in common with those of central vision in strabismic amblyopia and hence peripheral vision has been proposed as a model for strabismic amblyopia (Levi, 1991; Levi & Carkeet, 1993). Non-strabismic anisometropic amblyopia, on the other hand, is thought to represent degraded foveal vision, since the impairment can be nulled by a task-invariant scaling of stimuli. That is, a single scaling of size and contrast allows an anisometropic

amblyope to perform various visual tasks as well as normal individuals do, or nearly so (Hess & Demanins, 1998; Levi, 1991; Levi & Carkeet, 1993). In other words, anisometropic amblyopes see the scaled stimulus nearly as well as normal observers see an unscaled stimulus.

Overlap masking is a reduced sensitivity of the target produced by an overlapping distractor. It is independent of eccentricity and its extent scales with the size of the signal (Levi, Klein, & Hariharan, 2002; Pelli, Palomares, & Majaj, 2004). Overlap masking depends on overlap and decreases rapidly when distractor-target spacing is increased beyond contiguity. It is thought to represent interference by the distractor's stimulation of the feature detector that normally responds to the target.

Among the amblyopic deficits discussed above, abnormal spatial interaction (through overlap masking and crowding) seems to be an important limit to daily vision. Overlap masking in central vision and crowding in peripheral vision are both mechanisms by which nearby objects reduce recognition (Levi, 2008; Levi, Hariharan, & Klein, 2002b; Levi, Klein et al., 2002; Pelli et al., 2004; Pelli & Tillman, 2008). Crowding is a decreased ability to recognize a target in clutter (Bouma, 1970) with no loss of detectability (Pelli et al., 2004). Crowding is unlike overlap masking, which does affect detection, making the target disappear. A crowded target is unrecognizably jumbled, but still detectable.

Critical spacing S_{critical} is the minimum center-to-center spacing of the flankers (from the target) that eliminates their interference. The critical spacing of overlap masking is proportional to target size and independent of eccentricity; the critical spacing of crowding is proportional to eccentricity and independent of target size (Pelli et al., 2004). At fixation, critical spacing scales with target size and is accounted for by overlap masking (Levi, Klein et al., 2002). In the periphery, critical spacing increases in proportion to eccentricity and is accounted for by crowding.

Amblyopia impairs both detection and identification of a target in clutter (Bonneh, Sagi, & Polat, 2004; Ellemberg, Hess, & Arsenault, 2002; Hess & Jacobs, 1979; Levi, Hariharan, & Klein, 2002a; Levi & Klein, 1985; Polat, Bonneh, Ma-Naim, Belkin, & Sagi, 2005). A recent study compared flanked and unflanked letter acuity in a large cohort of amblyopes, finding that flanked acuity is highly correlated with unflanked acuity in non-strabismic anisometropic amblyopia but not in strabismic amblyopia (Bonneh et al., 2004). Flanker effects in amblyopic central vision are not yet well understood. Based on the above discussion of existing models for strabismic and non-strabismic anisometropic amblyopia, here we ask whether eccentricity or blur in a normal eye can mimic the central effects of strabismic and non-strabismic amblyopia.

More generally, it has recently been suggested that object recognition is usually limited by spacing, not size (Pelli & Tillman, 2008). Measuring flanked and unflanked acuity with various spacings allows us to expose both the spacing and the size limits.

The world is cluttered, so the flanked acuity may be more directly relevant to everyday vision than unflanked (ordinary) acuity. There is some evidence that reading speed and crowding improve together during childhood (Atkinson, 1991; Atkinson, Anker, Evans, Hall, & Pimm-Smith, 1988; Atkinson, Pimm-Smith, Evans, Harding, & Braddick, 1986; Kwon, Legge, & Dubbels, 2007; Pelli & Tillman, 2008) making it potentially useful to have a convenient clinical test for crowding.

2 Methods

Stimuli were generated by an Apple G4 PowerBook using MATLAB with the Psychophysics Toolbox extensions and presented on a gamma-corrected Sony G400 monitor with the (green) background luminance set to 30 cd/m^2, the middle of the monitor's range (Brainard, 1997; Pelli, 1997). All stimuli were displayed at 60% Weber contrast.

2.1 Observers

Twenty one observers participated in our study. Eighteen were amblyopic (twelve were strabismic, six of whom had both strabismus and anisometropia; and six were non-strabismic anisometropes) and three had normal vision. Amblyopia is diagnosed when a complete eye examination reveals that the best corrected visual acuity is either poorer than 20/30 or is at least two lines worse than that of the contralateral eye, in the absence of any obvious structural anomalies or pathologic signs. We classified an amblyope as non-strabismic if associated with amblyogenic anisometropia but not strabismus; and as strabismic if associated with an early-onset, constant, and unilateral deviation at both near and far, whether or not they had anisometropia. In the text that follows we will often describe observers as either strabismic or non-strabismic; however, in the Figures we will separately color-code amblyopes with pure anisometropia (green), pure strabismus (red), and strabismus with anisometropia (blue), i.e., we follow the color code used by McKee et al. (2003). The detailed characteristics of each of the normal and amblyopic observers are listed in Table 1. All observers except VC and SF have central or near central (< 0.5 deg) steady fixation, as determined via visuoscopy. Strabismic-&-anisometropic observer VC has large eccentric fixation (about 8 deg) in her amblyopic (right) eye. Strabismic amblyopic observer SF has unsteady eccentric fixation in his amblyopic (left) eye. In order to examine SF's fixation pattern more carefully, we recorded a highly magnified view of his retina as he attempted to fixate a 6x6 min cross presented at the center of a 2.5x2.5 deg field for 20 seconds, using an Adaptive Optics Scanning Laser Ophthalmoscope (AOSLO - (Roorda, Romero-Borja, Donnelly III, & Queener, 2002). This method allows the target image to be superimposed synchronously on the retinal image, and makes it possible to accurately locate the target relative to the fovea. This recording shows that SF initially fixated within 0.5 deg nasal to the fovea (right of the fixation target). Fixation was maintained near the fovea for about 3 seconds and then drifted up to several degrees nasalward (see Discussion). The amblyopic eye of each amblyopic observer and the preferred eye of each

normal observer were tested monocularly. All normal observers had or were given substantial experience (hundreds or thousands of trials) in experiments that required peripheral viewing. The experimenter monitored every observer's eye position to ensure that fixation was maintained, discarding the few trials in which it was not, which comprise less than 5% of the total number of trials.

Observer	Age (yrs)	Strabismus (at 6 m)	Eye	Refractive error (diopters, D)	Line letter VA (single letter VA)	Stereo*	Threshold spacing (deg)	Acuity size (deg)	Crowding -acuity ratio	Eq. blur (D)	Eq. ecc. (deg)
Normal											
AF	22	None	R	+0.25/-0.50x180	20/12.5	20”	—	—	—	—	—
			L	+0.25/-0.25x25	20/12.5		0.123	0.083	1.48	0	0.19
EJ	21	None	R	-2.50/-0.50x83	20/12.5	25”	—	—	—	—	—
			L	-3.00	20/12.5		0.190	0.143	1.33	0.33	0
SS	28	None	R	-0.25	20/12.5	20”	0.138	0.103	1.34	0.13	0
			L	pl/-0.25x119	20/12.5		—	—	—	—	—
Strabismic-&-not-anisometropic											
JS	22	L EsoT 6-8$^{\Delta}$ & HyperT 4-6 $^{\Delta}$	R	+1.25	20/16	fail	—	—	—	—	—
			L	+1.00	20/40 (20/32^{+1})		0.257	0.102	2.52	0.15	2.06
SF	19	L ExoT 6$^{\Delta}$	R	-1.50/-0.25x90	20/12.5^{+1}	fail	—	—	—	—	—
			L	pl/-1.00x30	20/125^{+1}(20/80^{+2})		0.993	0.523	1.90	1.58	0.94
GW	58	R EsoT 4-6$^{\Delta}$	R	pl	20/63^{-2}(20/24^{+2})	fail	4.398	0.353	12.46	1.05	20.17
			L	+0.50/-0.75x180	20/16^{-1}		—	—	—	—	—
JZ	19	L EsoT 4$^{\Delta}$	R	pl/-0.50x95	20/16^{+2}	fail	—	—	—	—	—
			L	-0.25/-0.50x50	20/63^{+2} (20/32^{-1})		0.440	0.173	2.54	0.45	2.13
BN	22	L EsoT 3-4$^{\Delta}$	R	+5.50/-2.25x5	20/16^{+2}	fail	—	—	—	—	—
			L	+5.50/-1.50x175	20/50^{-2} (20/25^{-2})		0.638	0.210	3.04	0.58	3.01
CL	19	R EsoT 4$^{\Delta}$	R	-0.75	20/50^{+2} (20/32^{-2})	fail	0.538	0.255	2.11	0.73	1.32
			L	-0.25/-0.50x55	20/16^{-2}		—	—	—	—	—
Strabismic-&-anisometropic											
SM	55	Alt. ExoT 18$^{\Delta}$	R	+2.75/-1.25x135	20/40 (20/25^{+1})	320”	0.455	0.208	2.19	0.57	1.48
			L	-2.00	20/16^{-2}		—	—	—	—	—
JD	19	L EsoT 3$^{\Delta}$	R	+2.50	20/16	fail	—	—	—	—	—
			L	+5.00	20/125 (20/125^{+2})		0.765	0.413	1.85	1.24	0.86
AW	22	R EsoT 4-6$^{\Delta}$ & HypoT 4$^{\Delta}$	R	+2.75/-1.0x160	20/80^{-1} (20/50^{-1})	fail	0.638	0.258	2.47	0.74	1.99
			L	-1.00/-0.50x180	20/16^{-1}		—	—	—	—	—
GJ	23	R EsoT 4-5$^{\Delta}$	R	+3.50/-1.00x97	20/63^{+1} (20/40^{-1})	fail	0.805	0.200	4.03	0.55	4.81
			L	pl	20/16^{-1}		—	—	—	—	—
AP	24	L EsoT 4-5$^{\Delta}$ & HyperT 2-3$^{\Delta}$	R	-1.25/-0.50x175	20/16^{-2}	fail	—	—	—	—	—
			L	-0.50/-0.25x60	20/50^{+1}(20/40^{+2})		0.580	0.225	2.58	0.63	2.18
VC	23	R ExoT 5-6$^{\Delta}$	R	+4.25/-1.50x10	20/200^{-4} (20/125^{-1}) 20/12.5^{-1}	fail	17.740	0.958	18.52	2.92	31.18
			L	pl/-0.50x170			—	—	—	—	—
Non-strabismic (purely anisometropic)											
SC	27	None	R	+0.50	20/16^{+2}	fail	—	—	—	—	—
			L	+3.25/-0.75x60	20/50^{+2} (20/40^{-2})		0.332	0.220	1.51	0.61	0.24
CJ	22	None	R	-15.00/-1.25x150	20/125^{-4} (20/125^{+1}) 20/16^{-2}	200”	0.936	0.512	1.83	1.55	0.81
			L	-6.00			—	—	—	—	—
AM	48	None	R	+0.75/-0.70x95	20/12.5	200”	—	—	—	—	—
			L	+2.00	20/32^{-2} (20/25^{-2})		0.240	0.200	1.20	0.55	0
RA	15	None	R	-2.00/-1.75x155	20/32^{+1} (20/32^{+1})	70”	0.423	0.253	1.67	0.72	0.53
			L	+0.25/-0.25x60	20/12.5		—	—	—	—	—
SWP	24	None	R	-0.25	20/16^{+2}	30”	—	—	—	—	—
			L	+1.75/-0.25x45	20/32^{+2} (20/32^{+2})		0.383	0.250	1.53	0.72	0.27
SW	42	None	R	+2.00/-0.50x90	20/12.5^{-2}	200”	—	—	—	—	—
			L	+4.25/-1.25x120	20/80^{-2} (20/63^{-1})		0.675	0.493	1.37	1.49	0

Table 1: Observer characteristics. The rightmost 5 columns (threshold spacing, acuity, crowding-acuity ratio, equivalent blur, and equivalent eccentricity) are plotted in Results. *Stereopsis was measured using Randot “Random Dot Geometric Form” test (Stereo Optical Co.).

2.2 Unflanked & flanked letter identification

For each amblyopic observer, we measured the threshold size for letter identification, with and without flankers, with central viewing, by the amblyopic eye. For each normal observer, the

same measurements were made at 5 different eccentricities. *Threshold spacing S = sA'* is the center-to-center spacing in deg between target and flanker at threshold size, where *s* is the spacing factor (multiple of the letter size) and *A'* is the flanked acuity in deg. *Acuity A* is the threshold size in deg without any flanker, not its reciprocal (one over size). In Results we report the threshold spacing *S* and the (unflanked) acuity *A*. Our measurement of flanked and unflanked acuity to test for crowding is computerized, which allows us to vary size and spacing systematically and control duration, but is otherwise similar to some older printed tests, such as Tommila's (1972) flanked and unflanked tumbling E charts and the Cambridge Crowding Cards (Atkinson et al., 1988; Atkinson et al., 1986).

Figure 1. Unflanked and flanked letter identification tasks. The observer is asked to fixate the center of the fixation mark and to identify the target letter. The target letter is subsequently presented, briefly, either alone (unflanked) or surrounded (flanked) by four random letters of the same size. The center-to-center letter spacing in deg between the target and the flankers scales with letter size and is *s* times the letter size, where *s* is usually 1.1. The results with larger spacings (up to 6 times the letter size) plotted in Fig. 2 are an exception to this. In each case, we use an adaptive procedure (QUEST) to determine the threshold size (covaried with spacing) for 50% correct identification.

The fixation mark consisted of 4 black diagonal lines (0.1 deg thick) forming an X (2 deg wide and 2 deg high) with a 1 deg diameter gap in the center. The same fixation mark was used for both central and peripheral viewing. Observers were instructed to fixate the invisible intersection point of the lines. In the unflanked letter identification task, the target, a single letter, was presented for 200 ms, either centered at fixation, or in the lower visual field at one of these eccentricities: 1.25, 2.5, 5, 10 deg. In the flanked letter identification task, the target, the letter to be identified, was flanked by four letters (above, right, below, and left). All 5 letters were presented in the same manner as the unflanked letters (Fig. 1). The target (and each flanker, if present) was randomly selected (with replacement) from nine letters of the Sloan alphabet DHKNORSVZ, displayed at 60% contrast as a bright green letter on a dimmer green background. We omit C from the Sloan alphabet because it has been shown that C and O are much less discriminable than any other pair of letters in that alphabet (Elliott, Whitaker, & Bonette, 1990). Letter contrast is defined as the ratio of luminance increment to background. Each presentation was initiated by clicking the mouse and followed by a response screen, showing the nine possible choices for the target. The observer identified the target by using a

mouse-controlled cursor to point and click on the chosen answer. Correct identification was rewarded by a beep.

The Sloan font is uppercase-only. Every letter in each trial has the same height and width, which we take as the letter *size*. For flanked letters, the center-to-center spacing between any flanker and the central letter is the letter size multiplied by s. The letter spacing factor s is 1.1 unless indicated otherwise. (The unflanked case may be designated $s = \infty$.) In our experiments, we adjusted the letter size using QUEST to measure the threshold size for unflanked and flanked letter identification. Our threshold criterion is 50% correct. Each run of 40 trials of the same condition yields one threshold estimate for that condition. Thresholds presented here are the geometric means of estimates from at least 4 runs.

Using a fixed spacing factor s, our threshold measurement procedure covaries the spacing and size when measuring threshold for flanked letter identification. In most of our experiments, this (i.e. $S = sA'$) is an efficient way to estimate critical spacing (Levi, Song et al., 2007). *Critical spacing* S_{critical} is the minimum spacing between the target and flankers that eliminates (or nearly eliminates, depending on the threshold criterion) the effect of the flankers (Bouma, 1970). As we will see in Results, threshold spacing in peripheral vision (eccentricity $\varphi \geq 1.25$ deg) equals critical spacing over a broad range of letter spacing (tight to loose, $1.1 \leq s < 4$), but threshold spacing can be larger than critical spacing when letter spacing is extremely loose ($4 < s$). In that case ($4 < s$) the flankers have no effect and the threshold spacing is limited by acuity ($S \geq sA$).

2.3 Spacing

Flanked acuities with larger flanker-target spacings were measured at fixation, and at 1.25 deg and 5 deg eccentricities of one normal observer (SS), and at the fixation of both one non-strabismic amblyopic observer (SW) and one strabismic-&-anisometropic amblyopic observer (AW). The center-to-center spacing factors s (multiples of the letter size) between flanker and target that we used are: 1.1, 1.6, and 2.2 at 0 deg (fixation), 1.1, 1.6, 2.2, 3.3, and 5.5 at 1.25 deg, and 1.1, 2.2, 3.3, and 6 at 5 deg for SS; 1.1, 1.6, and 2.2 for SW; and 1.1, 2.2, 3, and 4 for AW. The procedure is as described above for flanked letter identification. For every experiment, we plot threshold spacing S. For this particular experiment, we also plot the flanked acuity A'. Threshold spacing $S = sA'$ is the product of the spacing factor s (multiple of the letter size) and the flanked acuity A'.

2.4 Timing

The temporal sequence of presentations in a trial is: fixation mark (until 400 ms after the observer's "I'm ready" click), stimulus (200 ms), and response screen (until the observer's response click). The stimulus consists of the target, with or without flankers.

These experiments were conducted over three years and some aspects evolved over that time. Initially we used the same methods as in our previous paper (Levi, Song et al., 2007). At that time, the fixation mark stayed on continuously through the stimulus presentation until it was overwritten by the response screen. Later, when measuring very poor acuities (e.g. with high optical blur), we found that a very large target would overwrite parts of the (fixed size) fixation mark, so we changed our procedure to remove the fixation mark before displaying the target. We have compared thresholds measured in the two ways (fixation mark present or absent during the target presentation) for key conditions, both with and without flankers, and find no difference, so we do not distinguish them in the results reported here.

There were no temporal gaps in the sequence, so it seemed possible, though unlikely, that there might be forward masking from the fixation mark or backward masking from the response screen. That concern can be put to rest: Introducing a 300 ms blank screen between the fixation mark and the stimulus and another 300 ms blank screen between the stimulus and the response screen had no effect on thresholds for the key conditions we tested.

2.5 Optical blur

One normal observer, SS, repeated the unflanked and flanked (at the spacing of 1.1 times the letter size) letter identification tasks at 0, 1.25, and 5 deg eccentricities while wearing blurring lenses (net +0.25, +0.50, +0.75, +1.00, +1.50, +3.00, +6.00, or +8.00 D for foveal viewing at the distance of 5, 1, or 0.56 m; net +0.50, +0.75, or +1.00 D for 1.25 deg eccentric viewing at the distance of 2.5 m; and net +0.50, or +1.00 D for 5 deg eccentric viewing at the distance of 1 m) in order to investigate the effect of optical blur. Two strabismic-&-anisometropic amblyopic observers, AP and GJ, and one non-strabismic amblyopic observer, SW, also repeated the same tasks at fixation while wearing a blurring lens which has the corrective refractive power plus an extra refractive power (net +1.00 or +1.25 D for AP, net +0.75 or +1.25 D for GJ and net +0.50 or +1.25 for SW) at the viewing distance of 2.5 m. The procedure is the same as described above for the unflanked and flanked letter identification.

Pinhole. We also measured acuities with a small artificial pupil (1.5 mm diameter) both for normal observer SS with a 0, +1, or +1.5 D lens and for a non-strabismic amblyope SW with a corrective lens.

2.6 Pupil size

The optical defocus produced by our blurring lenses increases the size of the eye's point spread function in the retinal image (Campbell & Gubisch, 1966). Optically, that point spread function determines how blurry the retinal image is. The size of the point spread function resulting from a given amount of defocus (in diopters) depends on the pupil size. Depth of field (i.e. tolerance of defocus) is greater at smaller apertures because more defocus (D) is required

to produce the same blur in the retinal image. Pupil size affects the optical blur and the retinal illuminance, both of which affect the target's visibility.

Of course, the optical aperture is different when we compare thresholds with and without the 1.5 mm pinhole. The pinhole improved the MTF (Modulation Transfer Function) but reduced retinal illuminance by roughly fivefold. To disconfound the two effects of the pinhole, we separately used a neutral density filter (density 0.7, 20% transmission) combined with an artificial pupil (3.5 mm) to assess the isolated effect of reducing retinal illuminance.

Most of our conclusions are based on comparisons of visual functions under flanked and unflanked conditions, and a change in pupil size between these two conditions would make it hard to compare them, but we have avoided that problem by basing our main conclusions on comparisons of measurements within individuals at the same luminance and by alternating flanked and unflanked identification runs. All experiments were performed with the same dim overhead lighting. We are confident that each observer's pupil size (3 – 4 mm) is not significantly different between flanked and unflanked trials (see Discussion).

3 Results

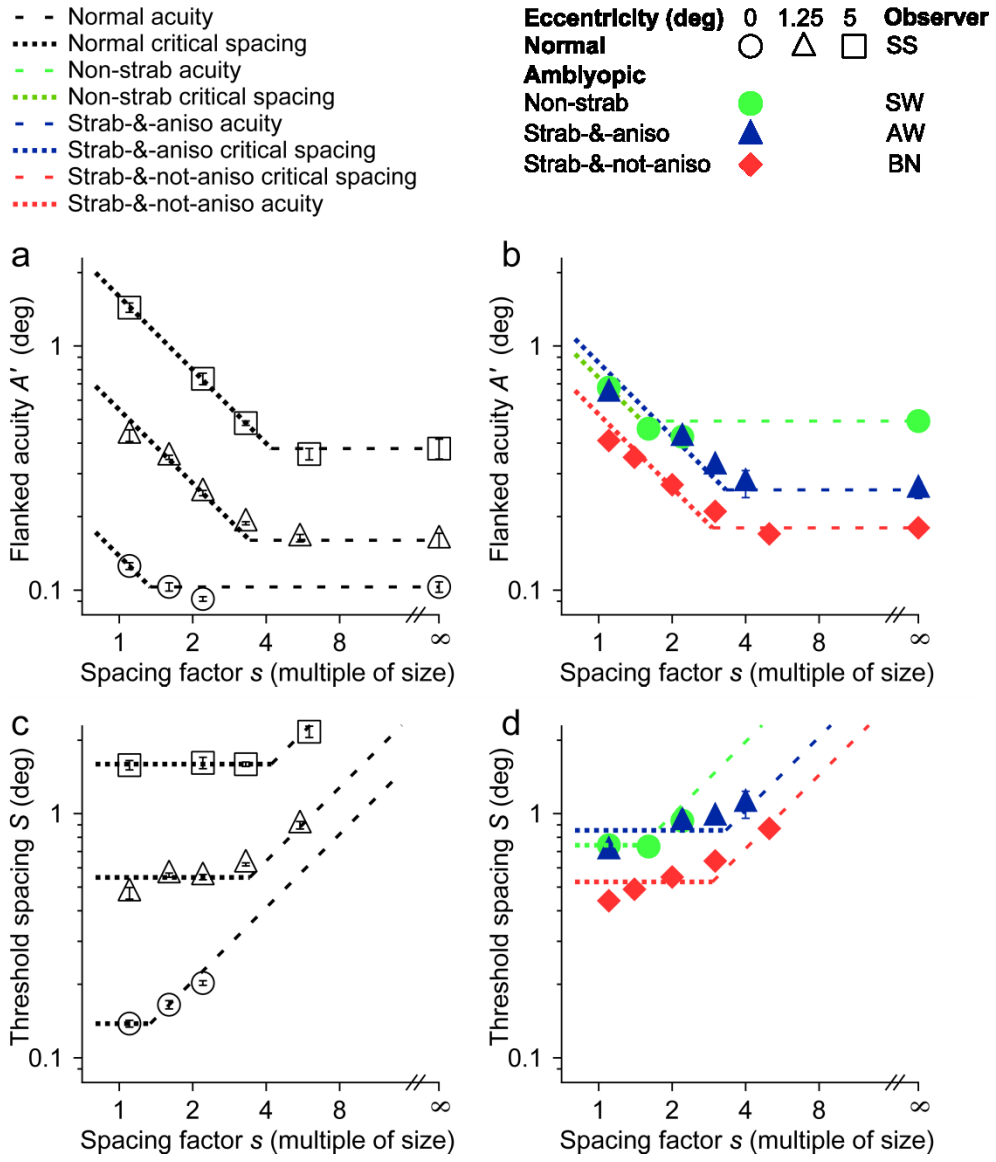

Figure 2. Flanked letter acuity (a & b) or threshold spacing (c & d) vs. letter spacing factor (multiple of the letter size) for normal (a & c) and amblyopic (b & d) observers. Thresholds for the normal observer are measured at 0 deg (circle), 1.25 deg (triangle), and 5 deg (square) eccentricities; thresholds for the non-strabismic amblyope (green) and the strabismic amblyopes (red, blue) are measured at fixation. The error bars on each data point indicate plus-or-minus one standard error. The same data and models are plotted twice: in the upper graphs (a & b) as flanked acuity *A'* and in the lower graphs (c & d) as threshold spacing *S*. Threshold spacing $S = sA'$ is the product of the letter spacing factor *s* and the flanked acuity *A'*. For each observer, the horizontal line (dashed) in the upper graphs (a & b) is the (unflanked) acuity *A* (rightmost point), and the horizontal line (dotted) in the lower graphs (c & d) is the critical spacing $S_{critical}$, estimated as the

geometric mean of the points that lie above the (extended) dashed line. The data and lines are converted back and forth between upper and lower graphs by the relation log S = log s + log A'.

3.1 Size and spacing

We begin with a systematic examination of the size and spacing requirements for identification of a flanked letter by a normal observer at three eccentricities (Fig. 2ac) and three amblyopes at fixation (Fig. 2bd). The horizontal scale is the letter spacing factor s, the center-to-center letter spacing expressed as a multiple of letter size. In the upper graphs (Figs. 2ab), the vertical scale is flanked acuity A'. In the lower graphs (Figs. 2cd), it is threshold spacing S. Upper and lower graphs are different views of the same data. In the log-log coordinates of Fig. 2, each dashed line represents a size limit (i.e. acuity A), and each dotted line represents a spacing limit (i.e. critical spacing S_{critical}, due to crowding or overlap masking). The lines have been trimmed in the graphs so that only the higher (more severe) limit is shown. The data points are all close to the higher limit, showing that the two limits, size and spacing, together account for all the data

$$S = \max (sA, S_{\text{critical}}). \qquad (1)$$

This model has two degrees of freedom (acuity A and critical spacing S_{critical}) for each observer at each eccentricity.

Amblyopes. The amblyopic results (Fig. 2bd) are well fit by the same model, and anticipate some of our main findings. Comparing left and right, we find that the two strabismic amblyopes' results at fixation (filled triangles and diamonds in Fig. 2bd) are much like those of the normal observer viewing eccentrically (1.25 deg in this case, open triangles in Fig. 2ac). The non-strabismic amblyope's results (filled circles in Fig. 2bd) are like those of the normal at zero eccentricity (open circles in Fig. 2ac) but shifted up (in these log coordinates) to higher (worse) flanked acuity and threshold spacing.

3.2 Eccentricity and blur

Normal vision at increased eccentricity has often been suggested as a model for amblyopia, as noted above. Optical defocus (blur) is another appealingly simple model, since the main effect of blur is to impair acuity and poor acuity is the main diagnostic criterion of amblyopia. The two models are very different. Increasing eccentricity and adding blur have qualitatively different effects on letter identification by normal observers (Fig. 3). When viewing directly, adding blur worsens acuity and threshold spacing for letter identification (open circles in Fig. 3) by the same proportion. In the log-log coordinates, the slope of the regression line (not shown) of thresholds at fixation with blur is 0.99±0.02 (M±SE), which is not significantly different from 1, so we fit and display a unit-slope line (dotted) log S = 0.14 + log A, i.e. S = 1.4A. In other words, adding blur at fixation (open symbols) increases both thresholds by the same

proportion, so their ratio *S/A* is preserved. On the other hand, increasing eccentricity (filled black symbols) results in a disproportionate impairment of threshold spacing. This is the well-known crowding effect. The slope of the regression line (dashed) of thresholds at various eccentricities is 1.75±0.17 in the log-log coordinates, telling us that, as eccentricity is increased, threshold spacing increases much faster than acuity. Note that the three filled gray symbols, representing the three normal observers viewing directly, scatter along the dotted line for blurred direct viewing, suggesting that this variation among normal individuals reflects differences in their blur (optical and neural).

The blur line (dotted) is remarkable, maintaining perfect proportionality over a 40:1 range. What could account for this? If the flankers had no effect, then the flanked acuity would equal the unflanked acuity $A' = A$ and the threshold spacing would be $S = sA' = sA$, but s is 1.1 in these measurements, and the ratio of threshold spacing to acuity S/A is 1.4±0.03, which is much larger than 1.1. Thus the flankers are effective, and we are measuring a spacing limit, not acuity. Blur smears the target's image on the retina. The smearing worsens acuity for the target and extends the image of each flanker, which may create enough overlap with the target, at the retina, to produce overlap masking. The measured threshold spacing of 1.4*A* over a 40:1 range (0.14 – 5.20 deg) of *A* suggests a smearing whose extent is a constant fraction of the acuity size. If the measured threshold spacing of flanked letter identification is always limited by smearing (optical and neural) then our results suggest that there may be a universal minimum spacing limit of wA, where $w = 1.4$, for identification of a flanked letter.

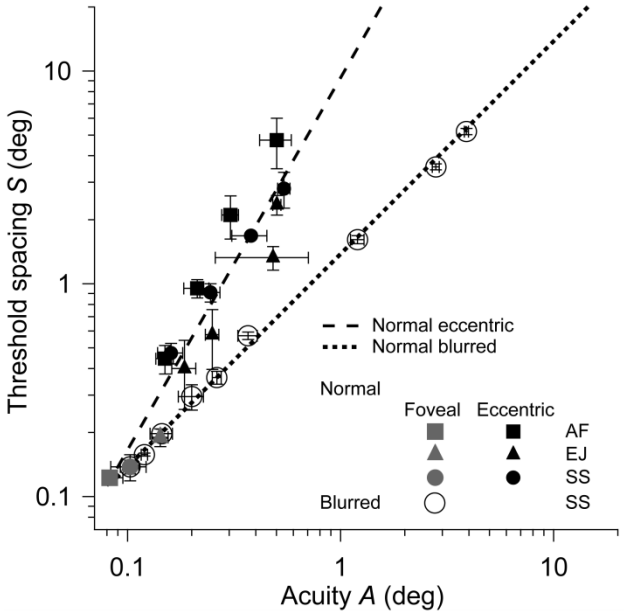

Figure 3. Effects of eccentricity and blur on acuity and threshold spacing in normal vision. Filled gray symbols represent the thresholds at fixation, and filled black symbols represent the thresholds at various eccentricities in the periphery of three normal observers. Refractive errors (if any) were fully corrected. Open

circles represent the thresholds at fixation of one normal observer wearing blurring lenses of various refractive powers (see Methods). The dashed regression line for the no-blur data at various eccentricities is $\log S = 0.97 + 1.75 \log A$, where A is acuity in deg and S is threshold spacing in deg. The regression line (not shown) for the zero-eccentricity data at various blurs is $\log S = 0.13 + (0.99 \pm 0.02) \log A$. Since that slope is insignificantly different from 1, we fit and display a line (dotted) with unit slope $\log S = 0.13 + \log A$, i.e. $S = 1.4A$. Note that the three filled gray symbols are all at fixation, so the differences among them are not an effect of eccentricity. They all lie on the blur line (dotted), suggesting that this variation among normal individuals reflects differences in their blur (optical and neural).

3.3 Strabismic and non-strabismic amblyopia

The amblyopic results (at zero eccentricity with no added blur) are plotted separately for non-strabismic (Fig. 4a) and strabismic amblyopes (Fig. 4b). For non-strabismic amblyopes (Fig. 4a), as for the normal observers with added blur, threshold spacing is approximately proportional to acuity. All data points fall near the blurred-normal line (dotted) and far from the eccentric-normal line (dashed). The regression line (solid) for all non-strabismic amblyopes has a log-log slope of 1.15±0.16, which is not significantly different from one, indicating that non-strabismic amblyopia is like normal vision with added blur, and unlike normal vision at increased eccentricity.

Compared to non-strabismic amblyopes (Fig. 4a), the strabismic amblyopes (Fig. 4b) show larger variance, but (with two exceptions discussed below) they lie well above the blurred-normal line (dotted) and near the eccentric-normal line (dashed). Since the strabismic-&-not-anisometropic (red symbols) and strabismic-&-anisometropic results (blue symbols) in Fig. 3b are similar, we combined them into one "strabismic" group, regardless of whether anisometropia is an associated condition or not. The regression line (solid) for all strabismic amblyopes has a log-log slope of 1.67±0.17, which is not significantly different from that for normals at increased eccentricities (log-log slope 1.75±0.17).

Fig. 4 shows that the amblyopic data are clustered by amblyopic type, i.e., the strabismic cluster (Fig. 4b) is higher than the non-strabismic cluster (Fig. 4a) at any given acuity. Given this arrangement, the two clusters cannot be distinguished by threshold spacing or acuity alone (i.e. a vertical or horizontal line, not shown), but are well distinguished by the combination (e.g. a tilted line, not shown). In fact we will see below that the ratio of threshold spacing to acuity S/A perfectly separates non-strabismics from strabismics in our 18 amblyopes (Fig. 6).

Note that the results for one strabismic-&-not-anisometropic amblyope (SF) and one strabismic-&-anisometropic amblyope (JD) fall close to the blurred-normal regression line (dotted). JD had participated in a host of experiments, including many experiments on crowding, and performed millions of trials with his amblyopic eye. SF had also participated in many experiments, and in particular, he had participated in an intensive training experiment involving roughly 50,000 trials of Vernier acuity, designed to treat adult amblyopes. As a consequence, his

Vernier acuity and his Snellen acuity had both improved substantially. We suspect that this very extensive experience resulted in a reduction in their crowding, similar to the perceptual learning observed by Chung (2007) in peripheral vision.

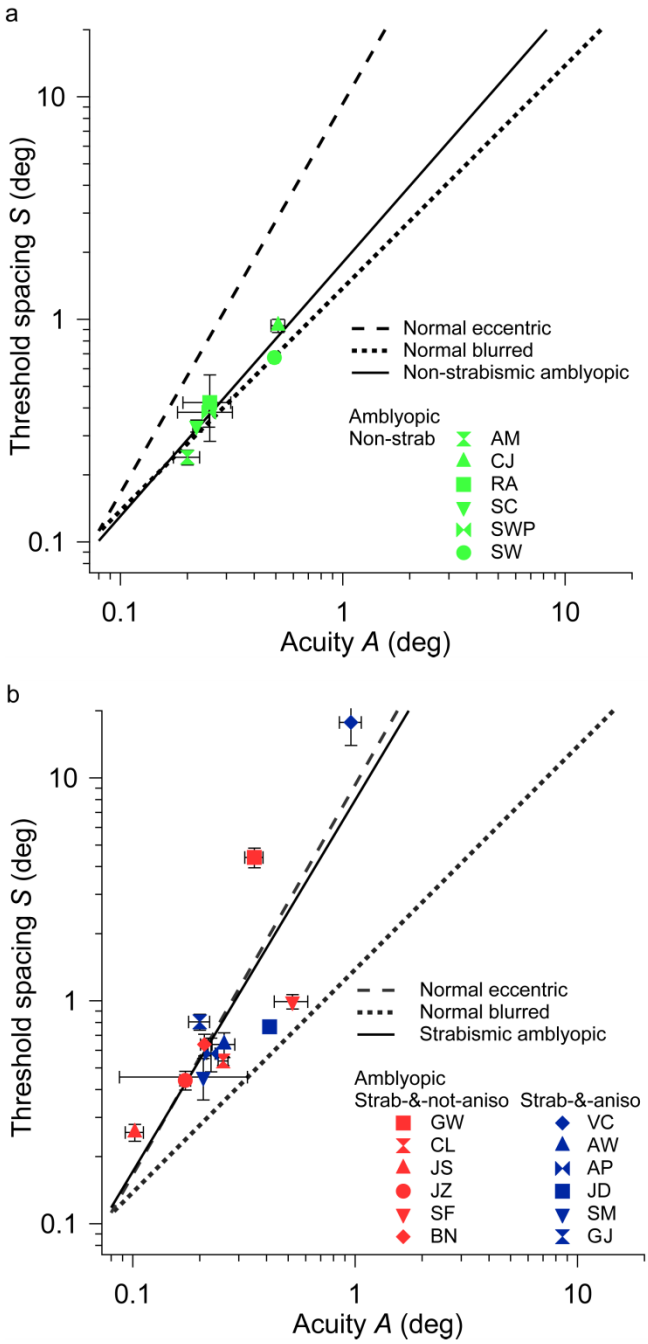

Figure 4. Threshold spacing vs. acuity for (a) non-strabismic (green) amblyopes and (b) strabismic (with or without anisometropia, blue and red) amblyopes. Amblyopic observers' threshold spacings are plotted against acuities. The dashed and the dotted lines are regression lines for normal eccentric and normal blurred results respectively, from Fig. 3. The solid lines are the regression lines of (a) non-strabismic amblyopes' thresholds,

log S = 0.26 + 1.15 log A, and (b) strabismic amblyopes' thresholds, log S = 0.90 + 1.67 log A. This graph also shows that the combination of threshold spacing and acuity is much better at distinguishing strabismic from non-strabismic amblyopes than is threshold spacing or acuity alone.

The parameters of each linear regression in the log-log coordinates are listed in Table 2. *RMS* (Root Mean Square) error is the square root of the mean of the squared differences between the log data and the regression line. The results plotted in Fig. 4 and summarized in Table 2 show a qualitative difference between strabismic and non-strabismic amblyopia in the effect of flankers. The increased-eccentricity model and the added-blur model provide reasonable fits to the threshold spacings and acuities of strabismic and non-strabismic amblyopes, respectively.

	Normal with various blurs	Non-strabismic amblyopic	Normal at various eccs.	Strabismic amblyopic
a	0.13	0.26	0.97	0.90
Slope *b*	0.99	1.15	1.75	1.67
SE of *b*	0.02	0.16	0.17	0.17
RMS error	0.026	0.053	0.155	0.286
Correlation	0.998	0.962	0.944	0.883

Table 2. Linear regressions of log threshold spacing versus log acuity: log $S = a + b \log A$.

3.4 Combining blur with eccentricity or amblyopia

For the normal observer, the effect of optical blur on threshold spacing and acuity is strikingly different at fixation than in the periphery (Fig. 5). Unlike blur at fixation, blur at 5 deg in the lower visual field worsens the acuity much faster than it worsens the threshold spacing, i.e., the square symbols shift much more markedly rightward (worsened acuity) than upward (increased threshold spacing), resulting in a flatter log-log slope. The regression line for 5 deg eccentricity with blur (log-log slope 0.13±0.05) is almost level compared to the regression line for blurred direct viewing (log-log slope 0.99±0.02), and the regression line for 1.25 deg with blur lies about halfway between those for direct viewing and for 5 deg eccentricity (log-log slope 0.49±0.06). Thus, farther in the periphery, threshold spacing is less affected by optical blur. For strabismic amblyopes (blue symbols), as for the normal at increased eccentricity, optical blur at fixation worsens the acuity faster than it increases the threshold spacing. The regression log-log slopes are 0.57±0.08 (GJ) and 0.45±0.07 (AP), both of which are substantially smaller than that for normal direct viewing with blur (log-log slope 0.99±0.02), but not significantly different from that at 1.25 deg eccentricity with blur (log-log

slope 0.49±0.06). Unlike this, with optical blur, non-strabismic amblyopes (green symbols) show a proportional relationship between threshold spacing and acuity (log-log slope 1), similar to normal direct viewing with blur (dotted line).

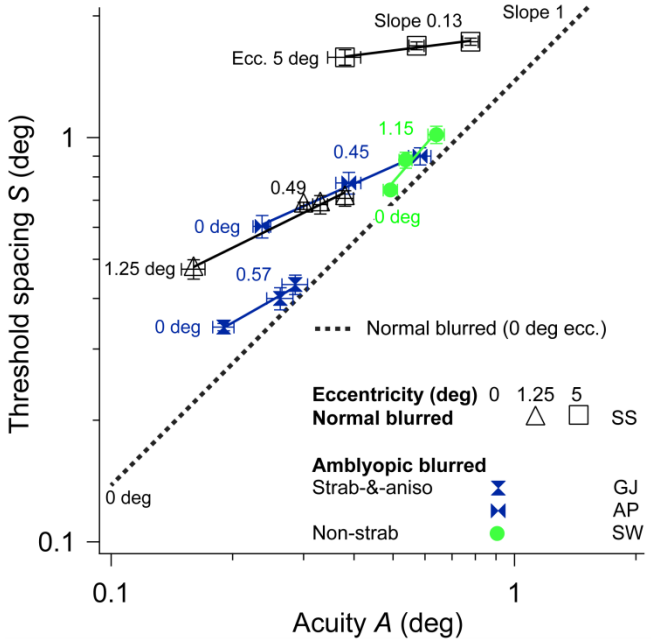

Figure 5. Effect of optical blur on the normal at increased eccentricity (open symbols) and amblyopes (filled symbols). The normal observer (open symbols) was tested at eccentricities of 0 deg (dotted line), 1.25 deg (open triangle), and 5 deg (open square); amblyopes (filled symbols) were tested at fixation (0 deg). Each measurement was obtained while the observer was wearing a blurring lens (see Methods) except for the leftmost data point for each observer, which was measured with refractive error (if any) fully corrected. The dotted regression line is a unit-slope line for normal direct viewing with blur, from Figure 2. Each solid line is a regression line for a different observer tested over a 1 D range of defocus (see Methods). The equation for SS at 1.25 deg is: $\log S = 0.07 + 0.49 \log A$; SS at 5 deg: $\log S = 0.25 + 0.13 \log A$; GJ: $\log S = 0.06 + 0.57 \log A$; and AP: $\log S = 0.06 + 0.45 \log A$.

4 Discussion

First, we present a very simple model for legibility of a flanked letter that accounts for all our results in terms of size and spacing limits due to acuity, overlap masking, and crowding. Second, we show that flanked and unflanked acuity, together, accurately distinguish strabismic from non-strabismic amblyopia, although this is not possible with either measure alone. Third, we recommend a simple clinical test to measure the crowding-acuity ratio. Finally, we show that strabismic or non-strabismic amblyopia is much like normal vision at increased eccentricity or with added blur, respectively.

4.1 Size and spacing

In a systematic exploration of the size and spacing requirements for identifying a flanked letter—at various eccentricities by normal and amblyopic observers—we found that all the data points are close to whichever limit, size or spacing, is more severe. Thus the two limits, size and spacing, together account for all the data (Fig. 2). That is nice, but we can go a step further and identify the failure mechanism responsible for each limit. We consider acuity, crowding, and overlap masking. The normal data are on the left (Fig. 2ac) and the amblyopic data are on the right (Fig. 2bd).

Acuity. The size limit (dashed line) in Fig. 2 is acuity. The vertical position of the horizontal dashed line in Fig. 2ab is set to go through the measured acuity (the point at infinite spacing). Thus acuity, represented by the dashed lines, accounts for the data points at loose spacings (letter-spacing factor $s >> 1$).

Crowding. The spacing limit (dotted line) could be crowding or overlap masking. At nonzero eccentricity, the critical spacing of crowding is known to be "roughly half" the eccentricity (Bouma, 1970) and, indeed, for the normal observer the spacing limit (dotted) is 0.6 and 1.8 deg at eccentricities of 1.25 and 5 deg, which correspond to fractions of 0.5 and 0.4. At zero eccentricity, the threshold spacing or flanked acuity is accounted for by overlap masking, not crowding, as discussed below. Thus crowding accounts for all thresholds at nonzero eccentricities except for those at very loose spacings, which are accounted for by acuity.

Overlap masking. Overlap masking is independent of eccentricity, and its extent scales with the size of the signal (Levi, Klein et al., 2002; Pelli et al., 2004). Overlap masking depends on the overlap of target and flanker and decreases rapidly when flanker-target spacing is increased beyond contiguity. Note that the retinal image is an optically blurred image of the display, so the target and flankers extend farther and overlap more in the retinal image than at the display. As noted in Results, the proximity of the target and flankers (e.g., spacing factor of 1.1) makes overlap masking a possible mechanism. (We find that the neural deficit of non-strabismic amblyopia is like optical blur, so the effective blur or "smearing" in normals and amblyopes may be a result of both optical and neural blur.) We suppose that the extent of smearing is a fixed fraction of the acuity size, so we expect the critical spacing of overlap masking to be proportional to acuity. This prediction is borne out beautifully in the normal blur data of Fig. 3. The ratio of threshold spacing to acuity is a fixed 1.4 over a 40:1 range of size (0.14 – 5.20 deg). Applying this spacing limit $S = 1.4A$ to the S vs. s data in Fig. 2, we find that it accounts for only the lower leftmost point in Fig. 2ac. Thus, for our data, overlap masking accounts for the threshold spacing at fixation when the spacing is tight ($s < 1.4$). The rest of the normal data ($s > 1.4$) are accounted for by crowding or acuity.

A model for legibility of a flanked letter. The lines in Fig. 2 represent a simple model for the size and spacing requirements of letter identification. There are three size-and-spacing limits

to legibility. A flanked letter is legible if and only if all three limits are respected. The acuity limit is that the flanked letter size must be at least acuity A, so the spacing will be at least $S_{acuity} = sA$. The crowding limit is that spacing must be at least the critical spacing $S_{crowding}$ of crowding. The overlap-masking limit is that spacing must be at least $S_{masking} = wA$. (The value is $w = 1.4$ for an adult normal observer, SS, tested with the Sloan font with four flankers, but may be larger for children and smaller for less-bold fonts.)

$$S = \max (S_{acuity}, S_{crowding}, S_{masking}) \quad (2)$$

$$= \max (sA, S_{crowding}, wA) \quad (3)$$

For any given acuity A, the three limits are independent. Apparently there is no interaction among these three causes of failure.

Amblyopes. For the non-strabismic amblyope (Fig. 2bd, green), as for the normal, only the data point with tight spacing ($s = 1.1$) at fixation is accounted for by overlap masking. Increasing the spacing from tight ($s = 1.1$) to loose ($s = 1.6$) switches the spacing limit from overlap masking $wA = 1.4A$ to acuity $sA = 1.6A$. Using tight spacing, we find a fixed ratio $S/A = 1.4 \pm 0.03$ for the normal over a wide range of optical blur (Fig. 3) and practically the same ratio 1.5 ± 0.09 for the non-strabismic amblyopes, though their blur is mostly neural (Fig. 4).

Crowding and reading. Recent work shows that the critical spacing for reading is equal to the critical spacing for crowding (Levi, Song et al., 2007; Pelli & Tillman, 2008; Pelli et al., 2007). When text is more closely spaced than critical, reading slows to a crawl. Critical spacing is very much larger in the periphery and in strabismic amblyopes. The maximal reading rate is greatly reduced in the periphery, but is unaffected by amblyopia. This surprising result is predicted by the uncrowded span model (Pelli et al., 2007), given the observation that the amblyopic crowding deficit is strictly central. Amblyopia greatly increases the small critical spacing (flanked letter acuity) in the central visual field, without affecting the larger critical spacings found more peripherally (Levi, Song et al., 2007), which determine the uncrowded span and thus reading rate.

4.2 Crowding-acuity ratio

We find, in close agreement with Bonneh et al. (2004), that the effect of flankers on acuity is qualitatively different in strabismic and non-strabismic amblyopes. The difference between strabismic and non-strabismic amblyopia is apparent in the combination of flanked and unflanked acuity, but not in either alone (Fig. 4).

We define the *crowding-acuity ratio* W as the ratio of threshold spacing S to acuity A, $W = S/A = sA'/A$. Empirically, given a spacing factor s, the crowding-acuity ratio is just the effect of flankers on acuity (equivalent to the "crowding ratio" or "crowding index" A'/A used by

Atkinson et al. (1988) and Levi, Yu, et al. (2007)). Theoretically, the crowding-acuity ratio tells us about the relative importance of spacing (due to crowding or overlap masking) and size (due to acuity). *W* equals *s* when flanked legibility is limited by size (*A'* = *A*), and *W* exceeds *s* when flanked legibility is limited by spacing (*A'* > *A*).

Stereopsis. We have combined all the strabismic amblyopes' data, regardless of anisometropia, into a single group for several reasons. First, it is clear from Fig. 4b that the data from strabismic amblyopes with and without anisometropia (blue and red) have similar distributions. By grouping them together, we obtained a larger sample of strabismic amblyopes. A large-scale study of amblyopia found that reduced visual resolution and loss of binocularity are key in determining the pattern of visual deficits (McKee et al., 2003).

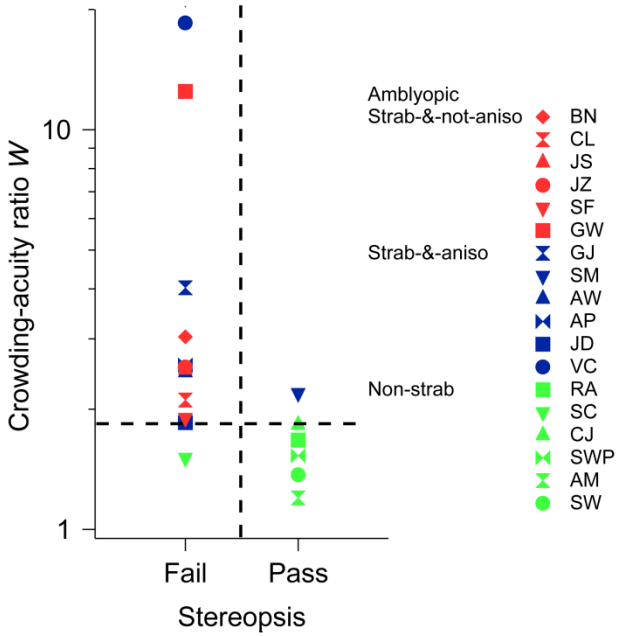

Figure 6. Crowding-acuity ratio vs. status of stereopsis for amblyopes. Amblyopes who failed the stereopsis test are plotted as "Fail"; everyone who has some amount of stereopsis is plotted as "Pass". The vertical dashed line divides the amblyopes into "Fail" and "Pass" groups, and the horizontal dashed line, *W* = 1.84, divides the amblyopes into two groups with large and small crowding-acuity ratio.

Fig. 6 and Table 1 show that all but one of the strabismic amblyopes (with or without anisometropia) failed the stereopsis test, whereas all but one of the non-strabismic amblyopes have some stereopsis. Indeed, the one strabismic amblyope who "passed" the stereopsis test had considerably poorer stereoacuity than the five non-strabismics who passed. Fig. 6 plots the crowding-acuity ratio, which is an indicator of crowding, against the status of stereopsis of each amblyopic observer. The two measures, stereopsis and the crowding-acuity ratio, are both practically perfect in dividing the two kinds of amblyopia in our 18 amblyopes. The crowding-acuity ratio test makes no mistake (Fig. 6); the stereopsis test misclassifies two of the

18 amblyopes (lower left and upper right).

Three diagnostic indicators. Thus, among our 18 amblyopes, we find near-perfect agreement among three diagnostic indicators: history of strabismus, absence of stereopsis, and a high crowding-acuity ratio ($W > 1.84$). Note that the cut-off points for these binary classifications were conventional and pre-determined for strabismus and stereopsis, but the 1.84 cut off for the crowding-acuity ratio was determined after the fact, to best agree with the strabismus indicator.

Optimizing the flanked acuity test. Most of the results reported here were collected with tight spacing, a letter-spacing factor s of 1.1 (Fig. 1). What value of s would be optimal for a clinical test? When measuring flanked acuity, the letter-spacing factor restricts the testing range; it imposes a floor sA on the measured threshold spacing S. Supposing that we routinely measure the patient's unflanked acuity A, the added value of also measuring flanked acuity A' is diminished if the flankers are too far away to have any effect ($A' = A$). This can be avoided by using tight spacing.

It is well known that using a letter chart instead of isolated letter to measure visual acuity has value in evaluating contour interaction (Morad, Werker, & Nemet, 1999; Tommila, 1972; Wick & Schor, 1984). Currently, the most common commercially-available acuity charts have loose spacing, $s > 1.4$, making them less than optimal for measuring flanked acuity. For example, the Bailey-Lovie chart has $s = 2$, as does the widely used EDTRS chart. The charts that have tighter spacing are the Davidson-Elkridge illiterate E chart, and the Cambridge Crowding Cards (Atkinson et al., 1986), which have $s = 1.5$. As noted above, to measure flanked acuity, we recommend using a chart with tight spacing.

Testing patients. Plotting S vs. A for a normal observer at various eccentricities or amounts of blur traces out either of two lines (dashed or dotted) in a log-log graph (Fig. 3). The steep upper line (dashed) is limited by crowding. The unit-slope lower line (dotted) is limited by overlap masking. (We know that the limit is overlap masking, not acuity, because the crowding-acuity ratio $W = S/A = 1.4$ is much larger than the spacing factor $s = 1.1$.) We find that amblyopes (at zero eccentricity without added blur) follow these two lines (Fig. 4). Strabismics lie near the steep upper line (dashed), which is limited by crowding. Non-strabismics lie near the unit-slope lower line (dotted), which is limited by overlap masking.

In the absence of crowding, the threshold spacing plotted in the unit-slope lower line is $S = \max(wA, sA) = \max(w, s)A$. Thus, reducing s below w has no effect, but increasing s beyond w would raise the unit-slope lower line up, closer to the steep upper line, which will not move. The net effect is to push the two groups together, making them harder to separate. Thus, as noted above, we recommend that s be less than w. Making s larger than w pointlessly restricts the test's range, diminishing its diagnostic power.

4.3 Equivalent eccentricity and blur

Strabismic amblyopia is like increased eccentricity. A number of studies have reported large flanker effects in strabismic amblyopes, even in those who have only mild defects in unflanked visual acuities (Bonneh et al., 2004; Hess & Jacobs, 1979; Levi, Hariharan et al., 2002a). In the current study, superimposing the regression lines for normal vision (from Fig. 3) on Fig. 4b shows that the strabismic amblyopes' regression line (solid) lies above the blurred-normal regression line (dotted), i.e., for any given acuity, strabismic amblyopes have larger threshold spacing than that of the normal with added blur. However, strabismic amblyopic results are reasonably well described by the regression line for normal observers at increased eccentricities (dashed). We therefore hypothesize that, as at increased eccentricities for normal vision, the threshold spacing for strabismic amblyopia is mediated by crowding. If our hypothesis — that strabismic amblyopia can be modeled by increased eccentricity — is correct, then adding optical blur to strabismic amblyopes at fixation should result in a similar relationship between the threshold spacing and acuity as that for normals at increased eccentricity. Indeed, Fig. 5 shows that, as for normals at increased eccentricity, the threshold spacing increases much more slowly than the acuity does when optical blur is added at fixation for strabismic amblyopes. Again, these results for strabismic amblyopes suggest that the impaired spatial resolution (acuity) of the amblyopic eye cannot explain the increased threshold spacing of strabismic amblyopia.

Non-strabismic amblyopia is like blur. Non-strabismic amblyopes show a proportional relationship between threshold spacing and acuity, and their data closely match the blurred-normal regression line for direct viewing (Fig. 5). The fact that the threshold spacing for non-strabismic amblyopic central vision can be reproduced in the normal simply by scaling the acuity size of the stimuli suggests that a common mechanism, namely overlap masking, is responsible for the threshold spacing at fixation in both normal and non-strabismic amblyopic observers. Moreover, adding optical blur at fixation of non-strabismic amblyopes resulted in a proportional increase in threshold spacing and acuity. This proportionality is also seen in the results for normal direct viewing with blur (dotted line in Figs. 3 and 4). In fact, scaling effects have been previously reported in other visual functions for non-strabismic amblyopia. For example, comparing Vernier acuity and visual resolution reveals a linear relationship between them (Levi & Klein, 1982; Levi & Klein, 1985). Another example is that the abnormal contour integration for the amblyopic eye of non-strabismic amblyopes becomes nearly normal once the target visibility is equated between the amblyopic and non-amblyopic eyes, i.e., the contrast and spatial scale of the stimuli are adjusted for the amblyopic eye such that its performance in detection equals that of the non-amblyopic eye (Hess & Demanins, 1998). Consistent with our results, a recent large-scale study found that the flanked letter acuity is better correlated with the unflanked letter acuity for non-strabismic amblyopia than for strabismic amblyopia (Bonneh et al., 2004).

Eccentricity trumps blur. Fig. 5 shows that adding optical blur at increased eccentricity (instead of at fixation) results in a disproportionately small increase in the threshold spacing relative to the acuity. Threshold spacing is hardly affected by blur in the periphery, but strongly affected at fixation. Hence, the spatial resolution of the eye does not contribute significantly to the flanker effect at large eccentricities. In other words, it is the eccentricity, not the acuity, which determines the peripheral flanker effect. This shows that crowding, rather than overlap masking, determines the threshold spacing at increased eccentricity. Consistent with our conclusion, many studies have shown that the critical spacing in the periphery is determined by crowding, which is size-independent and eccentricity-dependent (Chung, Levi, & Legge, 2001; Intriligator & Cavanagh, 2001; Levi, Hariharan et al., 2002b; Pelli et al., 2004; Strasburger, 2005); see Levi (2008) and Pelli & Tillman (2008) for recent reviews.

Higher contrast letters appear "distinct" when viewed with the amblyopic eye. Irvine (1945) noted, "If the good eye is blurred to a visual acuity equal to that of the amblyopic eye the contrast to the patient is obvious, i.e., to the good eye the minimal visible letter is blurred and hazy, whereas to the amblyopic eye it is black, easily seen, but is uninterpretable". We asked our amblyopic observers to compare the suprathreshold appearance of our target letters in the two eyes, and our results confirm Irvine's observation – the letters appear equally distinct in the two eyes. Our medium contrast (60%) stimuli are perceived to have equal contrast in the two eyes of both strabismic and non-strabismic amblyopes. This nearly normal suprathreshold contrast perception has been previously reported in amblyopia (Hess & Bradley, (1980). Higher contrast stimuli are perceived veridically in both strabismic and non-strabismic amblyopes.

We also confirmed that blurring the non-amblyopic eye to the same the visual acuity level as the amblyopic eye (using plus lenses) does not mimic the perception of amblyopia. Both strabismic and non-strabismic amblyopes report that letters look blurrier when viewed with the (blurred) non-amblyopic eye than with the amblyopic eye. This is by no means contradictory to our model that non-strabismic amblyopia is like blur. Rather, the "equivalent blur" of non-strabismic amblyopia is not a simple optical blur, but an "internal blur" that results from long-standing physiological alterations.

Eccentricity dependence. It is well known that both acuity and critical spacing are approximately proportional to target eccentricity (Bouma, 1970; Levi, Hariharan et al., 2002b; Pelli et al., 2004; Tripathy & Cavanagh, 2002). For example, Toet and Levi (1992) found that acuity at a given eccentricity can be estimated by $A = A_0 (1 + \varphi/\varphi_2)$, where A_0 is the foveal acuity, φ is the target eccentricity, and φ_2 is the eccentricity at which the foveal acuity doubles. For acuity A, φ_2 is about 2 deg. For critical spacing, $S = S_0 (1 + \varphi/\varphi_2)$, φ_2 is about 0.3 deg (Toet & Levi, 1992). Similarly, we find that φ_2 is 2.6 and 0.4 deg for acuity and threshold spacing, respectively, for normal observers. Because the φ_2 values for threshold spacing and acuity are very different, the ratio of threshold spacing to acuity increases substantially with eccentricity within the range of our data (Fig. 7).

Equivalent eccentricity. In order to display the difference in flanker effects between non-strabismic and strabismic amblyopes more intuitively, we define the *equivalent eccentricity* (Levi & Carkeet, 1993) to be the eccentricity in a normal that gives the same crowding-acuity ratio as that for the amblyope at fixation. As noted above, acuity and threshold spacing have different φ_2 values, so the ratio of the two changes with eccentricity. The data are quite scattered, so the regression line (dashed) in Fig. 7 describes, roughly, how the crowding-acuity ratio depends on eccentricity. The rectified inverse function of this regression line is our equivalent-eccentricity model of strabismic amblyopia.

Equivalent blur. We define the *equivalent blur* of a given acuity as the amount of defocus for a normal observer which yields that acuity. As shown in Fig. 8, a simple model $A = k\sqrt{b^2 + B^2}$ describes the normal relationship between acuity and defocus, where A is acuity, k is a proportionality constant, b is the intrinsic blur, and B is the external blur (defocus, in diopters) added to the test eye (Levi & Klein, 1990a, 1990b; Watt & Hess, 1987; Watt & Morgan, 1984). The inverse function of this fitted model for how acuity depends on optical blur is our equivalent-blur model of non-strabismic amblyopia.

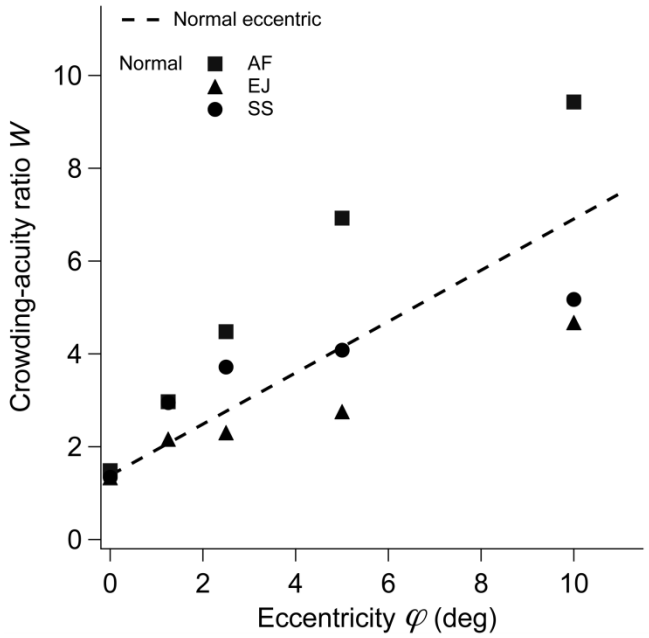

Figure 7. Crowding-acuity ratio W vs. eccentricity φ for normal observers. The rectified inverse function of the regression line $W = 1.38 + 0.55\varphi$ is our equivalent-eccentricity model of strabismic amblyopia, $\varphi = \max(0, 1.82W - 2.51)$.

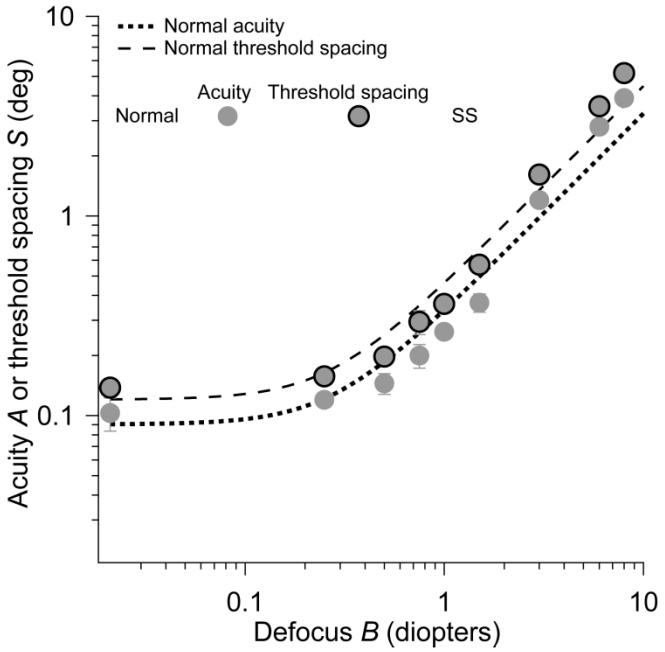

Figure 8. Acuity and threshold spacing vs. defocus in normal central vision. Each grey disk without or with a black edge represents the acuity or threshold spacing, respectively. The fitted curve (dotted) for acuity is $A = 0.33\sqrt{0.08 + B^2}$; the fitted curve (dashed) for threshold spacing is $S = 0.45\sqrt{0.07 + B^2}$, where B is defocus in diopters. The inverse of the dotted curve for acuity is our equivalent-blur model of non-strabismic amblyopia. The ratio S/A = 1.4±0.03 is not significantly different from w = 1.4, indicating overlap masking.

Fig. 9 is a scatter diagram, plotting equivalent blur against equivalent eccentricity for each amblyope. Note that the equivalent blur is based solely on acuity whereas the equivalent eccentricity is based on the crowding-acuity ratio. Non-strabismic and strabismic amblyopes' data fall into two clusters: low and high equivalent eccentricity. The average equivalent blurs are not significantly different between strabismics (0.93±0.21) and non-strabismics (0.94±0.18). The equivalent eccentricities are all larger in strabismic amblyopes (blue and red, ranging from 0.86 to 31.18; 6.01±2.75) than in non-strabismic amblyopes (green, ranging from 0 to 0.81; 0.31±0.13). All strabismic amblyopes (blue and red) are to the right of the line (0.84 deg) and all non-strabismic amblyopes (green) are to the left of the line.

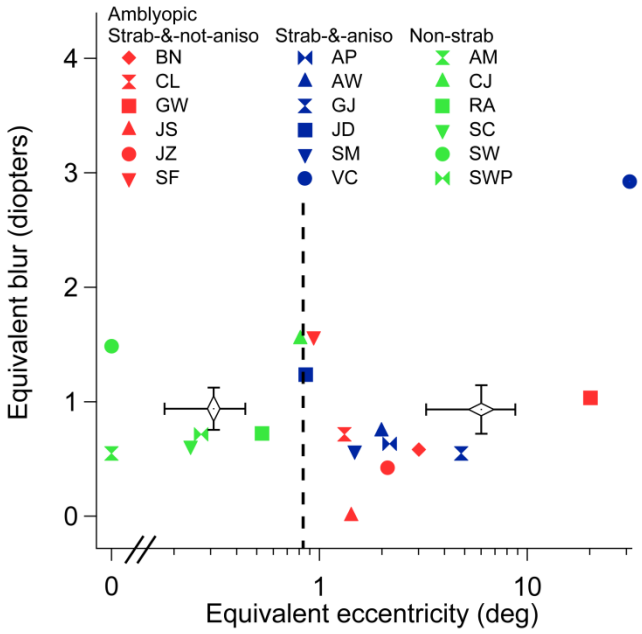

Figure 9. Equivalent blur vs. equivalent eccentricity for amblyopes. Each filled colored symbol shows one amblyope's equivalent blur and equivalent eccentricity. Open black diamonds show means for all non-strabismic (left) and strabismic (right) amblyopes. The dashed vertical line, separating strabismics from non-strabismics, is at 0.93 deg equivalent eccentricity. Since equivalent eccentricity is just a monotonic transformation of the crowding-acuity ratio, that ratio is equally effective as a diagnostic criterion.

Null hypotheses. The simplest explanation for the success of the equivalent-blur and equivalent-eccentricity models is that the models are literally true. Perhaps strabismic amblyopic eyes fixate poorly and thus view stimuli eccentrically, and non-strabismic amblyopic eyes focus poorly (or have uncorrected high-order aberrations) and thus have greater optical blur than eyes with normal vision. We did further experiments and analyses to test these null hypotheses.

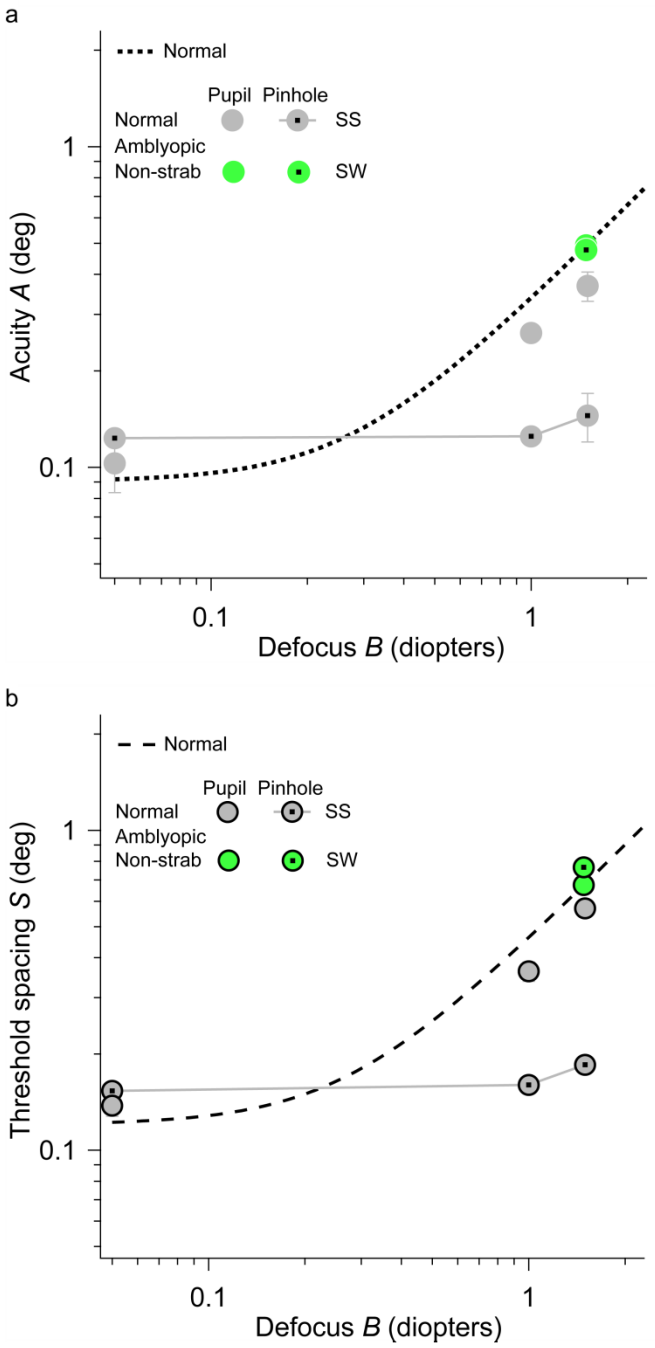

Figure 10. Acuity (a) and threshold spacing (b), with and without pinhole, vs. defocus in normal and amblyopic central vision. Disks without or with black edges represent acuity (a) or threshold spacing (b), respectively, of a normal observer (grey) and a non-strabismic amblyope (green). Use of a pinhole is indicated by a black dot centered in the disk symbol. The natural pupil diameter is 3 – 4 mm and the pinhole diameter is 1.5 mm. The dotted curve in (a) is our equivalent-blur model for non-strabismic amblyopia. Normal data are plotted against defocus; non-strabismic amblyopic data are plotted against the corresponding equivalent blurs (to match acuity of the normal when both have natural pupils) for that observer. The *S/A* ratios for the blurred

normal (1.4±0.03) and the amblyope (1.4) are not significantly different from $w = 1.4$, indicating that the threshold spacing was limited by overlap masking.

Pinhole relieves optical blur but not amblyopia. Our results show that the performance of non-strabismic amblyopes is well modeled by adding optical blur to normal central vision. However, the results we have already presented cannot exclude the possibility that the non-strabismic amblyopes are indeed limited by optical blur, perhaps because of higher-order optical aberrations, or because their accommodation is less accurate. We think that these optical accounts are unlikely for two reasons. First, a recent study has shown that there is no significant difference in higher-order aberrations between children with strabismic and non-strabismic amblyopia and children without amblyopia (Kirwan & O'Keefe, 2008). Second, an optical explanation would predict that the non-strabismic amblyope's pinhole acuity would be better than his acuity with normal pupil size (about 3 – 4 mm), since the pinhole greatly decreases the effect of defocus and eliminates most other optical aberrations (Artal, Marcos, Iglesias, & Green, 1996; Campbell & Gubisch, 1966).

Our measurements (Fig. 10) confirm the optical benefit of the pinhole in normal vision and reject the null hypothesis that the non-strabismic amblyopic deficit is optical. We applied various amounts of defocus to blur the normal, viewing directly. We found that at a similar acuity level, the blurred normal benefitted greatly from the pinhole (1.5 mm), but the non-strabismic amblyope did not. However, in addition to the pinhole's visually beneficial effect of narrowing the eye's point spread function, it also has the deleterious effect of reducing the retinal illuminance by roughly fivefold. We used a neutral density filter (density 0.7, 20% transmission) to assess the isolated effect of the change in retinal illuminance on the normal observer. For a normal observer with +1.5 D defocus (the equivalent blur for SW is around +1.5 D) the pinhole improves acuity by 2.5x, but a similar luminance reduction produced by the neutral density filter worsens acuity by 1.1x. The large effect of the pinhole and the small effect of pure luminance reduction (by the neutral density filter) together suggest that luminance reduction plays a negligible role in the effect of the pinhole on acuity.

Thus, since the equivalent blur deficit, unlike real optical blur, is not relieved by a pinhole, we reject the null hypothesis that the non-strabismic amblyopic equivalent-blur deficit is due to optical blur. The amblyopic impairment modeled by equivalent blur must be a neural deficit in perception.

Strabismic amblyopes fixate well enough. Our results show that strabismic amblyopic performance is well modeled by increased eccentricity. The null hypothesis would be simply that the strabismic amblyopes fixate poorly, and that their visual acuities were therefore indeed measured in the periphery. We used a direct ophthalmoscope to assess fixation of each observer by estimating the distance of the fixation star from the fovea. All the strabismic amblyopes except VC and SF have near-central fixation (< 0.5 deg). These deviations are much too small to explain their (large) equivalent eccentricities (1 to 31 deg). One of the exceptions, VC, has

large steady temporal eccentric fixation (about 8 deg) in her amblyopic (right) eye. However, the equivalent eccentricity for VC (based on her crowding-acuity ratio) is 31 deg which is much greater than her eccentric fixation (8 deg). Therefore, her amblyopia cannot be accounted for by eccentric fixation. The other exception, SF, fixates unsteadily with his amblyopic eye, initially at fixation, and then sometimes at fixation but sometimes several degrees right of fixation. However, in our experiment, each stimulus is brief (200 ms), so unsteady fixation is unlikely to affect the measured visual acuity (Higgins, Daugman, & Mansfield, 1982). This may help to explain why SF's equivalent eccentricity (1 deg) is small compared to other strabismic amblyopes, in spite of the fact that he has unsteady fixation with drifts of up to several degrees away from the designated point for fixation. If SF were typically fixating extrafoveally, we would expect that he would have a larger, rather than a smaller, equivalent eccentricity. Thus we reject the null hypothesis for all our strabismic observers. The amblyopic deficit modeled by equivalent eccentricity is not simply eccentric fixation and must be a neural deficit in perception.

Our contribution. That strabismic and anisometropic amblyopia are different is old news (Hess & Bradley, 1980; Levi & Klein, 1982). And this paper is not the first to propose modeling amblyopia by increased eccentricity or blur. However, this is the first evidence that increased eccentricity models only strabismic amblyopia and the increased blur models only non-strabismic amblyopia.

4.4 Amblyopia screening

It is well established that acuity for "surrounded" optotypes (i.e. flanked acuity) is much more sensitive to strabismic amblyopia than is acuity for "isolated" optotypes (unflanked acuity), and the test designers largely heed this (Ehrlich, Reinecke, & Simons, 1983; Thomas-Decortis, 1959). In charts the other letters act as flankers, or a single target letter can be surrounded by flankers, as in Fig. 1.

There is a substantial clinical literature on measuring acuity, with and without flankers, to screen for amblyopia. Our findings are mostly consistent with that literature, with one important caveat. That literature treats all flanker effects alike. No attempt is made to distinguish crowding (critical spacing independent of target size) from overlap masking (critical spacing proportional to target size). The clinical literature has instead assumed that the flanker effect in strabismic amblyopia (i.e. crowding) is simply an exaggerated version of the flanking effect in normals and non-strabismics amblyopes (i.e. overlap masking). Fifty years ago, Thomas-Decortis (1959) found the same modest flanker effect in normals and non-strabismic amblyopes, and a much bigger flanker effect in strabismic amblyopes. However, while confirming her results, Stuart and Burian (1962) confused the issue by advancing the unhelpful "thesis that all sensory phenomena observed in strabismic patients are exaggerations of pre-existing physiologic phenomena." They conclude "that crowding is a universal phenomenon, … correlated with … visual acuity … exaggerated with any form of strabismic

amblyopia." The mistaken assumption that the flanker effects have the same cause in both strabismic amblyopia and normals persists to this day. This has led to two errors in the design of tests to screen for amblyopia. To our knowledge, all commercially available acuity tests for amblyopia suffer from one or the other of these two faults. Either the flankers are insufficiently close to the target or the flankers are insufficiently similar to the target. As noted earlier, our results suggest the need for tighter-spacing than is commercially available.

5 Conclusions

Size and spacing. First, we systematically explore the size and spacing requirements for identifying a letter among other letters by normal and amblyopic observers and present a very simple model that accounts for all our results by visual limits on size and spacing due to acuity, overlap masking, and crowding. We measure flanked acuity A' and unflanked acuity A, where A' and A are the threshold sizes of the target letter with and without flanking letters. *Threshold spacing S* is the spacing at threshold size, i.e. the threshold center-to-center spacing of the target and flankers $S = sA'$, where the *spacing factor s* is the ratio of letter spacing to letter size (e.g. 1.1). A very simple model of flanked-letter legibility accounts for all our spacing thresholds, $S = \max(S_{\text{acuity}}, S_{\text{crowding}}, S_{\text{masking}})$. In general, for each eccentricity, we find that a flanked letter is legible if and only if it is larger than a critical size A (the acuity limit) thus $S_{\text{acuity}} = sA$ and the flankers are farther than the critical spacing of crowding S_{crowding} (the crowding limit) and the critical spacing of overlap masking $S_{\text{masking}} = wA$ (the overlap-masking limit). In particular, at fixation (with or without added blur), for normals and non-strabismic amblyopes, there is no crowding, so legibility of a flanked letter is limited by overlap masking if the letter spacing is tight ($s < w$) and limited by acuity if the letter spacing is loose ($s > w$). In normal peripheral vision (1.25 and 5 deg) and strabismic amblyopia, legibility is limited by crowding for letter spacings ranging from tight to loose ($1.1 \le s < 1.4$) and limited by acuity if the letter spacing is extremely loose ($s > 1.4$).

Crowding-acuity ratio. Second, strabismic amblyopia is easily distinguished from non-strabismic amblyopia by the combination of threshold spacing and acuity (obtained by measuring flanked and unflanked acuity), but not by either alone. We calculate the ratio of threshold spacing S to acuity A, which we call the *crowding-acuity ratio* $W = S/A = sA'/A$. W is an index of crowding that tells us about the relative importance of spacing (crowding) and size (acuity). W equals s when flanked legibility is limited by size ($A' = A$, i.e. no effect of flankers), and W exceeds s when flanked legibility is limited by spacing ($A' > A$). At fixation, all our strabismic amblyopes have a crowding-acuity ratio W greater than 1.84, and all our non-strabismic amblyopes have a crowding-acuity ratio less than 1.84. Among our 18 amblyopes, we find near-perfect agreement of three diagnostic indicators: history of strabismus, absence of stereopsis, and a high crowding-acuity ratio ($W > 1.84$).

Clinical assessment of crowding and screening for amblyopia. We recommend measuring

both unflanked and flanked acuity. Measuring at fixation is interesting in the context of amblyopia and development, and may be done with printed charts. Peripheral measurement will require some way of ensuring fixation away from the target. Some current screening tests for amblyopia measure flanked letter acuity. Our results suggest that the sensitivity of most of these tests is curtailed by use of flankers that are either not sufficiently similar to the target or not sufficiently close to the target letter. Our model predicts that these tests can be improved by using tightly spaced letter (or letter-like) flankers. This will increase sensitivity for detecting strabismic amblyopes while maintaining specificity.

Equivalent eccentricity and blur. Finally, we show that strabismic and non-strabismic amblyopia are much like normal vision at increased eccentricity or with added blur, respectively. In normal observers, increasing eccentricity worsens both acuity and the crowding-acuity ratio. Adding blur similarly worsens acuity, but has no effect on the crowding-acuity ratio. Strabismic amblyopia is much like increased eccentricity and non-strabismic amblyopia is much like increased blur. In particular, the threshold spacing of strabismic amblyopes is limited by crowding, whereas that of non-strabismic amblyopes is limited by overlap masking. Equivalent eccentricity and blur accurately model effects of size and spacing in strabismic and non-strabismic amblyopia, respectively. Additional tests confirm that both kinds of amblyopia are in fact neural deficits of perception, not just poor optics or fixation.

A SURVEY OF LETTER ACUITY

1 Introduction

In the last chapter, we asked observers to identify a briefly presented (i.e. 200 ms) medium contrast (i.e. Weber contrast 0.6) bright letter, without any artificial pupil in a dim room with the mean background luminance 9.6 cd/m^2. In Atkinson's study (1988), or in a clinical setting, visual acuity is measured using a printed chart with high – contrast (i.e. Weber contrast < -0.9) black letters in a bright environment (e.g. 70.4 cd/m^2), and the time of exposure to the letter stimulus is infinite. When other conditions (e.g. letter font, center-to-center letter spacing – 1.5x letter size, and threshold criteria) are more or less the same, these two kinds of stimuli produce significantly different visual acuities and flanked (*A'*) – to – unflanked (*A*) acuity ratios (i.e. *A'/A*). Retinal image contrast is proportional to stimulus contrast; whereas retinal illuminance is correlated with stimulus background when pupil size is fixed, and it also affects the shape of the contrast sensitivity function (CSF). For a short enough exposure (i.e. within the temporal summation period), there exists a trade-off between contrast and duration according to Bloch's law, and as a consequence, the perception threshold is a constant product of contrast and duration under proper conditions. Moreover, reducing pupil size improves the ocular optics, i.e., point spread function (PSF), but reduces retinal illuminance. Here we explore the effects of various factors on flanked and unflanked visual acuities and hope to extend the legibility model to account for this larger range of conditions. More specifically, we vary letter polarity, contrast, duration, background, and pupil size, so that we can unconfound their effects on flanked and unflanked acuities.

In our pilot data, we observe that in the fovea, when the medium-contrast briefly presented letters are replaced by high-contrast (-0.9) black letters with infinite duration, the unflanked acuity improves significantly, but the flanking effect measured by *A'/A* ratio extends even farther, suggesting a foveal limit for flanked letter identification. Recent studies have shown that ordinary masking instead of crowding accounts for the spatial interaction in the fovea (Pelli et al., 2004). Here, we ask whether it is always overlap masking that limits foveal vision. Could foveal vision be limited by crowding under certain circumstances?

2 Methods

The methodology for the present study is the same as that for the last series of experiments in "Three limits in letter identification by normal and amblyopic observers". Stimulus polarity, contrast, duration, and background luminance were varied systematically. Polarity was reversed through reversing the luminance increment of the letter stimuli while fixing the background

luminance. Contrast was varied through either manipulating the pixel values or applying a neutral density filter for the observer. Letter stimuli were presented with durations ranging from 26.67 ms to infinity, and the latter will sometimes be referred to as "static" in this report. Pupil size was also varied through artificial pinholes of different sizes.

Cambridge Crowding Card was used to measure the visual acuities for some observers following the instructions from the manual (Atkinson et al., 1988). The Cambridge Crowding Card will be referred to as Card in this report.

3 Results

3.1 Overview: CRT letter vs. print-like letter

Observer SS	print-like	print-like	CRT	CRT
Contrast	-0.91	-0.91	0.6	0.6
Duration (ms)	infinity	infinity	200	200
Pupil (mm)	4.8	2.0	5.0	2.0
Background (cd/m^2)	79	79	33	33
Background (td)	1,430	248	648	104
Spacing factor *s*	1.5	1.5	1.5	1.5
Unflanked *A*	0.053	0.053	0.100	0.080
Flanked *A′*	0.064	0.064	0.100	0.093
A′/A	1.20	1.20	1.00	1.16

Table 1. Fovea, CRT (0.6-contrast 200 ms bright) letter vs. print-like (infinite duration, -0.91-contrast dark) letter. The print-like letter acuity *A* is roughly half that for a 0.6-contrast 200 ms bright letter, and flanked acuity *A'* is two-thirds. Thus the *A'/A* ratios are different.

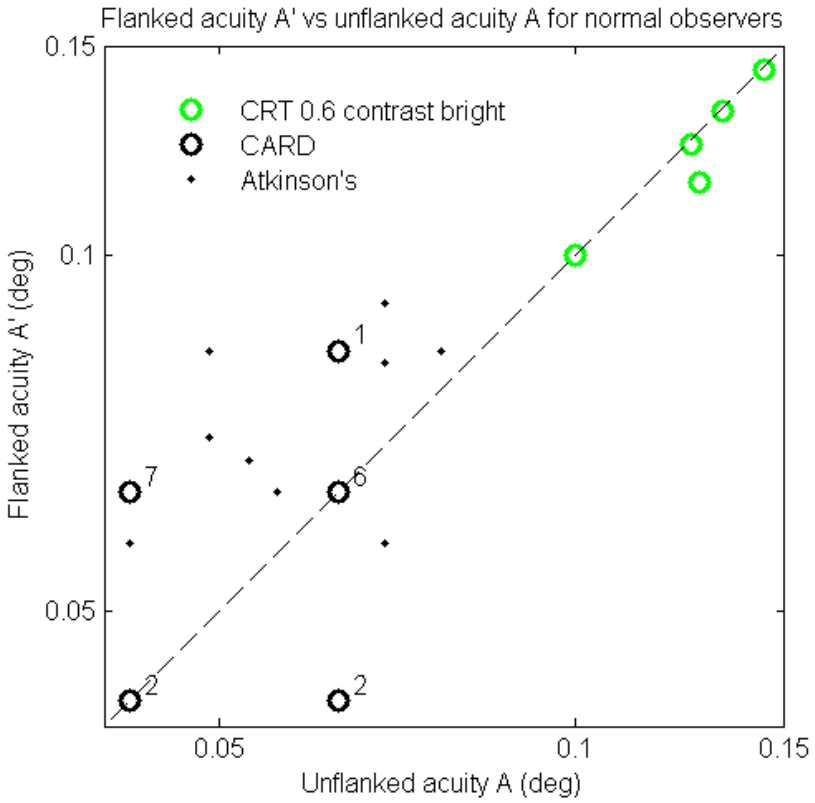

Fig. 1 Flanked acuity *A'* vs unflanked acuity *A* for normal observers. The letter-to-letter spacing is 1.5 multiples of the letter size. *A'* vs *A* of different stimuli (i.e. CRT, Cambridge Crowding Card, and Atkinson's reported data) are plotted on the log-log scale. Since Card data are coarsely categorized (line acuity), there are some overlaps which are indicated by a number next to each black circle. The dashed line is equality *A'=A*.

For 0.6-contrast 200 ms bright letter, our legibility model is

$$S = \max\left(S_{\text{acuity}}, S_{\text{crowding}}, S_{\text{masking}}\right) \qquad 1)$$

$$= \max\left(sA, S_{\text{crowding}}, wA\right) \qquad 2)$$

where w = 1.4 predicts that for s = 1.5 > w = 1.4, at the fovea, A'/A = 1, i.e. no effect of the flankers. However, the print-like letters give A'/A = 1.2 for s = 1.5 at the fovea. This implies that for print-like letters, either 1) the value of w of overlap masking is different (i.e. w = 1.2x1.5 = 1.8), or 2) the flanked acuity limit is not overlap masking. 1) Intuitively, 1.8 is a fairly loose spacing that is unlikely to induce overlap masking. We will present data, below, in Fig. 10 showing that blurred data for print-like letters rule out this possibility. 2) For print-like letters, some other factors (e.g. crowding) limit flanked acuity. Along with the "failure" of the model

prediction in print-like letter is the 2-fold decrease of acuity threshold *A*. Further study is necessary to confirm that the flanked acuity limit in the fovea is crowding (see below).

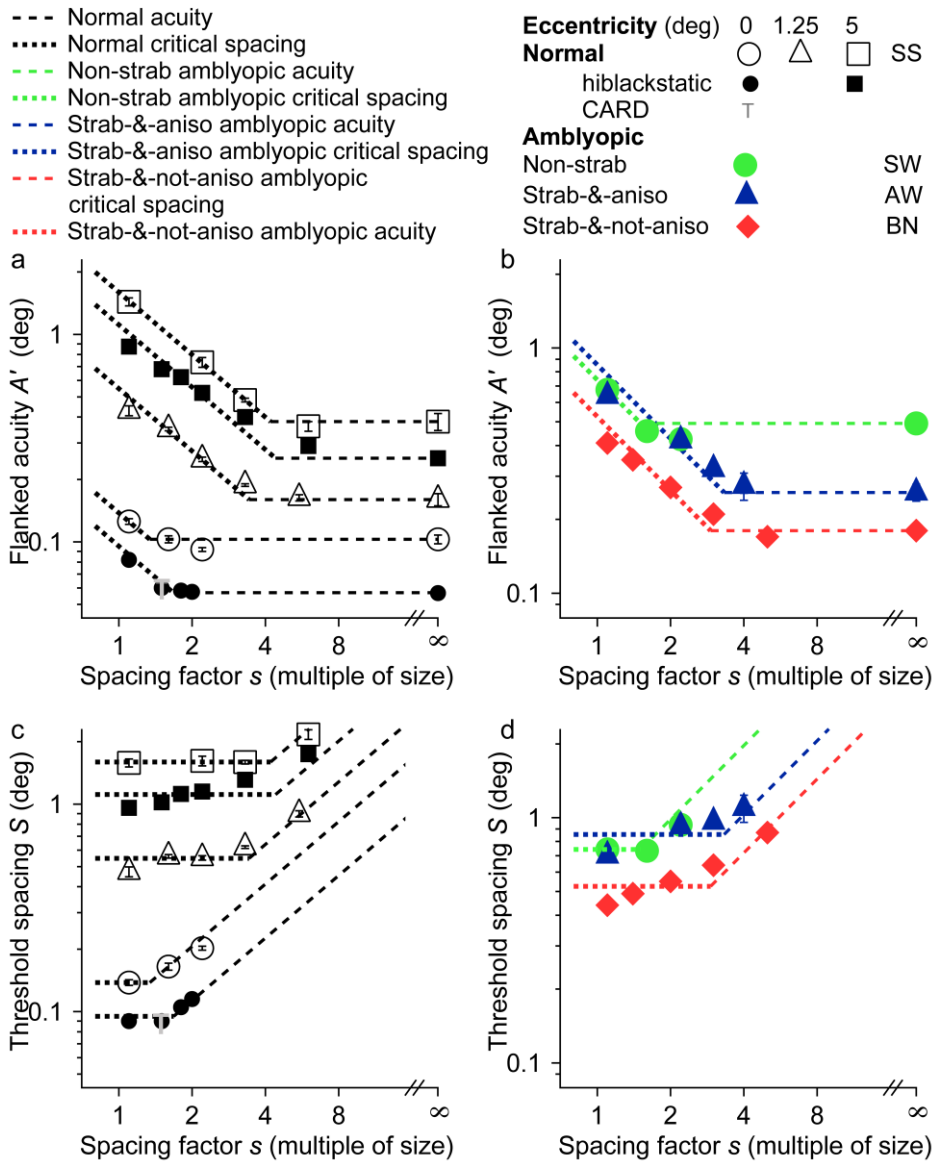

Fig. 2. Similar to Fig. 2 in the last chapter. *A'* or *S* vs. spacing factor *s*. Dotted line: crowding or overlap masking limit. Dashed line: acuity limit. The knee point (x-coordinate) is at the crowding-acuity ratio *W*=*S*/*A*. The "T" symbols in panels a & c are located on the solid disks. The contrasts are -0.91 for print-like stimuli (solid black symbols) and 0.8 for the rest. Duration is either static or 200 ms.

At the fovea (empty & solid disks), print-like letter (solid disks) unflanked and flanked acuities *A* and *A'* are both smaller than those of 0.6-contrast brief letters (empty disks), hence the downward shift of both dotted and dashed lines. Since the decrease in *A* is greater than that

in *A'*, the knee point is shifted to the right for print-like letters. As mentioned above, for print-like letters at the fovea (solid black disks in panel a&c), if it were the overlap masking, i.e. *wA*, that limited *A'*, then *w*=1.68 (i.e., the horizontal coordinate of the knee point). If, however, crowding limits *A'*, then the critical spacing is represented by the dotted line of solid black disks in panel c --- 0.095 deg. We cannot rule out either of the two possibilities from these data because *S* is consistent with either limit. However, data with blur can clarify this question.

At 5 deg eccentricity, at first glance, it is remarkable that the print-like letter (solid squares) is obviously lower than 0.6 – contrast letter (empty squares), which would imply that the crowding critical spacing changes with contrast or duration. It turns out that duration plays a bigger role here. (see later section on *A* vs. duration and Fig. 15). For 0.6 – contrast letters, while the unflanked acuity *A* (dashed line) is worse than that of print-like letters, the threshold spacing (dotted line) is similar to that of print-like letters.

3.2 Fovea: contrasts (high vs. med), durations (brief vs. infinite), polarity, & pupil sizes (2 mm vs. natural).

3.2.1 Dark letter unflanked acuity

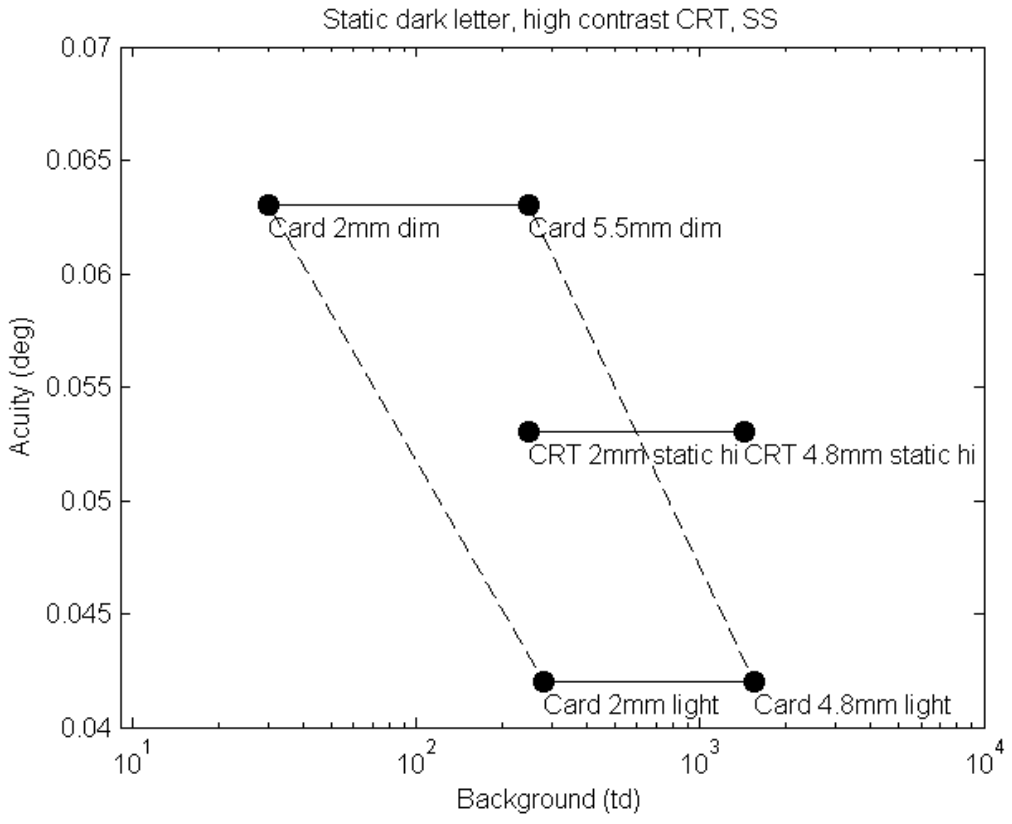

Fig. 3 Unflanked acuity vs background. Dark letter. Infinite duration (static). Each point is labeled by the task (CRT vs Card) and the pupil or pinhole size. Solid lines connect points (conditions) differing solely by addition

of pinhole. The Card acuities show the equal and opposite contributions of luminance and point spread thethe effect of pupil size on acuity. The 2 vs. 5.5 mm Card acuities at 280 td prove that increasing the aperture from 2 to 5 mm increases the point spread by 1.5x.

For acuity *A* we see three effects. Firstly, the dashed lines show that the unflanked acuity *A* depends on log background luminance. The dashed lines link points with the same or nearly the same pupil size, revealing a pure effect of retinal illuminance (background td). Acuity size drops about 0.02 deg per decade of illuminance. Secondly, the two Card points at around 200 to 300 td background reveal a pure effect of pupil size on acuity, presumably because the pinhole improves the eye's point spread function. Reducing the pupil from 4.8 to 2 mm reduces acuity size by 0.02 deg. Thus either a decade increase in retinal illuminance (with fixed optics) or a reduction of pupil size from 4.8 down to 2 mm (at fixed retinal illuminance) improves acuity by 0.02 deg.

The two effects of pupil size (illuminance and point-spread) on acuity normally cancel each other out: reducing the pupil reduces light (which worsens acuity) but narrows the point spread (which improves acuity). This is seen above. The top two points are from the dim room; the pinhole reduces the retinal illuminance with no effect on acuity, so the point moves left. Similarly, the bottom two points are from the bright room; again the pinhole moves the point left. Comparing the Card vs. CRT points with 2 mm pinhole reveals a 0.01 deg lower acuity with the Card task instead of the CRT task. That's a criterion effect.

3.2.2 Dark letter flanked acuity

When the letter is dark, we get exactly the same flanked acuity $A' = 0.064$ deg across all conditions, independent of pupil size and luminance. And, remarkably, there is practically no effect of task (CRT vs. Card). The CRT task is harder yet the measured value of flanked acuity is insignificantly better, by 0.003 deg, on the CRT. It is quite surprising to me that the effect of task and criterion differs between unflanked and flanked acuity. Based on difficulty, we'd expect the CRT acuity size to be higher; recall that unflanked acuity is 0.01 deg higher. This may be because the psychometric functions of flanked and unflanked acuities have different shape (e.g. slope). E.g. if the slope of flanked task is greater, then the effect of criterion change on the reported threshold will be smaller.

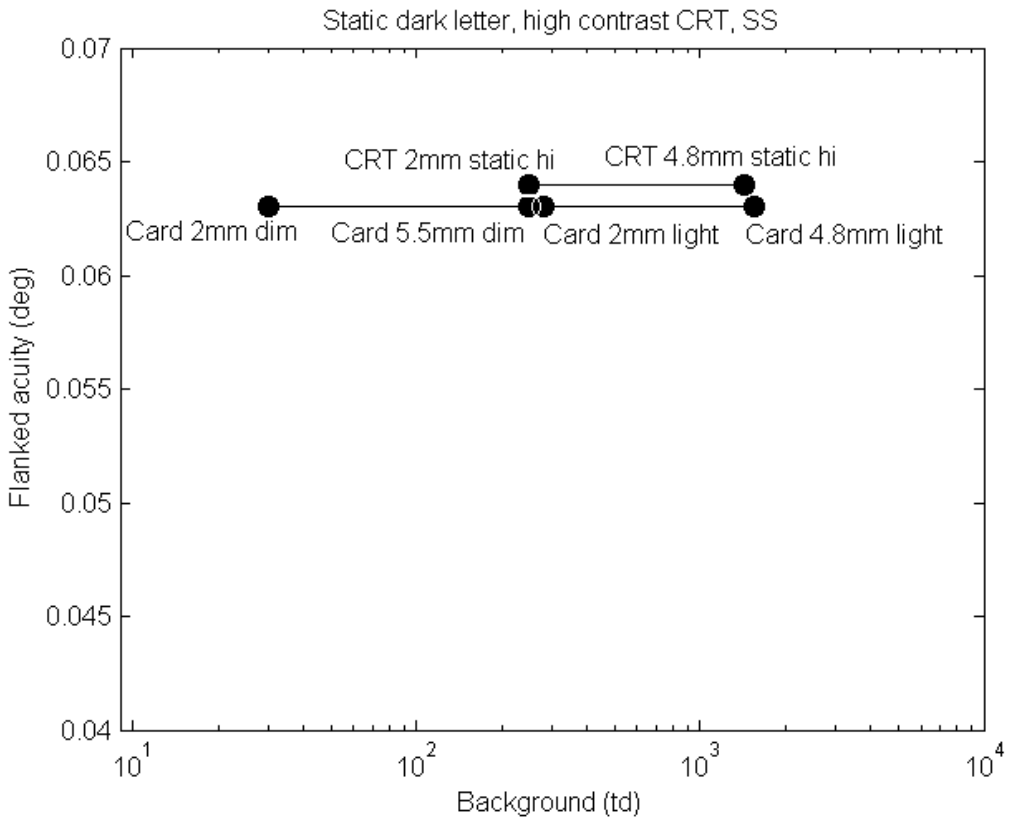

Fig. 4. Flanked acuity vs background. Letter-to-letter spacing is 1.5x letter size. Dark letter. Infinite duration (static). Each point is labeled by the test (CRT vs Card) and the pupil or pinhole size. The lines connect points differing solely by addition of a pinhole. The identical flanked acuity with 2 and 5.5 mm apertures at 280 td shows no effect of point spread. The identical flanked acuity at 30 and 280 td with 2 mm aperture shows no effect of retinal illuminance.

There are two Card points (2 mm and 5.5 mm) at a background of about 250 td. They reveal that a pure change of point spread has no effect on flanked acuity. Similarly, comparing the pair of Card points with the 2 mm pinhole shows that a tenfold drop in retinal illuminance has no effect on flanked acuity.

3.2.3 Unflanked acuity of various letter stimuli

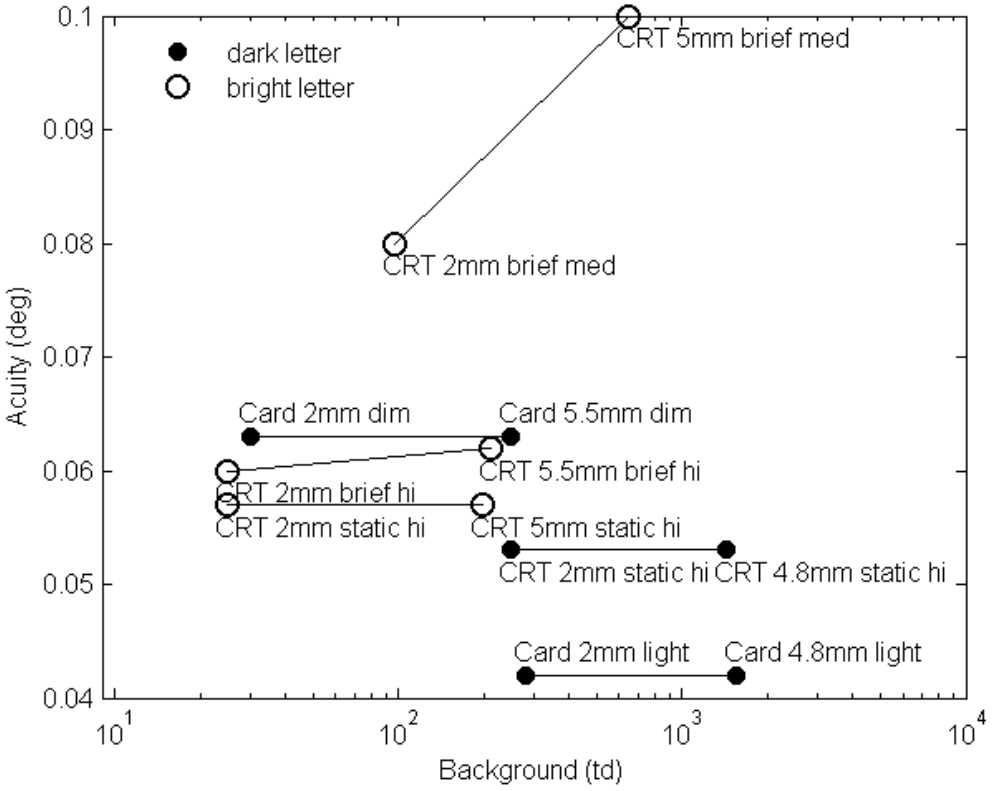

Fig. 5. Unflanked acuity vs background. Each point is labeled by the test (CRT vs Card) and the pupil or pinhole size, plus, for the CRT, the letter duration (brief vs infinity – static) and contrast (high vs medium). "med" (bright) contrast is 0.6; "hi" dark contrast is -0.9; "hi" bright contrast is 9 (letter is 10x background luminance). Points that differ solely by addition of a pinhole are connected by a solid line; they show that pupil size has a large effect at medium contrast, but practically no effect at high contrast. The upper two points, CRT brief med contrast, show a full effect of the point spread, and no effect of retinal illuminance. (See Fig. 14 for effect of duration.)

Above, in Fig. 3, we saw that the two effects of pupil size (on optical point spread and retinal illuminance) have nearly equal but opposite effects on acuity. That was for static black letters. At high contrast, a pinhole has no effect on acuity. Here we broaden the scope to consider brief presentation and bright letters.

There is a small effect of task (CRT vs. Card) which can be assessed by comparing the Card 2 mm point at 300 td with the dark-letter CRT static hi 2 mm point at the same background. The CRT point is 0.01 deg higher (worse) presumably because the computerized task imposes a higher criterion. If we were to "correct for" this difference we would shift all the CRT points down by 0.01 deg.

We can assess the effect of duration (hardly any) for *bright* letters, by noting the near coincidence of the points for CRT static and brief (i.e. “CRT static hi 5.0 mm” vs. “CRT brief hi 5.5 mm”), which are at nearly the same retinal illuminance and yield nearly the same acuity. In fact the two points were measured at the same background luminance (at the CRT) but the pupil is slightly smaller in the presence of the static bright letter (which has ten times higher luminance than the background).

So far we’ve considered only high-contrast letters. This includes all the points in Fig. 5 except the two upper points. The story for high-contrast letter acuity is surprisingly simple: effects of pupil size on acuity, mediated by retinal illuminance and point spread, are equal and opposite, yielding no net effect. Duration (static vs. 200 ms) has hardly any effect (at least for bright letters). Task makes a small difference (CRT is 0.01 deg above Card).

What can we say about the medium-contrast acuities? The letters were brief and bright, but we’ve just estimated that duration does not matter much and that polarity has only a modest effect (0.01 deg) at high contrast. The results below show that polarity doesn’t matter at medium contrast (Fig. 11). By elimination, we thus attribute most of the difference, the elevation of these points above all the high-contrast points, to the contrast. Note that the effect of pinhole on acuity is very different here. At high contrast (-0.9) we found, for both Card and CRT, that the pinhole caused the point to shift left, without affecting acuity. At medium contrast (0.60), our two points show a large drop associated with the leftward displacement. The drop is about what we’d expect from the improvement in optical point spread and that there is no effect of the reduction in retinal illuminance.

3.2.4 Flanked acuity of various letter stimuli

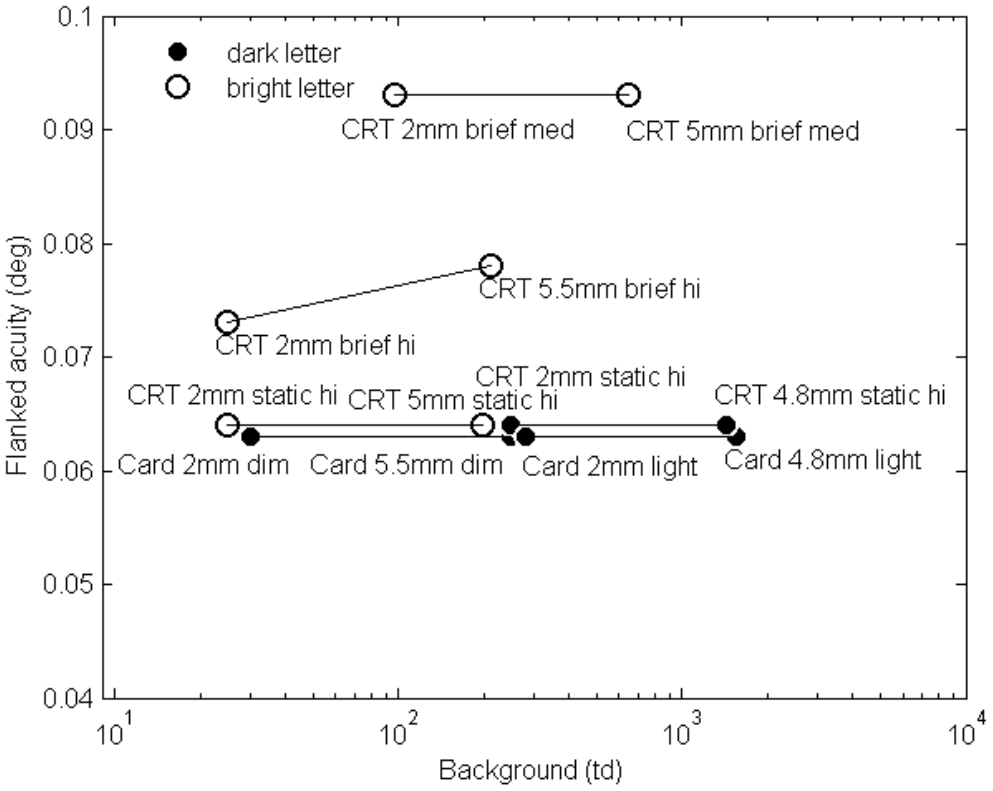

Fig. 6 Flanked acuity vs background. Letter-to-letter spacing is 1.5x letter size. Lines connect points that differ solely by addition of a pinhole, showing practically no effect of pupil size. The upper four points (brief, bright) show a large effect of contrast. The four Card points show no effect of pupil size, and no effect of point spread and retinal illuminance. Note that Fig 10 does show an effect of point spread function on flanked acuity.

We already examined flanked acuities for static high-contrast dark letters in Fig. 4, finding that the acuity is always 0.060 deg, unaffected by retinal illuminance and optical point spread, and hardly affected by task (CRT vs. Card). Here we see that polarity too, has no effect on flanked acuity for static high-contrast letters.

However, duration and contrast do matter. At high contrast, flanked acuities for brief letters are 0.01 to 0.015 deg higher than those for static letters. Flanked acuity for medium-contrast brief letters is 0.03 deg higher than for high-contrast static letters. Thus we summarize flanked acuity (and Fig. 6) by three values: 0.063 deg for static high-contrast letters, 0.075 deg for brief high-contrast letters, and 0.093 deg for brief medium-contrast letters. The same flanked acuity (0.063 deg) with 2 mm pinhole at 30 and 300 td shows that retinal illuminance does not affect flanked acuity. Similarly, the same flanked acuity with different pupils (2 and 5.5 mm) at similar retinal illuminances (near 250 td) shows that optical point spread also has no effect on

flanked acuity. Our data suggest that contrast polarity does not matter, because the combined effect is nil of reversing contrast polarity and reducing pupil (from 5 to 2 mm) at similar retinal illuminance (about 200 td): CRT static hi 5.0 mm (bright letter) vs. CRT static hi 2 mm (dark letter).

Flanked acuity, unlike acuity, is independent of point spread and retinal illuminance and task. Our results suggest that the critical spacing in the fovea is around 0.090° from 30 to 1500 td.

3.2.5 Print-like flanked & unflanked letter acuities

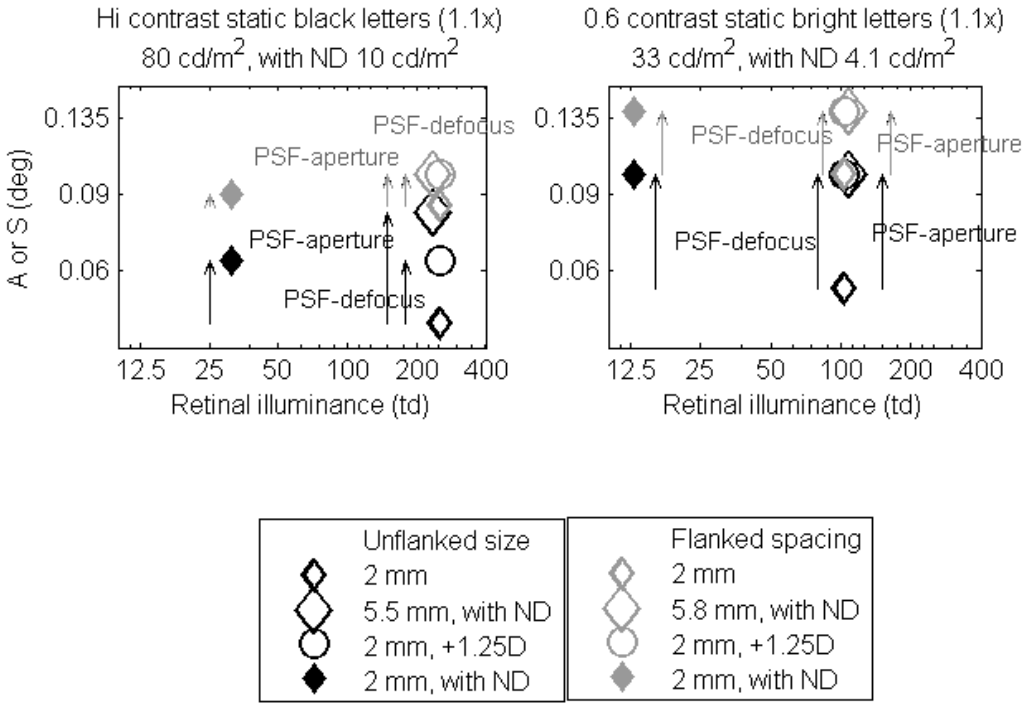

Fig. 7. Acuity *A* or threshold spacing *S* vs. retinal illuminance for high-contrast static black letters (left) and 0.6-contrast static bright letters (right). Letter-to-letter spacing is 1.5x letter size. Grey symbols represent threshold spacing for flanked letters; black symbols represent acuity for unflanked letters. Without ND filter (80 cd/m^2 for high contrast black letter and 33 cd/m^2 for 0.6 contrast black letter) and with ND filter (10 cd/m^2 for high contrast and 4.1 for 0.6 contrast); natural pupil, 2mm pinhole without blur, 2mm pinhole with blur are plotted in the same graph.

The 2mm 80 cd/m^2 condition (empty small diamonds) is the reference condition. For high contrast unflanked static black letters (left panel, black symbols), either adding blur (circle) or viewing without pinhole using dim background (empty large diamonds) worsens the acuity at

the same retinal illuminance. Thus when retinal illuminance is constant, the change in acuity is solely attributed to PSF change which is caused by either optical blur or enlarged pupil. On the other hand, decreasing retinal illuminance by lowering the background luminance also worsens acuity (solid diamond). This is consistent with Fig. 3. Therefore, high contrast static black letter acuity depends on PSF and retinal illuminance.

For high contrast flanked static black letters (left panel, grey symbols), adding blur, viewing without pinhole using dim background, or lowering the background luminance also worsens the threshold spacing S, but to a much less extent compared to high contrast letters (left, black). And the threshold spacing of all above conditions is around 0.09 deg. Recall that in Fig.4 we didn't see any difference in flanked acuity *A'* under similar different conditions, which might be due to the coarse scale of the Card. Therefore, high contrast static black letter threshold spacing is relatively independent of PSF or retinal illuminance, and 0.09 deg might represent the critical spacing of foveal crowding.

For 0.6 contrast unflanked static bright letters (right panel, black symbols), similar to high contrast unflanked dark letters (left, black), acuity depends on PSF and retinal illuminance. For 0.6 contrast flanked static bright letters (right panel, grey symbols), however, the effect of PSF and retinal illuminance on threshold spacing is comparable to that on unflanked acuity. That the extent of change in threshold spacing (right, grey) is somewhat smaller than that in acuity (right, black) might be because the smallest threshold spacing – 2mm 80 cd/m^2 (right, small grey empty diamond) is near 0.09 deg which is probably the lower bound of threshold spacing (i.e., critical spacing for foveal crowding).

Therefore acuity and overlap masking depending on PSF and retinal illuminance, but crowding is independent of these factors.

3.3 Pupil size and acuity

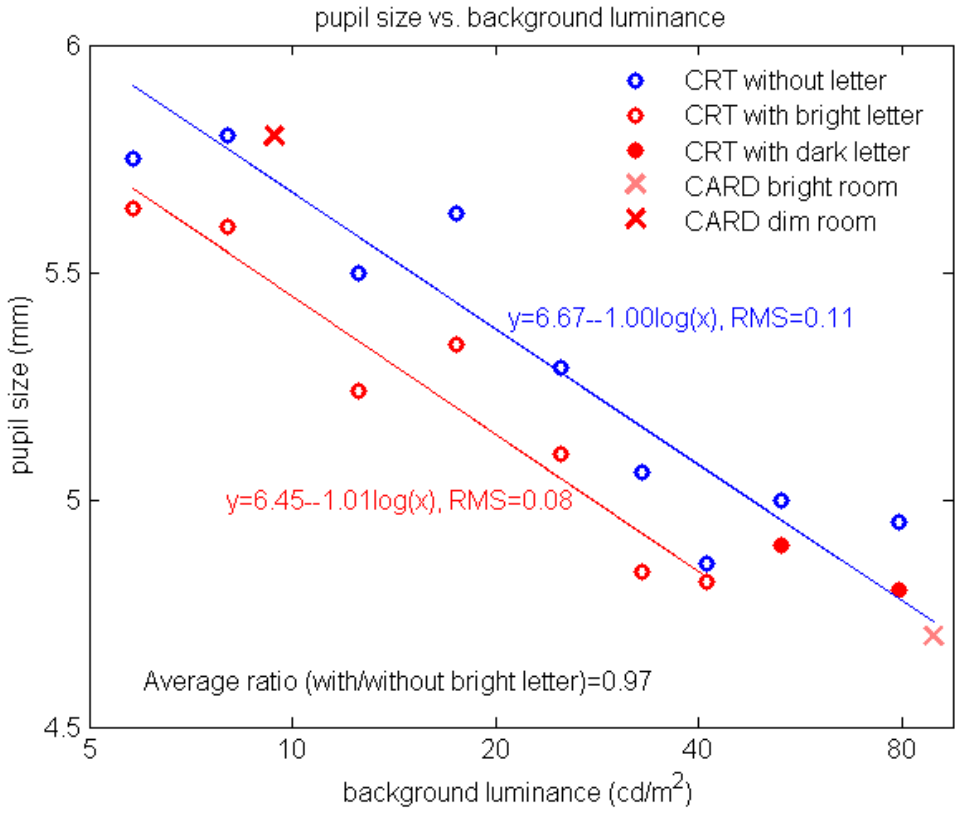

Fig. 8. Pupil size vs. background luminance. Pupil sizes are measured for CRT screen with (red circle) or without (blue circle) an acuity-sized letter present, and for the Cambridge Crowding Card in a bright (saturated red cross) or dim (pale red cross) room. The blue line is fitted to all CRT without letter (blue circle), CRT with dark letter (red dot), and Card (cross) data points. The red line is fitted to CRT with bright letter (red circle) points.

Pupil size is linearly related to log background luminance (Fig. 8). The presence of a bright letter on CRT screen reduces the pupil size slightly.

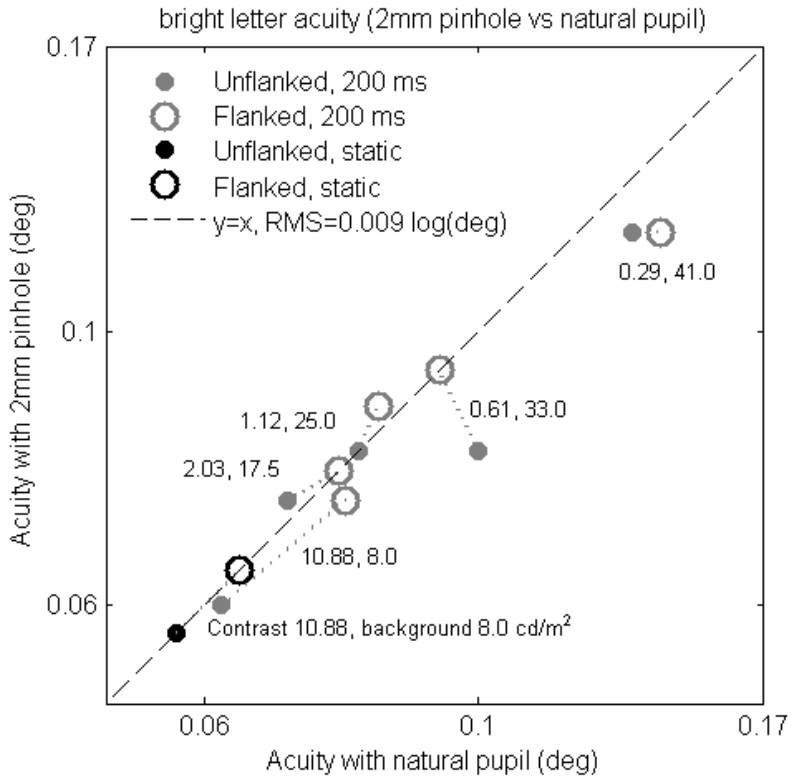

Fig. 9a. Pupil size and bright letter acuity. *A* (dot) and *A'* (circle) with 2mm pinhole are plotted against those with natural pupil. Letter-to-letter spacing is 1.5x letter size. Each pair of *A* and *A'* are connected by a dotted line. The equivalence line (dashed line) is superimposed. Contrast and background luminance are indicated for each pair of flanked/unflanked acuities. Grey symbols are brief (200 ms), and black symbols are static. All the high contrast conditions are on the line: no effect of pupil size on flanked and unflanked acuity. Both 0.6-contrast unflanked acuities are large and better with a small pupil. Only the lowest contrast (0.3) flanked acuity is affected by pupil size. This makes sense if we suppose that the threshold for these LARGE letters (>0.1 deg) is limited by cortical noise (which is independent of retinal illuminance), the aperture affects only the point spread function, not the limiting noise.

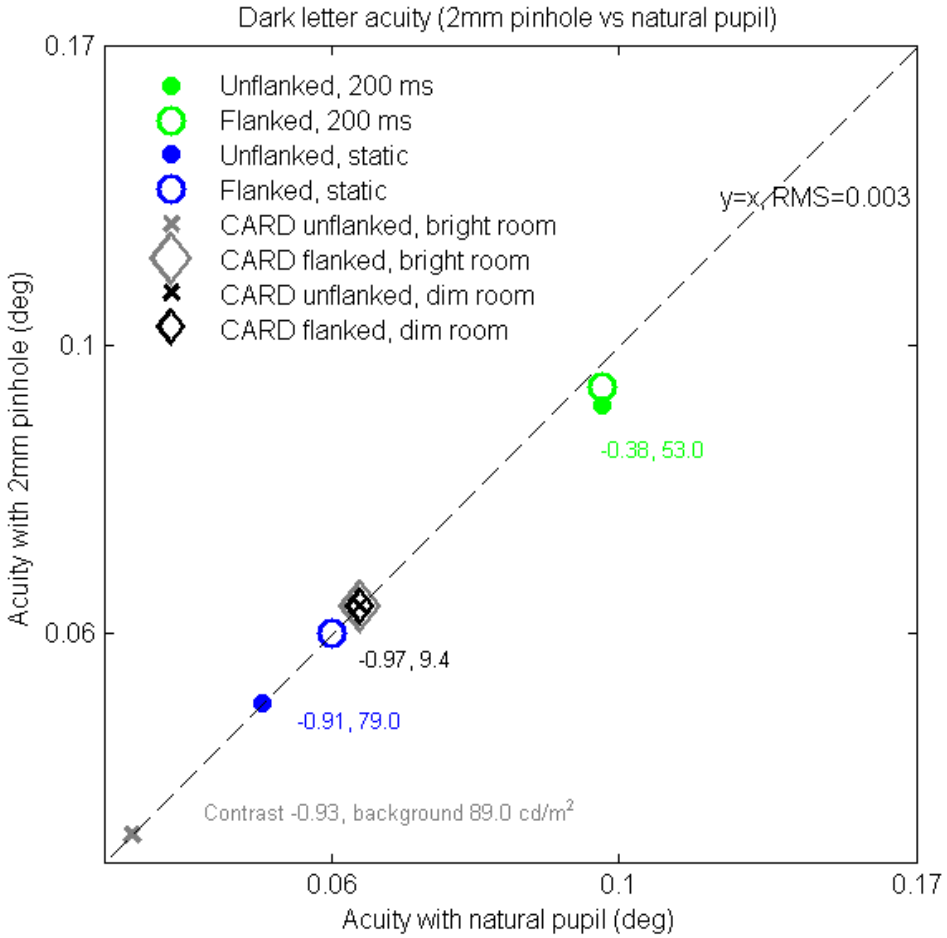

Fig. 9b. Pupil size and dark letter acuity. Letter-to-letter spacing is 1.5x letter size. *A* (dot for CRT, cross for Card) and *A'* (circle for CRT, diamond for Card) with 2mm pinhole are plotted against those with natural pupil. Each pair of *A* and *A'* have the same color (blue, green, grey or black). The equivalence line (dashed line) is superimposed. Contrast and background luminance are indicated for each pair of flanked/unflanked acuities. No effect of pupil size at medium and high contrast.

Adding a 2 mm pinhole improves higher acuity thresholds (>0.1 deg), but has little or no effect for lower acuity thresholds. This is consistent with the results in the last section where only high and medium contrasts data are available for analysis and those results show that high contrast letter acuity is not affected by pupil size whereas medium (0.6) contrast letter acuity is significantly improved by adding 2mm pinhole. As mentioned before, it seems that for high contrast letters, improvement of ocular optics and decrease of retinal illumination counteract each other, whereas for medium contrast letters ocular optics triumphs retinal illumination. An empirical example is that when visual acuity is measured in a clinic, a person with normal vision doesn't benefit from a pinhole, but a myopic patient can see much better with a pinhole.

From Fig. 9, we see that the effect of pupil size on acuity is small compared to that of contrast. Since the contrast value of dark letter makes more sense ([-1, 0]), we'll look at Fig. 9b only. The 2 mm pinhole reduces pupil size 2.5-fold and its effect on acuity is shown as the vertical distance from the line. The RMS deviation from the line is 0.003 log(deg) in Fig. 8b. Changing contrast causes a point to shift vertically and horizontally from one location to another. From Fig. 8b, the variation of contrast is comparable with that of pupil size (2~3 folds). Clearly points are spread out much more widely than they deviate from the line, therefore contrast but not pupil size plays a bigger role in determining acuity, at least within our data range.

3.4 Optical blur and acuity

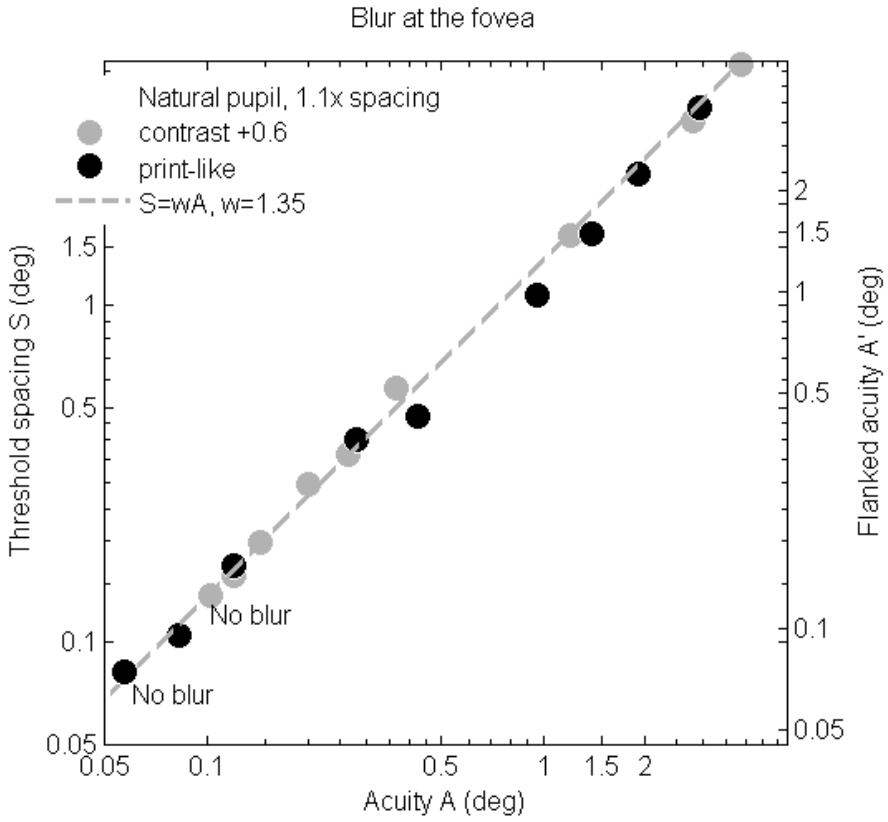

Fig. 10. Effect of blur on both 0.6-contrast 200 ms stimuli (grey) and -0.91-contrast static stimuli (black). Pupil sizes are 5.0 mm (0.6 contrast) and 4.8 mm (print-like). Background luminance is 33 cd/m^2 – 648 td (0.6 contrast), and 79 cd/m^2 – 1430 td (print-like). Data of 0.6 contrast (grey disks) are from the paper. The unit-slope line (grey dashed) is S=1.35A. The regression lines (not shown) are log(S)=0.98log(A)+0.10 (RMS=0.05) for print-like stimuli (black) and log(S)=0.99log(A)+0.13 (RMS=0.02) for 0.6 contrast 200 ms stimuli (grey). Letter-to-letter spacing is 1.1x letter size. The increase of threshold spacing (and flanked acuity) with blur shows that flanked acuity is limited by the point spread.

Grey and black disks follow practically identical trends, with very similar regression parameters. Both slopes are not significantly different from one. Thus $S=wA$, where $w=10^{0.132}=1.35$, describes both groups of data reasonably well. Therefore overlap masking limits the threshold spacing under blurred conditions and the model parameter $w=1.4$ (Eq. (1) & (2)).

We observe that, firstly, flanked acuity is the same for brief medium-contrast and static high-contrast letters. Secondly, the increase in foveal *S/A* ratio for print-like letters (without blur, Fig. 2) cannot be attributed to overlap masking. The flanked acuity of print-like letters without blur in the fovea is limited by some other factor (e.g. crowding).

3.5 Polarity and acuity

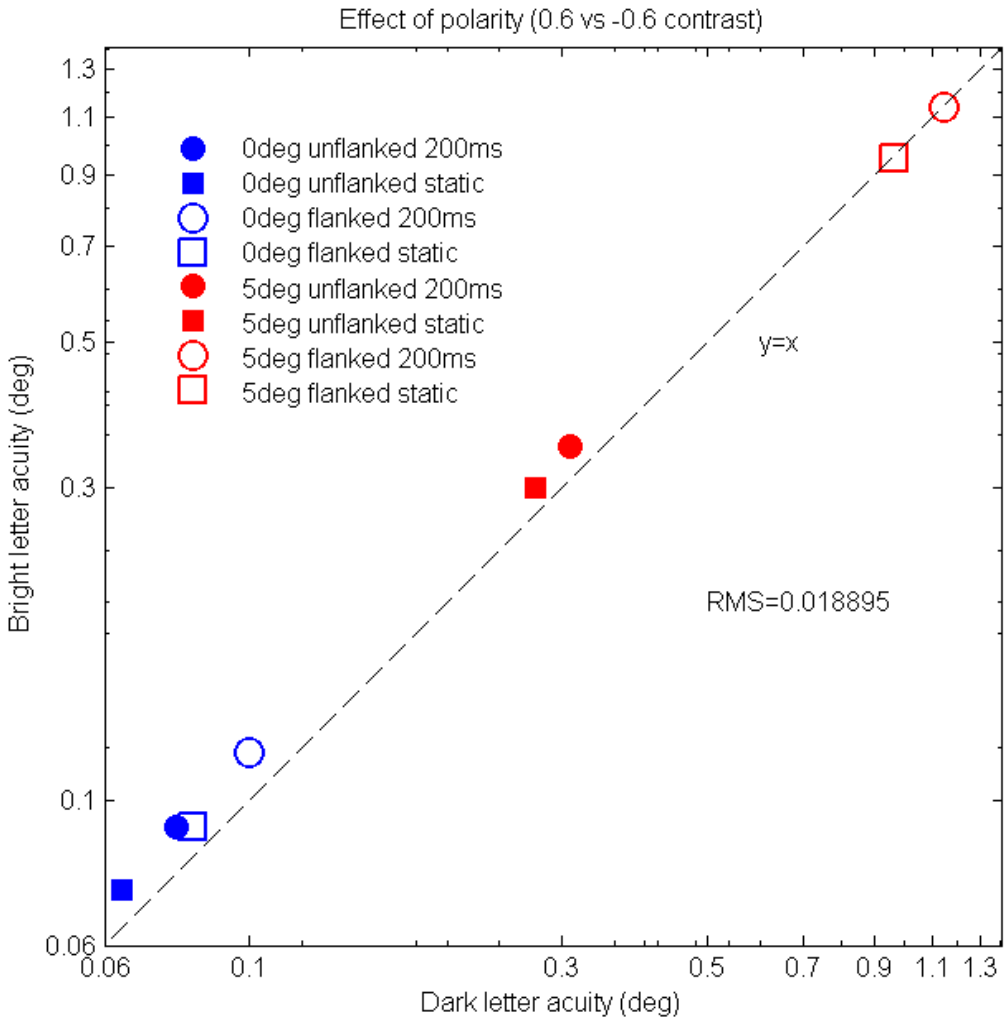

Fig. 11. Effect of polarity on *A* and *A'* at the fovea or in the periphery, for several durations. Letter-to-letter spacing is 1.1x letter size. Acuities for 0.6-contrast stimuli (bright) are plotted against those for -0.6 contrast stimuli (dark). Background luminance is 33 cd/m^2 for all data, pinhole size 4 mm. Data for durations of 200 ms (circles) or static (squares), eccentricities of 0 (blue) or 5 deg (red), and flanked (empty) or unflanked (solid) stimuli are indicated. No effect of polarity.

Plotted on log-log scales, the acuities in all 8 conditions (2 eccentricities, 2 durations, and unflanked/flanked acuity) lie on or near the equality line. The differences between dark and bright letter acuities are very small (RMS=0.02 log(deg)). And at high visual acuities (i.e. small letter sizes), the bright letter acuity is slightly worse than the dark letter acuity. This seems to be contradictory to Westheimer et al. have reported that when the letter stimuli with the reversed

contrast polarity (i.e. bright letters on a dark background) produced better acuities than the traditional ones (i.e. dark letters on a bright background) did (Westheimer, 2003; Westheimer, Chu, Huang, Tran, & Dister, 2003). There are two main differences between their studies and ours. First, the polarity reversal in their studies was literally switching the luminance levels of the letters and the background, thus the resulting contrast absolute value was much greater than that of the original contrast, by Weber contrast definition; whereas in the present study polarity reversal means fixing the background luminance and reversing the luminance increment of the letters, which generated exactly the same contrast absolute value with a different sign. Since the contrast of bright letter stimuli in Westheimer's studies is higher than that in the present study, it is not surprising that they observed better bright letter acuities, although both manipulations are interesting in understanding the effect of contrast polarity on the visual acuity. Second, in the reversed-contrast Snellen chart study by Westheimer et al., the observers' ages range from 20 to 88 years old. And although the average acuity is lightly better for the bright letter stimuli, their results showed that the difference was much more prominent for older observers, whereas for observers at around 20 ~ 30 years old there is not much difference in acuity between the two polarities. In the present study, the measurements for assessing contrast polarity effect were collected from observer SS who was 29 years old, and the advantage of using a reversed – contrast letter chart is not seen.

3.6 Contrast and duration

3.6.1 Acuity and threshold spacing

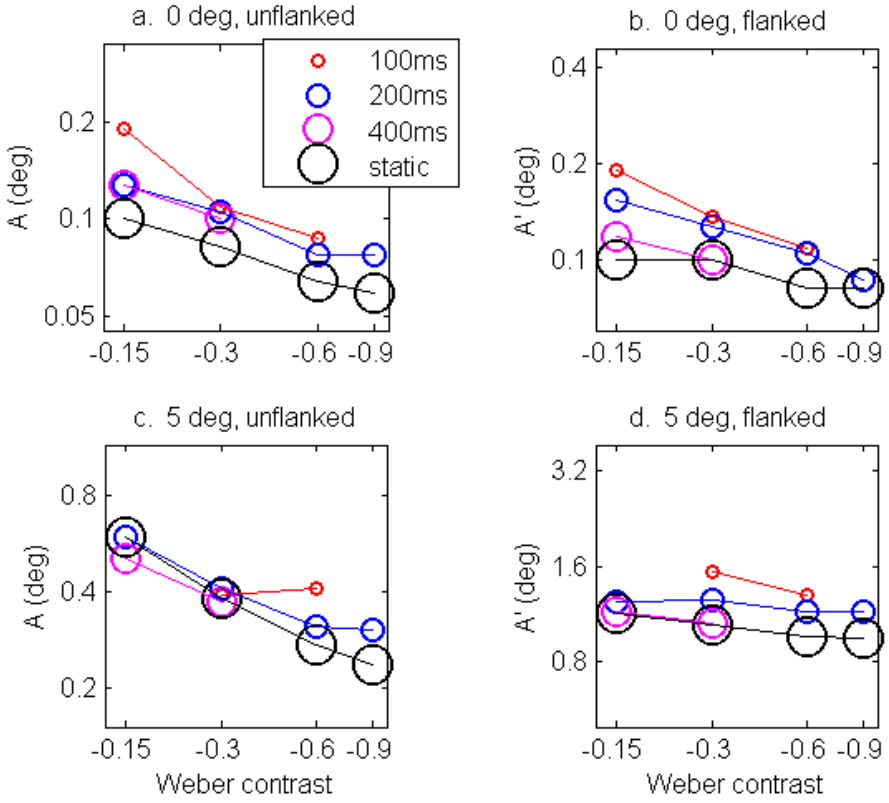

Fig. 12. *A* and *A'* vs. contrast. Duration (short to long) is denoted by circle size (small to large) and color. Letter-to-letter spacing is 1.1x letter size. Horizontal and vertical scales have equal log unit lengths. Background luminance 33 cd/m^2, pinhole size 4 mm. Duration seems to have little effect on flanked acuity at 5 deg ecc. Acuity improves with contrast. Flanked acuity does too, but not as much, and even less when it's peripheral (5 deg).

In Fig. 12, at each duration and eccentricity, flanked acuity is less affected by the 6-fold change in contrast than unflanked acuity. In particular, at 5 deg, flanked acuity vs. contrast is almost flat (Fig. 12d). The regression slopes are plotted in the following graph (Fig. 13).

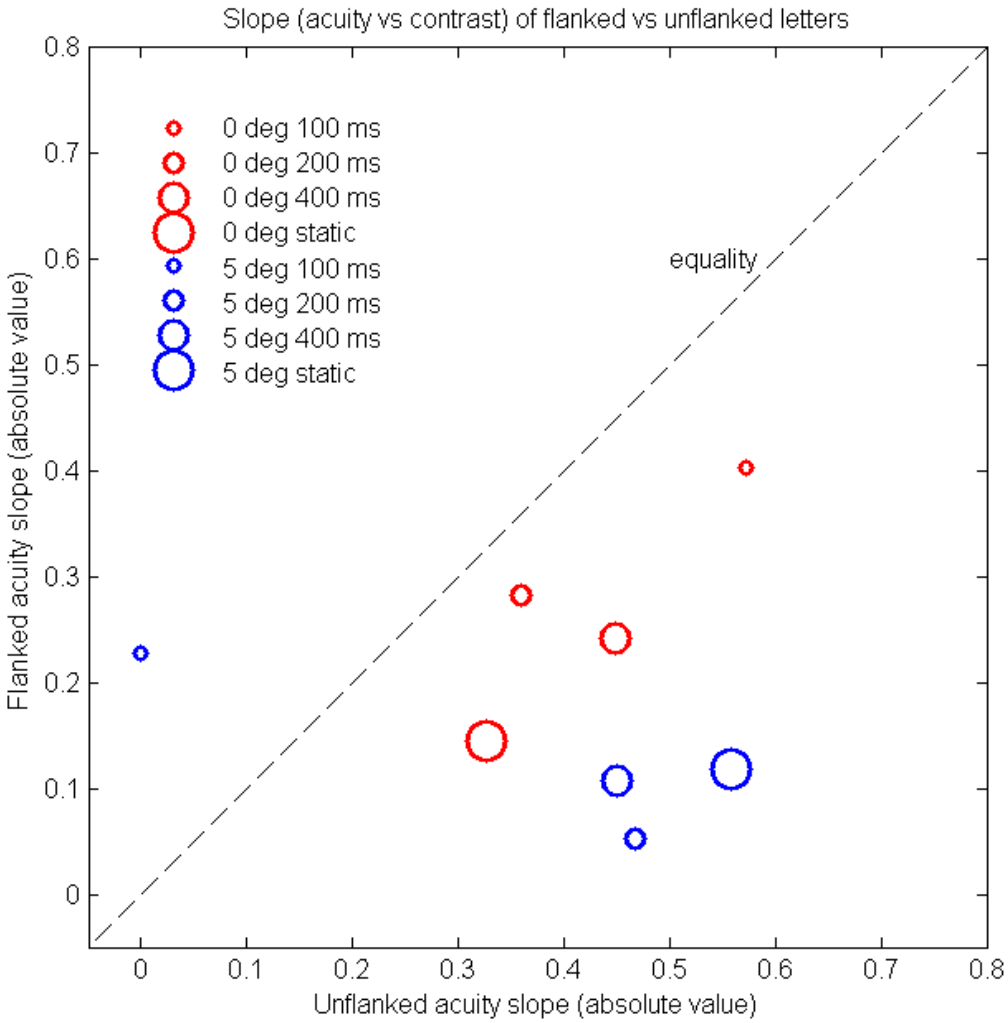

Fig. 13. Scatter plot of slopes (log acuity vs log contrast). Letter-to-letter spacing is 1.1x letter size. Each slope is obtained from the regression of log acuity vs. log contrast for the given duration, eccentricity, and flanked/unflanked condition, from the same-color symbols in Fig. 12. Duration is indicated by size, and eccentricity is indicated by color. Background luminance 33 cd/m^2, 4 mm pinhole.

The small blue dot might be an outlier, and more trials are needed to confirm this. Except for this 5 deg 100 ms point (small blue), all points lie below the equality line (dashed line). When contrast is varied, the rate of change in acuity is greater for unflanked letters than for flanked letters. Furthermore, blue points are below red points, while they cannot be separated horizontally. Therefore, the effects of contrast on various stimuli are in this order: unflanked 0 deg = unflanked 5 deg > flanked 0 deg > flanked 5 deg.

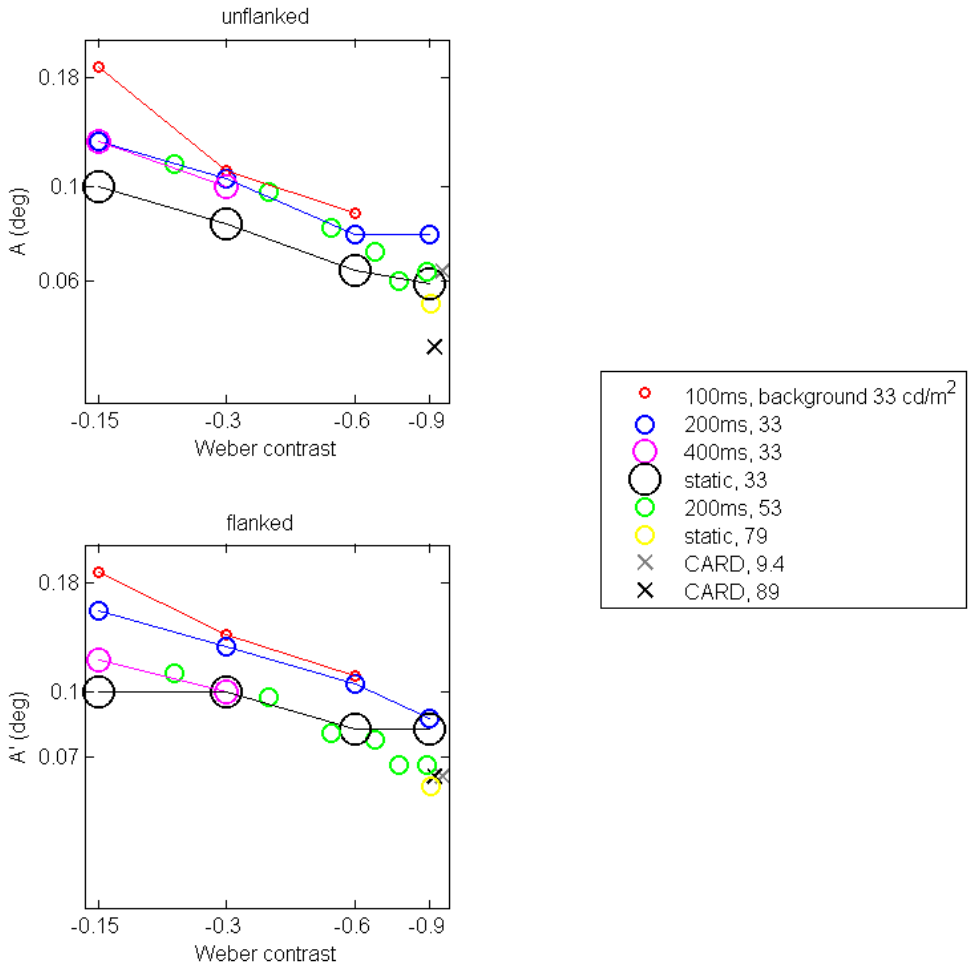

Fig. 14. *A* and *A'* vs contrast. The graphs are based on Fig. 12. Letter-to-letter spacing 1.1x letter size, 4 mm pinhole for 33 cd/m^2 background; letter-to-letter spacing 1.5x letter size, natural pupil for other backgrounds.) Previous CRT data at other background luminance (green and yellow circles) and Card data (grey and black crosses) are superimposed.

Contrast has similar effect on *A* and *A'* for different background luminance tested in our study in general. However, the brighter background (53 cd/m^2) seems to give better acuity for the same contrast and the same duration (comparing green circles with blue circles).

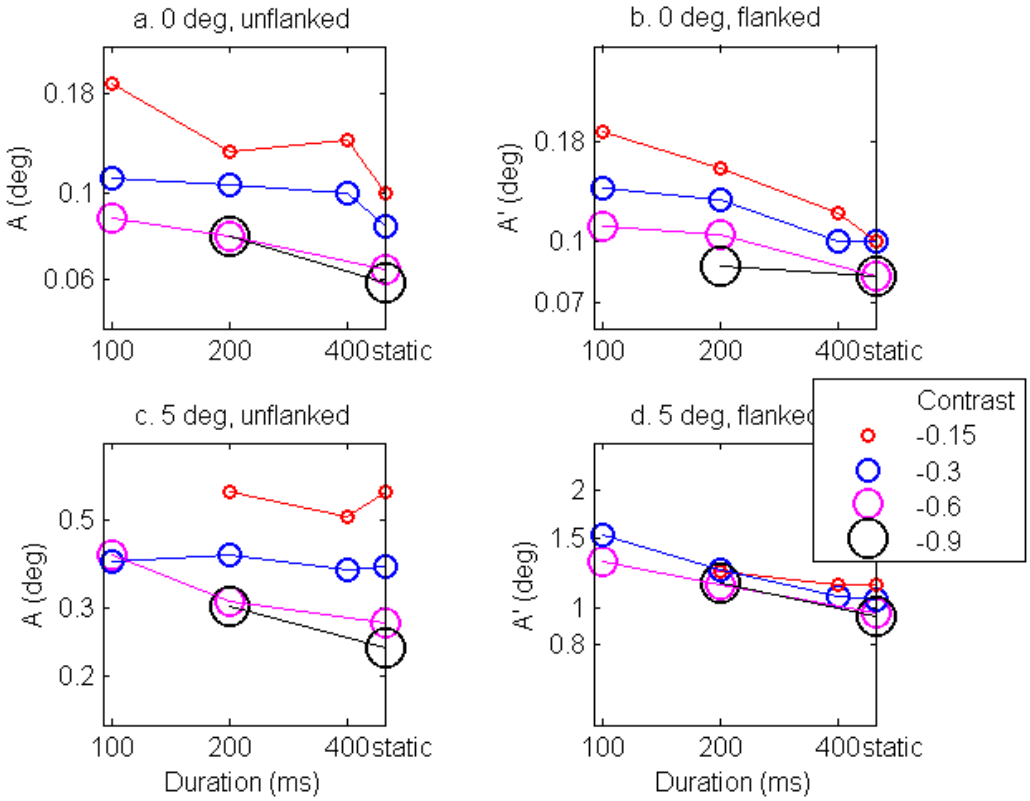

Fig. 15. Effect of duration. *A* and *A'* vs. duration. Letter-to-letter spacing is 1.1x letter size. Contrast (low to high) is denoted by circle size (small to large) and color. The rightmost points correspond to static presentation. Horizontal and vertical scales have equal log unit lengths. Note that there is hardly any effect of contrast on flanked acuity at 5 deg ecc. Background luminance 33 cd/m^2, pinhole size 4mm. The effect of duration is quite consistent with a log-log slope of -0.25 log acuity vs. log duration. The low contrast (-0.3, -0.15) letters at 5 deg seem flat, independent of duration. Low contrast results at 0 deg are ambiguous. Contrast DOES affect acuity. Contrast does affect flanked acuity when limited by overlap masking, but not when limited by crowding.

From Fig. 12 & Fig. 13, we see that in the periphery (5 deg), flanked acuity is not affected by contrast. However, flanked acuity at 5 deg does change with duration, as shown in Fig. 15d. Therefore, in the periphery, duration, but not contrast, seems to have significant effect on flanked acuity (or critical spacing). Baron & Westheimer reported that the photopic acuity measured using the Landolt ring improves with duration of exposure up to 400 ms and possibly longer (Baron & Westheimer, 1973), which agrees with the present findings.

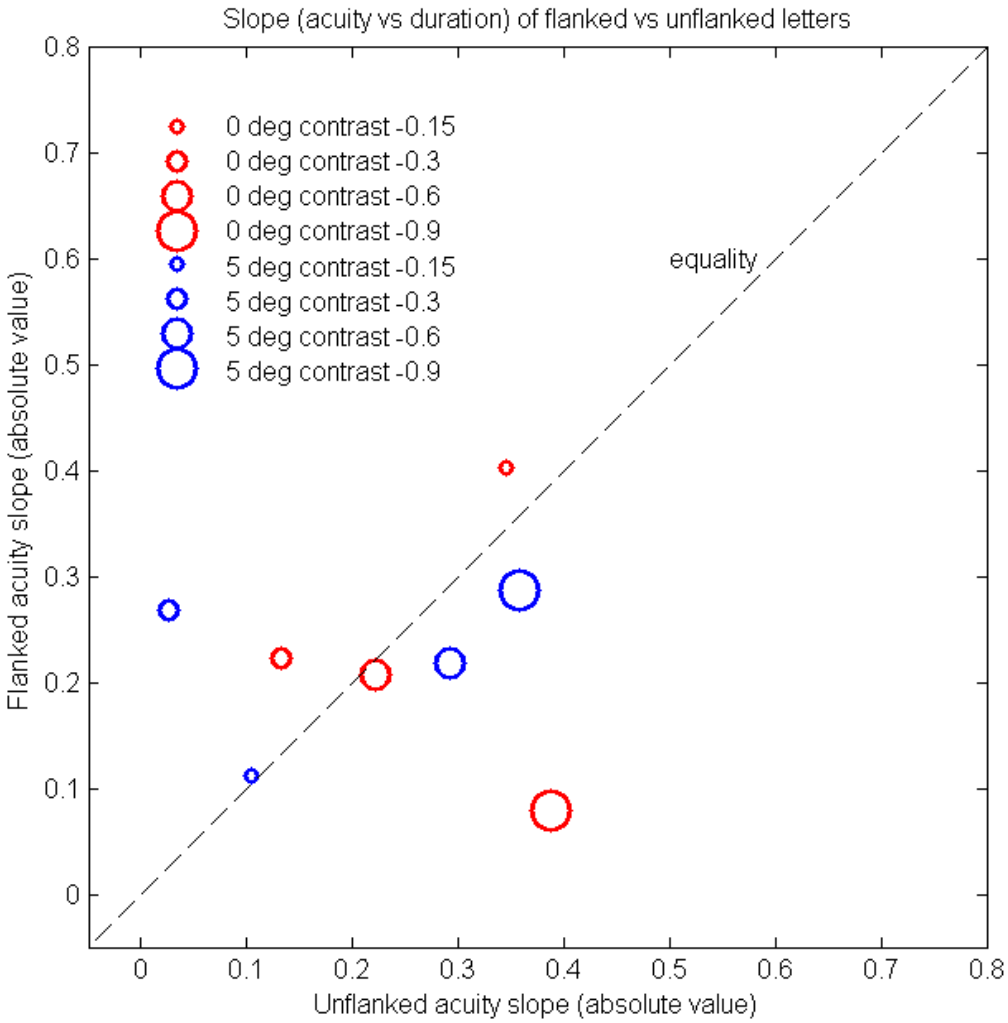

Fig. 16. Scatter plot of slopes (acuity vs duration). Letter-to-letter spacing is 1.1x letter size. Each slope is obtained from the regression of acuity vs duration for certain duration, eccentricity, and flanked/unflanked condition, from Fig. 13 (symbols connected by line segments). Contrast is indicated by size, and eccentricity is indicated by color. Background 33 cd/m^2, pinhole size 4mm.

Points in the fovea (red) and at 5 deg (blue) both scatter around the equivalence line and cannot be separated in any simple way. Therefore, duration has similar effect on acuities both in the fovea and in the periphery. However, when we examine points in Fig. 16 individually, we see that some points deviate far from the equivalence line, e.g. 0 deg high contrast (large red circle), for which duration has much greater effect on unflanked than on flanked acuities.

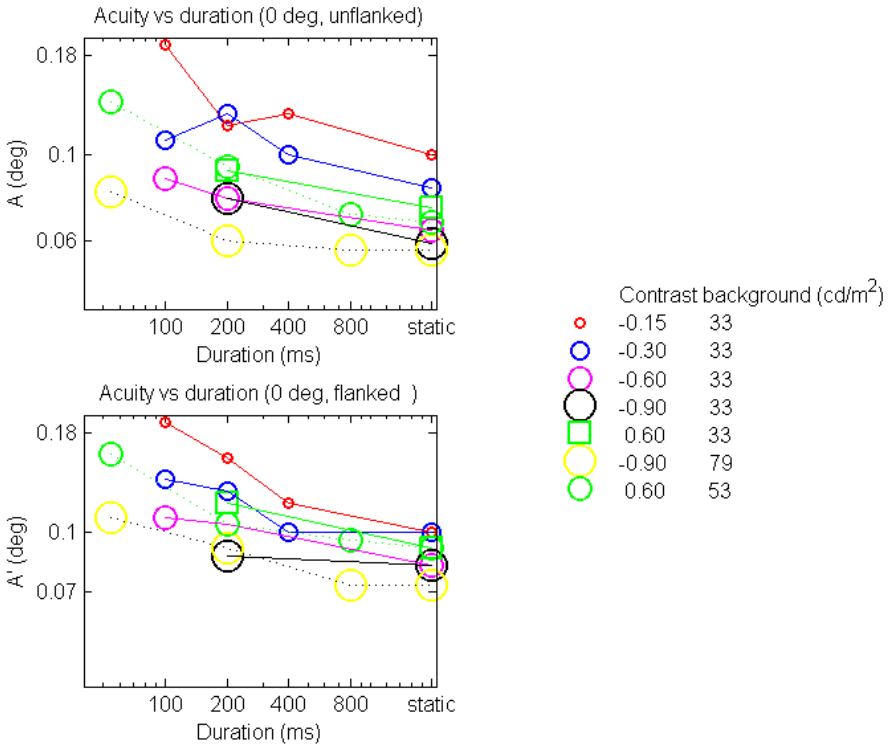

Fig. 17. *A* and *A'* vs duration. Letter-to-letter spacing 1.1x letter size, pinhole 4mm for 33cd/m^2 background; letter-to-letter spacing 1.5x letter size, natural pupil for others. The graphs are based on Fig. 15 a&b. CRT data of different background luminance or contrast (green and yellow circles or square) are also included.

In general, there isn't anything qualitatively different between different background luminances in terms of duration effect, except that for higher contrast and brighter background luminance (79 cd/m^2), unflanked acuity reaches the asymptote at shorter durations (comparing yellow and black circles in the upper panel).

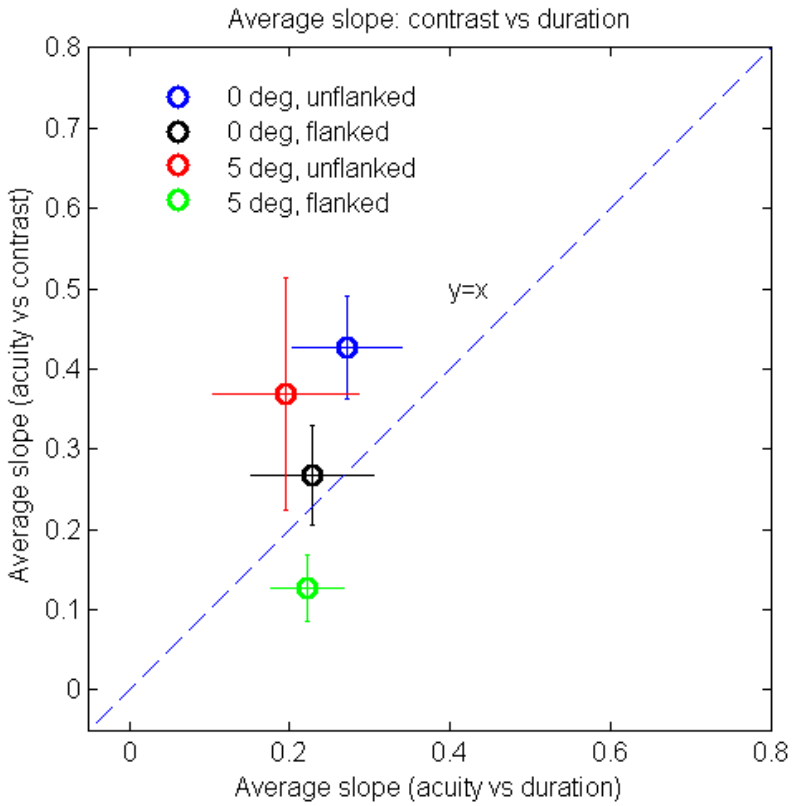

Fig. 18. Average slope (acuity vs contrast) vs average slope (acuity vs duration). Letter-to-letter spacing is 1.1x letter size. The length of each error bar indicates one standard error. Background 33 cd/m^2, pinhole size 4mm.

Note that all 4 points are located close to each other on the horizontal axis, and not horizontally separable, implying that duration has similar effect on acuity for all conditions (fovea or periphery, flanked or unflanked). Vertically, from top to bottom are 0 deg unflanked, 5 deg unflanked, 0 deg flanked, 5 deg flanked, in the same order as obtained from Fig. 13. Furthermore, for 0 deg unflanked stimuli, both contrast and duration, especially contrast, matter; whereas for 5 deg flanked stimuli, contrast contributes less than duration does.

Here we assume that the critical spacing for crowding depends on eccentricity only.

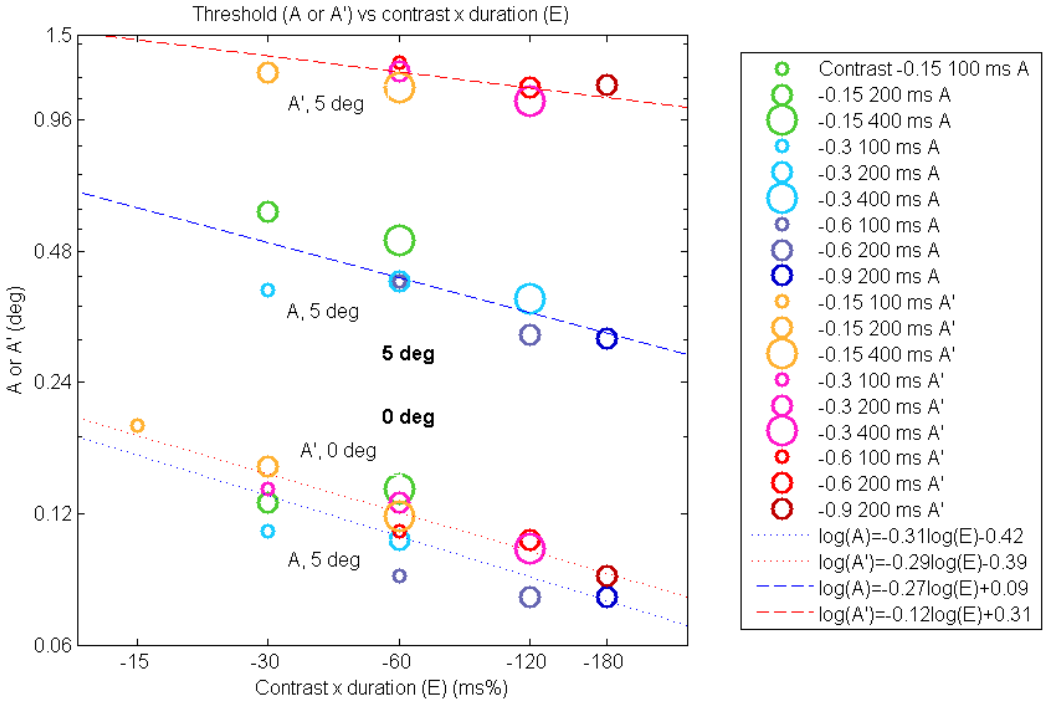

Fig. 19. Effect of contrast x duration at 0 and 5 deg. Unflanked (*A*, bluish) and flanked (*A'*, reddish) thresholds at various contrasts (color) and durations (size) are plotted against the contrast x duration product. Blue dotted line is the regression of 0 deg unflanked acuities; red dotted line 0 deg flanked acuities; blue dashed line 5 deg unflanked acuities; red dashed line 5 deg flanked acuities. Background luminance 33 cd/m^2, pinhole size 4mm. Horizontal and vertical scales have equal log units. Hardly any effect of flankers at 0 deg ecc. Huge (2x) effect of flankers at 5 deg ecc.

Fig. 19 shows how acuity changes with the product of contrast and duration. For all but the 5 deg flanked condition, acuities change with the product at a similar rate, as shown by similar regression slopes. At 5 deg, flanked acuity is more or less resistant to the contrast x duration product, probably because the change of flanked acuity at 5 deg is mostly attributed to duration, very little to contrast, as mentioned before.

At given contrast x duration product, the acuities vary. We did not see Bloch's law from this figure, probably because the durations of the stimuli we tested are too long (>=100).

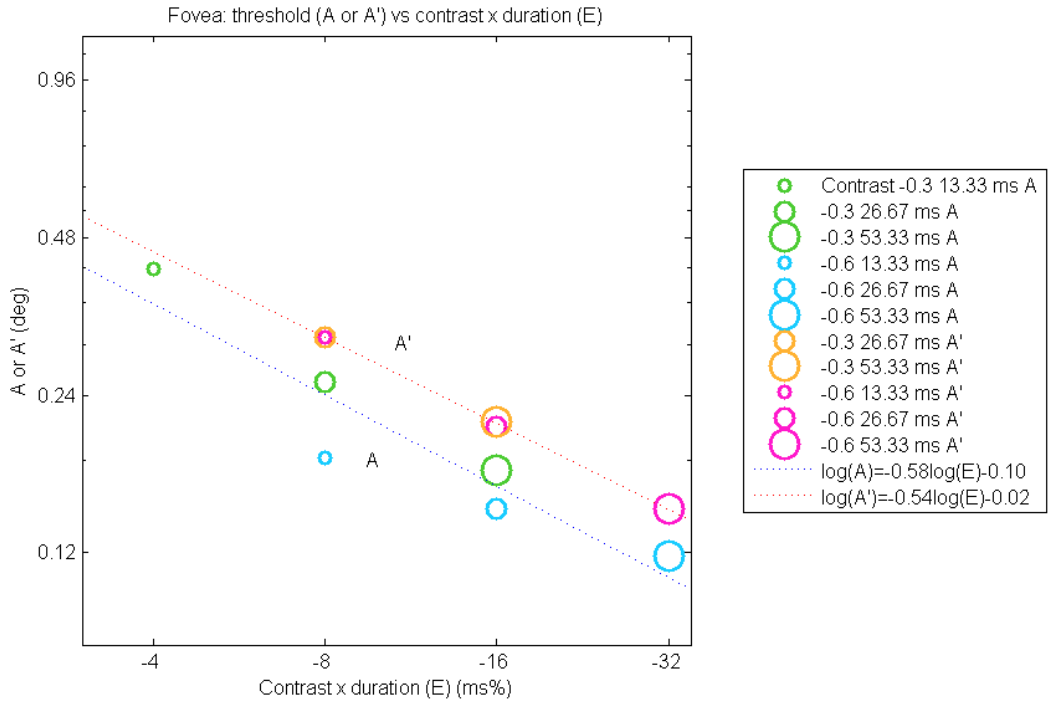

Fig. 20 *A* or *A'* vs contrast x duration for short durations (13.33 ms ~ 53.33 ms) in the fovea Letter-to-letter spacing is 1.1x letter size, pinhole 4 mm.

Fig. 20 and Fig. 19 plot the same variables but the range of the horizontal axis in Fig. 20 is shifted to the left of that in Fig. 19, i.e. stimuli in Fig. 20 have shorter durations (13.33, 26.67, and 53.33 ms).

Bloch's law implies that the effect of contrast is equivalent to that of duration on visual acuity (e.g. effect of a 2-fold increase in contrast should equal that of a 2-fold increase in duration). Since the increase in contrast has more significant effect on unflanked acuity than duration does, we still don't see Bloch's law for unflanked acuity. Similarly, since duration affects flanked acuity at 5 deg than contrast does, as mentioned before (Fig. 18), we don't see Bloch's law for flanked acuity in the periphery either (Fig. 19).

Since at even lower contrast (e.g. -0.15), *A'⁄A*=1 (following Fig. 21), we can assume that at lower contrast and short duration, Bloch's law applies to both *A* and *A'*. It seems that when the visibility of the target letter (unflanked letter or the central letter in a flanked stimulus) is very low, then contrast and duration contribute equally to the visibility and Bloch's law applies. Since the visibility of unflanked letter is higher than that of the flanked letter under the same condition, therefore it's easier to see Bloch's law in flanked acuity (Fig. 20).

3.6.2 Crowding-acuity ratio in the fovea

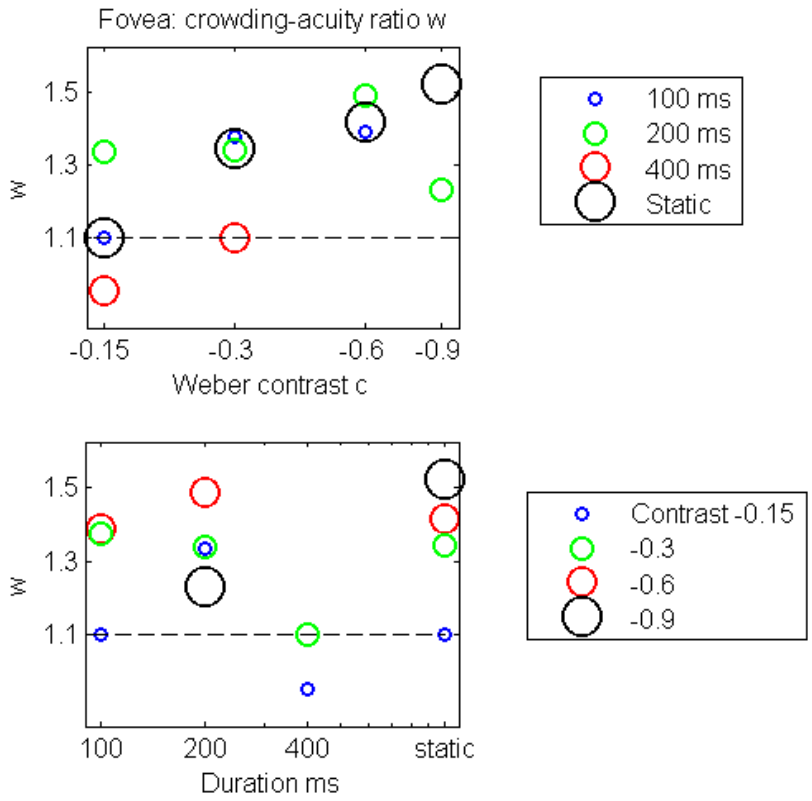

Fig. 21. Fovea: crowding-acuity ratio w vs. contrast or duration. Letter-to-letter spacing is 1.1x letter size. Background luminance 33 cd/m^2, pinhole size 4 mm.

Crowding-acuity ratio w varies with contrast and duration. In particular, it increases with contrast systematically. One might say that w is not a very robust index of spatial interaction which ideally should be stable across irrelevant stimuli parameters (e.g. contrast, duration). An interesting observation of Fig. 20 is that, the crowding-acuity ratio w is near or below 1.1 for low contrast (-0.15) and/or very brief (100 ms) stimuli. Since the target-flank spacing is 1.1 times the acuity size A, this result implies that for certain conditions (e.g. low contrast, brief presentation) the presence of flankers at 1.1x spacing does not affect the target identification (i.e., $A'=A$). This seems to be at odds with the legibility model, which imposes the overlap masking limit with the spacing parameter 1.4, i.e. S = max (sA, S_{crowding} , 1.4A), and doesn't seem to allow $A'=A$ for 1.1x spacing stimuli. The model successfully characterized data with optical blur, but perhaps very low contrast and very short duration set their own limits on visual acuities, which is different from overlap masking. Of course, under normal (non-extreme) circumstances, this shouldn't be an issue.

The relationship between A'/A ratio and A is revealed in Fig. 25.

3.7 Upgrading the legibility model

Recall that the legibility model (Eq. 1&2) specifies the forms of acuity and masking limits but not crowding, and it complicates the interpretation of foveal data of different scales, e.g. high contrast letter threshold spacing limited by crowding vs. low contrast letter threshold spacing limited by masking. It would be much clearer if we also have a function form for crowding limit that will give us one general formula of the model. Fig. 24 plots the threshold spacing against eccentricity with print-like letters. As previous studies, including the one by Levi, Song & Pelli (2007), have shown, critical spacing may be characterized by a linear function of eccentricity. In particular, in the form of φ_2 equation (equivalent to Bouma's law), $S=S_0(1+\varphi/\varphi_2)$ where S_0 is the critical spacing in the fovea and φ_2 is the eccentricity where the threshold spacing in the fovea doubles. The regression parameters of the plot in Fig. 23 are S_0=0.09 and b=0.2. Therefore, the legibility model

$$S = \max (S_{\text{acuity}} , S_{\text{crowding}} , S_{\text{masking}}) \qquad 1)$$

where

$S_{acuity} = sA,$

$S_{crowding} = S_0+b\,\varphi = 0.09+0.2\,\varphi,$

$S_{masking} = wA$

becomes

$$S = max\,(sA,\ 0.09+0.2\varphi,\ wA). \qquad 3)$$

In the fovea, when print-like letters (1.5x) are used, suppose A=0.05 deg, wA=1.4x0.05=0.07, sA=1.5x0.05=0.075 deg, crowding limit = 0.09 deg, and the maximum is the crowding limit, S=0.09 deg. When low contrast letters (1.1x) are used or if the optical system has uncorrected spherical aberration (blur), suppose A=0.1 deg, wA=1.4x0.1=0.14 deg, sA=1.1x0.1=0.11 deg, crowding limit=0.09 deg, and the maximum is masking limit, S=0.14 deg.

Quite reasonably, acuity limit and masking limit for threshold spacing is determined by acuity A that is dependent on factors such as optical blur and contrast; whereas crowding limit is relatively independent of these factors. However, critical spacing does depend on duration.

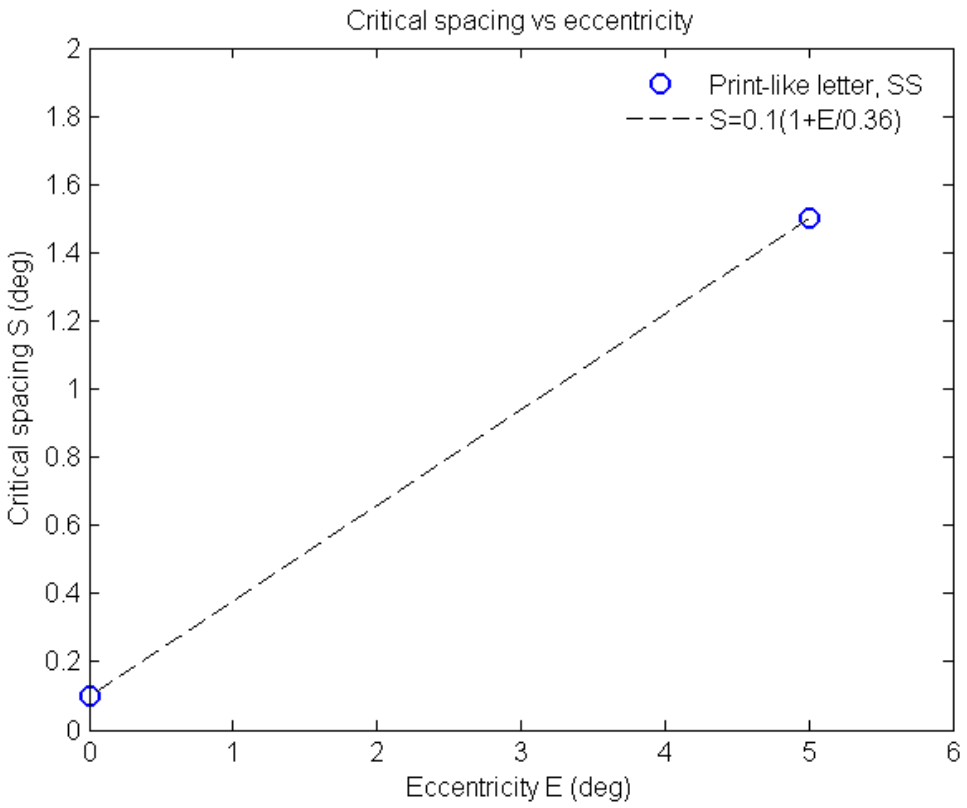

Fig. 24. Crowding critical spacing vs. eccentricity for print-like letters, assuming linear relationship.

3.8 Amblyopic screening

3.8.1 Foveal crowding

In the last chapter, using CRT-letters (medium contrast brief bright letters), overlap masking, but not crowding, accounts for foveal flanked threshold spacing. However, we observed that for high-contrast (-0.9) static print-like letters, threshold spacing improves less than acuity does, resulting in a greater crowding-acuity ratio (i.e. $w > 1.4$). This implies that for print-like letters, either 1) the extent of overlap masking is different (i.e. $w > 1.4$), or 2) the threshold spacing limit is not overlap masking at tight spacing. Adding blur to print-like letters rules out the first possibility, because the result shows that the extent of overlap masking or the effect of optical blur is constant across polarity, contrast, and duration, in particular, $w = 1.4$ for blurred print-like letters. Thus we conclude that the effect of tightly spaced flanks on print-like letters in the fovea is crowding. Because the critical spacing in the fovea is very small (i.e. < 0.1 deg), crowding is present only under near perfect conditions (e.g. high contrast, good optics, long presenting duration) that allow the threshold size to be small enough so that the threshold spacing is limited by crowding (see Fig. 10 for the upper left part of normal data at 0 deg). This is probably why some recent studies have claimed that crowding does not exist in the fovea,

since the stimuli used in those studies are either too big or too low contrast for crowding to occur (Levi, Klein et al., 2002; Pelli et al., 2004); see Levi (2008) for a discussion of foveal crowding. Nevertheless, earlier experiments that used simple stimuli (e.g. line segments, "T") did show crowding-like phenomena in the fovea, and our results confirm those findings (Latham & Whitaker, 1996; Levi, Klein, & Aitsebaomo, 1985; Toet & Levi, 1992).

3.8.2 Screening criteria

Fig. 25 plots crowding-acuity ratio W against unflanked acuity A for a wide range of the conditions that we tested, i.e., contrast, duration, polarity, pupil size (with and without 2mm pinhole), and eccentricity (0 deg and 5 deg), for normal observers and amblyopes. The horizontal line at $W = 1.84$ (yellow dashed) is the criterion obtained from the current study, which distinguishes strabismic amblyopia (red) from anisometropic amblyopia (green). For normal observers, crowding-acuity ratios at 5 deg are all above this criterion, and most of the normal foveal data are below. Examining more carefully the foveal data, we see that first, given an unflanked acuity A, the threshold spacing of 1.5x is somewhat greater than that of 1.1x flankers (i.e. squares are above circles in general). This effect of spacing on flanked threshold size is consistent with what was reported by Latham & Whitaker (1996). Second, and more importantly, in the fovea, all 1.1x spacing data points are well below the criterion line but a few 1.5x spacing points (including measures using the Cambridge Crowding Cards) are above the line. As argued before, a stimulus with a tight spacing (e.g. 1.1x) is better at differentiating strabismic from anisometropic amblyopia. Furthermore, a tight spacing (e.g. 1.1x) is also better at differentiating strabismic amblyopia from normal foveal vision. In other words, when using near optimal stimulus parameters crowding occurs in the fovea, but if letter-to-letter spacing is tight (e.g. 1.1x), $1.4 < W < 1.84$, which is still smaller than that found in strabismic amblyopia. In fact, we may say that the relative strength of crowding (i.e. critical spacing normalized by acuity) in the fovea is quite small compared to that in the periphery or that in strabismic amblyopes, for a tight spacing.

Our result suggests that a vision test of smaller letter-to-letter spacing (e.g. 1.1x) is more effective in screening for strabismic amblyopia and the crowding-acuity ratio W may be a useful criterion. Thus, measuring acuity and flanked acuity with a tight spacing provides a screening test for strabismic amblyopia that is robust across stimulus conditions.

4 Conclusions

In the fovea, unflanked and flanked acuities have different limits. The best unflanked acuity is 0.042 (Card) or 0.053 (CRT). The best flanked acuity is 0.063 (Card) or 0.06 (CRT).

The critical spacing in the fovea is 0.09~0.1 deg. In general, flanked acuity satisfies the acuity limit and the spacing limit, A'=max(A, 0.09 deg / s).

Pupil size is linearly related to (and wholly determined by) log background luminance, except that the prolonged presence of a bright letter reduces the pupil size slightly.

High-contrast letter acuity is independent of pupil size (i.e. natural pupil vs. a 2 mm pinhole). For low to medium contrast letters, however, adding a 2mm pinhole improves visual acuity 1.5x.

Optical blur increases flanked and unflanked acuity by the same proportion for both brief medium-contrast and static high-contrast stimuli.

While contrast magnitude has a large effect, contrast polarity has hardly any. Polarity has no effect on flanked acuity in the periphery. For other conditions, visual acuity is slightly better for dark letters.

Duration has similar effect on the visual acuity for both flanked and unflanked conditions, in both fovea and periphery.

Contrast effect on the visual acuity is in this order: unflanked 0 deg = unflanked 5 deg > flanked 0 deg > flanked 5 deg. Contrast has little effect on the flanked acuity at 5 deg.

In the periphery, for the flanked acuity, i.e., under crowding condition, duration is more important than contrast.

Screening: 1.1x stimuli can distinguish overlap masking / acuity and crowding, therefore they can be used to screen for strabismic amblyopia.

CLASSIFICATION IMAGES OF SPATIOTEMPORAL MECHANISMS FOR SIMPLE IMAGE FEATURS PERCEPTION IN NORMAL AND AMBLYOPIC OBSERVERS

1 Introduction

Spatial interactions of cluttered visual inputs affect both sensitivity and perceptual bias (e.g. apparent tilt) simultaneously. Crowding is normally described as the decreased sensitivity to a target among nearby similar distracters (Levi, 2008; Pelli et al., 2004). What is missing in this description is that the crowded perception is not necessarily featureless; rather, crowding is often associated with a perceptual bias determined by the cluttered features. Parkes et al. (2001) reported that the information of a crowded feature (i.e. orientation) is spatially pooled instead of being lost, and that the accessible average feature covertly serves as a perceptual pedestal (i.e. bias) which can either elevate or lower the feature detection threshold under certain conditions. This parafoveal effect of assimilation among slightly differently tilted objects was compared to a stronger repulsive effect, namely the tilt illusion, which refers to the exaggeration of the difference between the target and flankers when their orientations are grossly different (Solomon, Felisberti, & Morgan, 2004). These studies demonstrated the importance of not only the sensitivity loss but also the possible perceptual changes in understanding spatial interactions. While the spatial properties of crowding have been widely studied, the temporal properties of the spatial interactions have rarely been investigated. Westheimer et al. reported that flankers with positive stimulus onset asynchronies (SOAs) (i.e. flanker onset after target onset) have stronger interfering effects than those of simultaneously presented flankers on Vernier acuity. But no follow-up reports further pursued this question. In the present study, we systematically investigated the spatiotemporal interactions between flankers and the target, specifically on feature (i.e. orientation) perception, using the method of classification images.

Abnormal spatial interactions such as crowding are characteristic of strabismic amblyopia. Amblyopia is a developmental visual disorder with primarily reduced contrast sensitivity and other impaired visual functions (Ciuffreda et al., 1991; Levi, 1991; Levi et al., 1985). Crowding is closely related to many amblyopic visual deficits such as contour interaction, spatial distortion and reduced Vernier acuity (Bedell & Flom, 1981; Hess & Jacobs, 1979; Levi & Klein, 1985; Levi, Yu et al., 2007), as well as impaired daily visual functions such as reading (Levi, Song et al., 2007). It has been proposed that strabismic central vision can be modeled as the normal peripheral vision, and crowding is one of the most important characteristics shared by them (Levi, 1991; Levi & Klein, 1985; Levi et al., 1985). The temporal properties of amblyopic vision have not received nearly as much attention as amblyopic spatial vision.

Among the few studies on amblyopic temporal visual deficits, an abnormal spatiotemporal modulation function with reduced contrast sensitivity more markedly at low temporal frequencies and at medium to high spatial frequencies has been found (Bradley & Freeman, 1985; Levi & Harwerth, 1977; Manny & Levi, 1982a, 1982b). Interestingly, this defect of sensitivity at low temporal frequencies was much milder or absent for apparent contrast tasks using suprathreshold gratings (Manny & Levi, 1982a, 1982b), suggesting that the mechanism for detecting flicker at near-threshold contrast may differ from that at suprathreshold contrast. Moreover, at low spatial frequencies, little difference in temporal sensitivity has been noted between amblyopic and normal eyes (Bradley & Freeman, 1985; Manny & Levi, 1982a, 1982b). These studies suggest that the amblyopic spatiotemporal mechanism for detecting a simple image feature is abnormal – the spatial mechanism may be expanded with decreased resolution, and given the extant data we can at least expect that the temporal mechanism differs from that of the normal at high spatial frequencies. On the other hand, the amblyopic spatiotemporal template for identifying a crowded feature would be similar to that of the normal peripheral vision if both share the same mechanism for spatial interactions.

The method of classification images used in the present study is essentially a correlation analysis of the observer's decision with the random noise present in the stimuli. The purpose of this method is to estimate the detection template (i.e. strategy or mechanism) for performing a specific task (i.e. how the visual information is weighted) for an observer. Classification images were first introduced to vision research and named in the 1990's when Ahumada and Beard successfully obtained the human template for Vernier acuity task using this technique (Ahumada, 1996; Beard & Ahumada, 1998). Even earlier than that, Ahumada used a similar multiple regression method to study the template of auditory tone detection by correlating the observer's response with the auditory noise frequency (Ahumada & lovell, 1971). The classification image technique is closely related to the reverse correlation technique – a tool for neural receptive field analysis that was developed in the 1980's and 1990's (Jones & Palmer, 1987; Ohzawa, DeAngelis, & Freeman, 1997; Ringach, Hawken, & Shapley, 1997), and they both have been mathematically justified (Ahumada, 2002; Bussgang, 1952; E. de Boer, 1967; R. de Boer & Kuyper, 1968; Ringach & Shapley, 2004). Classification image methods have been widely applied in various fields of vision research since 1996, such as stereo vision, illusory contours, letter discrimination, crowding, and simple image feature detection as discussed above (Gold, Murray, Bennett, & Sekuler, 2000; Levi & Klein, 2002; Nandy & Tjan, 2007; Neri & Heeger, 2002; Neri, Parker, & Blakemore, 1999; Watson & Rosenholtz, 1997). This technique appeals to many researchers because first, its degree of freedom in space is much greater than that of the classic psychophysical experiments due to the large number of noise elements and levels one can choose, and the cost of efficiency (i.e. increase in number of trials) is only moderate. The high degree of freedom allows an observer to apply his / her strategy while performing a task, which will then be faithfully recorded in the results. Second, classification images are less arbitrary in probing the signal of interest by adding independent random noise. Finally, classification image result can be intuitively interpreted. Classification

image methods have also been applied in amblyopic vision studies. Levi et al. found that in amblyopia the templates for target detection and position discrimination were shifted to lower spatial frequencies, especially the latter which was substantially impaired at higher spatial frequencies. These abnormal templates as well as the high internal noise together account for the loss of performance for amblyopic vision (Levi & Klein, 2002, 2003; Levi, Klein, & Chen, 2008). Interestingly, there is evidence that the abnormal template for position discrimination can at least partly be corrected after training through perceptual learning (Li, Klein, & Levi, 2008). It should also be noted that the inverse Fourier transform of the template for target detection in the spatial frequency domain reported by Levi & Klein indeed has a "Mexican hat" shape in the spatial domain (Levi & Klein, 2003; Levi et al., 2008). In the present study, we applied spatial (one-dimensional) and temporal noise of the form of either luminance or orientation to the corresponding visual feature and estimated the two-dimensional spatiotemporal classification images for both normal and amblyopic observers.

A two-stage model consisting of a detection stage based on contrast energy and a subsequent identification stage based on image polarity has been proposed and tested (Neri & Heeger, 2002) using the method of classification images. Their study was the first time such a spatiotemporal mechanism for feature detection was directly demonstrated, and the resulting classification image resembled the spatiotemporal receptive field of a V1 neuron to some degree (DeAngelis, Ohzawa, & Freeman, 1993; Neri & Levi, 2006). The spatial profile of the classification image has a "Mexican hat" shape typically seen in both the neural receptive field and the behavioral "perceptive field" (DeAngelis et al., 1993; Hubel & Wiesel, 1959). However, the temporal profile of the classification image is rather widely distributed, and the often observed temporal inhibition (or transience) in detecting asynchronous light stimuli was absent (Kelly, 1971a, 1971b; Rashbass, 1970; Watson & Nachmias, 1977). A probable explanation for the pure-sustained temporal profile of the classification image is the possibly high temporal uncertainty associated with their task. Based on the experience of the author and many others, spatiotemporal classification image tasks can be quite challenging, and it is sometimes not easy to find a suitable stimulus configuration that ensures the desired perception. High uncertainty is not only inefficient in estimating the template, but also can severely diminish the value of the result. In fact, it has been recommended for classification image experimental design that the signal should be set significantly stronger than that of the noise in order to reduce uncertainty and to obtain the task relevant template (Tjan & Nandy, 2006). In the present study, we repeated Neri & Heeger's main experiments but reduce the temporal uncertainty by using a discrimination (instead of detection) task, in which the signal was an increment on a relatively high base that can be reliably localized temporally and spatially.

2 Experiment 1. The spatiotemporal mechanism for luminance discrimination.

2.1 Methods

2.1.1 Observers

Five observers with normal vision and six with amblyopia (including anisometropic and strabismic amblyopia) participated in our study. All participants had been exposed to hours of visual psychophysical experiments, and were naïve as to the purpose of the study, except for the author. None of the amblyopic observers has eccentric fixation. One amblyope, JS, had received intensive training with her amblyopic eye through perceptual learning, and her visual acuity as well as other visual functions of the amblyopic eye had improved substantially by the time she entered the current study. The detailed characteristics of each observer are listed in Table 1.

Observer	Age (yrs)	Strabismus (at 6 m)	Eye	Refractive error (diopters, D)	Line letter VA (single letter VA)
Normal					
SS	30	None	R	-0.25	20/12.5
			L	pl/-0.25x119	20/12.5
SK	19	None	R	-4.75/-1.00x165	20/16
			L	-3.00	20/16
CN	23	None	R	-0.50	$20/12.5^{+1}$
			L	-0.50	$20/12.5^{+1}$
EP	25	None	R	+0.75	$20/16^{+1}$
			L	+0.75	$20/16^{+2}$
MN	36	None	R	-1.25/-1.50x106	20/12.5
			L	-1.75/-1.00x73	20/12.5
Strabismic (including strabismic & anisometropic) amblyopic					
BK	62	L ExoT 8^{Δ}	R (NAE)	-1.50/-2.5x105	$20/12.5^{+1}$
		R hyperT 6~8^{Δ}	L (AE)	-3.00/-0.25x135	$20/25^{+1}$ ($20/20^{-2}$)
BN	22	L EsoT 3~4^{Δ}	R (NAE)	+5.50/-2.25x5	$20/16^{+2}$
			L (AE)	+5.50/-1.50x175	$20/50^{-2}$ ($20/25^{-2}$)
GW	59	R EsoT 4-6^{Δ}	R (AE)	pl	$20/100^{-2}$($20/32^{-1}$)
			L (NAE)	+0.50/-0.75x180	$20/16^{-1}$
GJ	24	R EsoT 4-5^{Δ}	R (AE)	+3.50/-1.00x97	$20/40^{-2}$ ($20/25^{+1}$)
			L (NAE)	pl	$20/16^{-1}$
Anisometropic amblyopic					
GD	45	None	R	+0.25/-0.50x90	$20/12.5^{-2}$
			L	+3.75/-1.00x30	$20/50^{+2}$ ($20/50^{+2}$)
JS	27	None	R (AE)	+1.00	Pre training: $20/25^{-2}$ ($20/25^{+2}$) Post training: $20/16^{+1}$ ($20/16^{+1}$)
			L (NAE)	+0.25	$20/12.5^{-1}$

Table 1. Observers characteristics.

2.1.2 Stimuli

Stimuli were generated by Matlab 7.01 with Psychtoolbox 2.0 and presented on a flat CRT monitor (39.6 x 29.7 cm, 1600 x 1400 pixels, 100Hz, NEC). At 50% brightness and 100% contrast, the luminance gradient ranges from 0.32 to 117.7 cd/m^2. The monitor was calibrated to generate a linear luminance function of pixel value. There were six conditions in this experiment:

Condition 1 (basic noise-signal). The background luminance is 58 cd/m^2. The basic

stimulus element is a 1.1 x 0.8 deg square composed of 11 vertical bars in juxtaposition. Each bar measures 0.1 x 0.8 deg, and is randomly assigned one of 11 luminance noise increments (from -6.9 cd/m^2 to 6.9 cd/m^2 with the step size 1.38 cd/m^2). A complete stimulus is a 0.42 sec sequence of 21 such elements (i.e. frames), each of which lasts 20 ms. The middle (6th) bar in the middle (11th) frame of the sequence is the target, and the rest are noise (i.e. distracters). The target luminance of each trial is randomly selected from one of two values: 94.7 cd/m^2 (high) and 86.4 cd/m^2 (low), and is noise free. Two red bars that are ½ and 1/3 in length and width abutting the middle bar of each frame from above and below serve as the spatial cue for the target and are present throughout a trial. These *noise-signal* sessions are the basic condition for both normal and amblyopic observers (Fig. 1).

Condition 2 (basic noise-noise). The luminance of the target bar was replaced by a fixed pedestal luminance (i.e. 86.4 cd/m^2) plus a noise luminance increment randomly selected in the same way as for any other distracters from the 11 possible values. In this case, the signal is "imaginary" but the target can still be spatially and temporally localized because of its relatively high base luminance. The rest of a *noise-noise* session is the same as the *noise-signal* sessions described above. This condition is also the basic setup for all other conditions.

Condition 3. For three normal observers, SS, SK, and MN, filtered stimuli were generated by convolving the original stimuli with a two-dimensional Gaussian filter in space and time that acts on the stimulus grid, with σ = 0.5 in each coordinate and the window size 3 x 3: $\begin{pmatrix} 0.0113 & 0.0838 & 0.0113 \\ 0.0838 & 0.6193 & 0.0838 \\ 0.0113 & 0.0838 & 0.0113 \end{pmatrix}$.

Condition 4. For one normal observer SK, the signal-to-noise ratio of the stimuli was decreased by increasing the noise luminance of the distracters. The step size of the luminance increment of the distracters was elevated from 1.38 cd/m^2 to 2.3 cd/m^2.

Condition 5. The signal-to-noise ratio of the stimuli was increased by either elevating the target visibility (i.e. increasing the difference between the high and low luminance values of a target) or reducing the noise (i.e. decreasing the absolute values of the luminance noise) or both. When presented in the normal periphery, the target luminance values were 108.6 cd/m^2 (high) and 78.3 cd/m^2 (low), and the range of noise luminance increments was reduced from [-6.9, 6.9] cd/m^2 to [-4.6, 4.6] cd/m^2 with the decreased step size 0.92 cd/m^2. The background luminance was lowered to 46.0 cd/m^2. For three amblyopic observers, BK, GW, and GD, the amount of modification varied slightly depending on individual performance.

Condition 6. In addition to the increased signal-to-noise ratio either for amblyopic eyes in the fovea or for normal eyes in the periphery, the bar width was increased from 0.1 deg to 0.3 deg, hence the fundamental frequency of the stimuli was decreased from 5 cpd to 1.67 cpd.

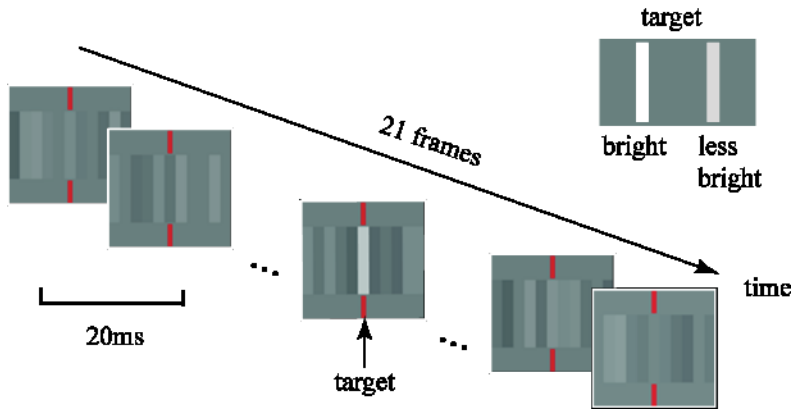

Fig. 1. Illustration of the stimuli and task for experiment 1.

2.1.3 Procedures

All experiments were done monocularly in a room with dim overhead light (10 cd/m^2). The viewing distance was 1 m. The stimuli were presented to the fovea of all normal and amblyopic observers. For some normal observers, the task was also performed at 2.5 deg in the inferior visual field, in which case, a fixation cross (20 x 20 min arc) was presented to the fovea.

2.1.3.1 Preliminary experiments

The luminance increment (i.e. noise step size) was set at the threshold for detecting a single bar on a blank screen. More specifically, a 40-trial session was completed by each observer. In every trial, either a target bar or a blank screen was presented for 20 ms, and the observer had to answer whether a bar was presented. The luminance of the bar was determined by Quest with the criterion set at 75%.

The lower target luminance in condition 1 was set to an easily visible level while the rest of the stimulus square was filled with the luminance of the brightest noise for normal observers. In a pre-session of 40 trials, a single stimulus frame but filled with uniform sum luminance of the background and the highest noise increment (among the 11 noise increments) was presented in the 2 intervals of each trial. In one of the two intervals, a brighter target bar was presented in the middle of the square, and its luminance is determined by Quest with a 95% criterion so that it must be easily detected. The observer had to respond as to which interval contains the target bar. The mean threshold luminance for all normal observers or the threshold luminance of individual amblyopic observer was taken as the low target luminance for different experimental conditions. The higher target luminance was set at around 75% threshold of discriminating a bright bar from the less bright bar of the fixed lower luminance described above. A similar 2-interval forced choice (2AFC) session of 40 trials was completed by every observer. A bar at the target location with the fixed lower luminance was presented in one interval, and one with a higher luminance was presented in the other interval. The observer had to answer which interval

contained the brighter bar. The higher luminance is a variable and was determined by Quest with a 75% criterion for each trial. The mean threshold for all normal observers or the threshold luminance for individual amblyopic observer was taken as the high target luminance for different experimental conditions.

2.1.3.2 Tasks

At the beginning of each session, target bars with high and low luminance were presented side by side and the observer instructed to memorize the luminance difference. Then there was a 15-trial training session with feedback. In each training trial, either a bright or a less bright target bar, but no noise, was presented, and the observer was asked whether it was a bright or less bright bar by pressing a key. Audio feedback was given.

The short training session was followed immediately by an experimental session. In each trial, the observer had to respond whether the target bar was bright or less bright by pressing a key (yes/no). No feedback was given. We used this discrimination task instead of a detection task in an attempt to avoid high temporal and spatial uncertainty, especially the former, which is often associated with such experiments and can severely contaminate the results. Each session has 200 trials and only one of the five conditions described above. A total of 2000 ~ 20000 trials were collected for each condition for each eye.

2.1.4 Data analysis

We used reverse correlation to compute the classification images. The stimulus sequence of each trial is characterized by a 21 (time) x 11 (space) noise matrix and a 1-0 (1 for high and 0 for low) target luminance. The noise at a given time and space has the uniform distribution over all eleven luminance noise levels. The response for each trial is either 1 (i.e. bright bar) or 0 (i.e. less bright bar). All noise matrices and responses are grouped and averaged into 4 categories:

Stimulus		1		0
Response				
1	Hit	S1R1 $\mu_{[1,1]}$ $\sigma_{[1,1]}$	False alarm	S0R1 $\mu_{[0,1]}$ $\sigma_{[0,1]}$
0	Miss	S1R0 $\mu_{[1,0]}$ $\sigma_{[1,0]}$	Correct rejection	S0R0 $\mu_{[0,0]}$ $\sigma_{[0,0]}$

Table 2. Categories of stimuli and responses in computing classification images.

The classification image is computed by

$$\mu = \mu_{[1,1]} + \mu_{[1,0]} - \mu_{[0,1]} - \mu_{[0,0]}$$

where $\mu_{[\cdot,\cdot]}$ is the average 21 x 11 noise matrix of a given stimulus and response category. Each element in the classification image μ represents the correlation of the noise at this spatial temporal location and the perception that the target is bright. Positive and negative correlations imply facilitation and inhibition respectively.

The statistical significance of each correlation element is represented by the z score,

$$z = \frac{2\bar{x}}{\sigma}$$

where $\bar{x}$ is the correlation at a given spatial temporal location, i.e., an element of the matrix μ;

$$\sigma^2 = \sigma^2{}_{[1,1]} + \sigma^2{}_{[1,0]} + \sigma^2{}_{[0,1]} + \sigma^2{}_{[0,0]}$$

$$\sigma^2{}_{[\cdot,\cdot]} = VAR(N_{[\cdot,\cdot]})/n_{[\cdot,\cdot]}$$

N and n denote the noise matrix and the number of samples respectively. The 95% confidence interval of correlation corresponds to z score >= 2.

2.2 Results

For the basic condition (condition 1), the task performance for the normal and nonamblyopic eyes was above chance, whereas for about half of the amblyopic eyes it was near the chance level (50%). Increasing the signal-to-noise ratio improved the performance in both the normal periphery on average and in the amblyopic fovea; so did decreasing the fundamental spatial frequency of the stimuli. For all but the first (basic) condition, the performance levels of all observers are comparable.

Condition	1	3	4	5	6
SS	68.3%	71.8%	--	73.7% *	75.2% *
SK	66.8%	63.8%	58.6%	68.1% *	73.5% *
MN	73.6%	69.3%	--	66.9% *	--

EP		69.2%	--	--	--	--
CN		70.2%	--	--	--	--
BK	NAE	63.0%	--	--	--	--
	AE	63.1%	--	--	68.9%	71.1%
GW	NAE	64.8%	--	--	--	--
	AE	55.7%	--	--	67.1%	67.1%
BN	NAE	63.5%	--	--	--	--
	AE	61.3%	--	--	--	--
JS	NAE	67.4%	--	--	--	--
	AE	64.9%	--	--	--	--
GJ	NAE	63.0%	--	--	--	--
	AE	53.2%	--	--	--	--
GD	NAE	65.8%	--	--	--	--
	AE	58.3%	--	--	77.1%	75.5%

Table 3. Discrimination task performance (percentage of correct responses) in all but the second conditions for the tested eyes of normal observers and both amblyopic (AE) and nonamblyopic (NAE) eyes of amblyopic observers. Condition 2 is excluded because the target position is filled by noise only. Asterisk denotes 2.5 deg in the parafovea.

All normal observers show similar templates for detecting a luminance increment on a bright bar embedded in spatiotemporal noise, which is more clearly revealed by the average of all normal classification images (Figs. 2, 3). First, a temporal integrative zone is present at the target location from nearly 40 ms before the target onset until 30 ~ 40 ms after the target offset. Around the same period of temporal summation, two spatial inhibition zones are symmetrically distributed 0.1 ~ 0.15 deg from the target. At the target location, almost immediately following the temporal summation is the temporal inhibition zone that peaks at about 40 ms and extends to about 100 ms after the target presentation. The spatial correlation profile at the time of the target presentation (Fig. 3, lower right graph) resembles a “Mexican hat” shape typical for a neural receptive field in lower visual levels (e.g. Retinal ganglion cells, LGN, and V1 neurons). The temporal correlation profile at the target location (Fig. 3, upper right graph) is consistent with the paired-pulse or flicker detection time course reported by others (Kelly, 1971a, 1971b; Rashbass, 1970; Watson & Nachmias, 1977). These results suggest that the summation-only temporal profile in the previous study did not reflect the true template used by the observer but may have been affected by the high temporal uncertainty (Neri & Heeger, 2002).

Another observation of Fig. 3 is that the statistically significant facilitative and suppressive locations, including those with smaller absolute correlation values, in the classification image show an alternating pattern that’s unlikely to be random, which suggests that part of the spatiotemporal template may be a product of the independent temporal and spatial functions, although obviously this is not true for the predominant mechanism or template.

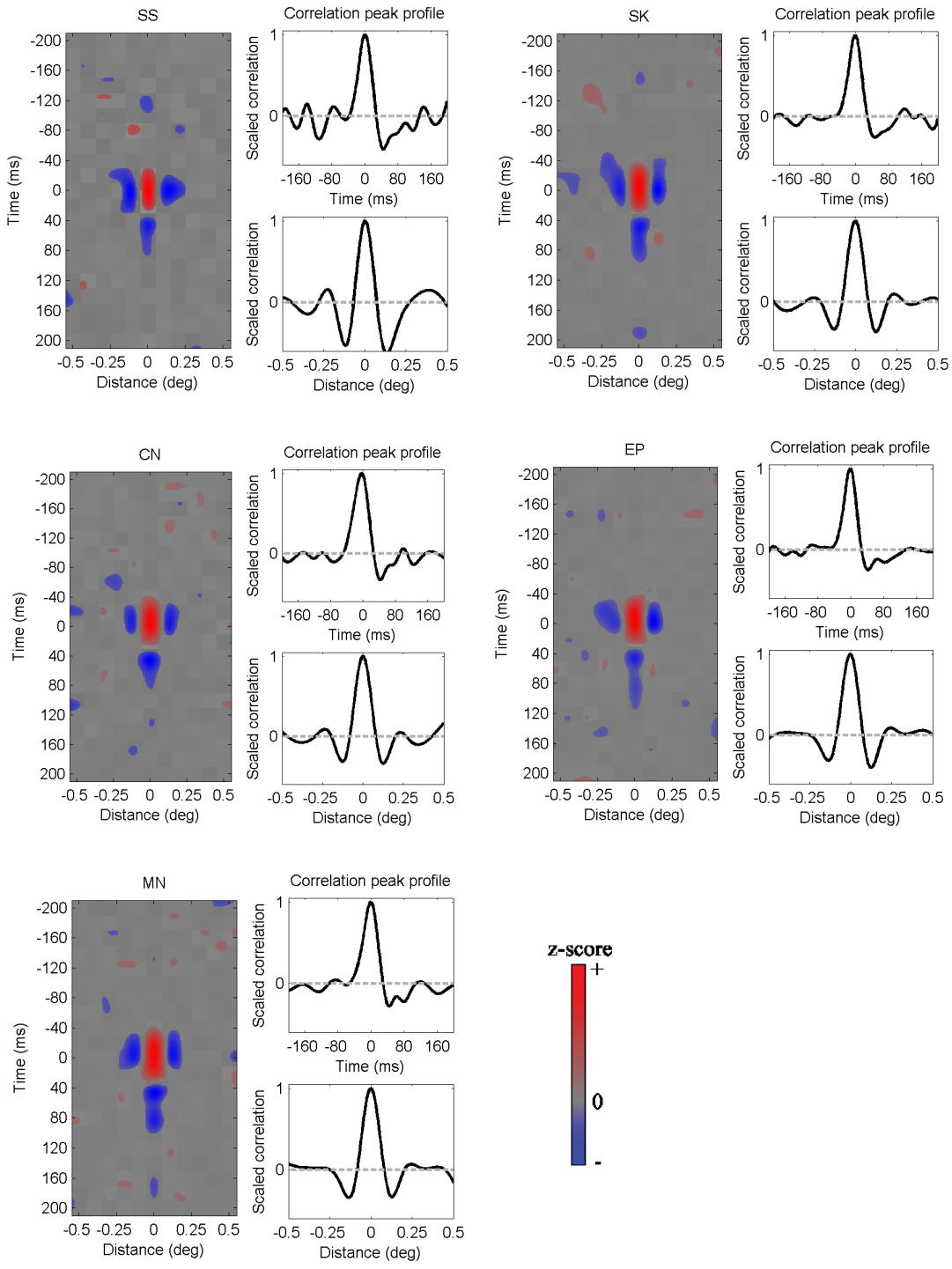

Fig. 2. Classification images (left) and the profiles (right) for detecting a luminance increment on a bright bar for each normal observer. Grey grids in the background of the classification image represent correlations at specific spatial (horizontal) and temporal (vertical) locations; the grey level corresponds to the correlation value (i.e. bright: positive correlation, dark: negative correlation). The statistically significant positive and negative correlations are overlapped by the corresponding red (i.e. positive) and blue (i.e. negative) z-score

image. The z-score image is generated by smoothing the original z scores ($z > 2$) using the bicubic spline model. The two graphs in the right half of each panel are smoothed profiles at the peak correlation locations (i.e. target locations). The solid black curve in the upper graph shows correlation vs. time at the target spatial location (i.e. 0 deg); the curve in the lower graph shows correlation vs. distance at the target temporal location (i.e. 0 ms). Correlations in these two graphs are scaled to have unit maximums. The curves are smoothed by the cubic spline model. The grey dashed line represents zero correlation. All normal observers demonstrate similar spatiotemporal templates that are averaged and shown in Fig. 3.

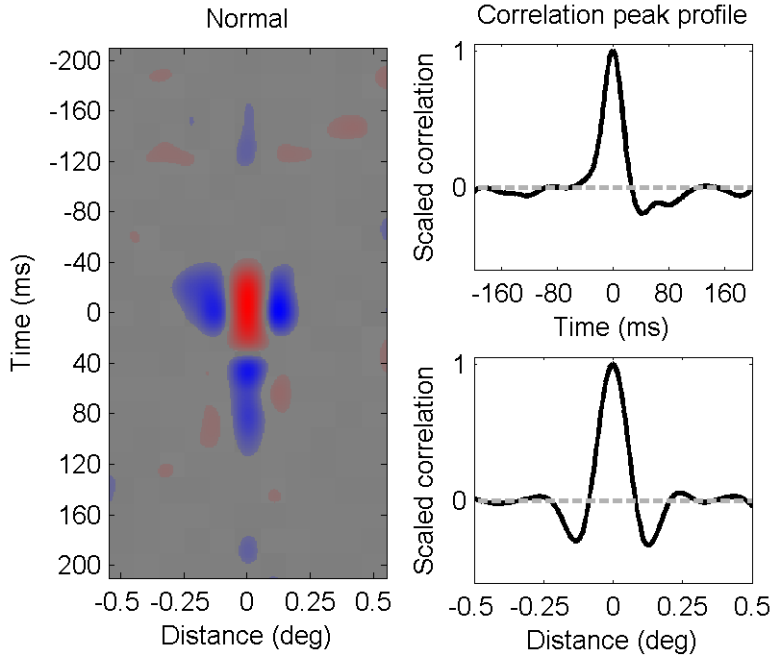

Fig. 3. Average classification image (left) and its correlation profiles at the peak correlation locations (i.e. target locations, right) of five normal observers. The background of the classification image appears uniform because the average of insignificant correlations is close to the expected value zero. The average template represented by both the classification image and the profiles is characterized by a positively correlated area at the extended target location, as well as negatively correlated neighborhoods surrounding the target in space and following the target in time.

The classification images of the nonamblyopic eyes are normal or nearly so for some amblyopic observers (i.e. BK, GW, GD and GJ), and subnormal for others (i.e. BN and JS) in that the temporal inhibition zone is missing. The classification images of amblyopic eyes are much noisier and lack inhibition. The temporal inhibition that normally peaks about 40ms after the target onset is absent in four out of five amblyopic eyes' results. The spatial inhibition adjacent to the target location is also reduced in size or absent for most amblyopic eyes. On the other hand, despite the reduction in inhibition, the temporal summation for amblyopic eyes doesn't seem to be much different from that of the normal.

Note that amblyopic observer JS shows interesting templates in both eyes – the template

for her nonamblyopic eye lacks the temporal inhibition whereas that of her amblyopic eye appears normal. As mentioned in Methods, JS is a mild amblyope and had received intensive perceptual training in her amblyopic eye. By the time she participated in the current study, the visual functions in her amblyopic eye had been substantially improved. Therefore, perceptual learning may have had an effect on the spatiotemporal mechanism for detecting a simple image feature.

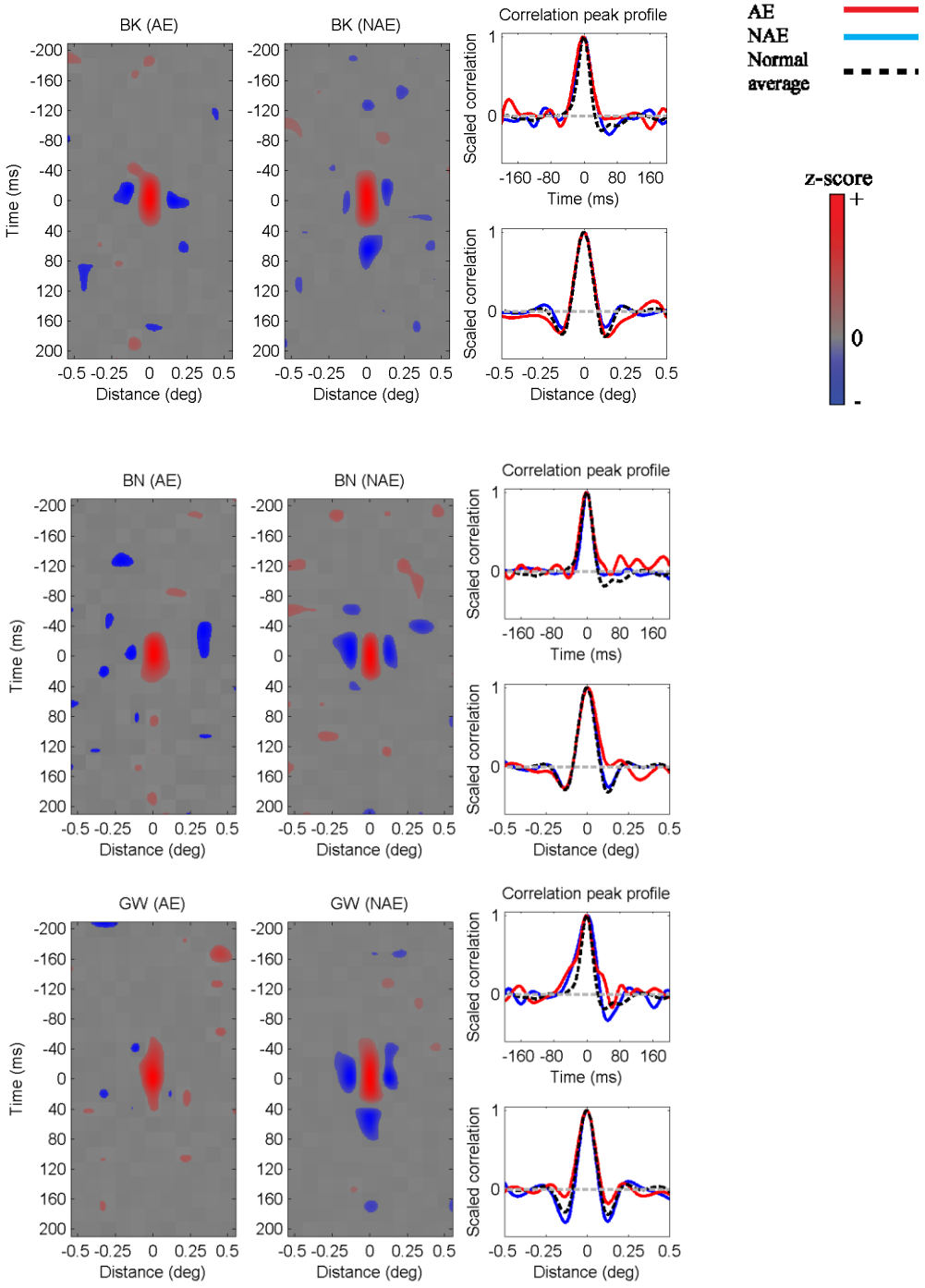

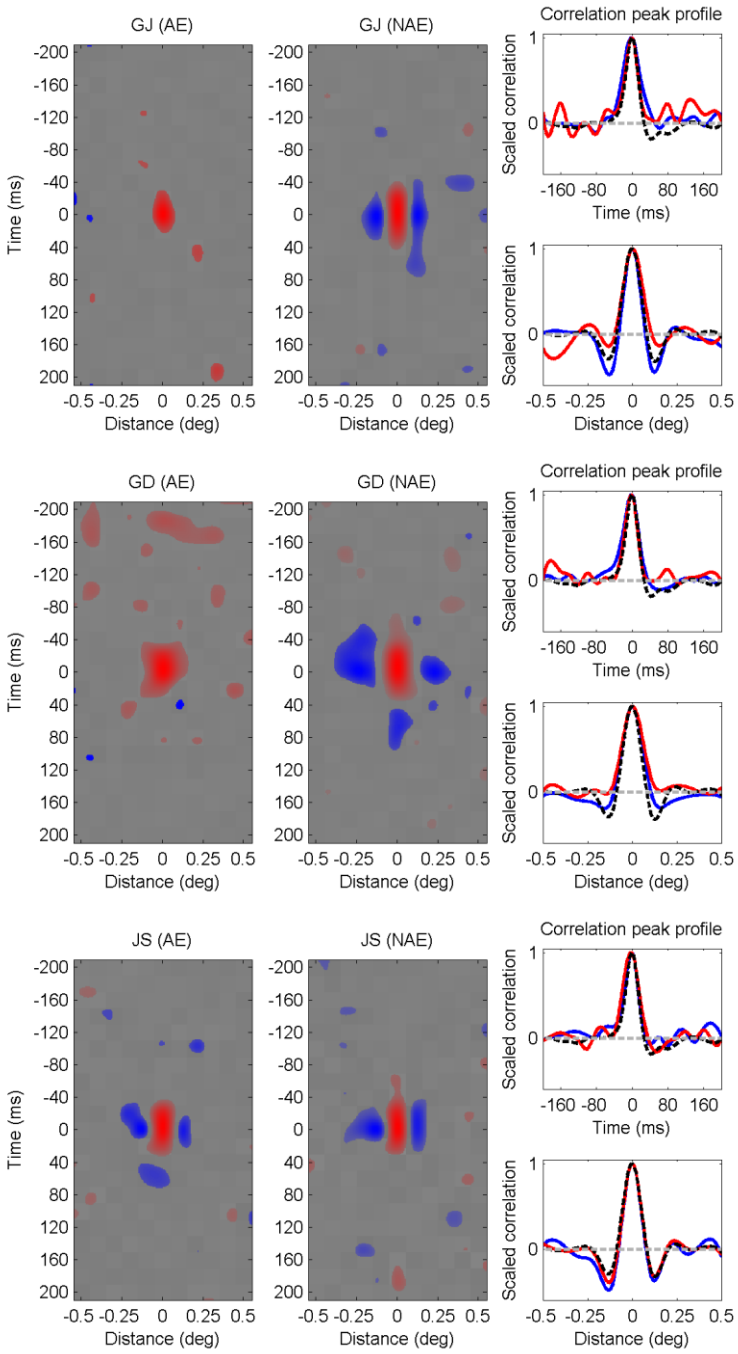

Fig. 4. Classification images (left & middle) and the profiles (right) of perceiving a bright bar for amblyopic observers in both amblyopic (AE) and nonamblyopic (NAE) eyes. The correlation value is represented by the grey level of the grids in the background of the classification images. Statistically significant correlations are overlapped by the red (positive) and blue (negative) z-score ($z > 2$) image which is smoothed by the bicubic spline model. Profiles at peak correlation locations (i.e. target locations) for both amblyopic (red solid) and nonamblyopic (blue solid) eyes are smoothed by the cubic spline model. The average normal profile (black dashed) is superimposed. The correlated areas (red) of the templates in both amblyopic and nonamblyopic eyes of all observers are not much different from those in the normal eyes, which are better shown by the matching

positive peaks of all three curves in the profiles. The negatively correlated areas are normal or subnormal in nonamblyopic eyes, but are generally incomplete or missing in amblyopic eyes.

In an attempt to understand what has caused the anomaly in the spatiotemporal template of the amblyopic eye, we presented modified stimuli to the normal fovea and hoped to reproduce the amblyopic template. First, the stimuli were blurred in time and space by a two-dimensional Gaussian filter (Methods). The blurred stimuli had little effect on the task performance (Table 3); neither did they regenerate the amblyopic template in the normal eye (Fig. 5). All components, especially the inhibition zones, are still present in the classification image, which distinguishes it from that of the amblyopic eye. However, the classification images do seem somewhat disorganized, and further investigation is required to draw any conclusion. Nevertheless, we can at least say that it is not simply the less clear image that caused the anomaly in amblyopic spatiotemporal template.

Second, the signal-to-noise ratio of the stimuli was decreased and the latter presented to normal observer SK. The rationale is that, perhaps the amblyopic eye could not detect any target and the resulting template is not relevant to this task, since after all, their performance (correct response rate in Table 3) is near the chance level (50%). Reducing signal-to-noise ratio did make the task much more difficult and SK's correct response rate decreased to 58%. However, SK's classification image does not resemble that of the amblyopic eye (Fig. 6). Another piece of evidence that the signal-to-noise ratio is not a significant factor in determining the template comes from the amblyopic eyes' null responses to stimuli with increased signal-to-noise ratio (Fig. 7). Enhancing the visibility of the target partially recovered the temporal inhibition of the amblyopic eye of GD but did almost nothing for the other two amblyopic observers. On the other hand, we know that these amblyopic observers did detect the target from their substantially improved performance (Table 3). Hence the low visibility of the target is not likely to be responsible for the abnormal amblyopic template either.

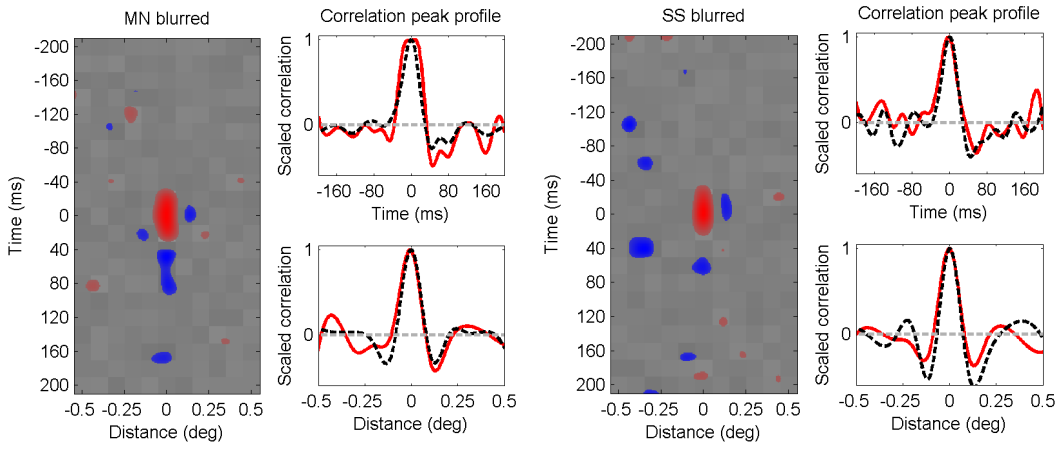

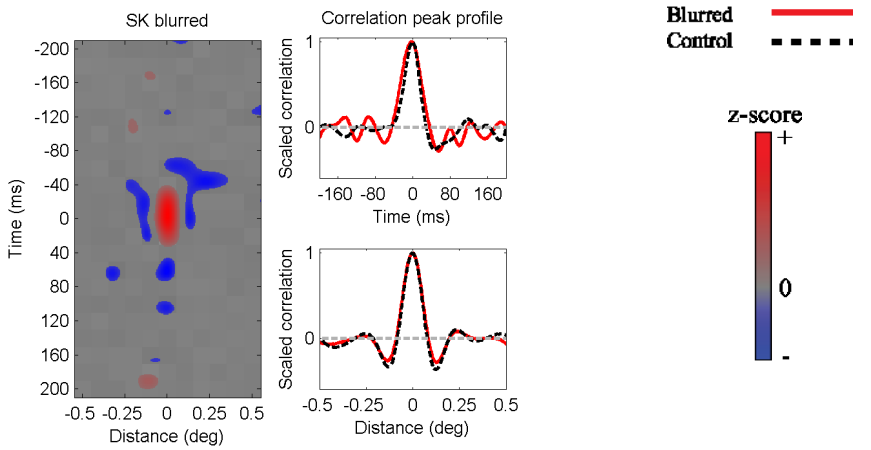

Fig. 5. Classification images (left) and the profiles (right, solid red) of for detecting a luminance increment on a spatially and temporally filtered bright bar for normal observers. The profiles for the control stimuli (dashed black, from the solid black curves in Fig. 2) of the same eye are superimposed. The classification images for the filtered stimuli are noisier, but both positive and negative correlated components are complete or nearly so.

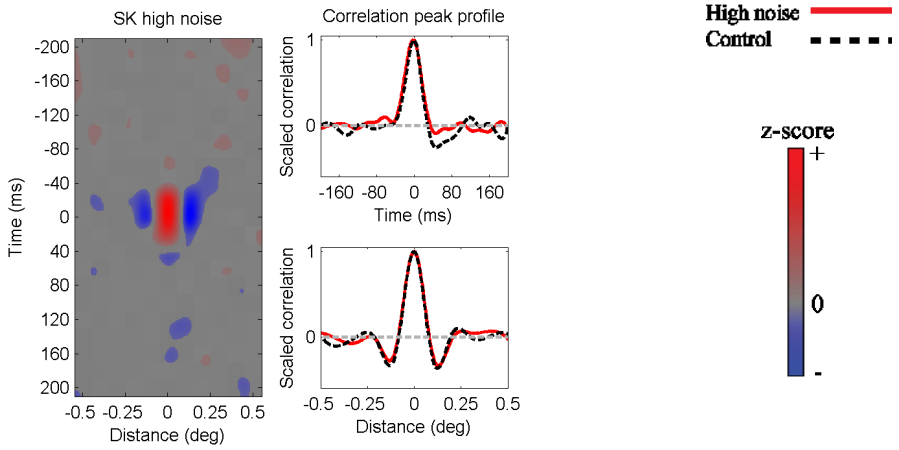

Fig. 6. Classification images (left) and the profiles (right, solid red) of perceiving a bright bar embedded in distracters with enhanced luminance noise for a normal observer. The profiles for the control stimuli (dashed black, from the solid black curves in Fig. 2) of the same eye are superimposed. The classification image for the noisy stimuli shows both positive and negative correlated components, although the amplitude of the negative correlation peak after the target is reduced.

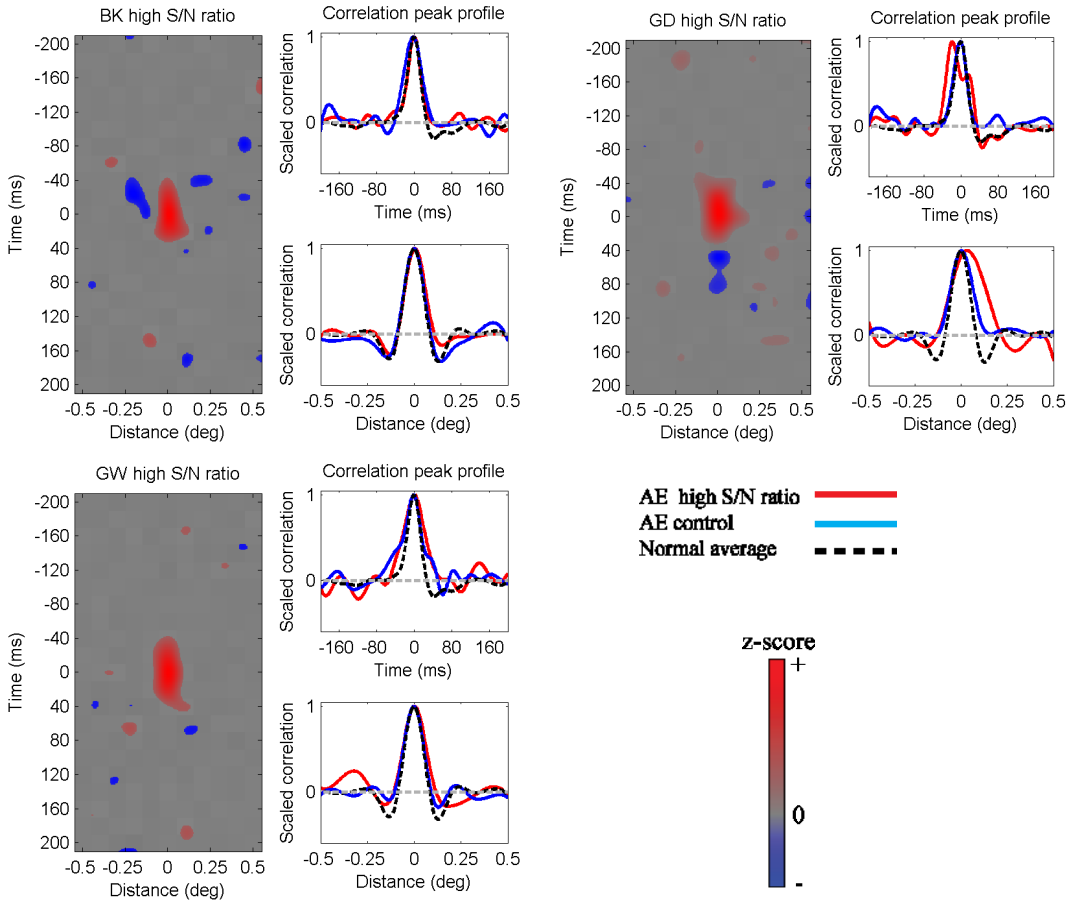

Fig. 7. Classification images (left) and the peak correlation profiles (right, solid red) of perceiving a bright bar of increased signal-to-noise ratio by raising the target visibility and reducing the luminance noise of distracters for amblyopic eyes. Profiles of the control stimuli for the same amblyopic eye (solid blue) as well as the average normal profiles (dashed black) are superimposed. Increasing the signal-to-noise ratio for the amblyopic eye partially restored the missing negative correlated area in the classification image for GD, but had little effect for BK or GW.

Another possibility to which the abnormal amblyopic template may be attributed is that the spatiotemporal mechanisms in the normal and the amblyopic eyes may be shifted on the scale of spatial frequency. More specifically, the template may vary with spatial frequency of the stimuli, and the relationship between them may differ for the normal and the amblyopic eyes. Therefore while 5 cycles/deg (i.e. the fundamental spatial frequency of the stimuli) probably elicits a template corresponding to mid-high spatial frequencies for the normal eye, it may elicit a template at the high end of the spectrum for the amblyopic eye. Presumably the template used by the normal eyes is more efficient than that used by the amblyopic eye.

To test the hypothesis that amblyopic template is shifted on the spatial scale, the

fundamental spatial frequency of the stimuli was decreased from 5 cpd to 1.67 cpd by widening each bar in the stimuli from 0.1 deg to 0.3 deg and presented to two amblyopic eyes. Finally, normal classification images are seen in both amblyopic eyes in response to the modified stimuli (Fig. 8). The substantial change in amblyopic template cannot be attributed to the task performance which on average is not significantly different from the previous condition (i.e. increased signal-to-noise ratio). Interestingly, the spatial correlation profiles in Fig. 8 show that the spatial extents and shapes of the templates depend on the relative distance of the stimulus elements (i.e. distance normalized by bar width) instead of the absolute distance in degree. This result is not inconsistent with the amblyopic spatial classification image for detection reported by Levi et al. (2008), which demonstrated a moderate shift of the amblyopic template towards lower spatial frequencies (i.e. wider and flatter spatial template). Since the target used in Levi & Klein's study was a fixed discrete frequency pattern (DFP) that had a negative-positive-negative luminance profile around the target, it did not examine the effect of signal spatial frequency like the present study does by changing the fundamental spatial frequency of the stimuli. This result of the present experiment may suggest that the spatiotemporal mechanism depends on spatial scale.

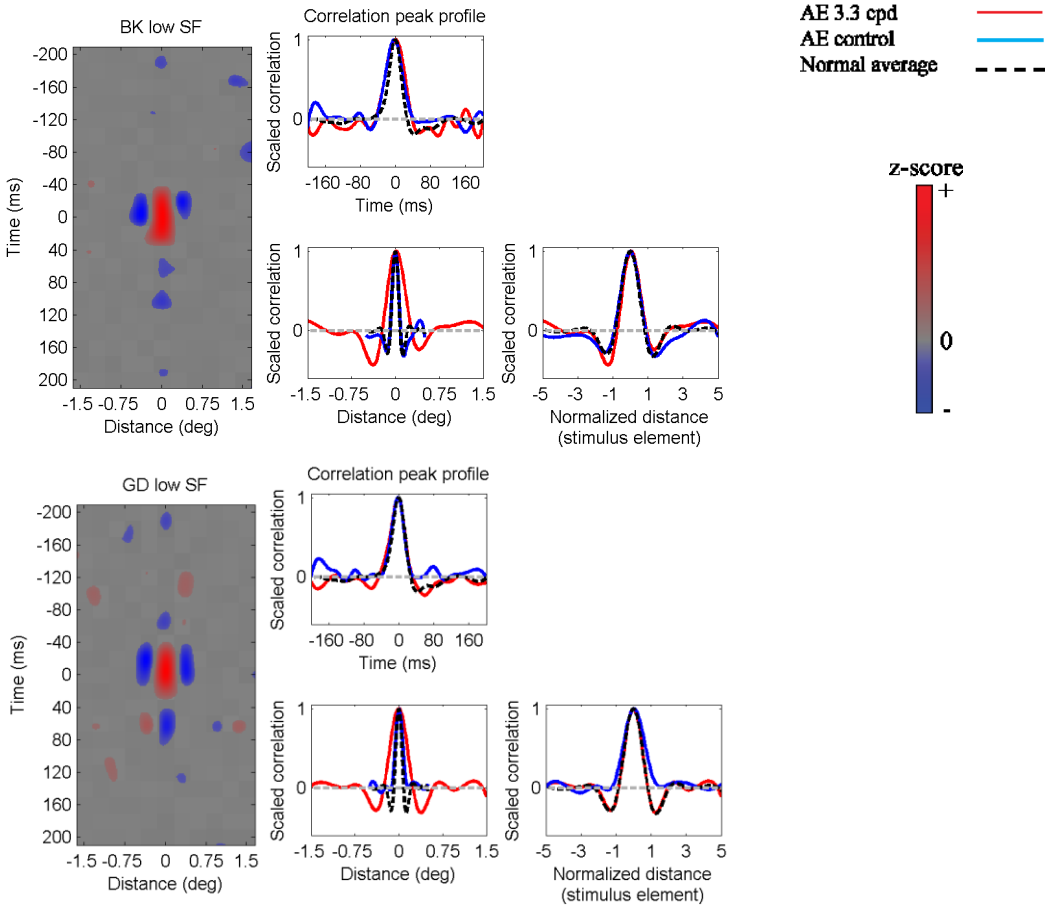

Fig. 8. Classification images (left) and peak correlation profiles (middle & right, solid red) of perceiving a bright bar embedded in similar distracters with decreased fundamental spatial frequency, for amblyopic eyes.

The bar width is increased to 0.3 deg. Profiles of control stimuli for the same amblyopic eye (solid blue) as well as the normal average profiles (dashed black) are superimposed. For correlation vs. distance profiles (lower middle) the distance is in degree. For correlation vs. normalized distance profiles (lower right) the distance in degree is normalized by the number of stimulus elements (i.e. number of bars). Classification images for both observers are corrected and appear normal with complete positively and negatively correlated zones. The correlation profile extent in space depends on the relative distance, but not the absolute distance in degree, in these conditions for both observers (lower middle and right).

As explained previously, we did not succeed in an attempt to reproduce the abnormal amblyopic template in normal eyes by either spatiotemporally blurring the stimuli or decreasing the signal-to-noise ratio of the stimuli. Because of the close connection between amblyopic foveal vision and normal peripheral vision, we estimated classification images from the normal periphery of two normal observers using stimuli with increased signal-to-noise ratio such that the performance levels were maintained above chance (Table 3). As Fig. 9 shows, like those of the amblyopic eye, the peripheral classification image inhibitory components of the normal eye are broken or missing.

The subsequent question is whether a normal foveal template can be generated in the periphery by scaled stimuli. Similarly, the bar width was increased from 0.1 deg to 0.3 deg to decrease the fundamental spatial frequency of the stimuli from 5 cpd to 1.67 cpd, and the stimuli were presented to the periphery for two normal observers. The resulting classification images show partial restoration in spatial inhibition but not in temporal inhibition (Fig. 10). Again, the spatial profile of the template depends on the relative distance, but not the absolute distance in degree. Therefore, normal peripheral vision and the amblyopic foveal vision may share spatial properties but differ in temporal properties.

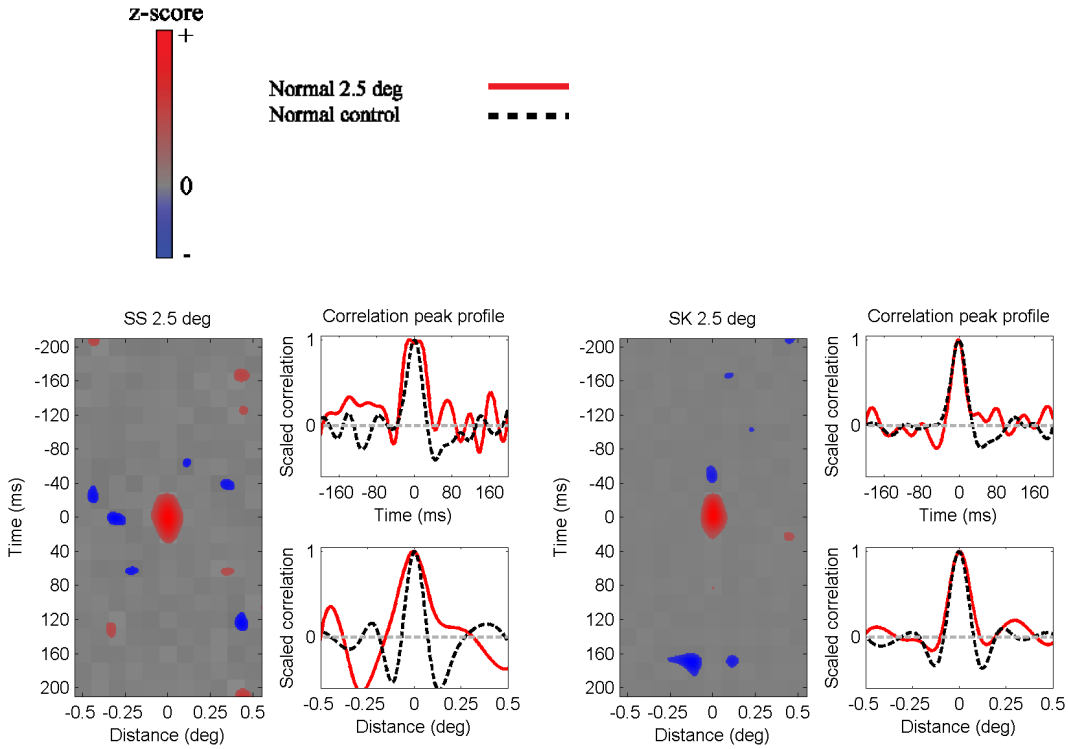

Fig. 9. Classification images (left) and peak correlation profiles (right, solid red) at 2.5 deg eccentricity for normal observers. Profiles in the fovea of the same eye (dashed black) are superimposed. Classification images in the parafovea of normal eyes are noisy and lack of regular anti-correlated zones seen in Fig. 2.

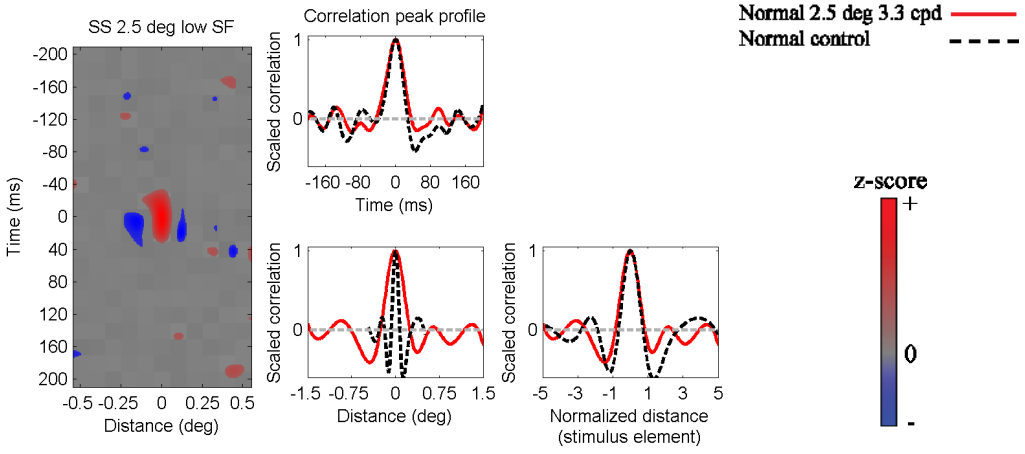

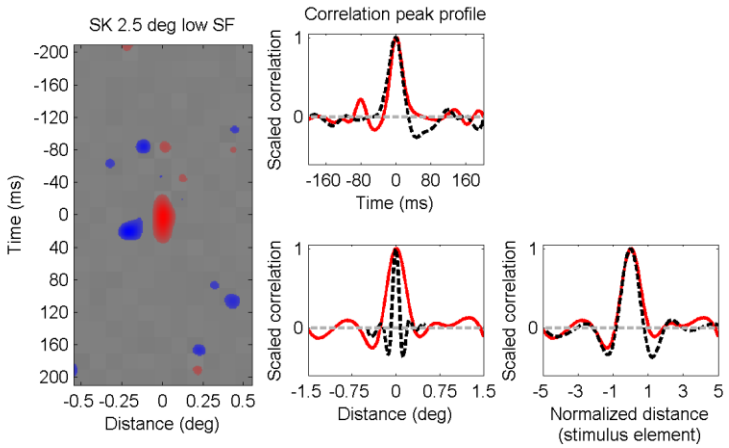

Fig. 10. Classification images (left) and peak correlation profiles (middle & right, solid red) of perceiving a bright bar embedded in similar distracters with decreased fundamental spatial frequency at 2.5 deg eccentricity for normal observers. The bar width is increased to 0.3 deg. For correlation vs. distance profiles (lower middle) the distance is in degree. For correlation vs. normalized distance profiles (lower right) the distance in degree is normalized by the number of stimulus elements (i.e. number of bars). Compared to Fig. 9, lowering the fundamental spatial frequency of stimuli partially, but not completely restored the missing (spatially) anti-correlated zones of the classification images. The correlation profile extent in space depends on stimuli but not absolute distance in these conditions for both observers (lower middle and right).

3 Experiment 2: The spatiotemporal interactions for orientation identification.

3.1 Methods

3.1.1 Observers

Two observers with normal vision and two with strabismic amblyopia participated. All participants had substantial experience with visual psychophysical experiments, and were naïve as to the purpose of the study except the author. None of the amblyopic observers has eccentric fixation. The detailed characteristics of each observer are listed in Table 4.

Observer	Age (yrs)	Strabismus (at 6 m)	Eye	Refractive error (diopters, D)	Line letter VA (single letter VA)
Normal					
SS	29	None	R	-0.25	20/12.5
			L	pl/-0.25x119	20/12.5
LL	26	None	R	-1.50	20/12.5
			L	-0.50	20/12.5
Strabismic amblyopic					
GJ	24	R EsoT 4-5$^{\Delta}$	R (AE)	+3.50/-1.00x97	$20/40^{-2}$ ($20/25^{+1}$)
			L (NAE)	pl	$20/16^{-1}$
AP	22	L EsoT 4-5$^{\Delta}$ &	R (NAE)	-1.25/-0.50x175	$20/16^{-2}$
		HyperT 2-3$^{\Delta}$	L (AE)	-0.50/-0.25x60	$20/50^{+1}$($20/40^{+2}$)

Table 4. Observers characteristics.

3.1.2 Stimuli

Stimuli were generated by Matlab 7.01 with Psychtoolbox 2.0 and presented on a flat CRT monitor (30.1 x 40.1 cm^2, 1600 x 1400 pixels, 100Hz, Sony). At 50% brightness and 100% contrast, the luminance gradient ranges from 0.32 to 117.7. The monitor was calibrated to generate luminance that is a linear function of pixel value.

The background luminance of the stimuli is 28.4 cd/m^2. A stimulus sequence for each trial is composed of 9 frames. For normal observers, in every frame, there are either 11 or 9 possible positions evenly distributed along a horizontal line; each of the 5 or 4 positions on one side is independently filled with a high contrast (90%) Gabor patch with a probability of 0.5 and these Gabor patches are positioned symmetrically on both sides; therefore the significant number of positions (excluding the target position) is 5 or 4 instead of 10 or 8 due to symmetry. Here we assumed symmetry in the noise effect on perception because the distance from each stimulus patch to the fovea is presumably the same for both normal (in the lower visual field) and amblyopic (at the fixation) eyes. The middle (6^{th} or 5^{th}) position is occupied by the target Garbor patch in the middle (5^{th}) frame and blank in all other frames. For amblyopic observers, there are only 4 possible positions on each side of the target. Each Gabor patch is tilted by a small angle either clockwise (i.e. left end higher, α) or counterclockwise (i.e. right end higher, $\pi - \alpha$) and the magnitude of the tilt (around 6 deg) was determined for each individual (discussed in Procedures). Again, the tilt of the Gabor patch is symmetric around the target position, i.e., if the Gabor patch at position 1 is tilted 6 deg clockwise, then the one at position 11 is also tilted 6 deg clockwise.

The target in the middle position of the middle frame was cued in time and space. A short red line segment below the target, a red solid circle around the target, or a red dotted circle around the target was used as the cue that appeared at the onset of the target and disappeared at

the offset of the target; hence the cue was synchronized with the target in time. Since there is no significant difference between the results of the solid circle cue and those of the dotted circle cue, they are combined as one group in the analysis. The duration of each frame was 40 ms, and the entire sequence was 0.36 sec (Fig. 11).

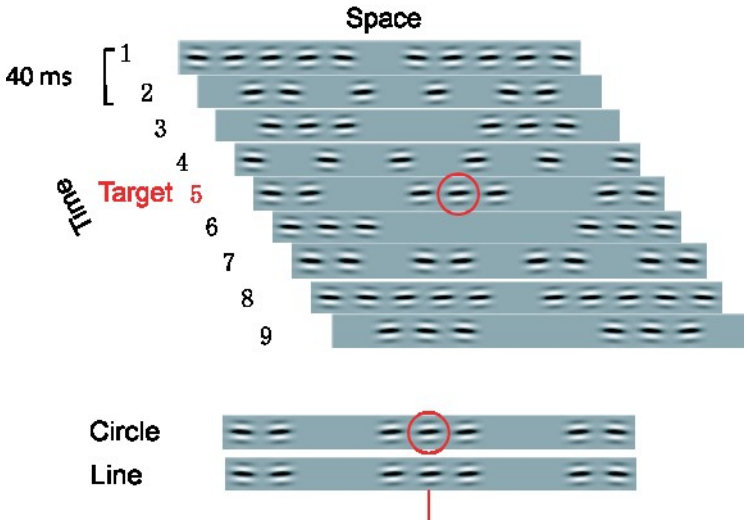

Fig. 11. Illustration of the stimuli and task for experiment 2.

A Gabor patch is mathematically defined as a two-dimensional sinusoidal wave multiplied by a Gaussian envelop:

$$G'(x,y) = -\lambda \cos\{v(x\sin\alpha + y\cos\alpha)\}\, e^{-\frac{x^2+y^2}{2\sigma^2}}$$

where α is the tilted angle of the Gabor patch; v is the frequency of the sinusoid; σ is the standard deviation of either dimension of the Gaussian function; and λ is a scaling constant.

The contrast of a Gabor patch is defined as the Weber contrast:

$$C = \frac{L_{max} - L_{background}}{L_{background}}, \qquad L_{background} \in (0, L_{max}]$$

Therefore, the Gabor patch with contrast C is:

$$G(x,y) = L_{background}\ [1 + CG'(x,y)]$$

where $C \in [0,1]$.

3.1.3 Procedures

All experiments were done monocularly in a room with dim overhead light (10 cd/m^2). The stimuli were presented at fixation in amblyopic eyes or at either 4 deg or 5 deg in the inferior visual field of normal eyes. A fixation cross (20 x 20 min) was presented to normal observers. The distance from the stimuli and the tested eye was 100 cm for normal observers or 300 cm for amblyopic observers.

3.1.3.1 Preliminary experiments

For each observer, the spatial frequency of the Gabor patches was chosen to be highly visible, and each Gabor patch contains 3 ~ 4 cycles. Since the Gaussian function has a standard deviation 0.4 ~ 0.5, only 2 ~ 3 cycles were visible in a Gabor patch. The stimulus size was determined by the spatial frequency and the number of cycles in a full patch. The tilt angle was set at the detection threshold absent of noise. In a 40-trial pre-session, the stimulus, a single Gabor patch in the target position and no distractor, was tilted by a small angle (clockwise or counterclockwise), and the observer responded whether the target was tilted or not (i.e. yes/no). The tilted direction (i.e. clockwise or counterclockwise) was randomly selected for each trial, and the angle was determined by Quest with the criterion 80% and. The threshold angle α was taken as the amount of tilt of Gabor patches for the observer. Table 5 summarizes the stimulus characteristics for each observer.

	Eccentricity (deg)	Spatial frequency (cycles/deg)	Cycles per stimulus	Size (deg)	Tilt α (deg)	Standard deviation σ (× size/2)
Normal observers						
SS	5	4.7	3.7	0.79	4.0	0.40
	4	4.7	3.7	0.79	5.0	0.40
LL	4	5.0	3.0	0.60	4.0	0.40
Amblyopic observers						
AP	0	8.5	3.2	0.38	6.2	0.46
GJ	0	9.0	3.4	0.38	6.3	0.46

Table 5. Stimulus (Gabor patch) characteristics for each observer.

3.1.3.2 Tasks

In each trial, a complete stimulus sequence was presented, and the observer had to answer whether the target Gabor patch was tilted clockwise or counterclockwise by pressing a key. No feedback was given. After every five trials, there was a training trial in which only the target

and the cue but no distractor was presented to the fovea of the observer, and the response to the training trial was not counted. Each block had 30 trials (not including training trials), and the number of blocks in each session was between 2 and 4 depending on the observer's schedule. A total of 750 ~ 1700 trials were collected for each condition for each eye.

3.1.4 Data analysis

Reverse correlation analysis

The reverse correlation method described in experiment 1 was used to compute the classification images for the current experiment. Using the notation from Table 2, we can code "clockwise tilt" as 1 and "anticlockwise tilt" as 0, and apply them to both the stimuli and the responses. The noise matrix is 9 (time) x 5 (space) or 9 x 4 for normal observers and 9 x 4 for amblyopic observers. The spatial positions are labeled mono-sided 1 to 5 from near to far relative to the target, due to the symmetry of distracters around the target. The noise at a given time and space has the following distribution:

$$N = \begin{cases} 0 & blank & P = 1/2 \\ -1 & clockwise\ tilt & P = 1/4 \\ 1 & counterclockwise\ tilt & P = 1/4 \end{cases} \qquad)$$

3.2 Results

Without distracters, the correct response rate is around 75% for each observer. With closely placed distracters, the performance is much worse for both normal peripheral and amblyopic central vision (Table 6), suggesting a crowding effect.

Observer	SS	LL	AP (AE)	GJ (AE)
Circle cue	59.6%	70.4%	58.9%	61.4%
Line cue	55.4%	69.4%	--	50.7%

Table 6. Discrimination task (2AFC) performance (percentage of correct responses) for the tested eyes of normal observers and the amblyopic eyes (AE) of amblyopic observers.

The main significant interaction between the distracters and the target is orientation assimilation (red areas), i.e., an observer is likely to perceive the target orientation as similar to that of the flankers, which is consistent with previous studies (Parkes et al., 2001; Solomon et al., 2004). This assimilation effect is strongest at locations immediately adjacent to the target for every observer, as shown by the narrow vertical red zones on both sides of the target in Fig. 12. The assimilation effect extends further in space for flankers presented simultaneously with the target, and is limited in space for flankers with non-zero asynchronies. Interestingly, at

locations beyond the assimilation area, the target-flanker interaction becomes repulsion (blue), i.e., an observer is likely to perceive the orientation of the target as opposite to that of the flankers. The repulsion effect in orientation perception as a function in space has not been documented before and will be referred to as "anti-crowding"; along with assimilation, the spatial interaction shows a "Mexican hat" profile (discussed below).

It seems unexpected that the assimilation zone for flankers with non-zero asynchronies is so narrow that the adjacent repulsion zone is still within the critical distance for crowding (i.e. 0.5 E = 2.5 deg at 5 deg ecc. or 2 deg at 4 deg ecc.). However, for flankers presented non-simultaneously with the target, the crowding effect on the spatially closest flankers was substantially relieved since the target position was not occupied. Hence the difference in spatial interactions at different asynchronies is not surprising. Accordingly, "anti-crowding" generally appears farther away from the target while it is on and closer to the target location while it is off. Thus "anti-crowding" occurs immediately adjacent to assimilation in space, as shown by the blue areas in the z-score image and the dark grey squares of the classification images, although not all are statistically significant. Note an exception that the extent of orientation assimilation for observer SS at 4 deg eccentricity is greatest at the frame before the target onset.

Another seemingly surprising result is that, the time when the target is on (i.e. time 0) does not coincide with the peak of the spatial interaction on perception (i.e. assimilation) in any condition, which may be similarly explained by the flankers being subject to more crowding while the target was on. This is partly consistent with the results of an earlier study on spatiotemporal interactions of Vernier acuity reported by Westheimer & Hauske (1975), discussed below.

The shape of the crowding map depends on the cue type. The circle cue induces a bimodal profile in time that demonstrates two crowding peaks about 80 ms before and 40 ms after the target presentation. The line cue, on the other hand, induces predominant crowding before and around the target presentation and is strongest near the beginning of the sequence. The observers' performance associated with the circle cue is moderately better than that associated with the line cue (Table 6). However, every observer expressed that the task was difficult and the guessing rate was high.

The amblyopic spatiotemporal interaction maps also demonstrate strongest orientation assimilation at the location adjacent to the target, with anti-crowding present at farther locations. A subtle observation is that the difference in classification image generated by circle and line cues for one amblyopic eye is not as marked as that for normal eyes. Moreover, although the target is crowded by flankers both before and after its presentation for both the normal and amblyopic eyes, while the effective flankers are distributed around and before the target presentation for normal peripheral vision, they are more widely distributed around and after the target presentation for amblyopic central vision. The greatest extent of orientation assimilation occurs while the target is on for most normal eyes; whereas it occurs after the target

presentation (i.e. while the target is off) for the amblyopic eyes. This is better illustrated by the smoothed classification images (Fig. 14 & 15), which show the difference in the bright area distributions in the normal and amblyopic eyes. However, in order to know whether or not these differences are significant or meaningful further investigation is necessary. In general, the amblyopic crowding map is not substantially different from that of the normal periphery.

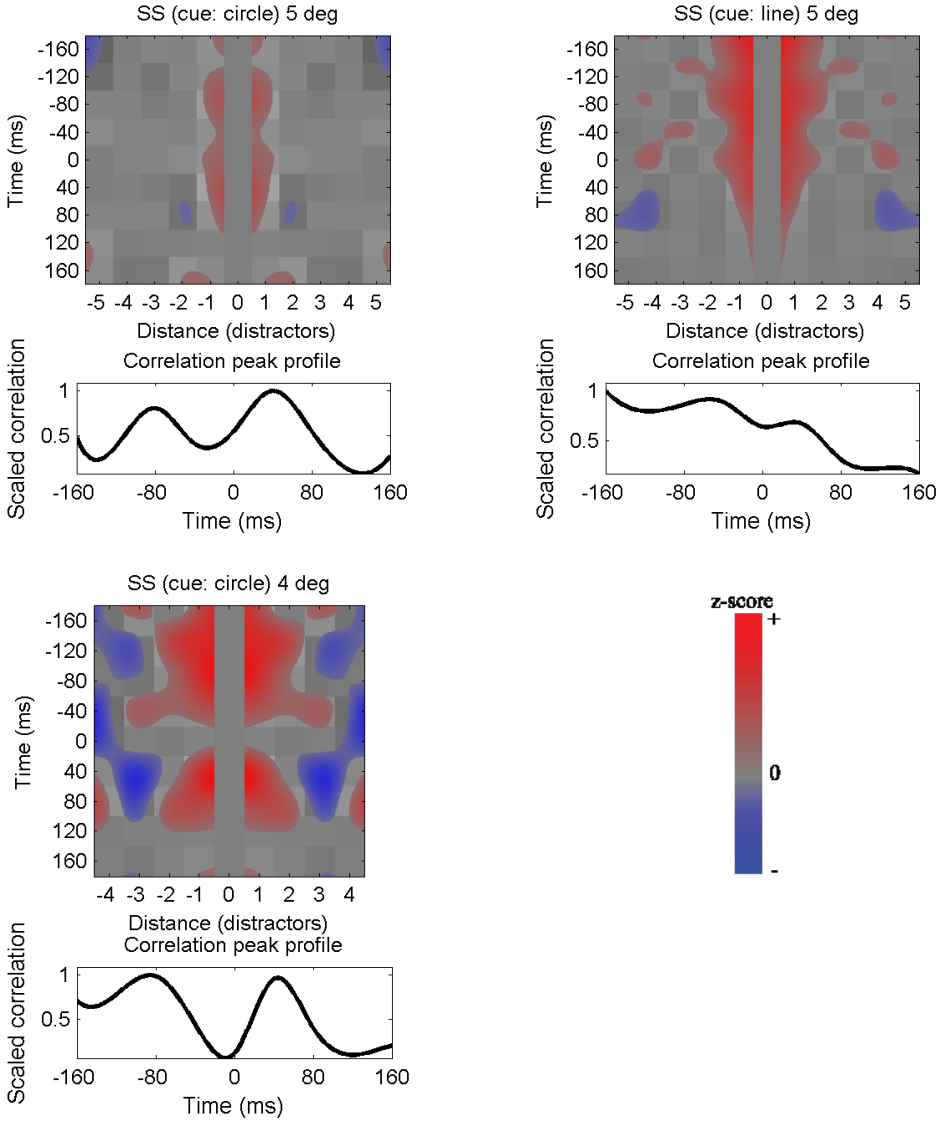

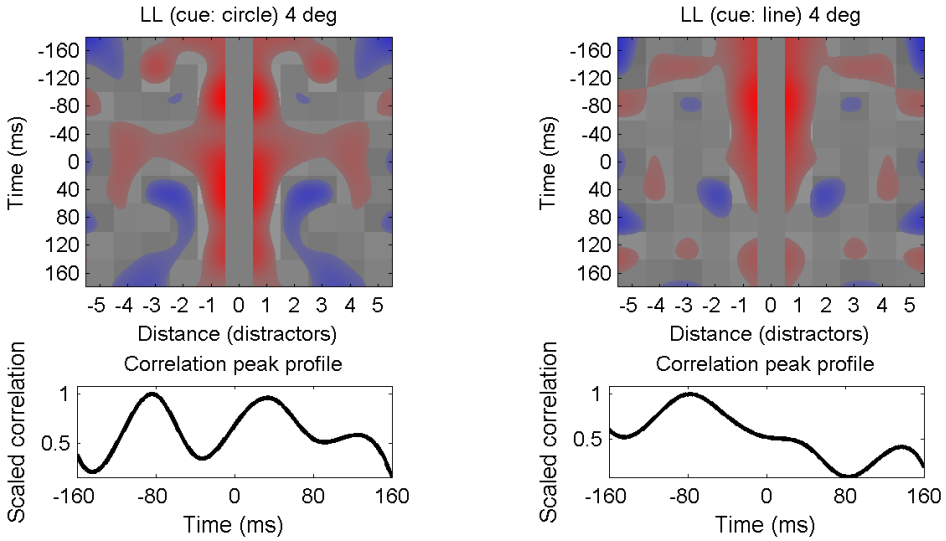

Fig. 12. Classification images (upper) and the correlation profile (lower) in time at the correlation peak in space (i.e. the location adjacent to the target, distance = 1) for normal observers at 5 deg or 4 deg below the fovea. Each classification image is generated by symmetric duplicating the original half image due to the symmetry assumption. The target location has no noise and is filled with zero correlation. The distance axes (horizontal) in the classification images are normalized by the number of distracters (Gabor patches). Positive (dark) or negative (bright) correlation means assimilation or repulsion respectively. The statistical significance of correlations is indicated by an overlapping red ($z > 2$) and blue ($z < -2$) z-score image.

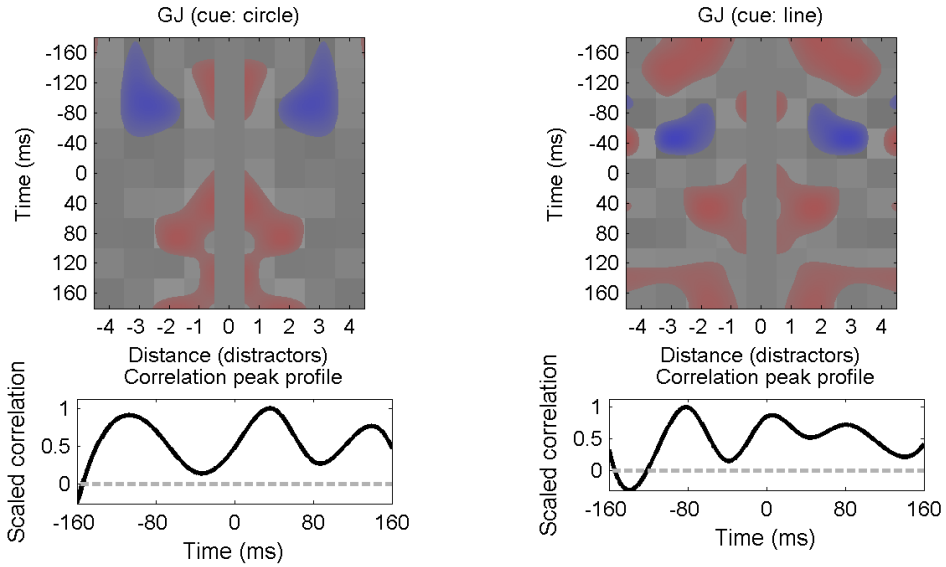

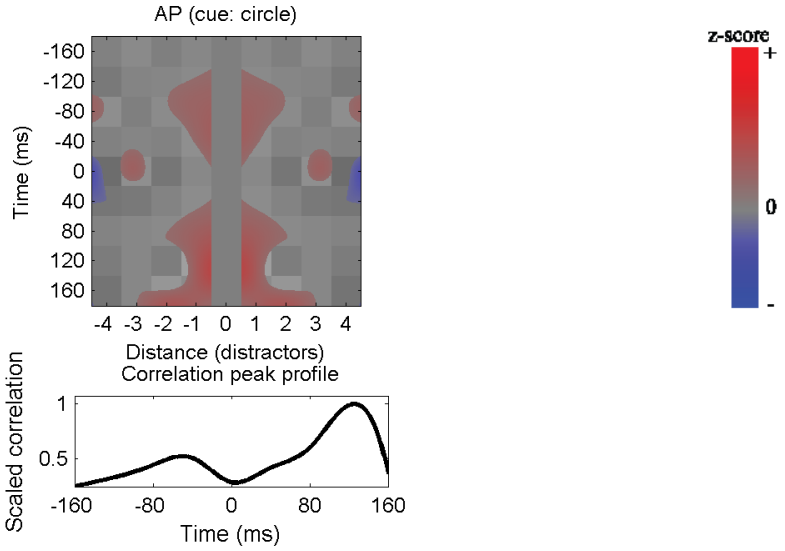

Fig. 13. Classification images (upper) and the correlation profile (lower) in time at the spatial location corresponding to the correlation peak (distance = 1) for amblyopic central vision. The statistical significant correlations are represented by an overlapping red ($z > 2$) and blue ($z < -2$) z-score image. Both Figs. 12 & 13 share the same color map.

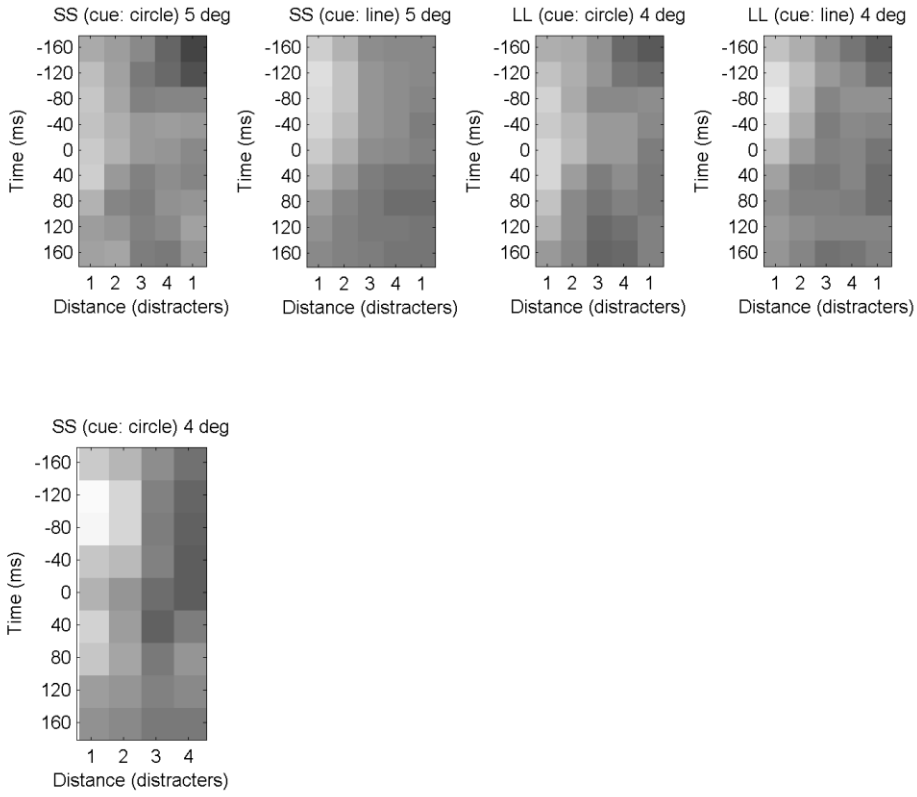

Fig. 14. Smoothed classification images for both cue types in the normal periphery (4 or 5 deg eccentricity below the fovea). Classification images were smoothed by a 3x3 Gaussian filter ($\sigma = 0.8$) that acts on the grid. The positively correlated locations concentrate around the time of target presentation for the circle cue, or before the target presentation for the line cue.

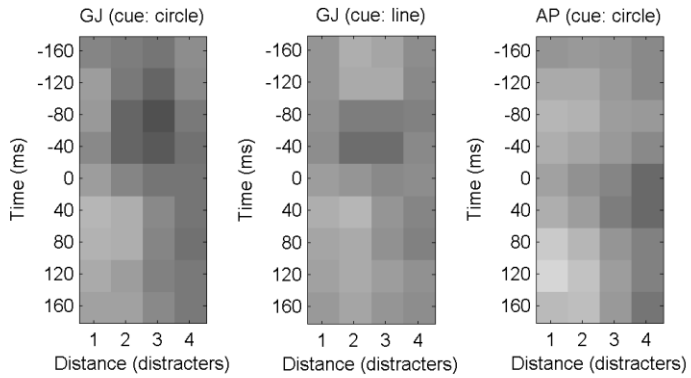

Fig. 15. Smoothed classification images for both cue types for amblyopic eyes. Classification images were smoothed by a 3x3 Gaussian filter ($\sigma = 0.8$) that acts on the grid. The positively correlated locations are mainly distributed after the target presentation for both types of cue.

4 Discussion

4.1 Temporal mechanisms for simple feature detection

Using a discrimination task and the method of classification images, we were able to estimate the spatiotemporal templates for luminance discrimination of both normal and amblyopic observers under various conditions. Our results for the normal template differs from what Neri & Heeger (2002) reported in that we showed the temporal inhibition component that peaks around 40 ~ 60 ms after the target presentation. As explained previously, we think this difference is due to the elimination of the temporal uncertainty using a discrimination task.

Our result also differs from the classic paired-pulse, three-pulse, or flicker sensitivity time course in that the latter is symmetric around the target presentation (time 0), i.e., there are two temporal inhibition lobes before and after the target presentation (Bergen & Wilson, 1985; Rashbass, 1970; Watson & Nachmias, 1977). Note that in the three-pulse study by Bergen & Wilson the 1st and 3rd pulses always had the same luminance. Although we are not certain as to the reason for such differences, we think they are probably related to two factors. First, the stimulus target in the present study has suprathreshold luminance, whereas the classic paired-pulse experiments were designed to test the luminance threshold. It has been suggested that the mechanisms involved in suprathreshold and near-threshold stimuli may be very different (Manny & Levi, 1982a, 1982b). Second, the presence of spatiotemporal noise that shares similar features with the target in our study could have unknown interaction that can affect the perception, especially since the classic paired-pulse experiments did not have a spatial variable at all. Further investigation is necessary to understand the mechanism underlying such

difference.

The classic paired-pulse temporal sensitivity time course has been fairly well modeled by a two-stage process by Rashbass (1970). The first (linear) stage is temporal filtering. A working model of the temporal impulse response function was proposed and developed by numerous people (Watson, 1986). The modeled function is composed of a transient and a sustained components. The transformed function (i.e. filter output of the stimulus input) is then processed at the second stage where the squared $\mathcal{L}_2$-norm (i.e. the sum of the squares of the filter output signal) of the function is computed, which serve as the base of decision criterion. This model correctly predicts that the paired-pulse sensitivity time course is determined by the autocorrelation function of the temporal impulse function that is always symmetric about the zero asynchrony (i.e. the target presentation time). As mentioned above, our result is not symmetric about the target presentation since the inhibition component is only present after the target offset, and therefore it cannot be accounted for by Rashbass' model. Neither can it be accounted for by a simpler model in which the second stage (i.e. summation of squares) is replaced by simply taking the maximum of the filtered signal to be the base for decision criterion, which predicts a horizontally flipped profile (Fig. 16).

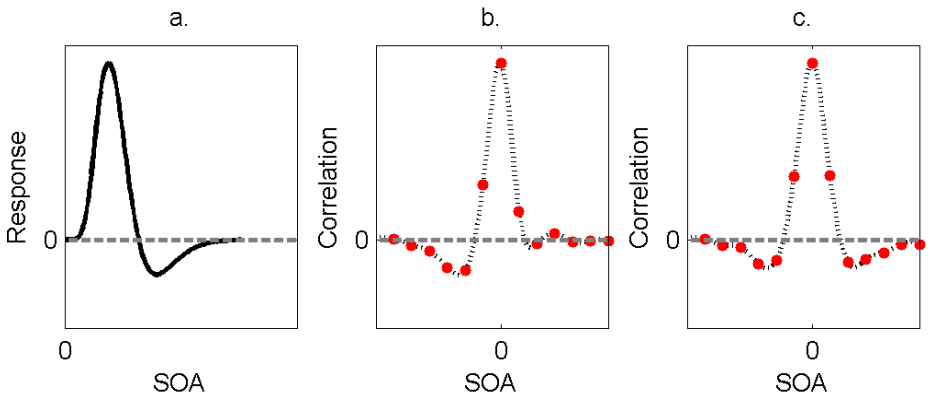

Fig. 16. a) The temporal impulse function – the working model. b) Simulated from 10,000 trials the temporal template profile by setting the decision strategy to be "report the presence of a signal if the maximum of the temporally filtered visual input is greater than a threshold". Red dots are simulated results, dashed curve is the smoothed profile. c) Simulated from 10,000 trials the temporal template profile using Rashbass' model. The decision strategy is "report the presence of a signal if the sum of squares of the temporally filtered visual input is greater than a threshold". In each of the three panels, the horizontal axis is the Stimulus Onset Asynchrony (SOA), and the y axis is either temporal response (a), or correlation (b & c). The dashed grey lines are at y = 0.

On the other hand, the asymmetric U shape of the temporal profile of the normal template for detecting a bright bar, whose inhibition component peaks at 40 ~ 60 ms and extends to about 100 ms after the target presentation, somewhat resembles the time course of the metacontrast or structure backward masking which typically has a U shape and the masking effect is strongest when the mask onset is 60 ~ 100 ms after the target onset (Breitmeyer & Ogmen, 2000). What

distinguishes these two visual functions is that there is no summation in backward masking, i.e., the masking effect always interferes with the target detection. This difference could be due to the fact that in our study the target and the distracter that may be considered as the "mask" are overlapping in space and uniform in structure (in terms of a single bar) whereas in metacontrast or structure backward masking the mask does not overlap with the target, or has structures different from that of the target. One possible mechanism of backward masking is that the propagation of the target elicited neural activity is interrupted by the mask presentation. Along the same line, it is reasonable to hypothesize that the detection of a bright bar relies on the proper pattern of neural activity, instead of the maximum activity or its "energy" that can be defined to be the summed squares as in Rashbass' model. A bright stimulus initiates a train of neural spikes whose rates form a pattern along time, which has been demonstrated to be similar to that of the temporal impulse function (Albrecht, Geisler, Frazor, & Crane, 2002). Neurons that receive these activities in the next stage may recognize specific patterns of the activities and respond according to the degree of matching. In the case of the present study, the temporal template profile has the typical shape of a temporal impulse response; therefore the neural activities elicited by an optimal stimulus (predicted by the template) will have a pattern that mimics the shape of the temporal impulse response, given that the stimuli have suprathreshold visibility. This pattern is likely to be recognized by the neurons of the next stage as coming from a strong visual stimulus. And the polarity of the target determines that the profile is asymmetric.

The temporal impulse function has been modeled to have a sustained and a transient component (Watson, 1986). A pure-sustained temporal impulse function is non-negative, whereas a pure-transient temporal impulse function has zero area (i.e. positive areas = negative area). And anything in between has both sustained and transient components. It has been found that stimuli of low spatial frequency are associated with transient temporal response and the transience weighs less or even disappears for stimuli of high spatial frequency. In the present study, the control stimulus has the fundamental spatial frequency 5 cpd, which was decreased to 1.67 cpd for the normal peripheral and amblyopic central vision testing. At the relatively high spatial frequency, the amblyopic template shows lack of inhibition both spatially and temporally, with the temporal summation hardly affected. Interestingly, the amblyopic template was completely restored to normal using stimuli with low spatial frequency. This is consistent with previous studies which also found that at low spatial frequency the difference in temporal sensitivity in both amblyopic and normal eyes was substantially decreased or even became unnoticeable (Bradley & Freeman, 1985; Manny & Levi, 1982a, 1982b). These results suggest that the temporal template profile as a function of spatial frequency is shifted towards the lower spatial frequency for amblyopic vision. When the stimuli were presented in the normal periphery, a template similar to that of the amblyopic eye was reproduced. Decreasing the fundamental frequency of the stimuli partly restored the spatial but not temporal inhibition mechanism. Therefore, we hypothesize that the spatial properties of normal peripheral vision are similar to that of amblyopic centric vision, but their temporal properties may be quite

different.

Both the normal peripheral vision and the amblyopic central vision are crowded in space and time. In contrast to the well studied spatial characteristics of crowding, the temporal properties of crowding have rarely been investigated. Note that the temporal properties of crowding are not the same as "temporal crowding" which often refers to the analogue of crowding in time, i.e., the target visibility is impaired by nearby temporal flankers that are presented at the target location (Pelli et al., 2004). The most relevant study on the spatiotemporal properties of crowding was done by Westheimer & Hauske (1975). They investigated the crowding effect on Vernier acuity by varying the target-flanker separation as well as asynchrony. With various target-flanker spatial configuration and fixed target presentation duration (50 ms), the crowding effect appeared at zero asynchrony and increased with target-flanker asynchrony up to 150 ms (i.e. backward crowding). In a recent preliminary study on letter crowding by Chung, a similar time course of crowding was found (to be submitted). We also showed that the strongest crowding effect did not occur during the target presentation in the present study. However, both backward crowding generated by post-target flankers and forward crowding generated by pre-target flankers exist in our results, especially in the normal periphery. It is not clear as to what caused this difference, but it may be related to the fact that the target was embedded in a relatively long sequence composed of 9 frames which lasted 0.36 sec in the present study, whereas the stimulus sequence in the previous studies had only two frames, one of which contained the target. The temporal order of the target and the flankers was unlikely to be mistaken by an observer for the 2-frame stimulus sequence, but could be confused for the 9-frame stimulus sequence. Further investigation is required to test this hypothesis.

4.2 Spatial mechanisms for simple feature detection

The results from experiment 2 illustrate the effect of spatial interactions on target orientation perception as a function of space and time. The orientation assimilation effect (i.e. positive correlation) is distributed close to the target location within the critical space for the tested eccentricities, therefore representing crowding (Parkes et al., 2001; Pelli et al., 2004). This orientation assimilation effect of crowding is consistent with previous reports (Parkes et al., 2001; Solomon et al., 2004). More and more evidence suggests that crowding emerges from feature integration over an undesirably large area following feature detection (Levi, 2008; Pelli et al., 2004), and that crowding is like texture perception (Balas, Nakano, & Rosenholtz, 2009; Levi & Carney, 2009; Parkes et al., 2001). Some explicit mechanisms have been proposed to explain crowding: averaging features from the clutter explained certain orientation configurations but not others, suggesting average may be a special case of more general pooling mechanisms (Parkes et al., 2001); Solomon et al. developed a unified model that accounted for both the sensitivity and the perceptual bias for crowding (assimilation) and the tilt illusion (repulsion), which incorporates a local modulated response followed by an opponent

mechanism for orientation identification (Solomon et al., 2004); a computational model that computes summary statistics over the crowding zone based on texture synthesis successfully predicted human performance under crowding condition for a variety of tasks (Balas et al., 2009). Admittedly, since the flanking effect on target orientation threshold is not the focus of the present study, the estimated spatiotemporal map for perceiving a crowded orientation is not intended to be a complete picture of crowding. Amblyopic spatiotemporal interaction maps differ from those of the normal periphery in some aspects such as the relative weights of forward and backward crowding, although the difference is small and will need more evidence to confirm.

An unexpected finding of experiment 2 is "anti-crowding" (i.e. repulsion) at locations farther away from the target, demonstrating an attraction – repulsion structure similar to the facilitation – inhibition spatial template for detecting a luminance increment of a bright bar in experiment 1 and those for other visual tasks. In physiology, retinal ganglion cells and LGN neurons both have the radial symmetric on / off receptive field with a center / surround profile; so do some V1 simple cells in selective orientations. However, the lower level visual neural receptive fields are unlikely to account for this center / surround spatial template associated with a wide variety of visual tasks that have been reported (Fig. 17). Wilson (1978) estimated the foveal line spread function with either a pure-sustained or pure-transient temporal modulation, and found the line spread function of a "Mexican hat" shape which can be modeled as the difference of Gaussian functions (DOG). In our experiment 1, a similar spatial profile for detecting a luminance increment of a bright bar was uncovered through classifying the independent random noise. The spatial extent of the stimuli was fixed in Wilson's study, whereas it was varied in our study by changing the individual bar width and accordingly the stimulus size, and the result implies that the center / surround template is associated with the image feature instead of the absolute distance, suggesting a higher level processing. Two different mechanisms, namely the centroid in the center and the feature repulsion in the surround have been reported for Vernier acuity localization (i.e. bias) in the fovea (Fig. 17c) (Badcock & Westheimer, 1985). Interestingly, the location-repulsive component in the surround was found to be independent of luminance polarity, which suggests a second stage of feature interaction. Foveal phase capture of a Gabor patch by inner flankers and phase repulsion by outer flankers also reflects the center / surround structure (Fig. 17d), and was explained by a shape interpolation (i.e. smoothing) mechanism (Levi, Li, & Klein, 2003). Data obtained from a wide range of separations from the original study clearly demonstrated that the attraction – repulsion mechanism depends on the stimulus feature (i.e. Gabor patch) rather than the absolute distance. In the periphery, a similar summation / inhibition spatial template was shown in experiment 1 using stimuli with relatively low spatial frequencies. As mentioned above, the center / surround spatial template has also been found in experiment 2 for orientation detection, which extends as far as 2.8 deg on each side of the target at 4 deg eccentricity. It seems that the center / surround structure, with the centroid effect much stronger than the surrounding subtractive effect as shown by the difference of their relative weights, is quite general for visual

perceptual mechanisms associated with both lower and higher level visual processes. Moreover, since the significance of such a spatial profile with both positive and negative components is to detect the change in an image, e.g. a bright light spot in the darkness or a shift in position or phase in an otherwise uniform texture, it is reasonable to hypothesize that crowding, which represents averaging or pooling in some sense, occurs in the centroid in the feature identification process (Fig. 18). The general center / surround mechanism is obviously limited by a certain spacing constraint (e.g. either effect disappears at a large enough spacing), but does not have a one-to-one relationship with the absolute distance; rather, it seems to be a function of the spatially ordered image feature. More specifically, when a feature is not crowded either because it is relatively isolated in space or very different from the surrounding features, it can occupy one of the off-on-off locations; whereas when some features are crowded, the pooled features as an ensemble are processed as one unit (on/off) for differentiation. This pooling – differentiation visual information processing probably exists at multiple levels.

It has been found that cueing a crowded target has no effect on identification sensitivity (Felisbert, Solomon, & Morgan, 2005). Similarly, the ratio of correct response with distracters is much lower than that without distracters even with spatiotemporal cueing in our experiment. However, we showed that a cue did affect the perception under spatiotemporal interactions, although the mechanism of different cueing effects caused by different cue types is not clear for now.

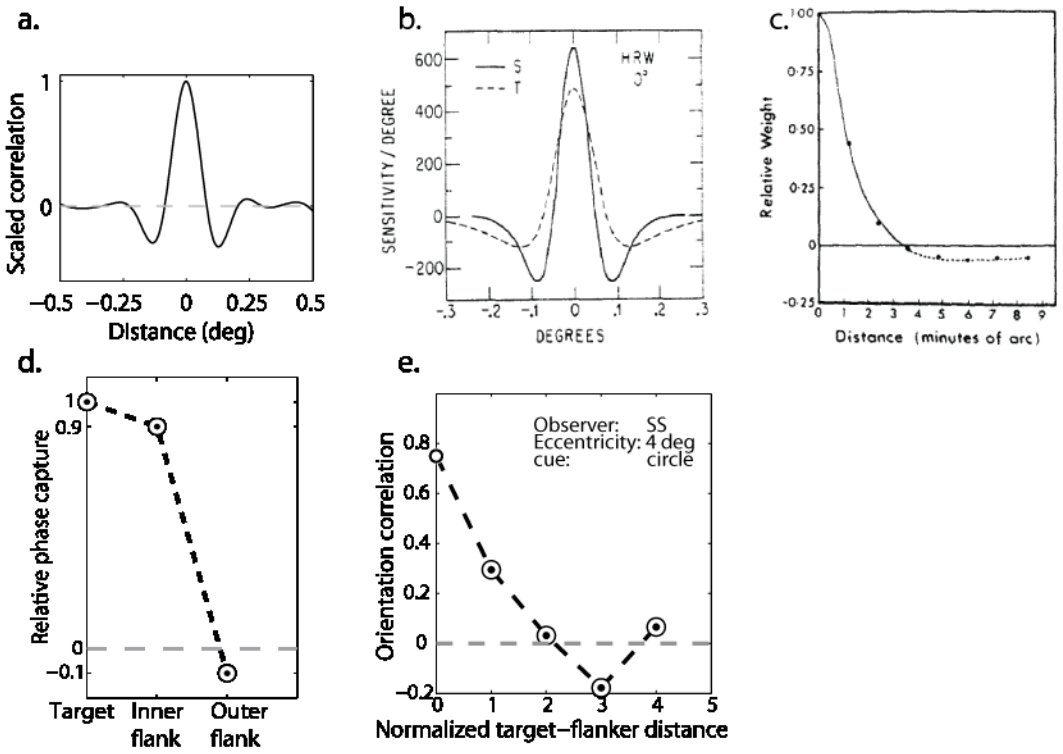

Fig. 17. Spatial profiles obtained from different visual tasks. a) Normal average foveal spatial profile from experiment 1. b) Estimated foveal line spread functions for two temporal modulation functions S (pure-sustained) and T (pure-transient) (Wilson, 1978). c) Foveal spatial profile of relative weights for perceptive target position (bias) in a Vernier acuity task (Badcock & Westheimer, 1985). d) Relative phase-capture spatial profile of a flanked target (Levi et al., 2003) in the fovea. This graph plots two points – the leftmost open and filled average symbols representing the tightest spaced inner and outer flankers respectively, in Fig. 7 of the original paper, in a slightly different way. e) Orientation correlation spatial profile at t = 40 ms (immediately following the target presentation) and 4 deg eccentricity from experiment 2. The distance is normalized by the stimulus element (i.e. Gabor patch). The data point at the target location (i.e. zero distance) is estimated as the correct rate in the absence of noise. All panels show a center/surround organization in different scales.

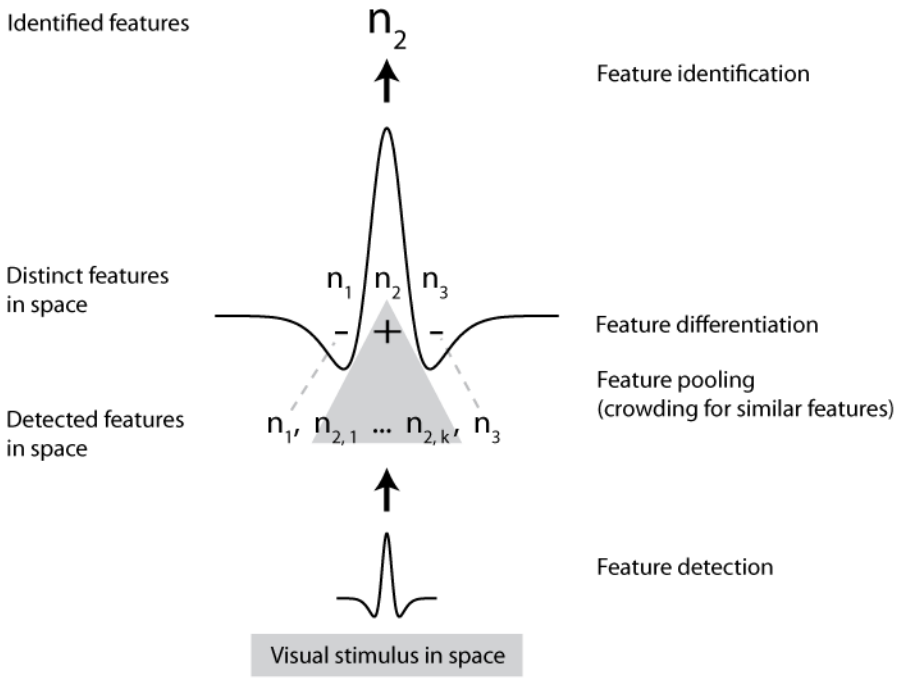

Fig. 18. Illustration of the general center / surround mechanism for feature identification. Feature detection and feature pooling processes are the same as the popular 2-stage crowding theory. The features (either distinct or after being pooled) are then differentiated, so any discontinuity in the feature map will be more likely to stand out. Note that the relative weight of summation is much greater than that of the subtraction.

FIXATIONAL EYE MOVEMENT IN NORMAL AND STRABISMIC AMBLYOPIC OBSERVERS

1 Introduction

1.1 Physiological fixational eye movements

Even when we are fixating on stationary targets our eyes are constantly moving. The miniature eye movements during fixation are the so-called fixational eye movements. They are different from the more familiar saccadic eye movements (e.g. visual search, reading) in many aspects such as scale (small vs. large), pattern of the trajectory (random vs. determinant), and awareness (unaware and involuntary vs. aware and voluntary). The discovery of fixational eye movements was made less than 300 years ago. Although the description of fixational eye movements as "tremor", "unsteadiness" or "wandering of gaze" is rather sparse from the early days due to the lack of data recording technology, scientists made impressive speculations that this "unsteadiness" of the eye helps to prevent "retinal fatigue", which has had a far-reaching influence on our understanding of fixational eye movements (Darwin, 1786; Jurin, 1738; Von Helmholtz, 1924). It is known that the visual system is not sensitive to unvarying stimuli, either in space or in time. Perceptual fading of an image caused by neural adaptation can be induced within only a few seconds by counteracting image movement with respect to the retina (Ditchburn & Ginsborg, 1952; Riggs & Ratliff, 1952). Hence the main goal of fixational eye movements is thought to prevent neural adaptation and the subsequent visual fading. The specific mechanisms to achieve this goal, however, are not completely understood (Rolfs, 2009).

By convention, fixational eye movements are categorized into 3 components based on the movement rate, size and frequency. Drifts are a low-velocity (< 30 min arc/sec) continuous movements interrupted by microsaccades, the small rapid shifts (about 3 ~ 120 deg/sec) of eye position that occur at frequency of 0.4~3Hz depending on individual, task, instruction, etc. The third component, tremor, is a small (about 0.1 ~ 0.5 min arc) high-frequency (about 30 ~ 100 Hz) movement superimposed on drift (Martinez-Conde, 2006; Martinez-Conde et al., 2004).

In general, studies of fixational eye movements can be summarized to have two purposes: 1) understanding the maintenance of fixation by quantitatively analyzing and modeling fixational eye movements; 2) correlating fixational eye movements with perception (e.g. perceptual fading) or physiological reaction (e.g. cortical neural firing pattern). Among the 3 components of fixational eye movement, microsaccades probably have received the most attention from researchers. Both psychophysical and physiological experiments have suggested that

microsaccades play significant roles in perception, which is not the focus of the current study, but see the recent review by Rolfs (2009). Rather, the focus of the current study is to develop quantitative characterization of the fixational eye movements.

Cornsweet (1956) studied drifts and microsaccades systematically for the first time. He concluded that drift is not under visual control and its randomness deviates the eye position away from its fixation, whereas the rate, magnitude and direction of microsaccades are correlated with fixational displacement, therefore microsaccades are responsible for correcting fixation errors generated by free drifts. This simple and quite plausible theory unfortunately was later challenged by many others who had observed different results that led to inconsistent conclusions, e.g., both microsaccades and drifts can be error correcting and error producing under the same circumstances (Boyce, 1967; Nachmias, 1959, 1961), and therefore microsaccades seem to serve no indispensible role in maintaining fixation (Kowler & Steinman, 1980; Steinman, Haddad, Skavenski, & Wyman, 1973). Furthermore, microsaccades can be voluntarily suppressed without increasing the fixation error, and it has been proposed that slow control (i.e. drift), but not microsaccade, maintains more stable and accurate fixation (Kowler & Steinman, 1979; Steinman, Cunitz, Timberlake, & Herman, 1967; Steinman et al., 1973). Surprisingly, our knowledge about oculomotor mechanisms of fixation in the presence of miniature eye movements is still largely from those early works.

Scientifically characterizing fixational eye movements is the basis for inferring their physiological functions. Fixational eye movement recording usually involves a large amount of data, and appropriate summarizing statistics are necessary for data analysis and visualization. Earlier analyses of fixational eye movements include qualitative description, empirical distribution estimation, and correlation analyses between different pairs of properties (e.g. displacement and velocity magnitude, displacement and microsaccade rate, time and microsaccade rate) along certain dimension (e.g. direction) (Cornsweet, 1956; Kowler & Steinman, 1979; Nachmias, 1959). There is no doubt that these descriptions are the fundamentals and are valuable or even sufficient for many purposes. However, it is not hard to see that it requires a number of combinations of properties of interest to get the complete picture (e.g. position vs. magnitude vs. direction), which may still be hard to visualize and confusing. More importantly, these semi-quantitative analyses are non-optimal for comparison across subjects and research groups. Therefore integrative quantitative analyses should be useful complementary tools for studying fixational eye movements.

Random walk has been a promising model for fixational eye movements (Engbert, 2006; Engbert & Kliegl, 2004; Vasudevan, Phatak, & Smith, 1972). Engbert, etc. (2004) used fractional Brownian motion model to analyze the variance of fixational eye movement on different time scales and found that fixational eye movements are persistent over short time scales (< 30ms) and anti-persistent over longer time scales, for which both drifts and microsaccades, especially the latter, are responsible. They also found that microsaccades play a

key role in controlling binocular disparity. Their study claims to have at least partly explained the contradictory roles of microsaccades (i.e. error producing and error correcting) and shows a nice abstraction of the nature of fixational eye movements as a whole. However, there was no rigorous model formulation or any analysis on domains such as time and location that are more familiar and intuitive.

Here, we introduce a parametric stochastic model to characterize fixational eye movements. Although a trajectory of the fixational eye movements appears erratic and lacks an organized pattern, it is different from a standard two-dimensional Brownian motion in that the latter is much more "wandering" whereas the former hardly deviates too far from the center. In fact, when time goes to infinity, the expected distance from the origin is infinity for Brownian motion. Therefore certain constraints must be imposed on the random walk model for fixational eye movement. A good candidate for these constraints – the potential function approach has been developed and applied to various analyses of location signals of moving particles, e.g. animal tracking, drifts, and soccer trajectories (Brillinger, 2007a, 2007b; Brillinger, Preisler, Ager, & Kie, 2001; Brillinger, Preisler, Ager, Kie, & Stewart, 2001). In the current study, we will integrate the potential function approach with stochastic modeling in addition to other statistical methods, and hope to reveal the order behind the seemingly random fixational eye movements.

The first step of studying fixational eye movements is eye tracking. Several generations of eye tracking technologies have been developed, including the contact lens optical lever (Ditchburn & Ginsborg, 1953; Krauskopf, Cornsweet, & Riggs, 1960) and video-based eye tracking (e.g. Purkinje image tracking, dual Purkinje image tracking). Video-based eye tracking is the most widely used method because it's non-invasive and relatively simple. Although eye tracking technologies today are much more sophisticated than 20 years ago with high temporal and spatial resolution, there is no way to know precisely where on the retina the target image is located, let alone the fact that an eye tracker can lose its calibration during a recording session. In our study, the fixational eye movements were recorded using Adaptive Optics Scanning Laser Ophthalmoscope, an advanced imaging apparatus that adaptively corrects higher-order refractive errors of the eye and dynamically grabs high definition retinal images. Ever since adaptive optics was first introduced to vision research by Liang, Williams & Miller (1997) who achieved "super vision" under the experimental conditions, this powerful tool has been applied to physiological, psychophysical and pathological studies of vision, including cone mosaic properties, color vision, retinal morphology for diseases (e.g. diabetes, glaucoma), etc. Its unprecedented ability of visualizing photoreceptors in living humans is of great value and potential to vision scientists. One interesting discovery made with the aid of AO is that the mean fixation position does not coincide with the highest cone density, but is displaced by 10 min on average (Putnam et al., 2005). The advance of AO techniques that made the current study possible is the development of Adaptive Optics Scanning Laser Ophthalmoscope (AOSLO) by Austin Roorda (2002). Using AOSLO one can obtain high-resolution dynamic

retinal images and each frame of the movie can be registered to regenerate the eye position. Moreover, by superimposing the target image onto the retinal image we know precisely where the fixation locus is.

Studying abnormal fixational eye movement under pathological conditions such as amblyopia and strabismus will provide us better understanding of not only pathological but also physiological significance of fixational eye movement.

1.2 Abnormal fixational eye movements in strabismic amblyopia

Amblyopia is a developmental visual disorder. Exposing to amblyogenic conditions (e.g. anisometropia, strabismus) during early life can cause the arrest of normal visual development and result in different types of amblyopia. Typical amblyopic visual defects include reduced contrast sensitivity, impaired position acuity, extensive crowding and spatial distortion (Ciuffreda et al., 1991; Levi, 1991, 2008; Levi & Carkeet, 1993; Levi, Song et al., 2007). Between the two most common types of amblyopia, anisometropic and strabismic amblyopia, the latter is thought to suffer from more severe cortical-level visual impairment (Levi & Harwerth, 1977; Levi & Klein, 1982; Levi & Klein, 1985).

It has previously been shown that abnormal fixational eye movement is associated with amblyopia and strabismus. These include enlarged drift, saccadic intrusion, and jerk nystagmus (Ciuffreda, 1979; Ciuffreda et al., 1979a; Ciuffreda, Kenyon, & Stark, 1979b, 1980; Schor & Hallmark, 1978). Saccadic intrusions are large biphasic saccades that interrupt accurate fixation. At least one phase of a saccadic intrusion is a saccade that deviates the eye from the fixation position. Jerk nystagmus is a type of pathological oscillation that increases in size when the patient attempts to fixate. The first phase of a jerk nystagmus is an error producing smooth movement and the second phase is a correcting saccade (Martinez-Conde, 2006). Strabismic amblyopes demonstrate not only markedly increased drifts in both velocity and amplitude, but also prevalent saccadic intrusions and jerk nystagmus. It has been found that saccades in strabismic amblyopic fixational eye movements can be voluntarily suppressed without affecting the accuracy of fixation, in which case the slow control (i.e. drift) is largely responsible for maintaining fixation (Schor & Hallmark, 1978). It has also been reported that strabismic amblyopes can shift between the eccentric fixation locus and the fovea for different fixational tasks (Siepmann, Reinhard, & Herzau, 2006).

In the current study, we applied a novel eye tracking technique (i.e. AOSLO) and modern statistical methods to characterize fixational eye movements in normal and strabismic amblyopic observers. In particular, **1)** unlike previous studies where fixation location on the retina can only be inferred without direct observation, AOSLO allows one to visualize the target image on the retina during fixation, thus the obtained fixation displacements are always reliable. This is especially important for strabismic amblyopes or other patients with eccentric and unstable fixation, because it is more difficult to calibrate the eye tracker and maintain its

accuracy during recording for these subjects. Besides, the intuition a researcher can have by directly viewing the retinal movements is very valuable. Although regular scanning laser ophthalmoscope (SLO) can also record retinal images during the fixational movements, the spatial resolution of the recording is much lower than that of AOSLO images which makes detailed analyses of drifts and microsaccades possible. **2)** Stochastic modeling with potential function approach and other statistical modeling methods are developed and applied to fixational eye movements. Allowing for randomness, statistical models are particularly suitable for fixational eye movements. The modeling methods in this report differ from previous analyses in several ways: ***first***, the fixational eye movements are treated as what it is – a process; and models are developed to characterize fixational eye movement components as functions of time (e.g. time-inhomogeneous potential function, Poisson point process). Due to the large amount of data and their random nature, this was not easy for earlier analyses. ***Second***, fixational eye movements are analyzed in their real space – two-dimensional plane. Previous studies usually had to deal with fixational eye movements' projections on horizontal and vertical axes separately. Two-dimensional representation (e.g. the potential function and the velocity vector field) substantially simplifies the analyses and is much more intuitive for data visualization. ***Third***, the randomness of fixational eye movement is captured by the noise element in the model. Just like velocity or position, noise is also two-dimensional, and it represents the uncertainties in both the magnitude and direction of fixational eye movements. In the present study, fixational eye movements are modeled as a two-dimensional random process constrained by the potential function, simple and natural. Moreover, the stochastic model with a potential function can standardize the quantification of fixational eye movements and will facilitate comparisons between subjects and research groups. **3)** We apply these statistical tools to study the abnormal fixation pattern in the strabismic amblyopic subject in detail, e.g., the eccentric fixation locations for different targets / tasks, contributions of different components to the abnormal fixational eye movements.

2 Methods

2.1 Subjects

Two subjects, one with normal visual acuity and the other with strabismic amblyopia, participated in this study. Data from 3 eyes, i.e., the preferred eye of the normal subject, and both the nonamblyopic eye and the amblyopic eye of the strabismic amblyopic subject, were recorded and analyzed. The detailed characteristics of each of the two subjects are listed in Table 1. The strabismic amblyopic subject has unsteady nasal eccentric fixation in his amblyopic eye.

Observer	Age (yrs)	Strabismus (at 6 m)	Eye	Refractive error (diopters, D)	Line letter VA (single letter VA)	Monocular fixation
Normal						
DR	21	None	R	pl	$20/16^{+2}$	Steady centric
			L	pl	$20/16^{+2}$	Steady centric
Strabismic amblyopia						
SF	20	L ExoT 6^{Δ}	R (NAE)	-1.50/-0.25x90	$20/12.5^{+1}$	Steady centric
			L (AE)	pl/-1.00x30	$20/125^{+1}(20/80^{+2})$	Unsteady nasal

Table 1. Subjects characteristics.

2.2 AOSLO fixational eye movements recording

Several fixation targets were used for different experimental sessions and different eyes, as listed in table 2 and 3. Only one target was used in each recording session. Fixation targets were enlarged to improve their visibility to the amblyopic eye with poor visual acuity. Observers' correct response rate for the tumbling E identification tasks are shown in table 2. The performance under each condition is way above the chance level (i.e. 25%), implying that the observers did identify the letter E targets while maintaining fixation. In these experiments, the fixation task (i.e. passive viewing or tumbling E identification) or the fixation target's shape and size did not make any difference in the characteristics of fixational eye movements for the normal or nonamblyopic eyes, but they are significant variables for the amblyopic eye. Therefore we combined data from all fixation targets/tasks for the normal and nonamblyopic eyes, but differentiated these conditions for the amblyopic eye.

	Fixation target	Target size (min arc) *(acuity size)*	Stroke width (min arc)	Correct response	
■	Dot	1	1	--	
+	Small cross	6	1.2	--	
+	Medium cross	20	4	--	
+	Large cross	30	6	--	
E	Small tumbling E	5 *(20/20)*	1	86.6% 78.7%	DR SF (NAE)

E	Medium tumbling E	20	*(20/80)*	4	65.0%	SF (AE)
E	Large tumbling E	25	*(20/100)*	5	66.2%	SF (AE)

Table 2. Fixation targets and observers' correct response rates for the tumbling E identification tasks. All correct response rates are much higher than the chance rate (25%). The normal (DR) and nonamblyopic (SF – NAE) eyes' performance is substantially better than that of the amblyopic eye (SF – AE). Medium and large sized letter Es generated similar performance in the amblyopic eye (SF – AE).

Subject (eye)	Fixation targets
DR (preferred eye)	Dot, Small cross, Medium cross, Small E
SF (NAE)	Dot, Small cross, Medium cross, Small E
SF (AE)	Small cross, Medium cross, Large cross, Medium E, Large E

Table 3. Fixation targets used for each subject (eye).

AOSLO can measure the wavefront of the eye and then compensate for its higher-order aberrations through a deformable mirror until the retinal image becomes clear and the photoreceptors recognizable. During imaging, the retina is scanned by 840 nm (i.e. infrared) laser at 30 Hz vertically and 16 KHz horizontally. Stimuli were generated by an amplitude-modulating Acousto-Optic-Modulator (AOM), which with sufficiently high switching frequency (50 MHz), can selectively turn the AOSLO laser beam on or off therefore effectively create 1-bit images (i.e. black targets on a red background) (Poonja, Patel, Henry, & Roorda, 2005). The imaging field is composed of 512 x 512 pixels and the field width is 2.5 deg for all eyes. Because of the high scanning rate in the horizontal direction (i.e. 16 KHz) the sinusoidal variation of the line speed must be corrected, i.e., equivalently, the horizontal pixel values are transformed according to a proper inverse sinusoidal function. Hence, the temporal resolution of the eye tracking is 33.3 ms; and after the sinusoidal correction, the spatial resolutions are about 14 sec arc in the horizontal direction and 18 sec arc in the vertical direction. Apparently, in AOSLO recorded eye movements tremor cannot be easily resolved due to its high temporal frequency (i.e. 30 ~ 100 Hz), although some more sophisticated image processing designed to extract inter-row movement can theoretically achieve very high temporal sensitivity (Stevenson & Roorda, 2005). In the current study we did not interpolate to obtain the between-frame eye positions, so tremor is not the subject of the report.

Before all imaging sessions, the pupil of the test eye was dilated by topical application of Tropic 0.1% and Phenyl 2.5%. The subject was instructed to fixate at the target (cross or dot) presented on a 2.5 x 2.5 deg screen in front and hold the gaze. When viewing the tumbling E target, the subject was asked to answer whether the opening of the letter E is directed up, down, left, or right, by pressing corresponding buttons on a keyboard. Each recording is either 10 or 20 seconds in duration. During the recording, the other eye is patched, and the subject's head is

fixed by a bite bar.

2.3 Retinal image processing

The raw data collected using AOSLO are movies of moving retina. Some image processing steps are required before one can get the eye movement trajectories. As mentioned above, the unprocessed movies are distorted because of the sinusoidal horizontal scanning rate. Therefore the first step is "de-warping". Simply speaking, an "artificial eye" composed of a regular spaced grid and its AO image served as the source to obtain the appropriate transformation, in this case an inverse sinusoidal transformation, which should be used for frame-by-frame correction of retinal images. The de-warped retinal movies store all eye position information that is yet to be extracted.

Cross correlation method is used to obtain relative positions of different frames in a movie. The position that corresponds to the maximal correlation between two images is the estimated relative position between them:

$$\boldsymbol{r} = arg\max_{\boldsymbol{\delta}}\left\{c(\boldsymbol{\delta})\sum_{\boldsymbol{x}} R(\boldsymbol{x})I(\boldsymbol{x}-\boldsymbol{\delta})\right\} \qquad 11)$$

where $\boldsymbol{r}$ is the estimated position of a frame relative the reference image; R and I are pixel values of the reference image and each retina frame respectively; $\boldsymbol{x}$ denotes the coordinate of each pixel in an image; $\boldsymbol{\delta}$ denotes the offset in position between the retina frame and the reference image; and $c(\boldsymbol{\delta})$ is the normalizing factor depending on $\boldsymbol{\delta}$. In practice, we applied a Fast Fourier Transform (FFT) as the computational tool to achieve the same goal. The FFT method is based on the discrete Fourier transform (DFT):

$$\boldsymbol{r} = arg\max\{c' \cdot \mathcal{F}^{-1}[\mathcal{F}(R)\cdot\mathcal{F}(I)]\} \qquad 12)$$

where c' is the normalizing function.

The processes of constructing reference frames are different for normal (including nonamblyopic) and amblyopic eyes. For normal and nonamblyopic eyes, for each movie, a frame of good image quality is picked out as the temporary reference frame, with which all movie frames are cross correlated. Then the position of each frame is adjusted such that it regenerates the movement of the eye, and this process results in a new movie in which the retina is stabilized. Averaging all frames of this stabilized-retina movie produces a sharp retinal image, which is used as the real reference image for frame registration. Since each movie has its

own reference image, these references themselves need to be cross correlated to correct for the baselines of all movies, i.e., eye trajectories of all movies can then be plotted on the same coordinates.

For the amblyopic eye, however, this method failed because the eye movements are simply too erratic to be captured by any frame. The solution to this problem is to build a retinal image that is big enough to register all frames. We selected pieces of recordings at different retinal locations that cover the range of the eye movement. Once the averaged images of those retinal locations were obtained using stabilized-retina movies in the same way described above, they were carefully stitched together manually with the aid of image editing software (Photoshop CS2). The resulting big picture of the retina is the reference for amblyopic retinal frame registration (Fig. 1).

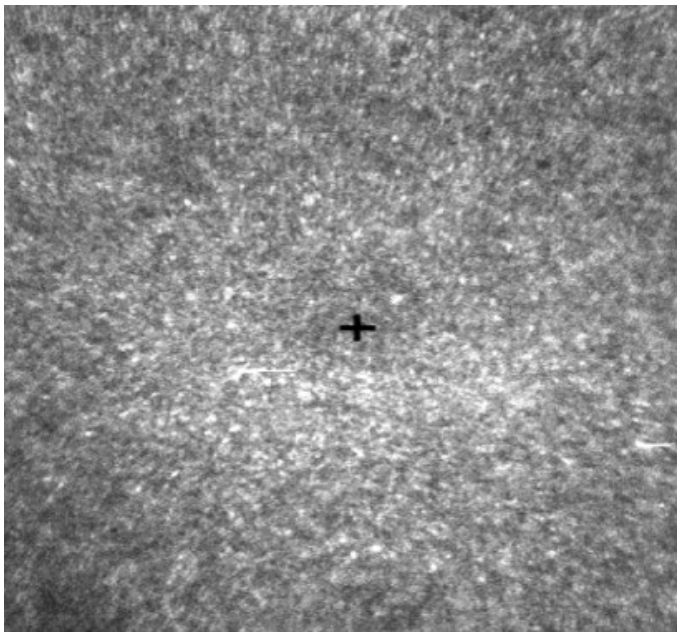

Fig. 1-1. Subject SF's nonamblyopic eye's retina image recorded by AOSLO during fixation. The fixation target – a small cross (6 min arc) is superimposed on the retina image and falls in the fovea. The field size is 2.5 × 2.5 deg^2, and the resolution is 512 × 512 pixels.

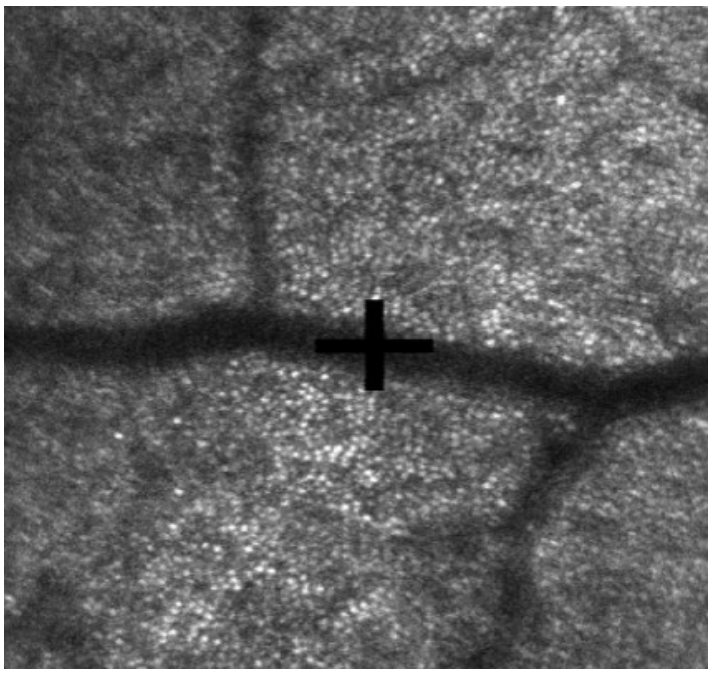

Fig. 1-2. Subject SF's amblyopic eye's retina image recorded by AOSLO during fixation. The fixation target – a medium cross (20 min arc) is superimposed on the retina image and falls in the periphery. The field size is 2.5 × 2.5 deg^2, and the resolution is 512 × 512 pixels.

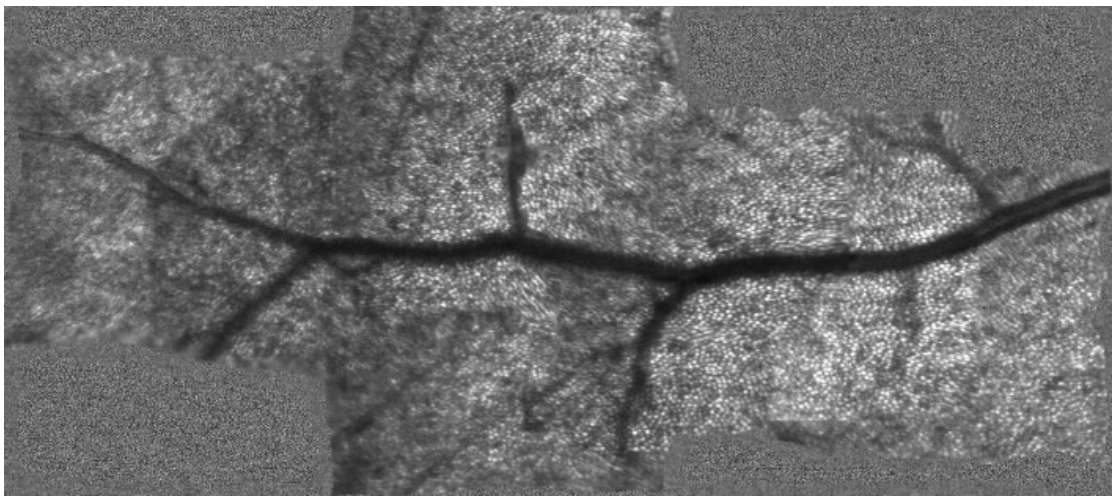

Fig. 1-3. The reference frame of subject SF's strabismic amblyopic eye. Multiple averaged frames centered at different locations are carefully stitched together to produce this reference frame that covers the range of the amblyopic eye's positions during fixational eye movements. The blank space near the edge is filled by Gaussian noise, and the edges of the retina area are low-pass filtered, so that the artificial features (e.g. edge) are obscured. The size of the reference image is about 3.5 × 8 deg^2, and the resolution of unit area is the same as that in Fig. 1-1.

The cross correlation method of extracting eye position information generates errors in a small number of frames. This is because first, the image quality varies from frame to frame;

second, since the temporal sampling rate is only 30 Hz, some very fast eye movement can produce distortion of the frame, which is poorly dealt with by cross correlation algorithm; third, the rotation movement of the eye cannot be captured by cross correlation either. Whenever an error occurs, the retina cannot be stabilized in the regenerated movie, and such errors are easy to spot just by visual inspection. Indeed, we screened all frames in the regenerated movies, marked those error frames, and excluded them in our data analysis. Out of all frames with acceptable image quality, about 2% are erroneously registered for the normal eye and the nonamblyopic eye, 2% for the passive-viewing (i.e. fixation target is a cross) series and 9% for the Tumbling E-recognition series for the amblyopic eye.

2.4 Labeling fixational eye movement components

The obtained fixational eye movement series is composed of 2 components, drift and microsaccades. Tremor is not resolvable due to the insufficient temporal sampling rate. We adapted and modified the principle used by Engbert & Kliegl (2003) to separate microsaccades from drifts. The magnitude of speed is calculated by taking the norm of the two-dimensional velocity vector. Median Absolute Deviation (MAD), instead of standard deviation (SD), of the speed distribution was calculated in order to minimize the effect outliers. The threshold speed for detecting microsaccades was set to be the sum of the median and 6 multiples of the MAD, i.e., a data point is labeled as drift if its speed is below the threshold and as microsaccades otherwise.

Since for some analyses we are only interested in the uninterrupted drift series, we extracted all drifts that are bounded by two microsaccades, relabeled the times of each such series from 0 to T_i, and subtracted the position vector of the first point ($t = 0$) from all points in each series. These drift series are sometimes referred to as sub-drifts.

Both the normal and the nonamblyopic eyes' movement data are centered at the average fixation locus, which coincides with the center of fovea (allowing some measurement error). The amblyopic eye's data are widely distributed and loosely centered at a peripheral location that is 4.5 deg from the fovea.

2.5 Data analysis

2.5.1 Stochastic process with potential function modeling

The fixational eye movement time series was transformed into state space, where each two-dimensional position is called a state. Drift is modeled as a random walk on the domain of this state space of discrete points. "Potential", a function of location state, predicts the infinitesimal direction and amplitude of the eye movement on top of random noise. An equation for motion can be written as a stochastic gradient system. In the time invariant case, it is:

$$\mathrm{d}r(t) = -\nabla V\big(r(t)\big)dt + \sigma\big(r(t)\big)dB(t), \quad \nabla = \left(\frac{\partial}{\partial x}, \frac{\partial}{\partial y}\right) \tag{13}$$

where $r(t) \in \mathbb{R}^2$ denotes the position (x, y) of the object at time t, $V(r)$ is a scalar-valued differentiable potential function at (x, y), σ is a 2×2 matrix at (x, y), and $B(t)$ is the standard Brownian motion in two-dimension. This equation says that within a small time interval, position change equals potential gradient plus some noise. The modified version for modeling fixational eye movement after dropping the time-invariant assumption and ignoring the noise correlation can be rewritten as

$$\Delta r_x(t) = -\mu_x(x, y, t)dt + \sigma_x(x, y, t)w(t) \tag{14}$$

$$\Delta r_y(t) = -\mu_y(x, y, t)dt + \sigma_y(x, y, t)w(t) \tag{15}$$

where $\mu_x = \partial V/\partial x$, $\mu_y = \partial V/\partial y$, $\sigma_x, \sigma_y \in \mathbb{R}$, $w \sim N(0, \sqrt{\Delta t})$. And more specifically,

$$\begin{aligned} \Delta r_x(t_i) &= r_x(t_{i+1}) - r_x(t_i) \\ &= -\mu_x(x, y, t_i)(t_{i+1} - t_i) + \sigma_x(x, y, t_i)w(t_i) \end{aligned} \tag{16}$$

$$\begin{aligned} \Delta r_y(t_i) &= r_y(t_{i+1}) - r_y(t_i) \\ &= -\mu_y(x, y, t_i)(t_{i+1} - t_i) + \sigma_y(x, y, t_i)w(t_i) \end{aligned} \tag{17}$$

The difference between the above equations and a general stochastic differential equation (SDE) is that here time is discrete and the functions μ_x and μ_y are the differential functions of the real-valued function V.

For a given t, suppose that the potential function can be written as a sum of basis functions, i.e., $V(x, y, t) = \varphi(x, y, t)^T \beta(t)$ with φ an L by 1 vector of known functions and β an L by 1 unknown parameter, then $\nabla V(x, y, t) = \nabla\varphi(x, y, t)^T \beta$. Let's assume constant variance across position for now, and equations 6) and 7) can be rewritten as

$$r_x(t_{i+1}) - r_x(t_i) = -\sum \theta_{x,m}(x, y, t_i)\beta_m(t_i)(t_{i+1} - t_i) + \sigma_x(t_i)w(t_i) \tag{18}$$

$$r_y(t_{i+1}) - r_y(t_i) = -\sum \theta_{y,m}(x, y, t_i)\beta_m(t_i)(t_{i+1} - t_i) + \sigma_y(t_i)w(t_i) \tag{19}$$

where $\theta_{x,m} = \partial\varphi_m/\partial x, \theta_{y,m} = \partial\varphi_m/\partial y$. Using ordinary least squares method we can solve the linear regression problem for an estimate of β in both the x and y coordinates, and obtain an estimate of the potential function V at time t_i. If the process is indeed time invariant (i.e. equation 1), then $V(x,y) = \varphi(x,y)^T\beta$, and all $r_x(t_i)$, $r_y(t_i)$, $\theta_x(\cdot,t_i)$, $\theta_y(\cdot,t_i)$, $\varphi(\cdot,t_i)$ can be stacked over different time points $t_1,\cdots,t_n$ by row, assuming σ constant. It comes back to a linear regression problem that can be solved using ordinary least squares (OLS) method.

In modeling the fixational eye movements, we chose the quadratic polynomial bases as φ, hence at some given time,

$$V(x,y) = \beta_0 + \beta_1 x + \beta_2 x^2 + \beta_3 y + \beta_4 y^2 + \beta_5 xy \qquad 20)$$

$$v_x(t_i) = \frac{r_x(t_{i+1}) - r_x(t_i)}{t_{i+1} - t_i} = -\beta_1 - 2\beta_3 x - \beta_5 y + \frac{\sigma_x}{t_{i+1} - t_i} w \qquad 21)$$

$$v_y(t_i) = \frac{r_y(t_{i+1}) - r_y(t_i)}{t_{i+1} - t_i} = -\beta_2 - 2\beta_4 y - \beta_5 x + \frac{\sigma_y}{t_{i+1} - t_i} w \qquad 22)$$

where v_x and v_y denote velocities in the x and y directions. Parameters βs can be solved using OLS.

Although r is defined as a process, i.e., a function of time t, it doesn't have to be so, in which case there is no time variable in the equations and only the position increment (i.e. Δr) but not the position itself (i.e. r) is meaningful. For the fixational eye movements, the continuous drifts are modeled by $r(t)$, whereas each microsaccade is modeled by Δr as a special case of the potential function approach. In practice, there is essentially no difference in the solutions of the two models.

2.5.2 Point process of microsaccades

Intuitively, the onset of a microsaccade appears rather random in time. One model is a Poisson Point Process. For a *small* time increment τ,

$$P(N(t+\tau) - N(t) > 0) \simeq E\big(N(t+\tau) - N(t)\big) \simeq \lambda(t)\tau \qquad 23)$$

where $N(t)$ is the random number of microsaccades that occurred by time t, i.e., $N(t+\tau) - N(t)$ is the random number of microsaccades in the time interval $(t, t+\tau)$; λ is called the

rate of a Poisson Process and can depend on time and location. Equation 13) says that the probability that a microsaccade occurs within the time interval $(t, t+\tau)$ approximately equals the rate λ times the length τ of the interval.

Equations 13) is generalized from the more standard form of Poisson Process, where the arriving time of each microsaccade since the last one is exponentially distributed with rate λ, and the numbers of microsaccades within a certain time interval has a Poisson distribution with rate λ.

$$P(T < t) = \lambda e^{-\lambda t} \tag{24}$$

$$P(N(t+\Delta t) - N(t) = k) = e^{-\lambda \Delta t} \frac{(\lambda \Delta t)^k}{k!} \tag{25}$$

In the present study, we make an assumption that the process of microsaccades is time homogeneous, i.e., rate λ is independent of t; it may only depend on location (x, y). In the spatial temporal case, equation 13) then becomes

$$\begin{aligned} &P(N(x, y, t+\tau) - N(x, y, t) > 0) \\ &\qquad \simeq E\big(N(x, y, t+\tau) - N(x, y, t)\big)\lambda(x, y)\tau. \end{aligned} \tag{26}$$

Equation 16) implies that the rate of a Poisson Process can be estimated from the expected number of points within an interval scaled by the length of the interval $(0, t)$. Assuming time homogeneity,

$$\lambda(x, y) = E[N(x, y) - N(x+\Delta x, y+\Delta y)] / \sum \Delta t \tag{27}$$

where $N(x, y)$ is the random number of events in the interval $(0, x) \times (0, y)$; $\sum \Delta t$ denotes the sum of durations corresponding to eye positions that lie within $(x, x+\Delta x) \times (y, y+\Delta y)$. We note that $\sum \Delta t$ can be represented by the total number of points (including both drifts and microsaccades) within $(x, x+\Delta x) \times (y, y+\Delta y)$ due to the equal distance temporal sampling. Then we have:

$$\lambda(x,y) = E\big(N_{sac}(\Delta x\Delta y)\big)/E\big(N_{total}(\Delta x\Delta y)\big) = \frac{f_{sac}(x,y)}{f_{total}(x,y)} \quad (28)$$

where $f(x,y)$ is the asymptotic density of points at (x,y) as $\Delta x, \Delta y \to 0$. Therefore we can estimate the rate in the following way:

$$\hat{\lambda}(x,y) = \frac{\hat{f}_{sac}(x,y)}{\hat{f}_{total}(x,y)} = \frac{[n_{sac}(x+\Delta x, y+\Delta y) - n_{sac}(x,y)]/(\Delta x\Delta y)}{[n_{total}(x+\Delta x, y+\Delta y) - n_{total}(x,y)]/(\Delta x\Delta y)} = \frac{n_{sac}(x+\Delta x, y+\Delta y) - n_{sac}(x,y)}{n_{total}(x+\Delta x, y+\Delta y) - n_{total}(x,y)} \quad (29)$$

where $n(x,y)$ denotes the number of observed microsaccades in $(0,x)\times(0,y)$.

2.5.3 The full model of fixational eye movements

We now integrate the above elements of models that characterize different movement components and aspects, and come to the full model of fixational eye movements starting from a microsaccade at time 0, followed by a drift until time T_1 when it is ended by the next microsaccade. Note that T_1 is assumed a random variable.

$$dr(t) = [S(r(t),t) - 1]\big[\nabla V_{drift}(r(t),t)dt + \sigma_{drift}(r(t),t)dB(t)\big] - S(r(t),t)\big[\nabla V_{sac}\big(r(t)\big) + \sigma_{sac}\big(r(t)\big)w\big], \qquad t \in (0, T_1] \quad (30)$$

where S indicates the onset of a microsaccade,

$$S(r(t),t)=\begin{cases}1, & with\ probability\ \ \lambda\big(r(t)\big)dt\\ 0, & with\ probability\ \ 1-\lambda\big(r(t)\big)dt\end{cases} \qquad 31)$$

The entire time series of fixational eye movement is the sum of individual series characterized by equation 20) and 21) over $T_1, T_2, \cdots, T_M$.

3 Results

There are total 21004 data points (≈700 sec) from the preferred eye of the normal subject DR, 15898 points (≈530 sec) from the nonamblyopic eye of the strabismic amblyopic subject SF, and 23787 points (≈793 sec) from the amblyopic eye of SF. The number of points (total length of observational intervals) recorded using different fixation targets from each eye is listed in table 4. Only correctly registered frames are counted.

# points (seconds)	Dot	Small Cross	Medium Cross	Large Cross	Small E	Medium E	Large E	**Total**
DR (normal)	5330 (177.7)	5198 (173.2)	4876 (162.5)	--	5600 (186.7)	--	--	**21004 (700.1)**
SF (NAE)	6493 (216.4)	2984 (99.5)	2912 (97.1)	--	3509 (117.0)	--	--	**15898 (530.0)**
SF (AE)	--	5092 (169.7)	2868 (95.6)	2600 (86.7)		7559 (252.0)	5668 (188.9)	**23787 (792.9)**

Table 4. Number of points (duration in seconds) of each fixation target for each eye. Only correctly registered frames are counted.

3.1 Normal eye

3.1.1 Overview

A 10-second sample of fixational eye movements from the normal subject DR is plotted in Fig.2. Two components, namely microsaccade and drift, are defined using a method reported by Engbert (2003). In general, these two components are differentiated by comparing their speeds to a threshold; microsaccades and drifts have speeds above and below the threshold respectively. Fig. 3-1 shows that the magnitude of speed $\omega \equiv \sqrt{{v_x}^2+{v_y}^2}$ of the fixational eye movements are narrowly distributed near zero, with a thin and long tail on the right hand side. To reduce the weight of the long tail, median absolute deviation (MAD) instead of standard deviation (SD) is used to represent the distribution width. The threshold that differentiates microsaccades from drifts is set at $median(\omega)+6MAD(\omega)$ (Engbert & Kliegl, 2003). Take the normal eye as an

example. Since ω ranges from 0 to 52.8 deg/sec, $MAD(\omega)$ = 0.16 deg/sec, and $median(\omega)$ = 0.28 deg/sec, therefore the threshold speed for the normal eye is 1.244 deg/sec. The resulting two component velocities for the normal eye are scattered in Fig.3-2. Drifts' two-dimensional velocity scatter resemble a bivariate Gaussian distribution with mean **0**, and microsaccades' velocities are roughly symmetrically distributed about both axes with some variation in magnitude and direction.

From Fig. 2, we see that the sample fixational eye movement is rather erratic but certainly not without any constraint, since the eye displacement is fluctuating around the horizontal and vertical zero lines (Fig. 2bc), and the trajectory seems to have an attraction near the fovea too (Fig. 2a). The eye position scatter (Fig.4) has a disc-like distribution with an outskirt in the upper field. The widths of the position distributions in both the horizontal and vertical axes measured by MAD are 0.1 deg and 0.15 deg respectively. These are consistent with the existent data on the scatter of fixation positions (Barlow, 1952; Snodderly & Kurtz, 1985).

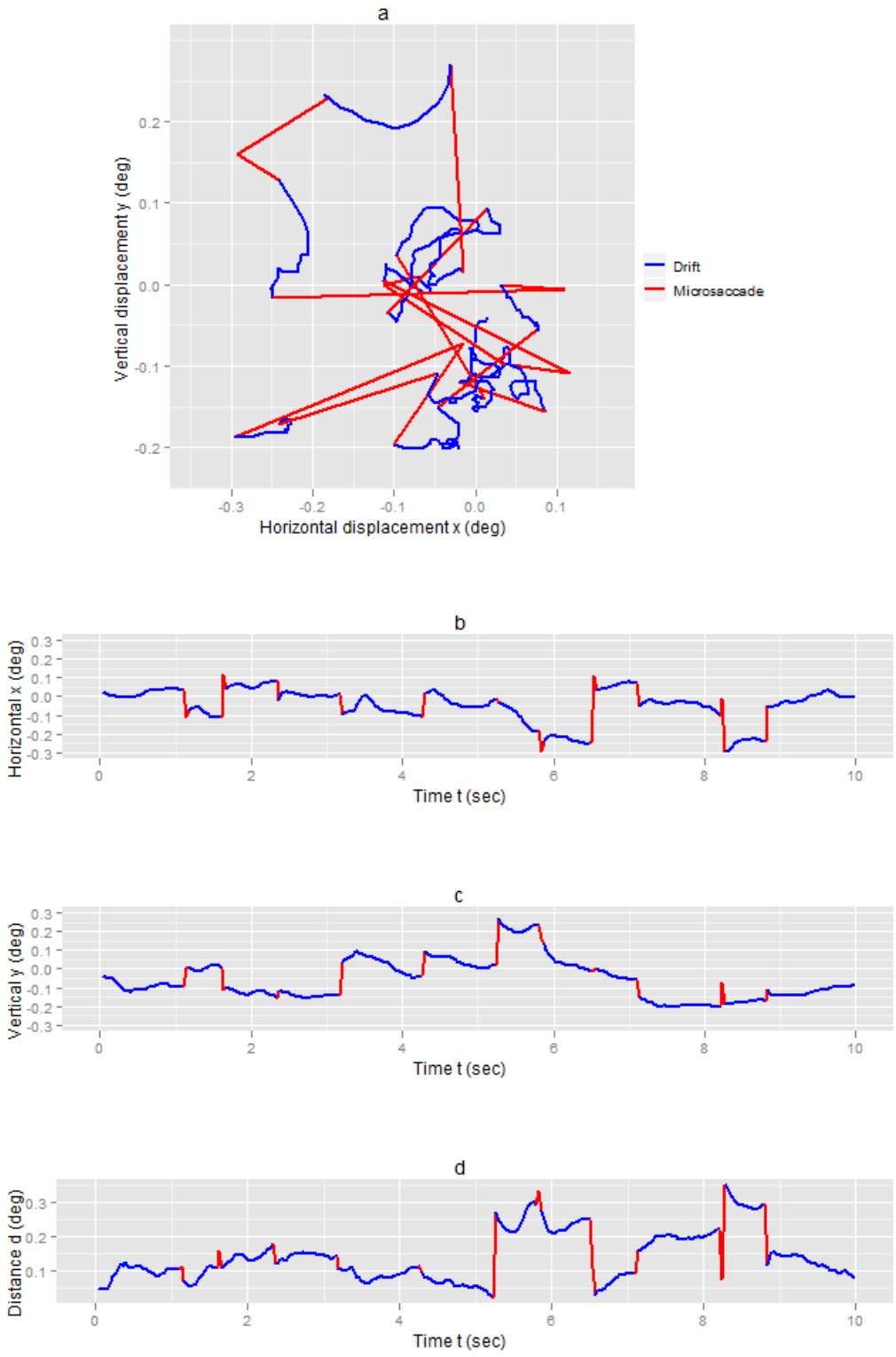

Fig. 2. A 10-second fixational eye movement sample from the preferred eye of the normal subject DR. a) Two-dim trajectory. b) Horizontal displacement x vs. time t. c) Vertical displacement y vs. time t. d)

Euclidian distance d from the fixation vs. time t. Blue and red traces are drifts and microsaccades respectively.

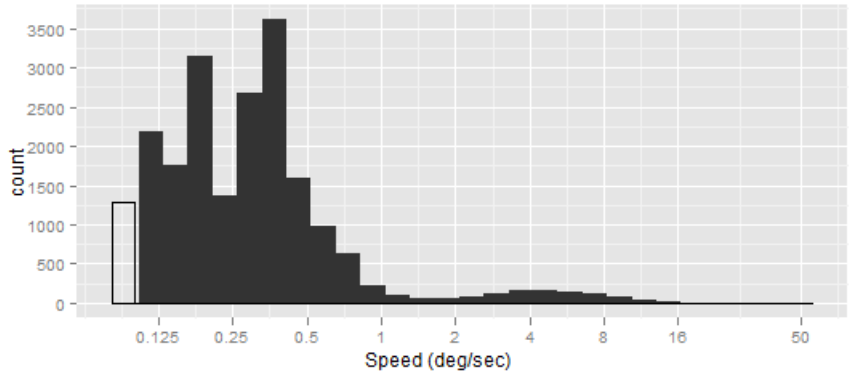

Fig. 3-1. Empirical distribution of speed magnitude ω (deg/sec) during the normal eye's fixation on a logarithmic axis. The unfilled bar on the left represents number of data points with zero speed. $Median\ (\omega)$=0.28 deg/sec, $MAD(\omega)$ = 0.16 deg/sec.

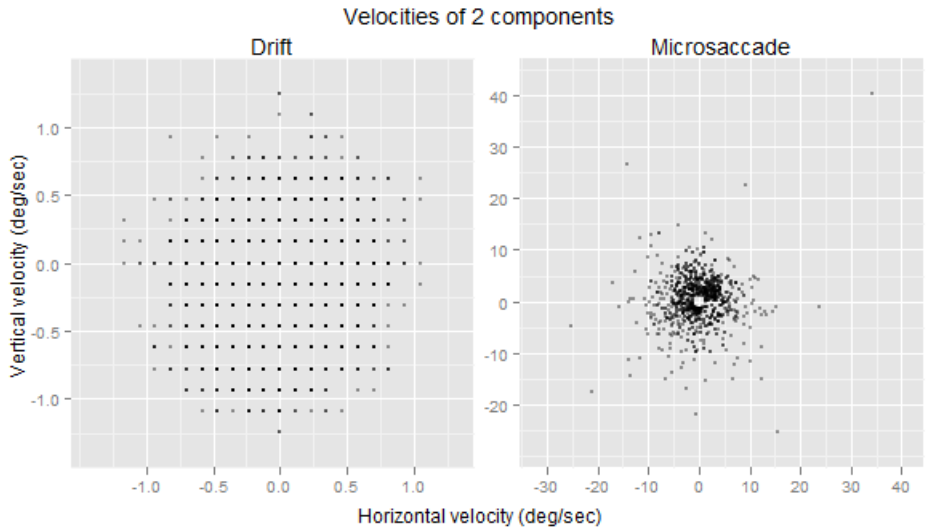

Fig. 3-2. Two-dimensional empirical distributions of drifts' and microsaccades' velocities for the normal eye. The threshold speed for detecting microsaccades is 1.244 deg/sec. Both drift and microsaccade velocities are roughly symmetrically distributed around the origin, except that the microsaccade velocities are denser in the 1st and 3rd quadrants and relatively sparse in the 4th quadrant.

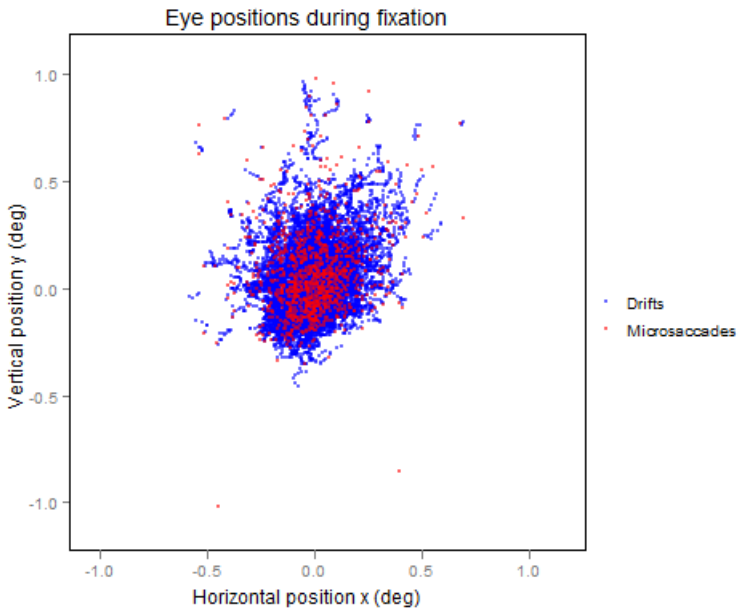

Fig. 4 Eye positions for drifts (blue) and microsaccades (red) during the normal eye's fixation. Both components' positions are approximately symmetrically distributed about both axes, but there is a bias in the upper field. $MAD(x)$ = 0.10 deg, $MAD(y)$ = 0.15 deg.

3.1.2 Microsaccades

Fig.5 summarizes the relation between microsaccade and fixation position, and reveals the role of microsaccades on fixation accuracy. Fig.5b shows that *on average*, the signed magnitude of microsaccades (i.e. $\Delta d > 0$ means error producing, and $\Delta d < 0$ means error correcting) is not significantly different from zero. However, it is incorrect to draw the conclusion that microsaccades did not play any role in maintaining fixation accuracy, because microsaccades are separated by drifts and therefore discontinuous. We give a simple example here. Suppose a microsaccade moves from position 1 to 0.3, and another microsaccade moves from position 0 to 0.7, then the average distance moved would be zero $(0.3 - 1 + 0.7 - 0 = 0)$ if we don't take positions into account. However the eye position has been moved from 1 to 0.7, i.e., it is closer to the origin by 0.3 after two microsaccades. Along the same line, we compared the starting distances of the error-correcting microsaccades and the ending distances of the error-producing microsaccades. Fig. 5c shows that indeed they come from 2 different distributions and the mean value of the starting distances of the error-correcting microsaccades is significantly greater than that of the ending distances of the error-producing microsaccades ($\overline{\Delta d'} = 0.09\ deg, SE(\Delta d') = 0.01$ deg). Previous studies implied that the trend of microsaccades is to move the fixation towards the target, but did not quantitatively characterize the shift of the eye position (Cornsweet, 1956; Ditchburn & Ginsborg, 1953). Our result confirms that on average microsaccades corrects for fixation inaccuracy.

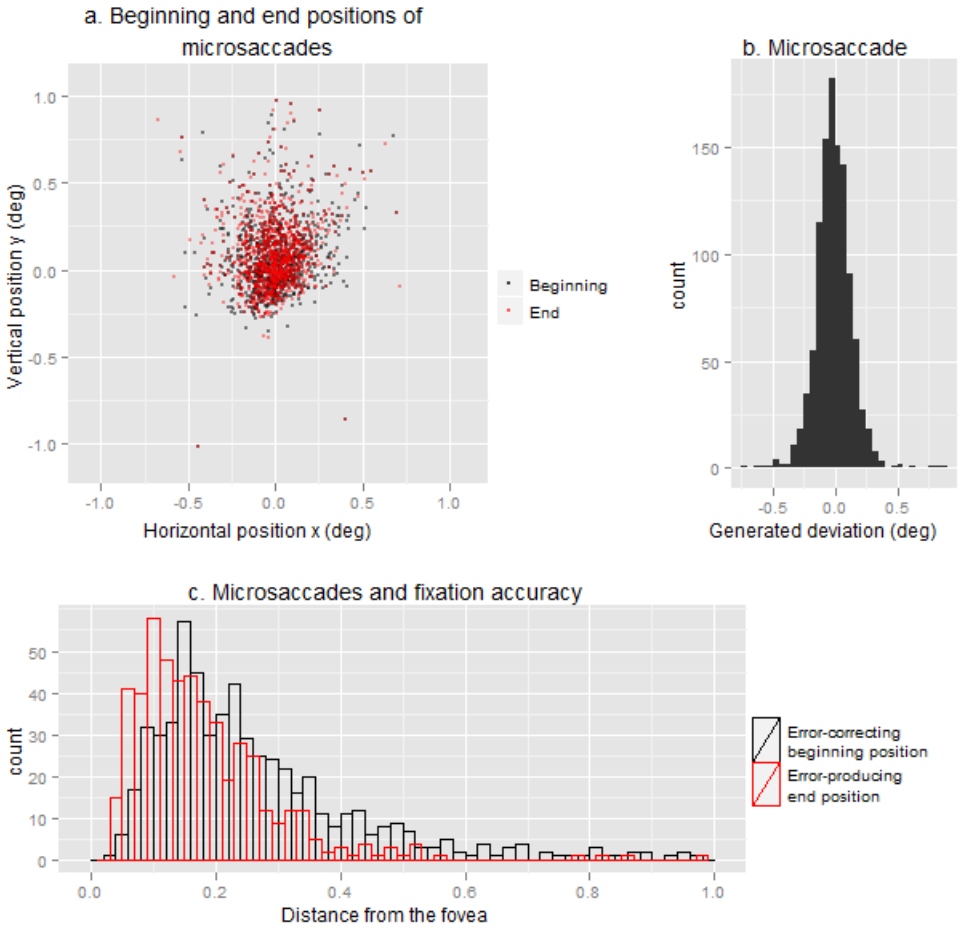

Fig. 5. Overview of microsaccades for the normal eye. a) Eye positions at the beginning (red) and the end (black) of microsaccades. b) Histogram of the fixation deviation from the fovea generated by a microsaccade, i.e., difference of the distance between the eye position and the fovea before and after a microsaccade. $\overline{\Delta d} = d_{end} - d_{start} = -0.006$, $SE(\widehat{\Delta d}) = 0.004$. c) Histograms of the error-correcting microsaccade' beginning position $d_{correct\ ,start}$ (black) and the error-producing microsaccades' end position $d_{error\ ,end}$ (red). $\overline{\Delta d'} = \bar{d}_{correct\ ,start} - \bar{d}_{error\ ,end}$ = 0.09 deg, $SE(\Delta d')$ = 0.01 deg.

3.1.2.1 Potential function of microsaccades

As explained in Methods, although the collection of microsaccades is not a continuous process, they can be characterized by the same potential function with noise approach. What distinguishes it from a stochastic process is the lack of a time variable in the model for microsaccades.

The empirical vector field of microsaccades' velocities is plotted in Fig.6a. The starting positions of all microsaccades are binned in small squares on the two-dimensional map, and within each bin the average velocity is represented by an arrow in the same direction and

properly scaled magnitude. From Fig. 6a, we see the trend of microsaccades pointing towards the fovea, which is better revealed by the smoothed velocity field of microsaccades (Fig. 6b). The potential function is assumed to have a quadratic form, and its gradient functions are then fitted to the velocity field (Eq. 10 ~ 12) using OLS. The reversal of the fitted potential function, $\hat{V}(x, y) \widehat{=} 1.09y - 7.89x^2 - 4.44y^2$, is graphed in Fig.7, and the predicted and residual velocity fields are plotted in Fig.8. The residuals on the upper border of the field tend to point outward, implying the somewhat over-fit of the quadratic function at large displacements above the fovea. The bowl-shaped potential function in Fig. 7 demonstrates the average dependence of a microsaccade on eye position. Intuitively, the microsaccadic eye movement can be thought as corresponding to a ball moving in a bowl, under an overdamped physical condition (i.e. large friction case). Just like a ball moving back towards the center is driven by greater force from near the edge, a microsaccade initiated at a relatively large displacement is more likely to be directed towards the fovea and has larger speed.

Model: $V(x, y) = \beta_0 + \beta_1 x + \beta_2 x^2 + \beta_3 y + \beta_4 y^2 + \beta_5 xy$

Coefficients	Estimate	Std. Error	t value	# Pr(>|t|)
β_1	-0.1296	0.1263	-1.026	0.305
β_2	1.0901	0.1291	8.441	<2e-16 ***
β_3	-7.8929	0.3928	-20.096	<2e-16 ***
β_4	-4.4391	0.2996	-14.814	<2e-16 ***
β_5	0.4092	0.4804	0.852	0.395
			Signif. codes:	0 '***' 0.001 '**' 0.01 '*' 0.05 '.' 0.1 ' ' 1
Multiple R^2	0.2276			
Adjusted R^2	0.2258			

Table 5. Summary of the microsaccade potential function regression for the normal eye. # Assuming independent identical distributed (i.i.d.) errors.

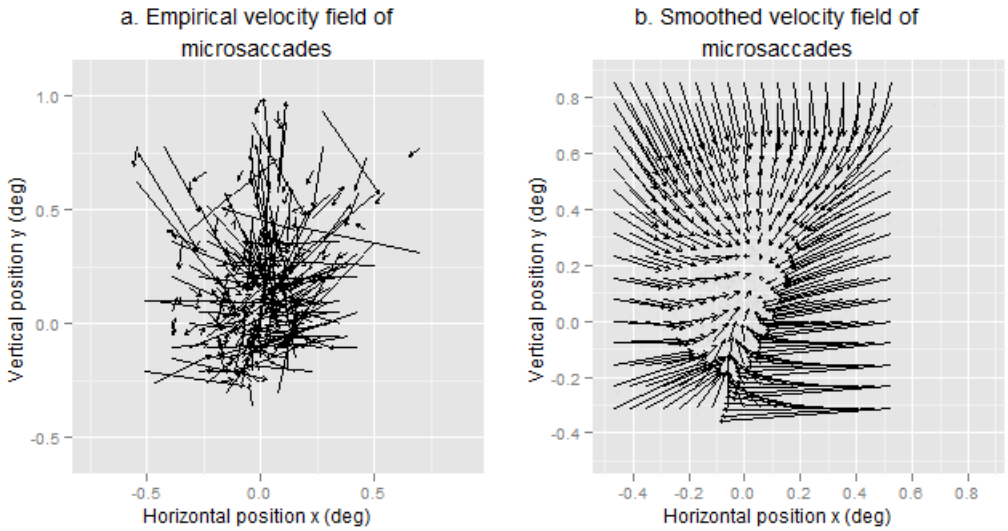

Fig. 6. a) Empirical and b) smoothed velocity fields of microsaccades of the normal eye. Each arrow represents the averaged velocity of microsaccades in a small bin. The beginning position of each arrow is absolute, whereas the end position (i.e. arrow head) and the length of the arrow may be scaled. The smoothed velocities are predicted by the semi-parametric spline smoothing of degree 4.

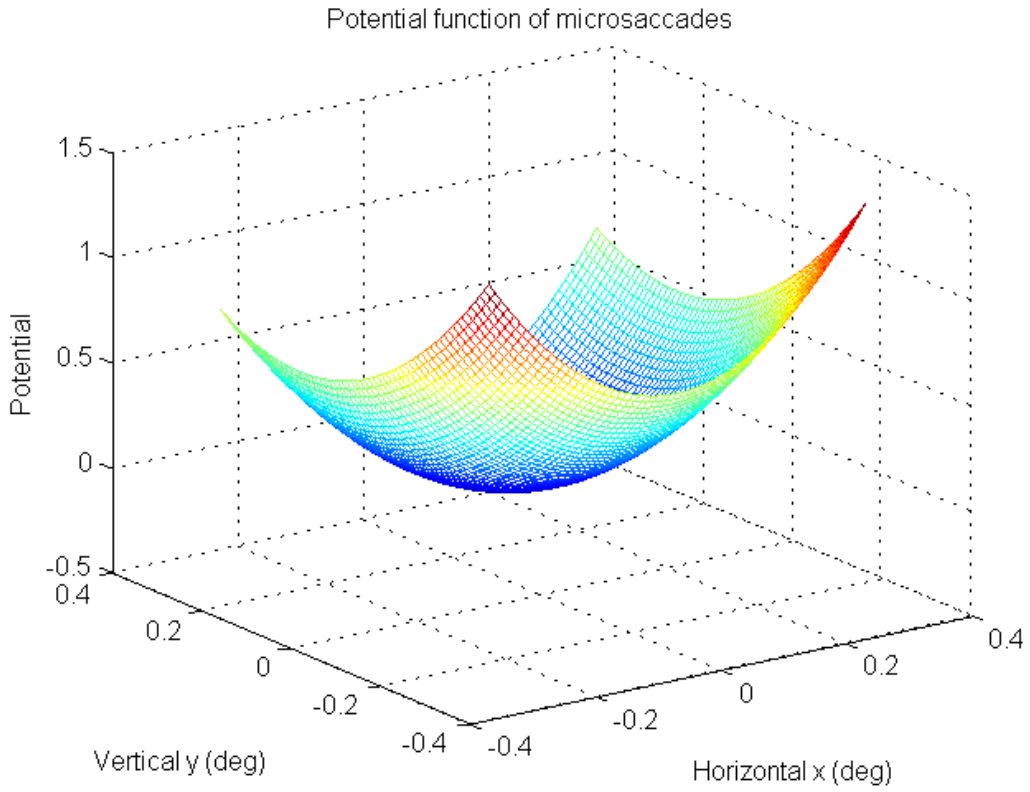

Fig. 7. Reversed potential function of microsaccades for the normal eye, $V(x,y) = 1.09y - 7.89x^2 - 4.44y^2$. The potential function is shifted to have zero intercept.

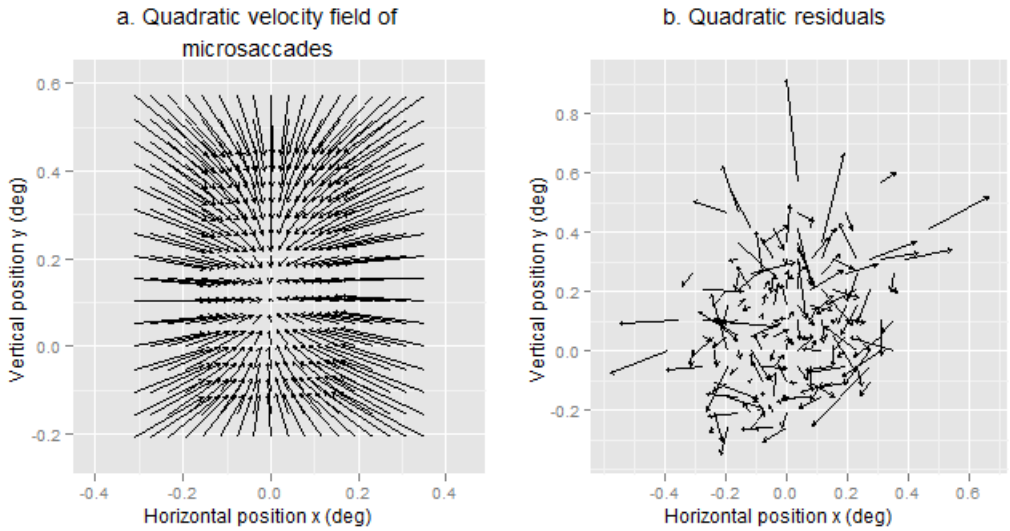

Fig. 8. a) Microsaccades' velocity field predicted by the fitted quadratic potential function for the normal eye, and b) the corresponding residual velocity field. The full model including all terms, regardless of statistical significance, is used.

The standard deviations of binned microsaccades at different locations are used as estimates of microsaccade velocity variability (i.e. noise, or randomness that cannot be predicted by the potential function) at different fixation positions in both horizontal and vertical directions (Fig. 9). We see that velocity deviation doesn't vary much over location, especially when compared to microsaccades' velocity range (1.244 ~ 52.8 deg/sec). We will therefore assume constant variance over location for microsaccade velocity. This variance can be estimated in several ways including from the empirical velocity deviation shown in Fig. 9. In particular, the estimates given by the fitted residuals of the potential function are: $\hat{\sigma}_x = \sqrt{\frac{RSS_x}{df}} =$ 3.80 deg/sec, $\hat{\sigma}_y = \sqrt{\frac{RSS_y}{df}} =$ 4.19 deg/sec, where RSS stands for residual sum of squares, and df is the residual degree of freedom.

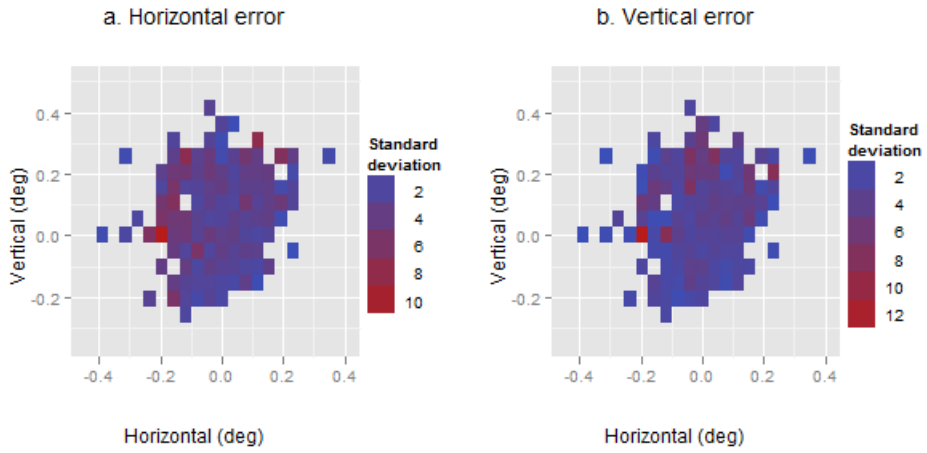

Fig. 9. Microsaccade a) horizontal and b) vertical velocity deviation vs. location for the normal eye. The velocity deviations are estimated directly from the standard deviations of the sample.

3.1.2.2 Poisson process modeling of microsaccades

We have studied the spatial properties of microsaccades using the potential function approach. The temporal properties of microsaccades are completely different from those of drifts because microsaccades are points "randomly" scattered in fixational eye movement time series. The Poisson point process may be a suitable model for the probability of the occurrence of a microsaccade as a function of time.

We know that a Poisson process with constant rate λ has exponentially distributed interval lengths (Eq 14). The histogram of all inter-microsaccade time intervals (without any bad frames) (Fig. 10-1a) and the corresponding *log-log* plot (Fig.10-1b) show that the highest frequency (i.e. density) is near 0.33 sec. Intervals longer than 0.33 sec are approximately exponentially distributed whereas intervals shorter than 0.33 sec are too infrequent for an exponential distribution. A mixture model with various rates from different locations cannot explain this result because the sum of monotonically decreasing models is also monotonically decreasing, which is not the case for inter-microsaccade intervals (Fig. 10-1ab). Instead, there seems to exist a 0.33 sec "refractory period" following a microsaccade, during which the next microsaccade occurs with relatively small probability. Beyond this refractory period, the occurrence of microsaccades is approximately a Poisson Point Process, i.e., within any short time interval a microsaccade occurs with approximately equal probability.

To examine the rates from different locations for microsaccades that are separated by 0.33 sec or longer intervals, the space domain (x-y coordinate of the eye positions) of fixational eye movement is divided into a set of rings that have equal width and are at different radial distances from the fovea. Each complete inter-microsaccade sequence is labeled in the way such that it belongs to only one subgroup (i.e. ring). Within each subgroup, logarithms of the

inter-microsaccade interval's empirical density function are fitted by a straight line, and then scaled and shifted to have -1 slope and zero intercept. As a consequence, the transformed data points (i.e. *log-log* frequency vs. interval length) lie along the line $y = -x$ (Fig. 10-2). We see that by taking into account of location variable (i.e. distance from the origin, data transformation from Fig. 10-2a to Fig. 10-2b) the linear relationship between *log* frequency and *log* interval length has improved. This result suggests that location is a significant factor that affects microsaccade rate.

Although the refractory period implies the existence of some dependence on the short time scale between microsaccades, we will assume that on average the occurrence of microsaccades can be approximated by a Poisson Process. It is easy to estimate microsaccade rate as a function of location, due to the equal distance sampling of fixational eye movement in time. Since each point represents the same time interval length (i.e. 0.033 sec), a properly scaled ratio of microsaccade's empirical two-dimensional density function to the sum of those for both microsaccade and drift is the map of the Poisson process model parameter (i.e. microsaccade rate λ, Fig. 11). Fig. 11 shows that the microsaccade rate (i.e. proportional to the probability of the occurrence of a microsaccade within a short time interval) does depend on location. In particular, a microsaccade is less likely to occur from near the fovea than it is when deviated from the fovea. For this subject DR, microsaccade rate is especially high in the upper field. The mean rate of microsaccade for the normal eye is 1.58 /sec.

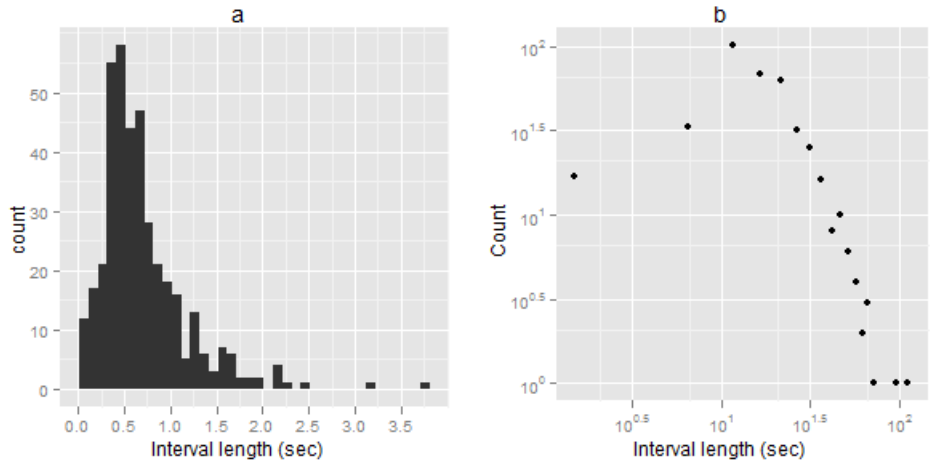

Fig. 10-1. a) Histogram of inter-microsaccade interval length for the normal eye. The peak of the histogram is near 0.33 sec. For intervals longer than 0.33 sec, the number of intervals decreases approximately exponentially as the interval length increases. b) *Log-log* plot of a). For intervals longer than 0.33 sec, *log* frequency decreases approximately linearly with *log* interval length.

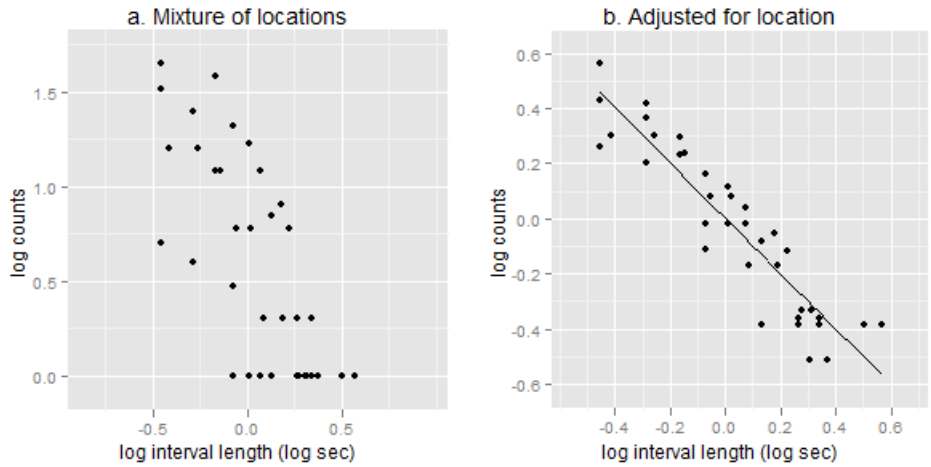

Fig. 10-2. For inter-microsaccade intervals of lengths greater than 0.33 sec only, a) mixture of *log* inter-microsaccade interval counts vs. *log* interval length for different eye positions of the normal eye. b) Adjusted *log* inter-microsaccade interval counts vs. *log* interval length for the normal eye. Each complete inter-microsaccade interval is classified into one of the subgroups that are at different radial distances from the fovea. Within each subgroup logarithms of interval counts are rescaled and shifted such that *log* inter-microsaccade interval counts vs. *log* interval length has slope -1 and zero intercept. The line $y = -x$ is the regression line for all data points in b). The transformation of data from a) to b) has at least partly adjusted for location.

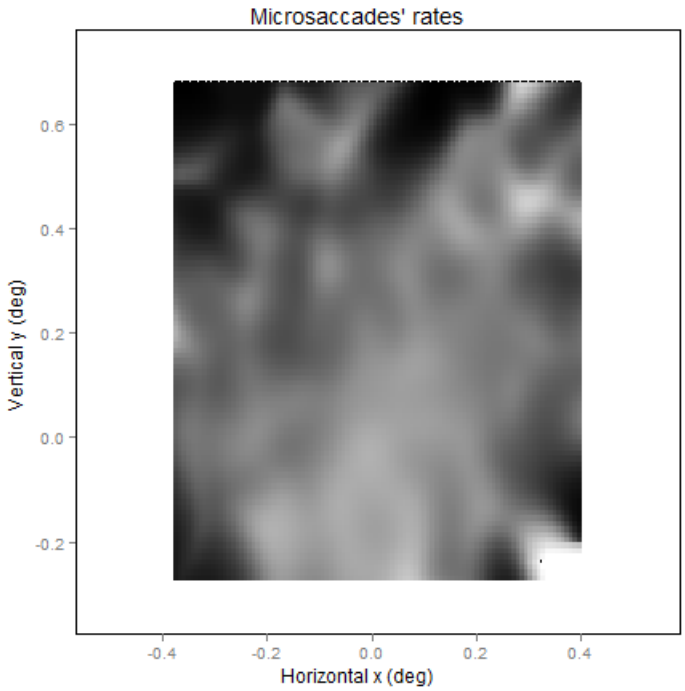

Fig. 11. Microsaccade rate map for the normal eye. Dark and bright pixels represent high and low rates respectively. Microsaccade rates are relatively low near the fovea and high at positions farther away from the fovea. The average microsaccade rate is 1.58/sec for the normal eye.

3.1.3 Drifts

A similar stochastic model with potential function approach will be applied to characterize drifts. However, unlike microsaccades, drifts are continuous movements within each inter-microsaccade interval. Since drifts may be time-variant within an inter-microsaccade interval, the potential function may depend on time.

3.1.3.1 Random walk model assumptions

Before approximating the fixational eye movement component, drift, by a diffusion, we need to check the Markov property and the normal assumption. Markov property means that for a random process, the likelihood of a future state depends on the present state only, not on any past states. Here, a state is defined to be the eye position (x, y), and it is equivalent to check that drifts have independent increments (scaled velocities).

The autocorrelation functions (ACFs) of drifts' velocities show no significant correlation at any non-zero lag in the vertical direction and two statistically significant but small correlations at lags 1 and 2 in the horizontal direction (Fig. 12). With some approximation, we will assume the velocities to satisfy the independence assumption, and assume the Markov property of

drifts.

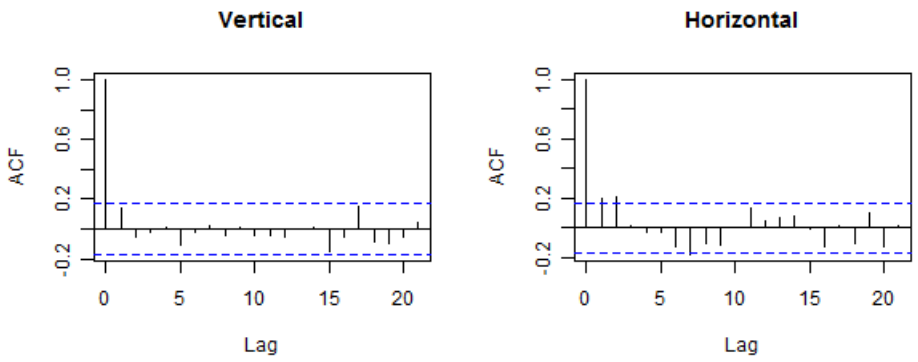

Fig. 12. Autocorrelation functions (ACF) of horizontal and vertical drifts' increments (i.e., scaled velocities) for the normal eye. Blue dashed lines denote borders of the 95% confidence intervals in both directions. X-axis is the time lag in integer, i.e., number of frames. Each unit (frame) represents 30 ms.

A diffusion process has normally distributed infinitesimal increments at any given time. Fig. 13 shows that drifts' velocities indeed can be approximated by Gaussian distributions. However, since we do not assume time or location invariance here, we further checked the velocity distributions at different times (following a microsaccade, see Methods) and locations (Appendix 1A). We consider that the normality assumption holds for all these conditions.

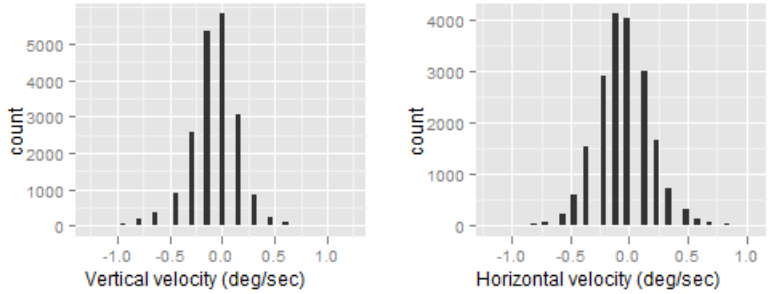

Fig. 13. Histograms of horizontal and vertical velocities of drifts for the normal eye. Both histograms show Gaussian-like shapes.

3.1.3.2 Potential function for drifts

Following a microsaccade, the average trajectory of drifts demonstrates a bias in the downward and leftward direction (Fig. 14-2), i.e. at any given time t, the expected velocity of a drift is non-zero, $E[dr(t)] \neq 0$. By examining the relative smooth trace composed of larger samples (n > 100, black), we see that the trajectory is not a straight line. In particular, the increments that immediately follows a microsaccade differ from the rest in both direction and speed magnitude (i.e. segment length). This observation suggests that drift is time variant.

Furthermore, this time-inhomogeneity is only partly reflected by the drift trajectory averaged over location in Fig. 14-2, because the interaction between time and space, i.e. the shape of the potential function assumed to depend on (x, y, t), may be more important.

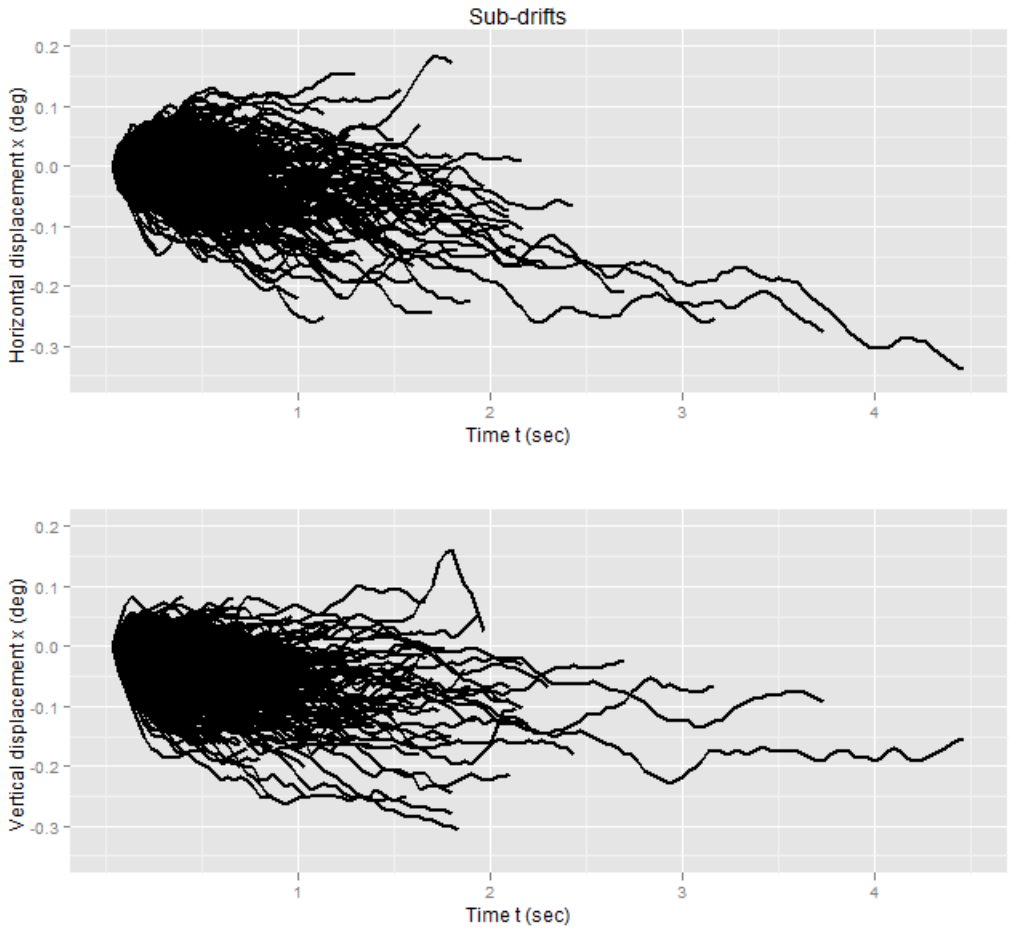

Fig. 14-1. Sub-drifts' displacements vs. time (following microsaccades) in horizontal and vertical directions for the normal eye (see Methods).

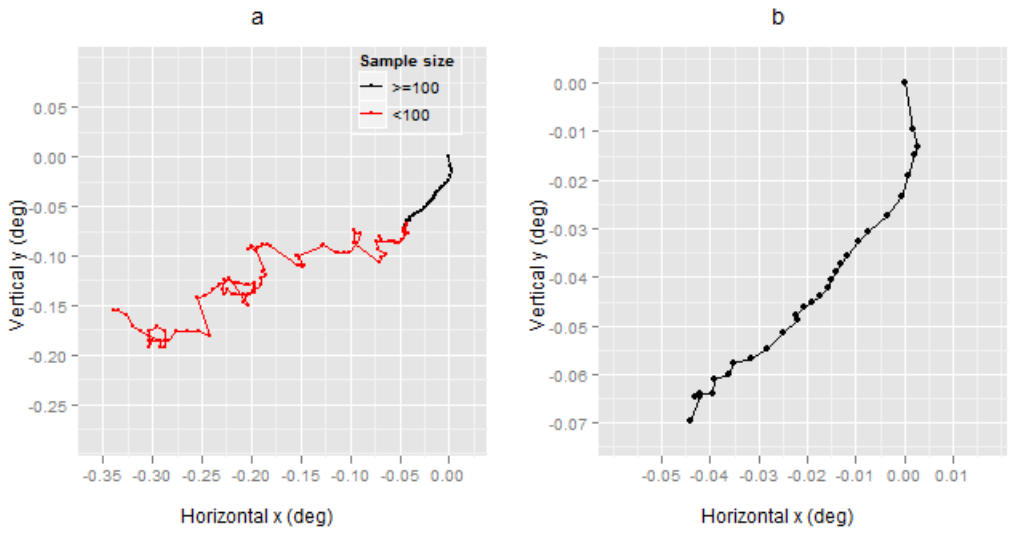

Fig. 14-2. Average trajectory of sub-drifts of a) any sample size or of b) only large sample size (i.e. greater than 100), for the normal eye. Black and red traces denote sample sizes greater than or less than 100 respectively. The trajectory starts at **0** since the position of the first point is subtracted from all points (see Methods).

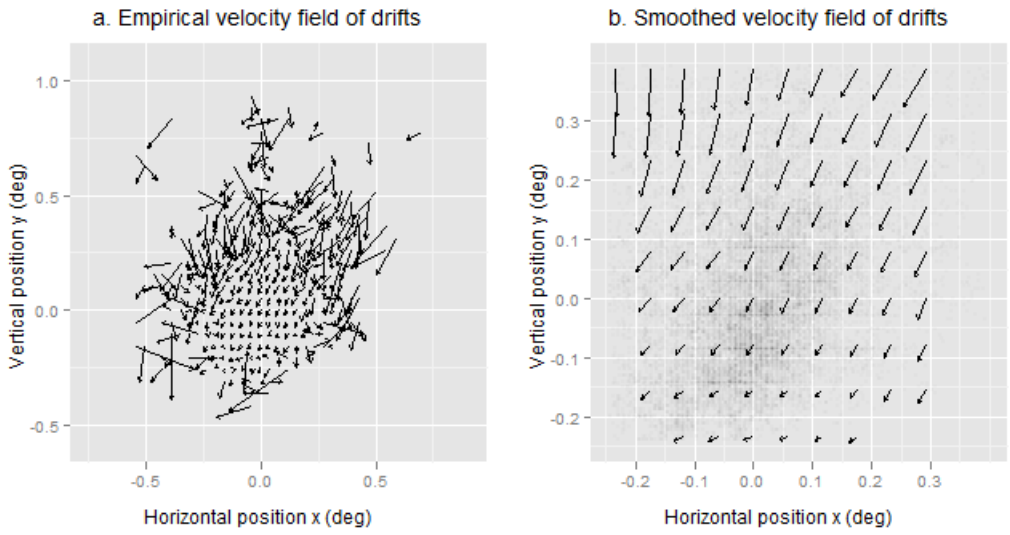

Fig. 15. a) Empirical and b) smoothed velocity fields of the drift for the normal eye. Each arrow represents the averaged velocity of drifts in a small bin. The beginning position of each arrow is absolute, whereas the end position (i.e. arrow head) and the length of the arrow may be uniformly scaled. The smoothed velocities are predicted by the semi-parametric spline smoothing of degree 4. Eye positions of original data are scattered as semi-transparent points in the smoothed velocity field.

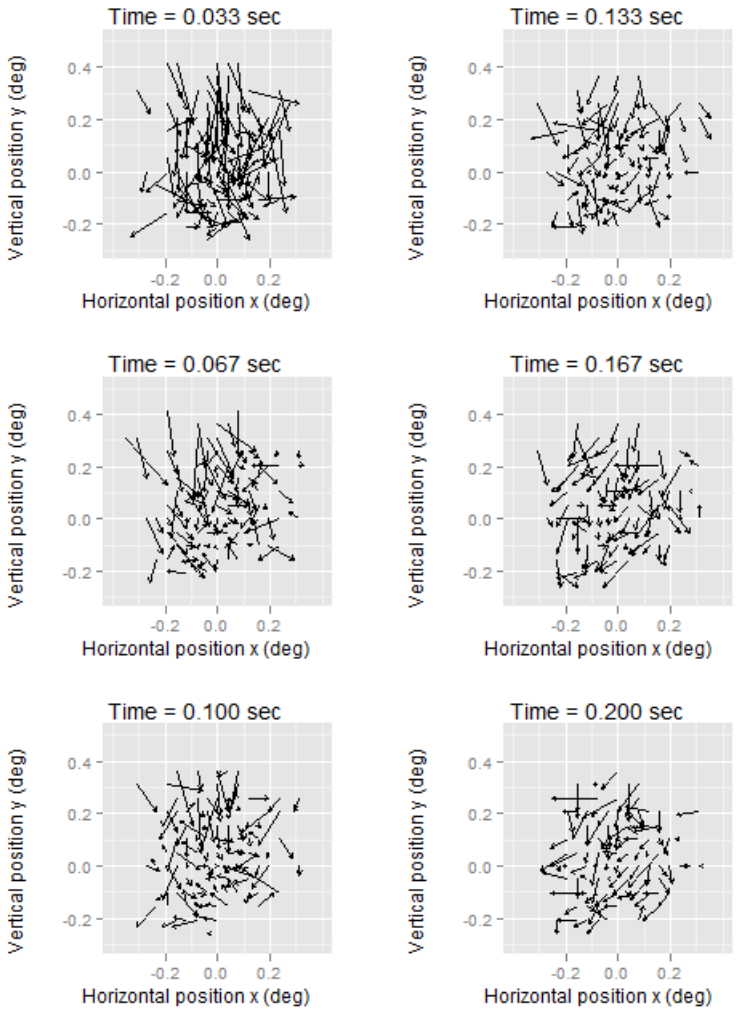

Fig. 16-1. Drift's empirical velocity fields at different times (following a microsaccade) for the normal eye. Each arrow represents the averaged velocity of drifts in a bin with small widths. The beginning position of each arrow is absolute, whereas the end position (i.e. arrow head) and the length of the arrow may be uniformly scaled.

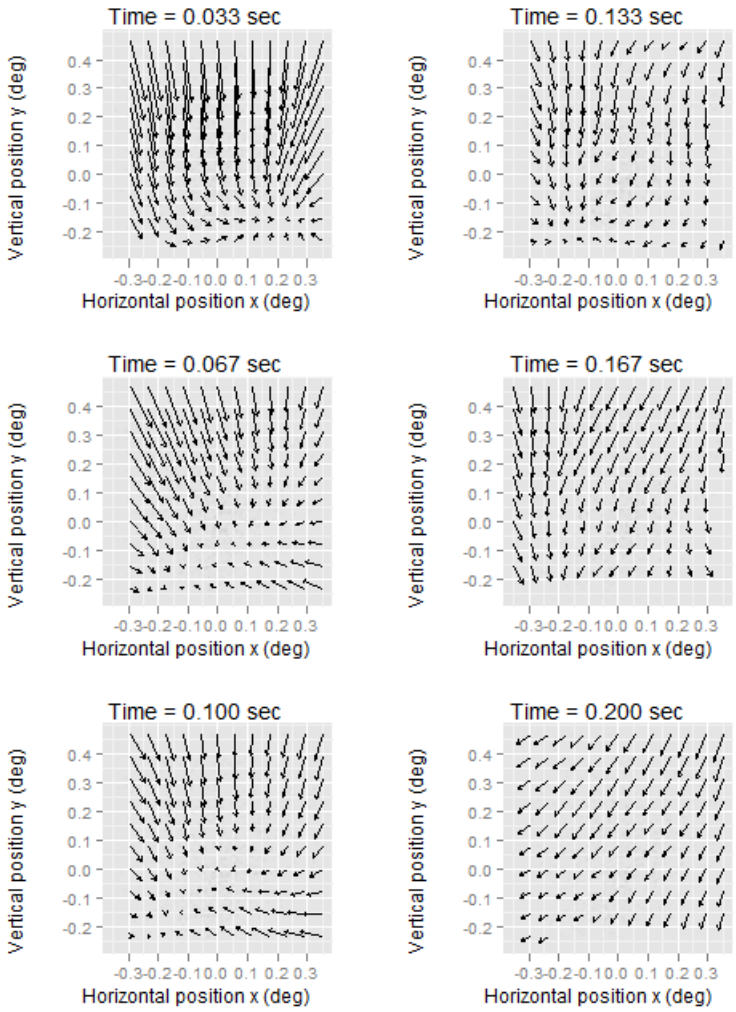

Fig. 16-2. Drift's smoothed velocity fields at different times (following a microsaccade) for the normal eye. The smoothed velocities are predicted by the semi-parametric spline smoothing of degree 4.

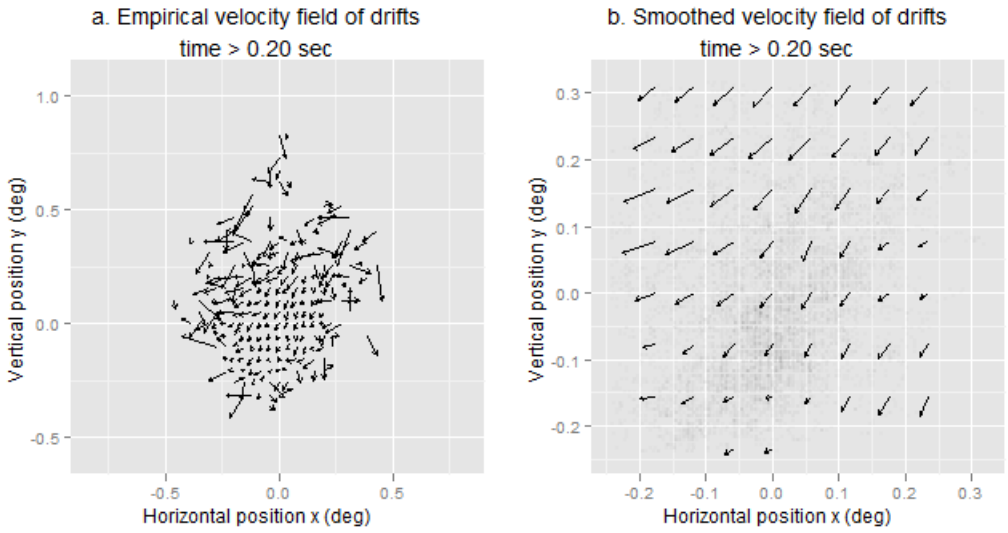

Fig. 16-3. a) Empirical and b) smoothed velocity fields of the drift after 0.20 sec following a microsaccade for the normal eye. Each arrow represents the averaged velocity of drifts in a small bin. The beginning position of each arrow is absolute, whereas the end position (i.e. arrow head) and the length of the arrow may be uniformly scaled. The smoothed velocities are predicted by the semi-parametric spline smoothing of degree 4. Eye positions of original data are scattered as semi-transparent points in the smoothed velocity field.

The empirical velocity field of drift averaged over time doesn't show any centric pattern. Instead, drifts at all positions seem to move downwards and leftwards at various speeds (Fig. 15). As suggested by Fig. 14, we suspect that time (following a microsaccade) may be a missing variable in Fig.15 that shows a mixture of models. To clarify this question, we explored the time effect on the drift potential function by calculating both empirical and smoothed velocity fields at different times (Fig. 16-1).

Immediately following a microsaccade, drifts, especially those from the lateral or nasal side of the fovea, are attracted towards somewhere below the fovea. As time increases, the leftward movement in the velocity field becomes more prominent, whereas the point of attraction disappears (Fig. 16). The gradients of the quadratic potential functions are fitted to drift velocities at different times (Fig. 17). The regression parameters are summarized in table 6. We see that within 0.1 sec following a microsaccade, the reversed potential functions are curved surfaces with global minimums (i.e. attraction points), whereas after 0.833 sec, the potential function is just a plane, These results suggest that drift does correct for fixation errors to some extent at the beginning for a short period of time, but becomes simple Brownian motion with constant rate at longer time lags after a microsaccade, which will eventually inevitably increase fixation inaccuracy. The residuals shown in Fig. 18-2 are rather random and lack any pattern, suggesting that the potential function models are good at capturing the trends in the drift velocity fields for the normal eye. Some earlier studies found no correlation between fixation displacement and the direction or amplitude of drifts and concluded that drifts are not under

visual control (Cornsweet, 1956); others discovered the slow control of fixation stability by drifts from the fact that an observer can learn to suppress microsaccades while still maintain accurate fixation (Kowler & Steinman, 1979; Steinman et al., 1973). Our results suggest that the seeming randomness of drifts may be due to the fact that the centric structure of the drift potential function only lasts for a short period of time following a microsaccade; hence its error-correcting ability is not shown when averaged over time (Fig. 16). Moreover, the voluntary slow control by drifts could act on the length of the time interval during which drift potential functions achieve points of attraction.

Model: $V(x,y) = \beta_0 + \beta_1 x + \beta_2 x^2 + \beta_3 y + \beta_4 y^2 + \beta_5 xy$

Time =1

Coefficients	Estimate	Std. Error	t value	Pr(>|t|)
β_1	0.04676	0.01419	3.296	0.001009 **
β_2	-0.22304	0.01456	-15.324	< 2e-16 ***
β_3	-0.17490	0.04711	-3.712	0.000214 ***
β_4	-0.42603	0.03590	-11.868	< 2e-16 ***
β_5	0.02027	0.05721	0.354	0.723151

Signif. codes: 0 '***' 0.001 '**' 0.01 '*' 0.05 '.' 0.1 ' ' 1

Multiple R^2	0.3323
Adjusted R^2	0.3296

Time =2

Coefficients	Estimate	Std. Error	t value	Pr(>|t|)
β_1	0.009359	0.010794	0.867	0.386
β_2	-0.075774	0.011014	-6.880	9.57e-12 ***
β_3	-0.196564	0.036810	-5.340	1.11e-07 ***
β_4	-0.269220	0.028671	-9.390	< 2e-16 ***
β_5	0.251318	0.045372	5.539	3.72e-08 ***

Signif. codes: 0 '***' 0.001 '**' 0.01 '*' 0.05 '.' 0.1 ' ' 1

Multiple R^2	0.1707
Adjusted R^2	0.1673

Time =3

Coefficients	Estimate	Std. Error	t value	Pr(>|t|)
β_1	-0.02430	0.01052	-2.309	0.021093 *
β_2	-0.04028	0.01071	-3.762	0.000177 ***
β_3	-0.15674	0.03730	-4.202	2.84e-05 ***
β_4	-0.23829	0.02859	-8.335	< 2e-16 ***
β_5	0.16688	0.04557	3.662	0.000262 ***

			Signif. codes:	0 '***' 0.001 '**' 0.01 '*' 0.05 '.' 0.1 ' ' 1
Multiple R^2	0.104			
Adjusted R^2	0.1003			

Time =4

Coefficients	Estimate	Std. Error	t value	Pr(>|t|)
β_1	-0.038612	0.009993	-3.864	0.000118 ***
β_2	-0.100925	0.010158	-9.935	< 2e-16 ***
β_3	-0.056105	0.036181	-1.551	0.121254
β_4	-0.175016	0.027420	-6.383	2.50e-10 ***
β_5	0.023931	0.043912	0.545	0.585882
			Signif. codes:	0 '***' 0.001 '**' 0.01 '*' 0.05 '.' 0.1 ' ' 1
Multiple R^2	0.1545			
Adjusted R^2	0.1509			

Time =5

Coefficients	Estimate	Std. Error	t value	Pr(>|t|)
β_1	-0.050795	0.009801	-5.183	2.58e-07 ***
β_2	-0.128660	0.009936	-12.949	< 2e-16 ***
β_3	-0.025857	0.036182	-0.715	0.475
β_4	-0.108837	0.027373	-3.976	7.45e-05 ***
β_5	-0.003460	0.043861	-0.079	0.937
			Signif. codes:	0 '***' 0.001 '**' 0.01 '*' 0.05 '.' 0.1 ' ' 1
Multiple R^2	0.1857			
Adjusted R^2	0.1821			

Time =6

Coefficients	Estimate	Std. Error	t value	Pr(>|t|)
β_1	-0.086430	0.009599	-9.004	<2e-16 ***
β_2	-0.108571	0.009711	-11.181	<2e-16 ***
β_3	0.046479	0.035807	1.298	0.1945
β_4	-0.061111	0.027660	-2.209	0.0274 *
β_5	-0.072400	0.043963	-1.647	0.0999 .
			Signif. codes:	0 '***' 0.001 '**' 0.01 '*' 0.05 '.' 0.1 ' ' 1
Multiple R^2	0.1814			
Adjusted R^2	0.1778			

Table 6. Summary of the drift potential function regressions at different times (following a microsaccade) for the normal eye.

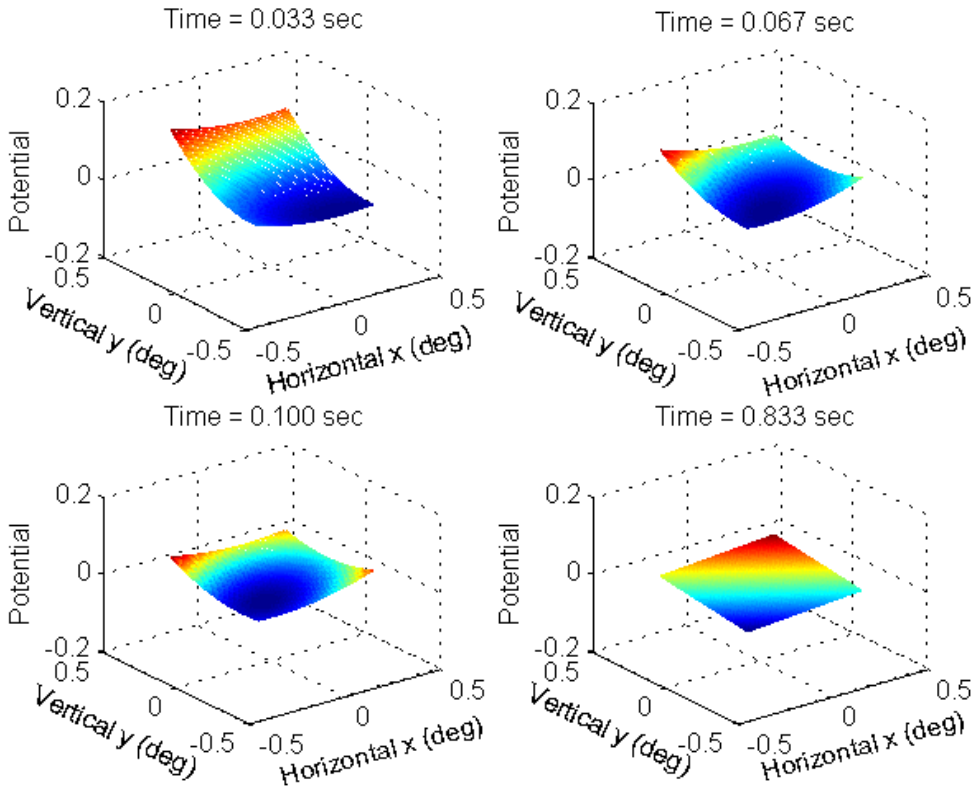

Fig. 17. Reversed potential functions of the drift at different times following a microsaccade for the normal eye. $V(x, y, t = 0.033) = 0.05x - 0.22y - 0.17x^2 - 0.43y^2$; $V(x, y, t = 0.067) = -0.08y - 0.20x^2 - 0.27y^2 + 0.25xy$; $V(x, y, t = 0.100) = -0.02x - 0.04y - 0.16x^2 - 0.24y^2 + 0.17xy$; $V(x, y, t = 0.833) = -0.04x - 0.05y$. Only statistically significant terms are included in above models and the graphs. All potential functions are shifted to have zero intercepts.

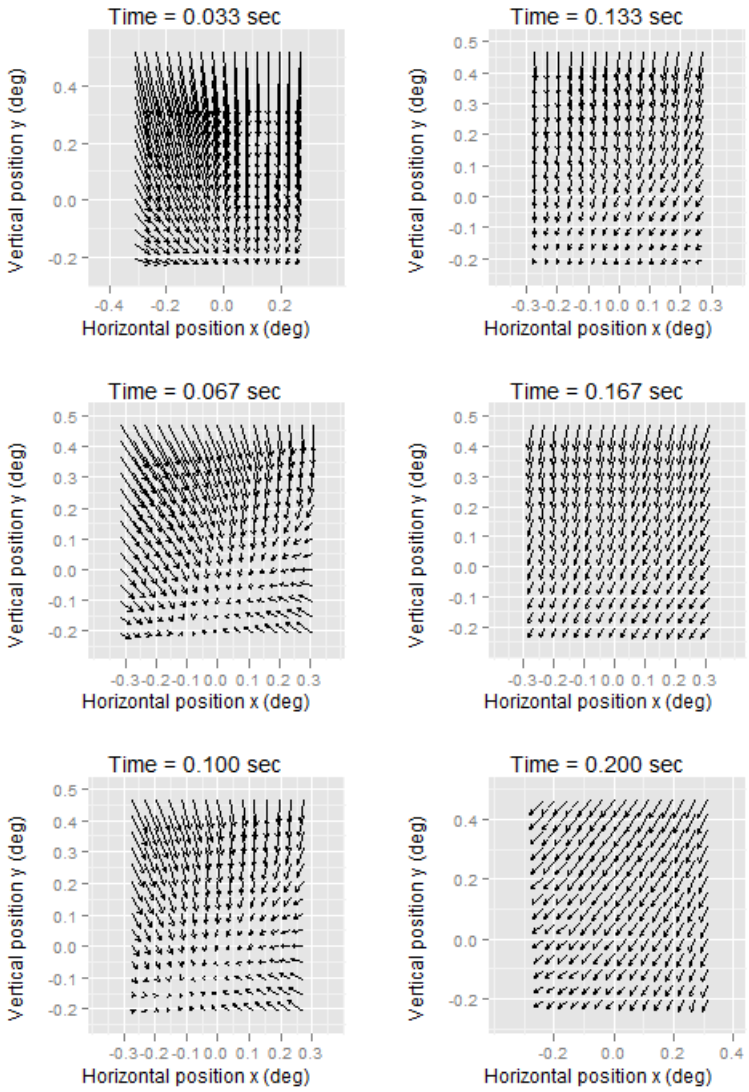

Fig. 18-1. Drift velocity fields at different times following a microsaccade predicted by fitted quadratic potential functions (Fig. 17) for the normal eye. The full model including all terms, regardless of statistical significance, is used.

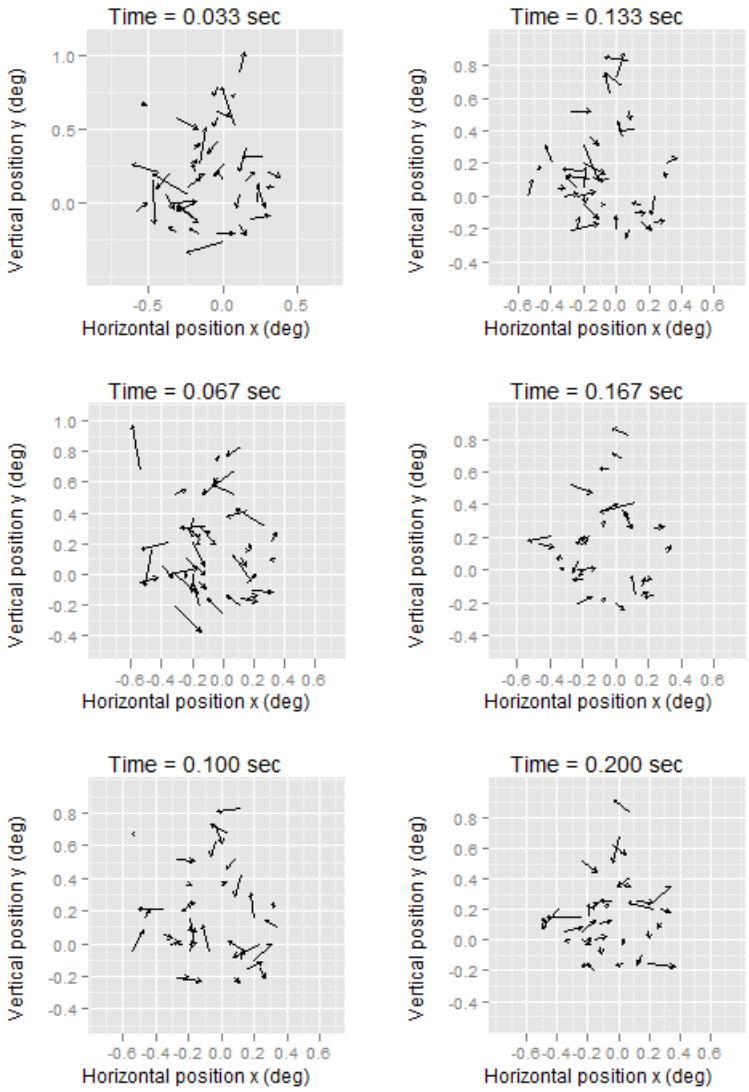

Fig. 18-2. Drift residual velocity field after the fitting of quadratic potential functions (Fig. 17) for the normal eye.

For all quadratic potential functions that have global maximums (i.e. $\beta_3\beta_4 - {\beta_5}^2 > 0$), the maximums (i.e. minimums of the reversed potential functions, or the attraction points) are superimposed on the scatter of eye positions in Fig. 19. For subject DR's tested eye, attraction points for drift only exist within 0.1 sec following a microsaccade. Note that Fig. 19 doesn't include maximums at lines achieved by some potential functions, so it's just a rough estimation of the non-random pattern of drift characterized by the potential function.

The fact that the attraction points in Fig. 19 are somewhat far from the fixation location may be explained by Fig. 20, where after 0.33 sec almost all significant coefficients (i.e., mostly β_1 and β_2) lie close to a horizontal line somewhere between 0 and -0.1, i.e., there exists a "bias potential". The bias potential function is obtained by fitting the quadratic form to the subseries

of drifts after 0.33 sec. The predicted velocities are calculated for all times from this bias function; the same model is then fitted to the residuals, which gives the new potential function with the bias removed. The attraction points achieved by "unbiased" potential functions are shown in Fig. 21, and the updated coefficients are plotted against time in Fig. 22. As we expected, all attraction points move closer to the fovea after the bias potential function is removed (Fig. 21). Moreover, updated coefficients are only significant at the beginning of the drift, suggesting that at longer lags the bias function alone sufficiently characterizes drift (Fig. 22).

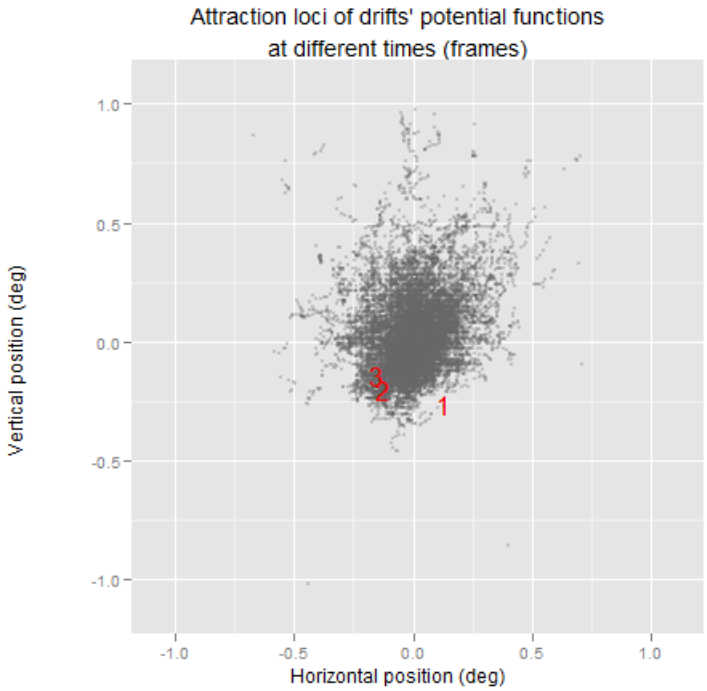

Fig. 19. Drift loci of attraction predicted by fitted potential functions at different times for the normal eye. Red text 1, 2, and 3 represents all existing attraction points that are of the 1st, 2nd, and 3rd frames, i.e., 0.033 sec, 0.067 sec, and 0.1 sec, following a microsaccade respectively. The attraction points are superimposed on the eye positions (grey dots).

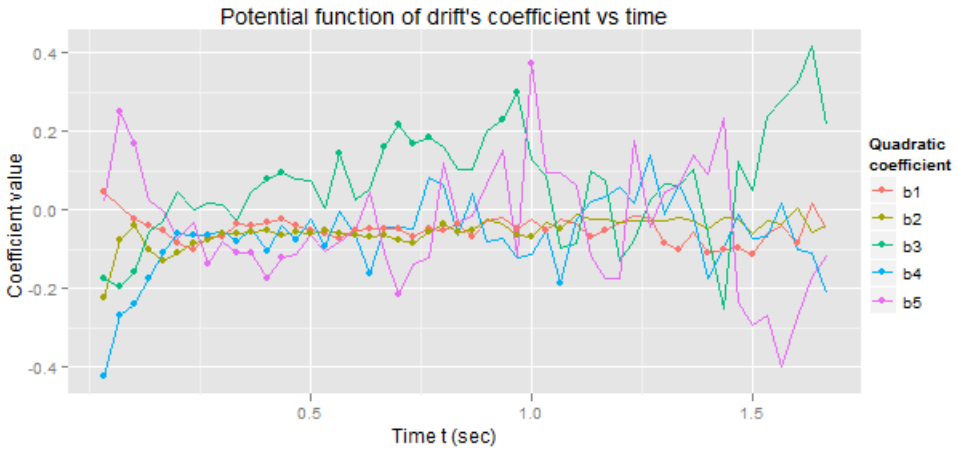

Fig. 20. Coefficients of the drift potential function vs. time (following a microsaccade) for the normal eye. Dots denote statistically significant values (p-value < 0.05). For t < 0.33 sec, most coefficients are statistically significant; for t > 0.33 sec, second-order coefficients gradually lose significance, whereas linear terms especially β_1 maintain approximately constant negative values that are significantly different from zero.

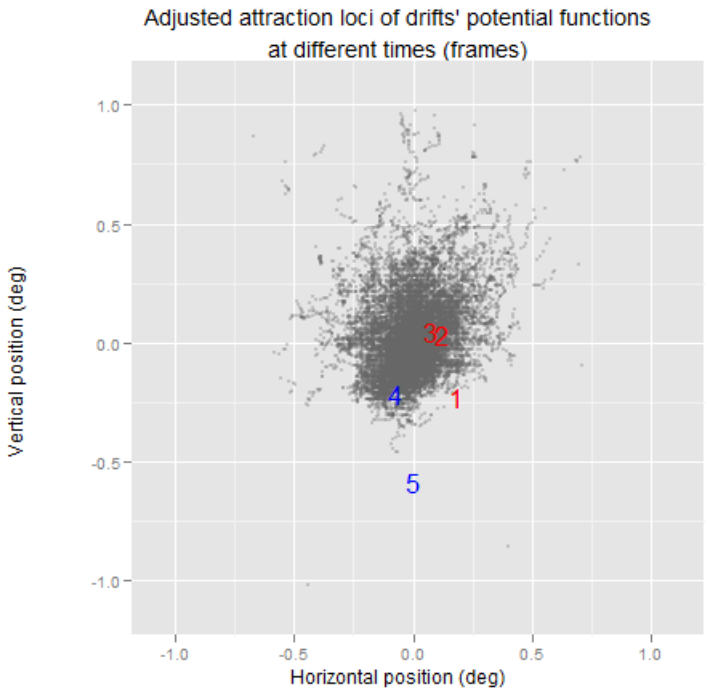

Fig. 21. Drift loci of attraction at different times following a microsaccade predicted by adjusted potential functions for the normal eye. The bias potential, i.e., potential functions fitted to drifts of longer lags after a microsaccade, is removed by fitting the model to the residuals of the bias potential. Attraction points 1, 2 and 3

(red) move closer to the fovea, and two new attraction points 4 and 5 (blue) appear after the bias potential is adjusted.

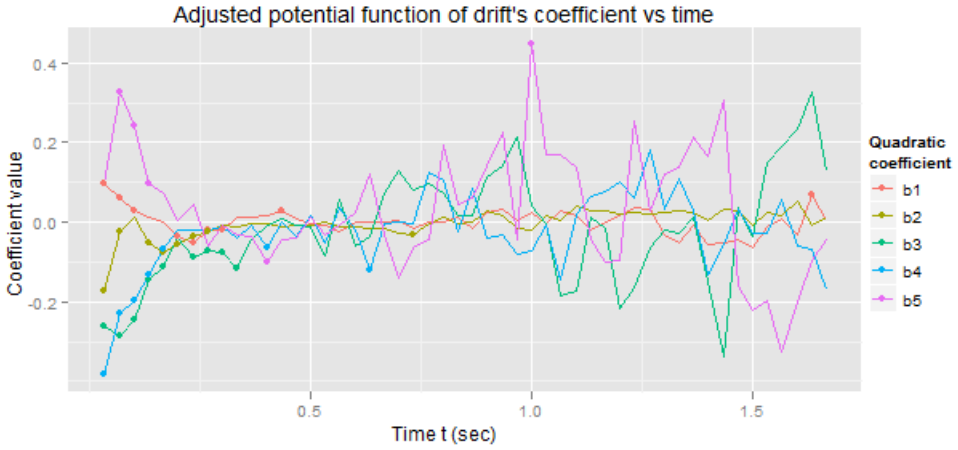

Fig. 22. Coefficients of the adjusted drift potential function vs. time (following a microsaccade). Dots denote statistically significant values. Once the bias potential is adjusted, only coefficients of short lags are still significant.

3.1.3.3 Noise of drifts

Drift velocity deviation does not vary much over location when compared to the relatively wide range of the velocity. Therefore, with some approximation, we will assume constant variance of drift velocity over location.

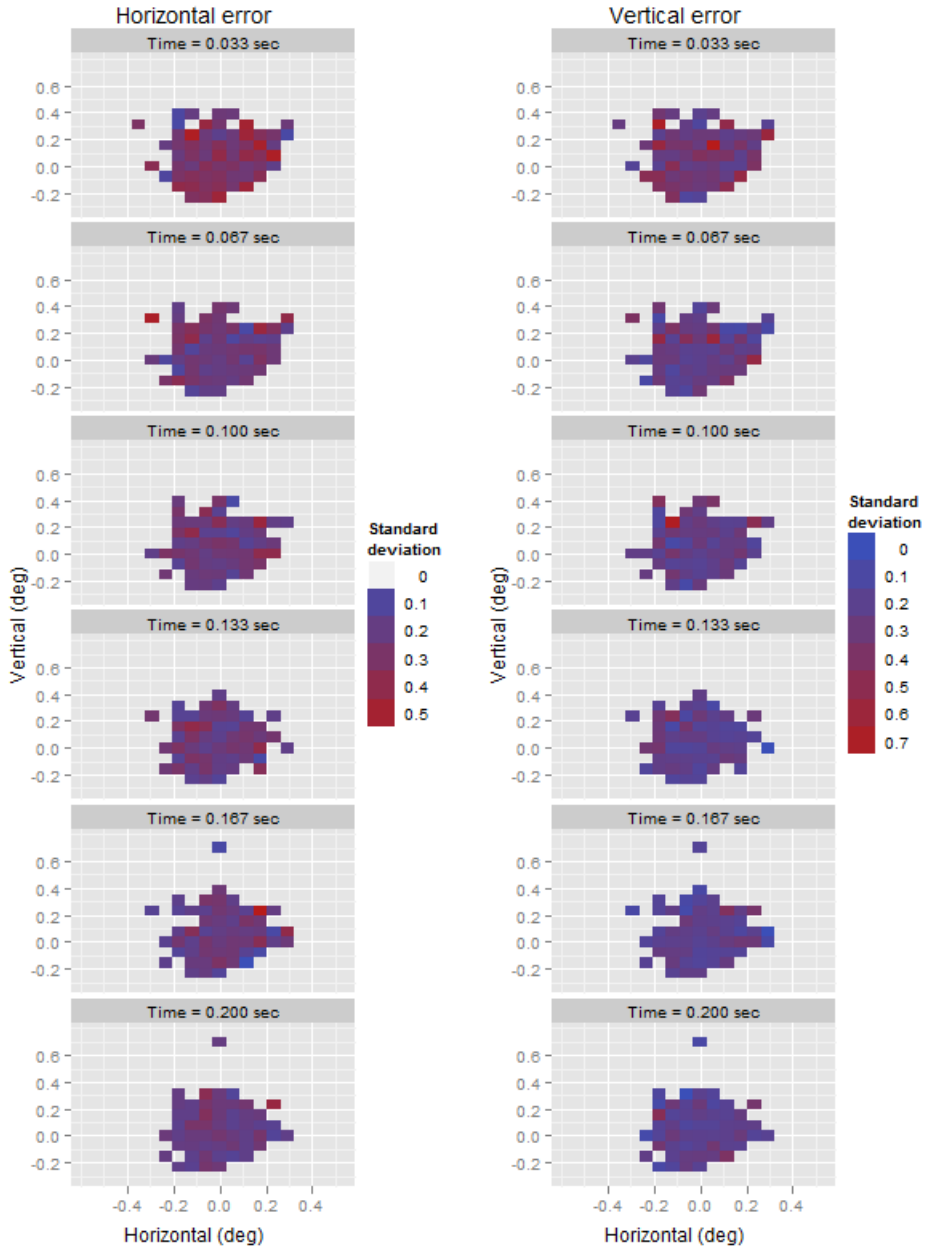

Fig. 23. Drift a) horizontal and b) vertical velocity deviation vs. location at different times (following a microsaccade) for the normal eye. The velocity deviation is estimated directly from sample standard deviations. At given time (row) and direction (column), the variation of drift velocity noise magnitude over location is relatively small.

Fig. 24a shows that drift velocity noise (i.e. randomness that cannot be predicted by the potential function) decreases with time and then oscillates around a horizontal line. We speculate that drift bears a constant level of intrinsic noise, which explains the oscillation of deviation about a horizontal line after about 0.33 sec. However, within the early period

following a fast movement – microsaccade, there may exist noise from other sources (e.g. the last microsaccade, the initiation of the drift, or the fixation error correcting force) superimposed to the intrinsic noise of drift. The noise associated with the early stage is more transient and decreases fast, whereas the sustained noise associated with the entire drifting process soon becomes the dominant source of noise. More specifically, the model is formed as

$$VAR(t) = VAR_{long} + VAR_{early}\, f(t) \qquad 32)$$

where on the right hand side the first term is the sustained intrinsic noise of drifts, and the second terms is the product of the early source of noise and a decaying function of time which we propose to have the form t^{γ} where γ is a negative real number. Eq 22) can be rewritten as

$$\sigma(t) = \sqrt{\beta_0 + \beta_1 t^{\beta_2}}\,. \qquad 33)$$

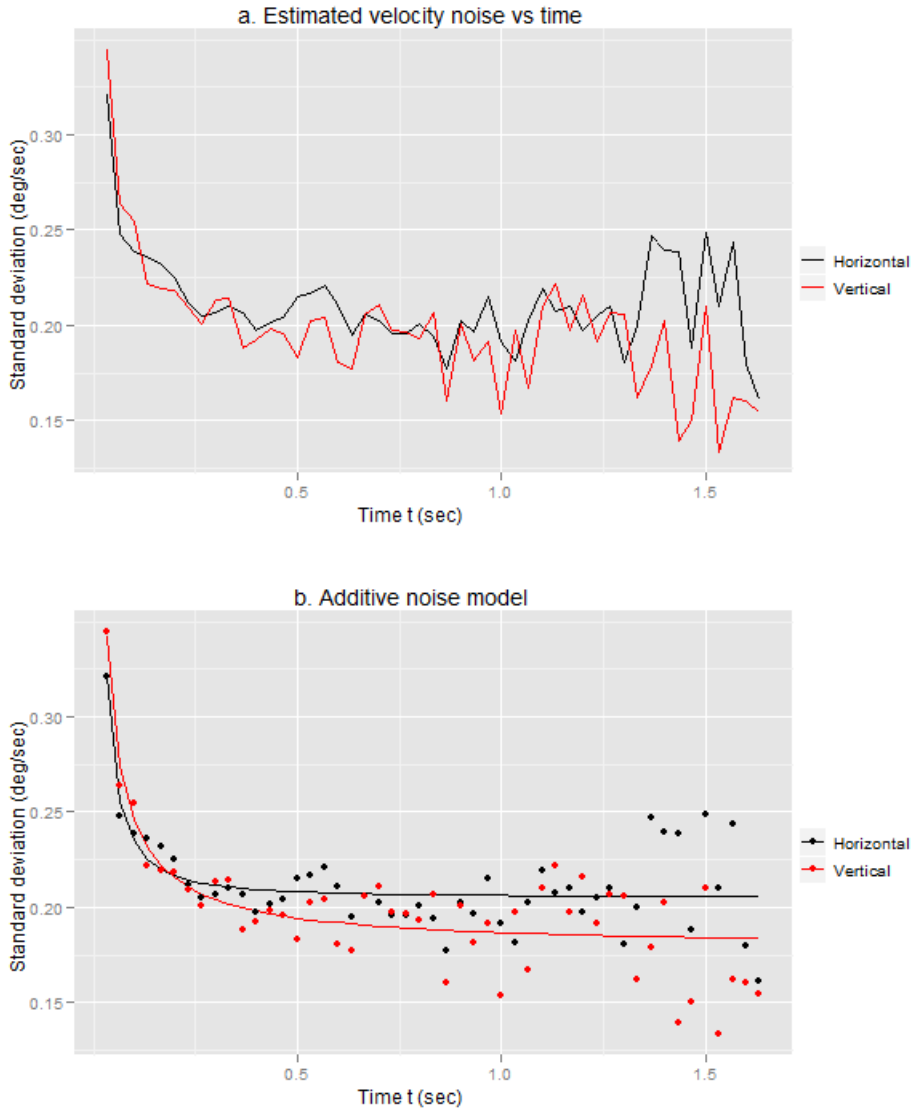

Fig. 24. a) Drift's horizontal (black) and vertical (red) velocity noise magnitude vs. time for the normal eye. The noise estimation is based on residuals of semi-parametric spline smoothing of drifts whose sample sizes are greater than 25 at each time point. b) Additive noise models (curves) fitted to sample noise, i.e., drift velocity noise (dots), in horizontal (black) and vertical (red) directions. The fitted models are $\sigma_x(t) = \sqrt{0.042 + 0.061t^{-1.396}}$ and $\sigma_y(t) = \sqrt{0.032 + 0.085t^{-0.987}}$.

Model: $\sigma_x(t) = \sqrt{\beta_0 + \beta_1 t^{\beta_2}}$

Coefficients	Estimate	Std. Error	t value	Pr(>|t|)
β_0	0.041980	0.001536	27.330	< 2e-16 ***
β_1	0.060973	0.007379	8.263	1.22e-10 ***

β_2	-1.396479	0.317738	4.395	6.47e-05 ***
			Signif. codes:	0 '***' 0.001 '**' 0.01 '*' 0.05 '.' 0.1 ' ' 1

Model: $\sigma_y(t) = \sqrt{\beta_0 + \beta_1 t^{\beta_2}}$

Coefficients	Estimate	Std. Error	t value	Pr(>|t|)
β_0	0.031893	0.002250	14.171	< 2e-16 ***
β_1	0.085327	0.006713	12.711	< 2e-16 ***
β_2	-0.987414	0.151342	6.524	4.72e-08 ***
			Signif. codes:	0 '***' 0.001 '**' 0.01 '*' 0.05 '.' 0.1 ' ' 1

Table 7. Summary of nonlinear additive noise model regressions in horizontal and vertical directions of the normal eye.

3.2 Nonamblyopic eye

When the amblyopic eye is patched, conventional ophthalmoscopic examination of the nonamblyopic eye of the strabismic amblyopic subject SF reveals no abnormality in fixation. In fact, we noticed that the nonamblyopic eye fixates exceptionally well monocularly. Similar findings were made from the retinal movement recordings using AOSLO – both the image quality and stability is very good. The eye movement data are analyzed using similar modeling approaches that have been applied to the normal eye in the last section.

3.2.1 Overview

While maintaining fixation, the nonamblyopic eye makes miniature movements at speeds that range from 0 to 44.89 deg/sec. Both the width and the median of the speed distribution are smaller in the nonamblyopic eye than in the normal eye (i.e. $MAD(\omega_{NAE})$ = 0.13 deg/sec, $MAD(\omega_{normal})$ = 0.16 deg/sec, $median(\omega_{NAE})$ = 0.24 deg/sec, $median(\omega_{normal})$ = 0.28 deg/sec). This implies that fixation of the nonamblyopic eye of the subject SF may be even more stable than that of the normal eye of the subject DR. Using the same method for the normal eye, the threshold speed of detecting microsaccades for the nonamblyopic eye is determined to be 1.044 deg/sec, which is also slightly smaller than the threshold for the normal eye 1.244 deg/sec (i.e. a difference of 1 ~ 2 pixels on average in frame-to-frame position increment). These results differ from previous findings of excessively unsteady fixation in the nonamblyopic eye (Bedell & Flom, 1985).

Interestingly, the velocity scatter in Fig. 26 shows an obvious asymmetry for both microsaccades and drifts, with the former skewed towards the left and the later towards the right. This asymmetry is probably associated with the nasal eccentric fixation of the amblyopic eye. More specifically, since the amblyopic (left) eye has nasal (right) eccentric fixation, the fact that the nonamblyopic (right) eye tends to make microsaccades towards the nasal (left) side suggests that it is probably conjugate with the amblyopic eye's error-correcting movement from the nasal fixation (right) towards the fovea (left). Fortunately the frequency and magnitudes of

these microsaccades are small enough to avoid any possible impairment of the nonamblyopic eye's visual acuity. These results are *opposite* to those reported from earlier studies that the fixational eye movements of the nonamblyopic eye of a esotropic were characterized by high-velocity nasal drifts alternating with temporal microsaccades (Bedell & Flom, 1985). We will see in the next section that drifts of the amblyopic eye are directed in a direction that's also different from previous results (Schor & Flom, 1975; Schor & Hallmark, 1978). Hence the fixational eye movements in the two eyes of the strabismic amblyope are somewhat conjugated, and this does agree with previous results (Bedell & Flom, 1985).

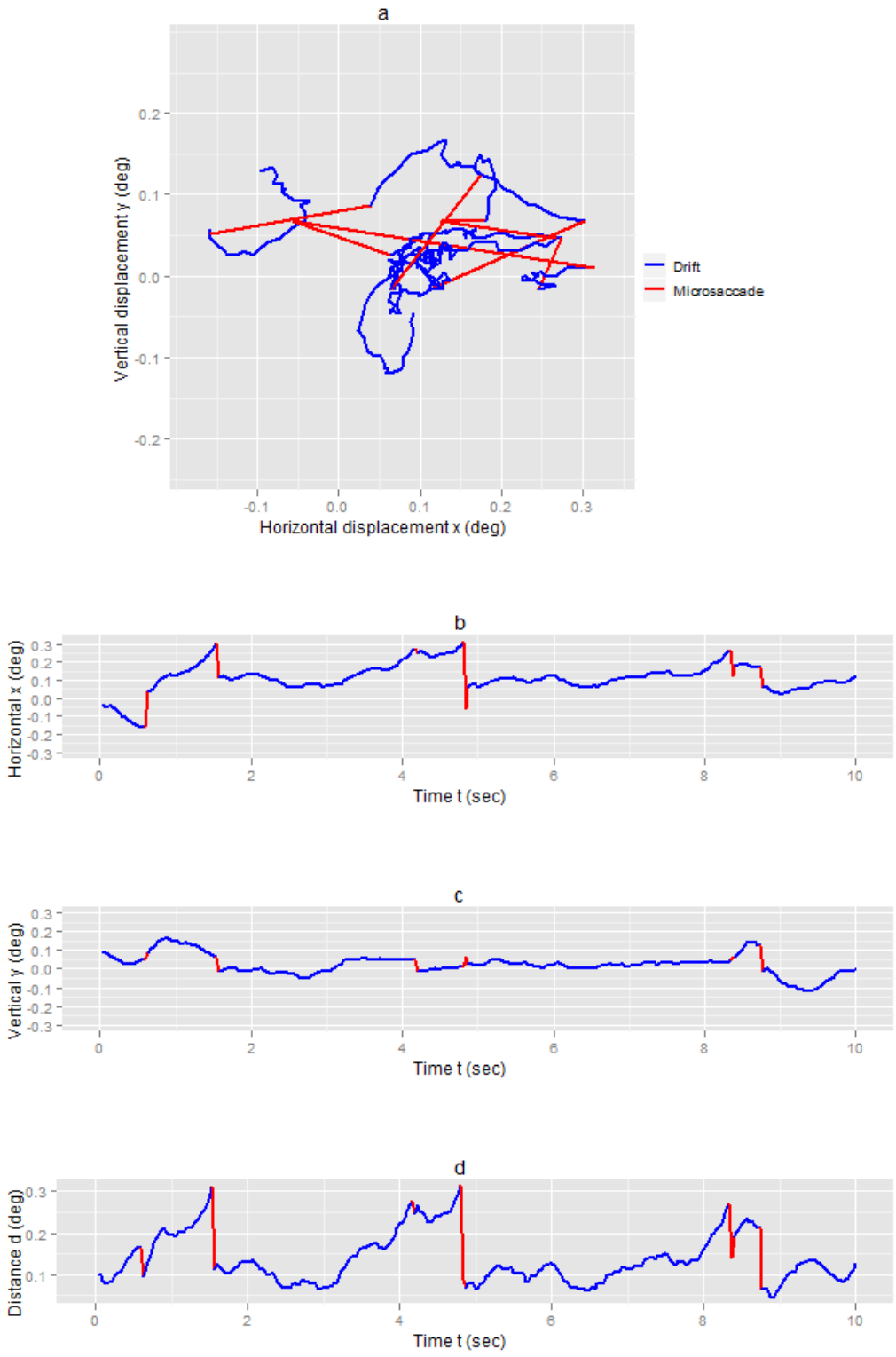

Fig. 25. A 10-second fixational eye movement sample from the nonamblyopic eye of the strabismic amblyopic subject SF. a) Two-dimensional trajectory. b) Horizontal displacement x vs. time t. c) Vertical displacement

y vs. time t. d) Euclidian distance d from the fixation vs. time t. Blue and red traces are drifts and microsaccades respectively.

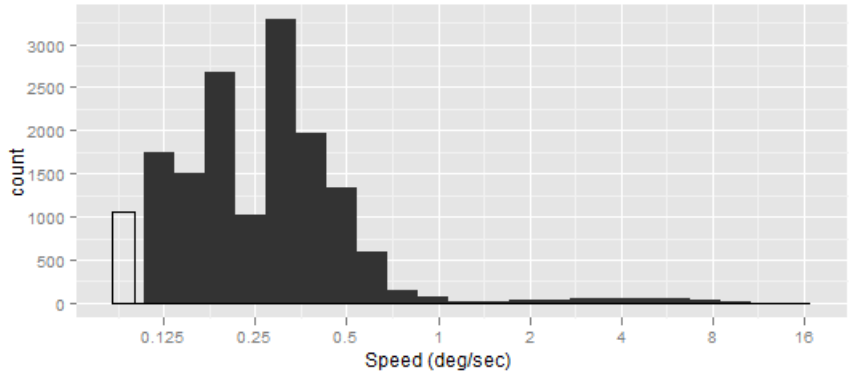

Fig. 26-1. Empirical distribution of speed magnitude ω (deg/sec) during the nonamblyopic eye's fixation on a logarithmic axis. The unfilled bar on the left represents number of data points with zero velocity. $Median\ (\omega)$=0.24 deg/sec, $MAD(\omega)$ = 0.13 deg/sec.

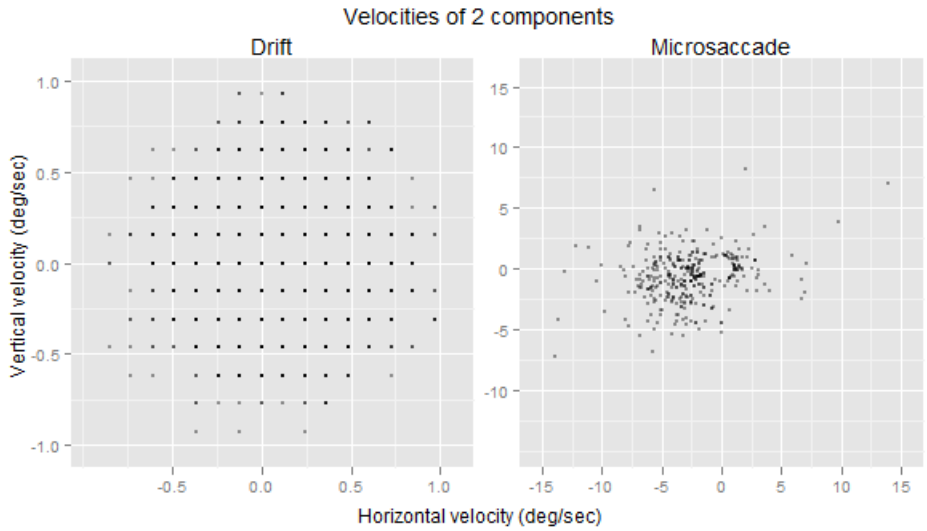

Fig. 26-2. Two-dimentional empirical distributions of drift and microsaccade velocities for the nonamblyopic eye. The threshold speed for detecting microsaccades is 1.044 deg/sec.

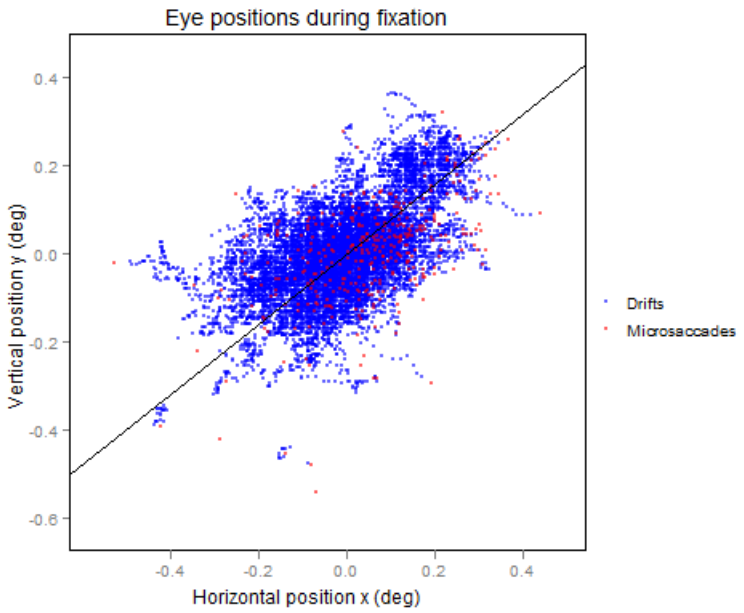

Fig. 27. Eye positions for drifts (blue) and microsaccades (red) during the nonamblyopic eye's fixation. The line $y = 0.7962x$ represents the principle component of the scattered positions, $EigV = (-0.7823, -0.6229)$, $EigD = 0.0214$, where $EigV$ representing the direction of the principle component is an eigenvector of the data's covariance matrix and $EigD$ is the corresponding (i.e. largest) eigenvalue.

3.2.2 Microsaccades

The distribution of eye positions during fixation has the largest variance along the direction of the vector (-0.7823, -0.6229), with the majority of positions clustered around the fixation location (Fig. 27). Similarly, the beginning and end positions of microsaccades are located along a line of the same slope (0.7962). Moreover, most microsaccades are elicited at the upper right quadrant and end at the lower left quadrant (Fig. 28a). This asymmetry is consistent with those in velocity distributions, and can also be explained by the conjugation of microsaccades of the nonamblyopic eye with those of the amblyopic eye.

Like the normal eye, microsaccade is error-correcting on average in the nonamblyopic eye when positions are taken into account ($\overline{\Delta d'} = 0.08deg, SE(\Delta d') = 0.01$deg; Fig. 28c).

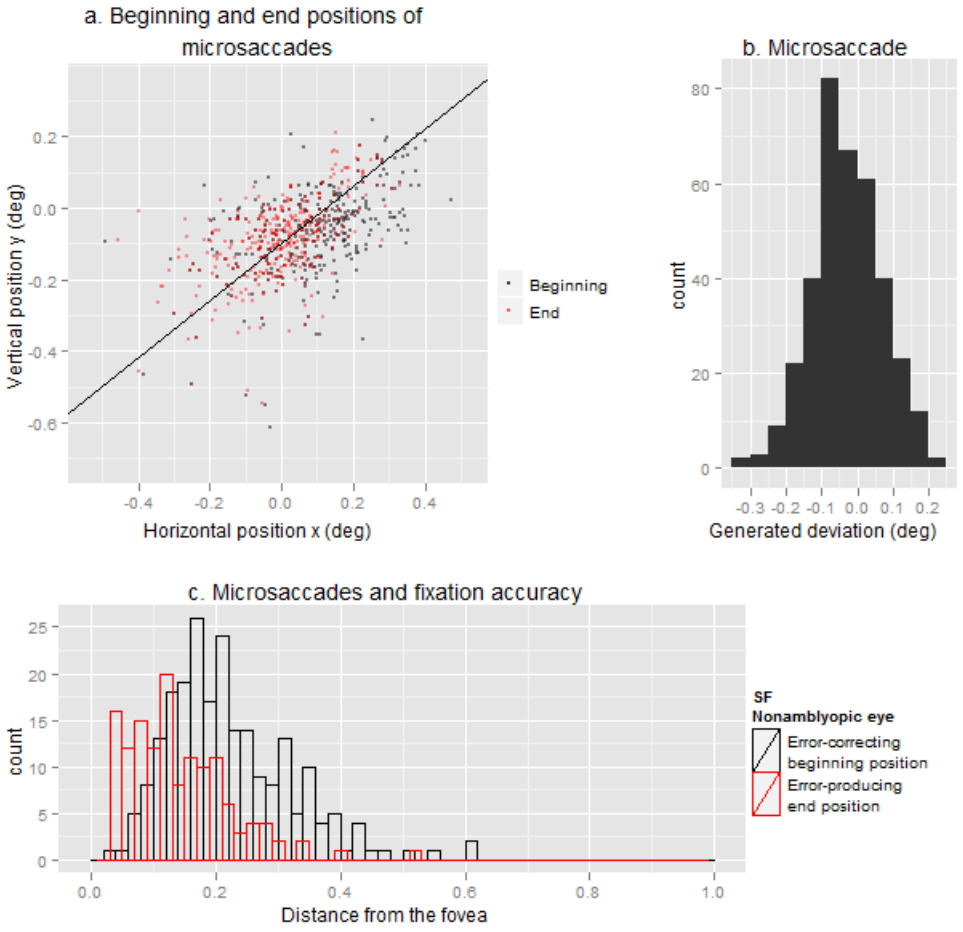

Fig. 28. Overview of microsaccades for the nonamblyopic eye. a) Eye positions at the beginning (red) and the end (black) of microsaccades. The line $y = -0.1 + 0.7962x$ represents the data's principle component, $V = (-0.7819, -0.6234)$, $D = 0.0214$. b) Histogram of the fixation deviation from the fovea generated by a microsaccade, i.e., difference of the distance between the eye position and the fovea before and after a microsaccade. $\overline{\Delta d} = d_{end} - d_{start} = -0.028$, $SE(\widehat{\Delta d}) = 0.005$. c) Histograms of the error-correcting microsaccade' beginning position $d_{correct\ ,start}$ (black) and the error-producing microsaccades' end position $d_{error\ ,end}$ (red). $\overline{\Delta d'} = \bar{d}_{correct\ ,start} - \bar{d}_{error\ ,end}$ = 0.08 deg, $SE(\Delta d')$ = 0.01 deg.

3.2.2.1 Potential function of microsaccades

Compared to the normal eye, the potential function of the microsaccades for the nonamblyopic eye is clearly asymmetric. The minimum of the reversed potential function (i.e. point of attraction) is in the lower left quadrant of the plane. This is consistent with the observation that microsaccades tend to move from the upper right quadrant towards the lower left quadrant (Fig. 28a).

Model: $V(x,y) = \beta_0 + \beta_1 x + \beta_2 x^2 + \beta_3 y + \beta_4 y^2 + \beta_5 xy$

Coefficients	Estimate	Std. Error	t value	Pr(>|t|)
β_1	-2.0128	0.1316	-15.295	< 2e-16 ***
β_2	-0.7799	0.1290	-6.045	2.39e-09 ***
β_3	-6.5089	0.4502	-14.458	< 2e-16 ***
β_4	-4.1204	0.5711	-7.215	1.37e-12 ***
β_5	3.2140	0.7585	4.238	2.55e-05 ***

Signif. codes: 0 '***' 0.001 '**' 0.01 '*' 0.05 '.' 0.1 ' ' 1

Multiple R^2	0.5056
Adjusted R^2	0.5022

Table 8. Summary of the microsaccade potential function regression for the nonamblyopic eye.

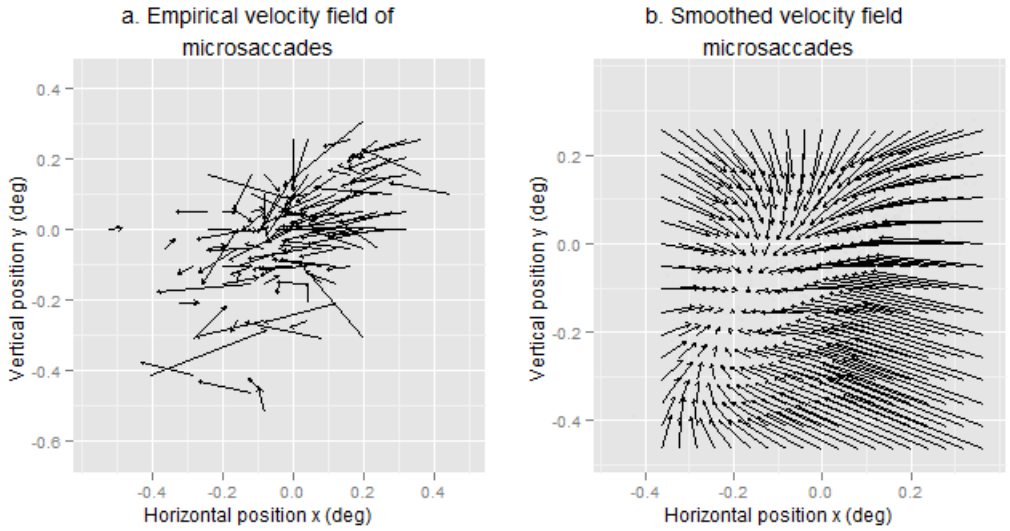

Fig. 29. a) Empirical and b) smoothed velocity fields of microsaccades of the nonamblyopic eye. Each arrow represents the averaged velocity of microsaccades in a small bin. The beginning position of each arrow is absolute, whereas the end position (i.e. arrow head) and the length of the arrow may be scaled. The smoothed velocities are predicted by the semi-parametric spline smoothing of degree 4.

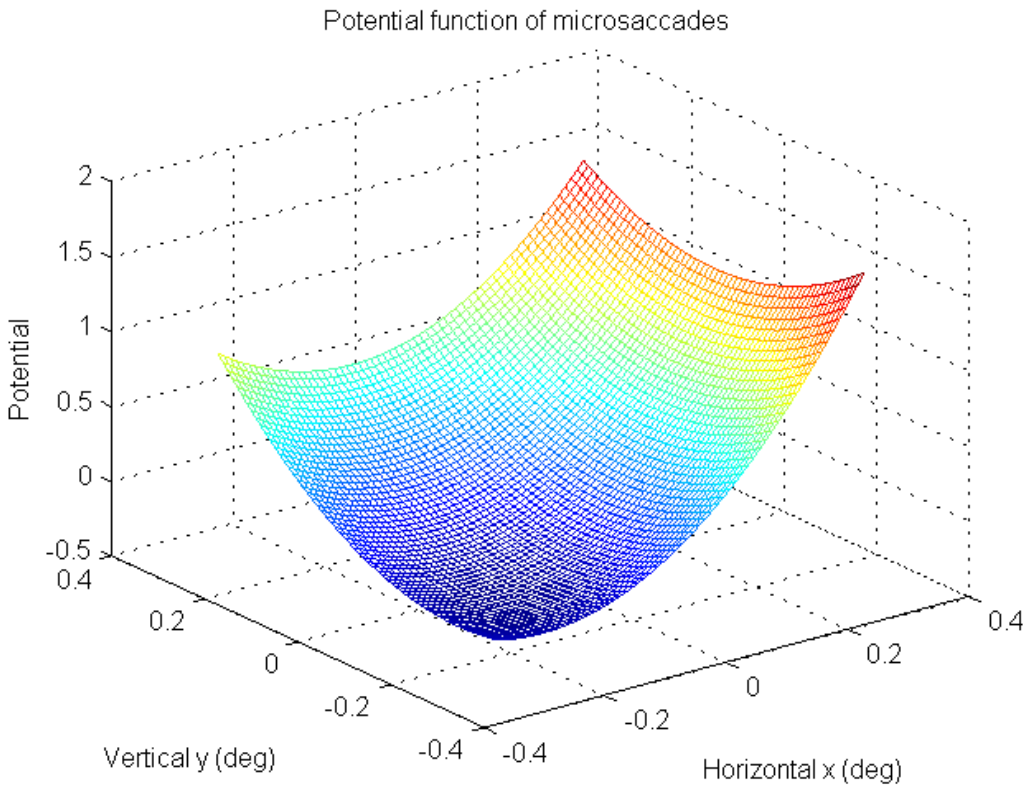

Fig. 30. Reversed potential function of microsaccades for the nonamblyopic eye, $V(x, y) = -2.01x - 0.78y - 6.51x^2 - 4.12y^2 + 3.21xy$. The potential function is shifted to have zero intercept.

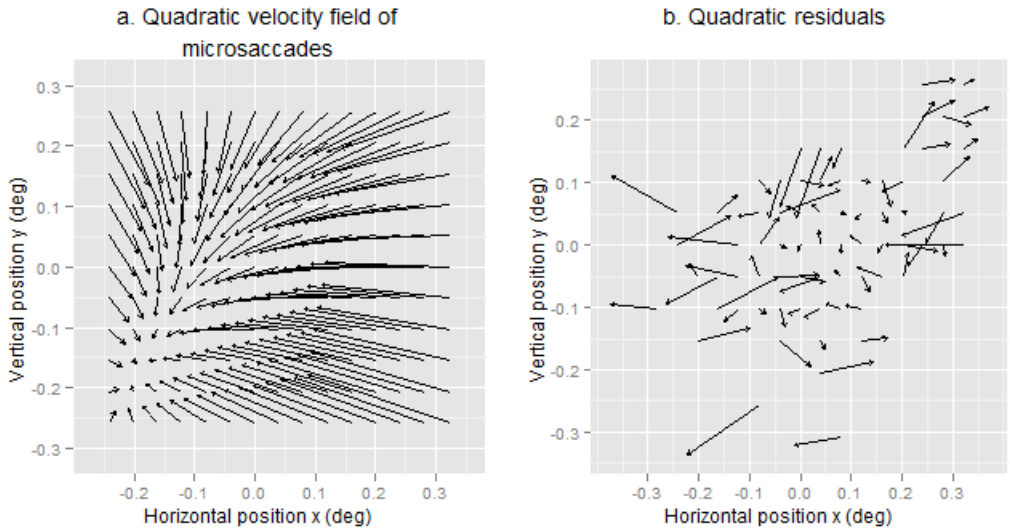

Fig. 31. a) Microsaccades' velocity field predicted by the fitted quadratic potential function for the nonamblyopic eye, and b) the corresponding residual velocity field. The full model including all terms, regardless of statistical significance, is used.

The empirical estimation of microsaccade velocity noise for the nonamblyopic eye from the sample standard deviation shows that it doesn't vary much over location, if we take into account that microsaccade speeds range much more widely, i.e., from 1.044 deg/sec to 44.89 deg/sec. Therefore we can assume approximately constant variance of microsaccade velocity in space. The velocity noise in both directions can be estimated from residuals of the potential function: $\hat{\sigma}_x = \sqrt{\frac{RSS_x}{df}} =$ 2.80 deg/sec, $\hat{\sigma}_y = \sqrt{\frac{RSS_y}{df}} =$ 1.81 deg/sec.

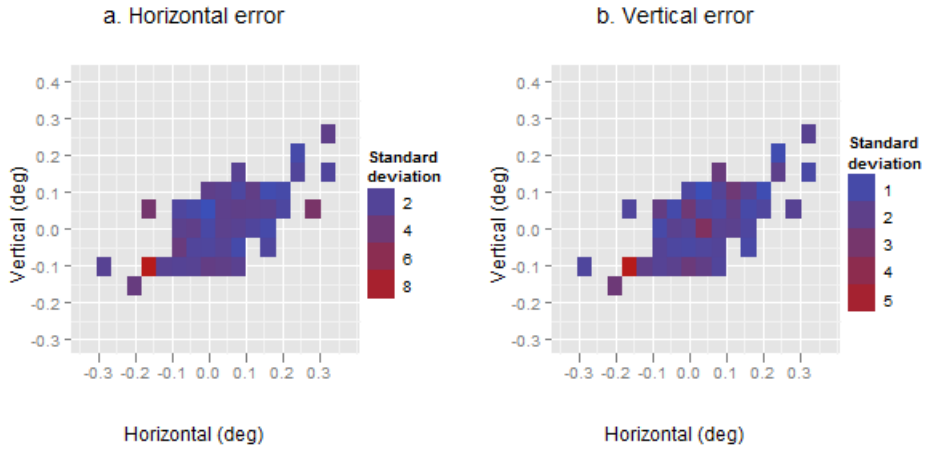

Fig. 32. Microsaccade a) horizontal and b) vertical velocity deviation vs. location for the nonamblyopic eye. The velocity deviation is estimated directly from the sample standard deviation.

3.2.2.2 Poisson process modeling of microsaccades

Similar to that of the normal eye, the distribution of the inter-microsaccade interval length demonstrates a longer refractory period of about 0.83 sec following a microsaccade. Beyond this period, the occurrences of microsaccades form a Poisson process with rate that depends on location.

Microsaccade rate is low in the center and higher at larger displacements. However, the low-rate center is shifted to the left side of the fovea by about 0.05 deg. Hence, a microsaccade is more likely to occur when the eye position is relatively in the right field than it is in the left field. And the potential function shows that a microsaccade elicited in the right field tends to move leftwards – a trend that has been demonstrated many times in SF's nonamblyopic eye. Another interesting finding is that the average rate of the occurrence of microsaccades is only 0.7/sec, which is fairly low compared to that of the normal subject DR's tested eye (i.e. 1.58/sec) and those from other normal observers reported by other investigators (Martinez-Conde et al., 2004). The low rate of microsaccade implies superb stable fixation in the nonamblyopic eye of the strabismic amblyope SF, which is consistent with what we observed using an ophthalmoscope or by viewing his retinal movements during fixation.

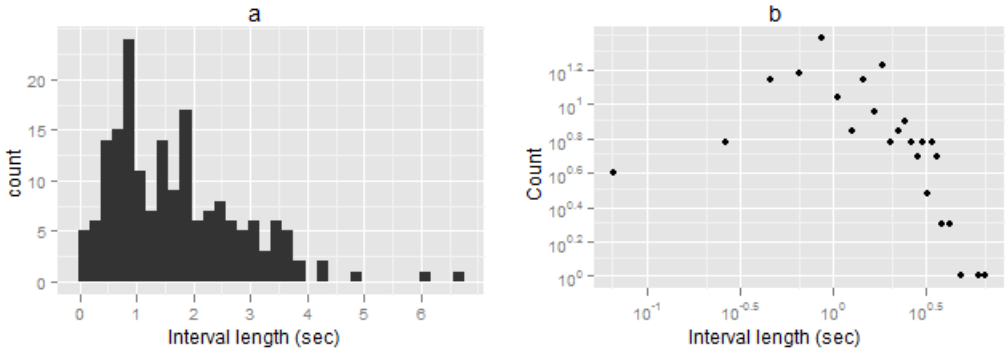

Fig. 33-1. a) Histogram of inter-microsaccade interval length for the nonamblyopic eye. The peak of the histogram is near 0.83 sec. For intervals longer than 0.83 sec, the number of intervals decreases approximately exponentially as the interval length increases. b) *Log-log* plot of a). For intervals longer than 0.83 sec, *log* frequency decreases approximately linearly with *log* interval length.

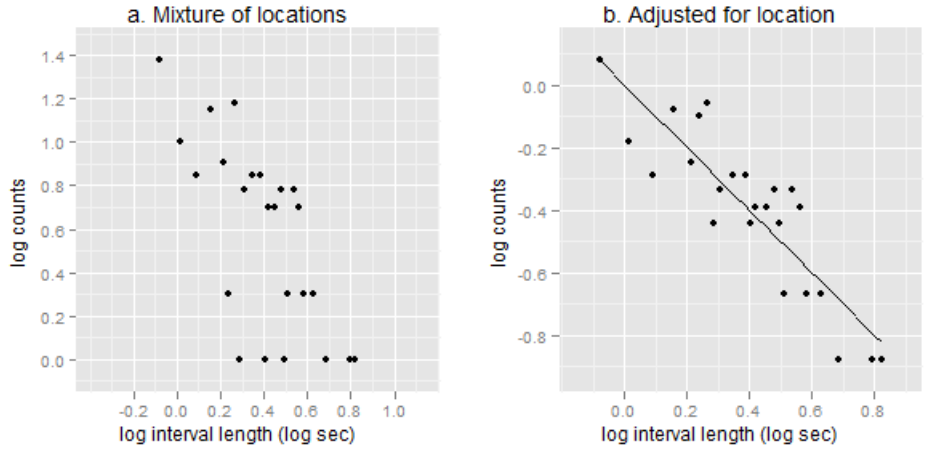

Fig. 33-2. For inter-microsaccade intervals of lengths greater than 0.83 sec only, a) mixture of *log* inter-microsaccade interval counts vs. *log* interval length for different eye positions of the nonamblyopic eye. b) Adjusted *log* inter-microsaccade interval counts vs. *log* interval length for the nonamblyopic eye. Each complete inter-microsaccade interval is classified into one of the subgroups that are at different radial distances from the fovea. Within each subgroup logarithms of interval counts are rescaled and shifted such that *log* inter-microsaccade interval counts vs. *log* interval length has slope -1 and zero intercept. The line $y = -x$ is the best fitted line for all data points in b). The transformation of data from a) to b) has at least partly adjusted for location.

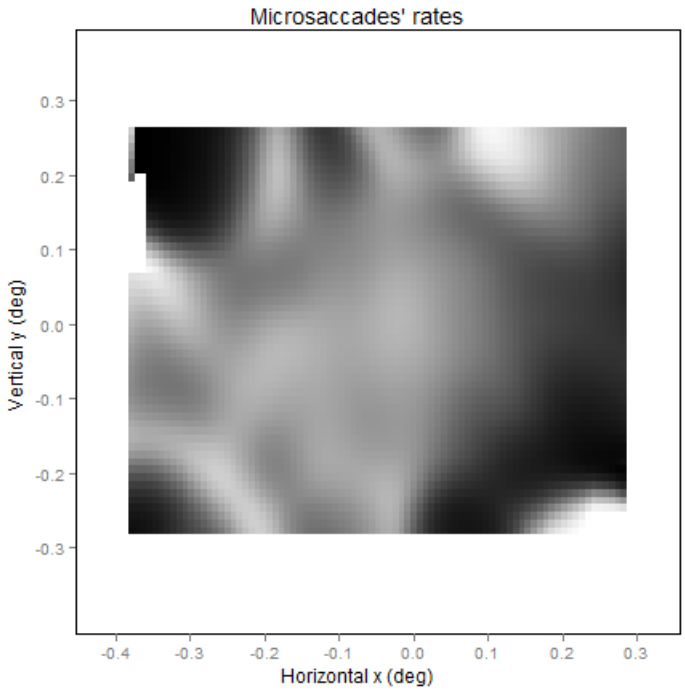

Fig. 34. Microsaccade rate map for the nonamblyopic eye. Dark and bright pixels represent high and low rates respectively. Microsaccade rates are relatively low near the fovea and high at positions farther away from the fovea. The average microsaccade rate is 0.7/sec for the nonamblyopic eye.

3.2.3 Drifts

The same methods have been applied to the nonamblyopic eye's data for assumption checks, and there is evidence that the assumptions for the random walk model hold for drifts in the nonamblyopic eye. Related results are in Appendix 2A.

3.2.3.1 Potential function of drifts

The average sub-drift moves in the reversed direction (i.e. rightward and upward) of the average microsaccade's movement. This finding seems to have completed the story about different components' contributions to the fixational eye movement in the nonamblyopic eye of strabismic amblyope SF – after a microsaccade, the nonamblyopic eye drifts away from the fovea towards the upper lateral side, probably as the amblyopic eye drifts towards its nasal side. At a certain point a microsaccade occurs and brings the gaze back towards the target that is located below and left of the current eye position. Microsaccades often overshoot, but on average they do correct for errors produced at least partly by drifts.

Like the normal eye, time is a factor that can't be ignored. Fig. 35 shows that time has substantial main effect at least on the speed magnitude (i.e. segment length and the average

two-dimensional increment), and possibly interaction with location too, i.e., the shape of potential function may change with time. Note that the trajectory of the average sub-drift after the initial period is less smooth than that of the normal eye, suggesting that the bias of drift for the nonamblyopic eye may not be as prominent or even well defined as that of the normal eye. The main trend of drift for the nonamblyopic eye is the rightward and upward movement during the early short period following a microsaccade.

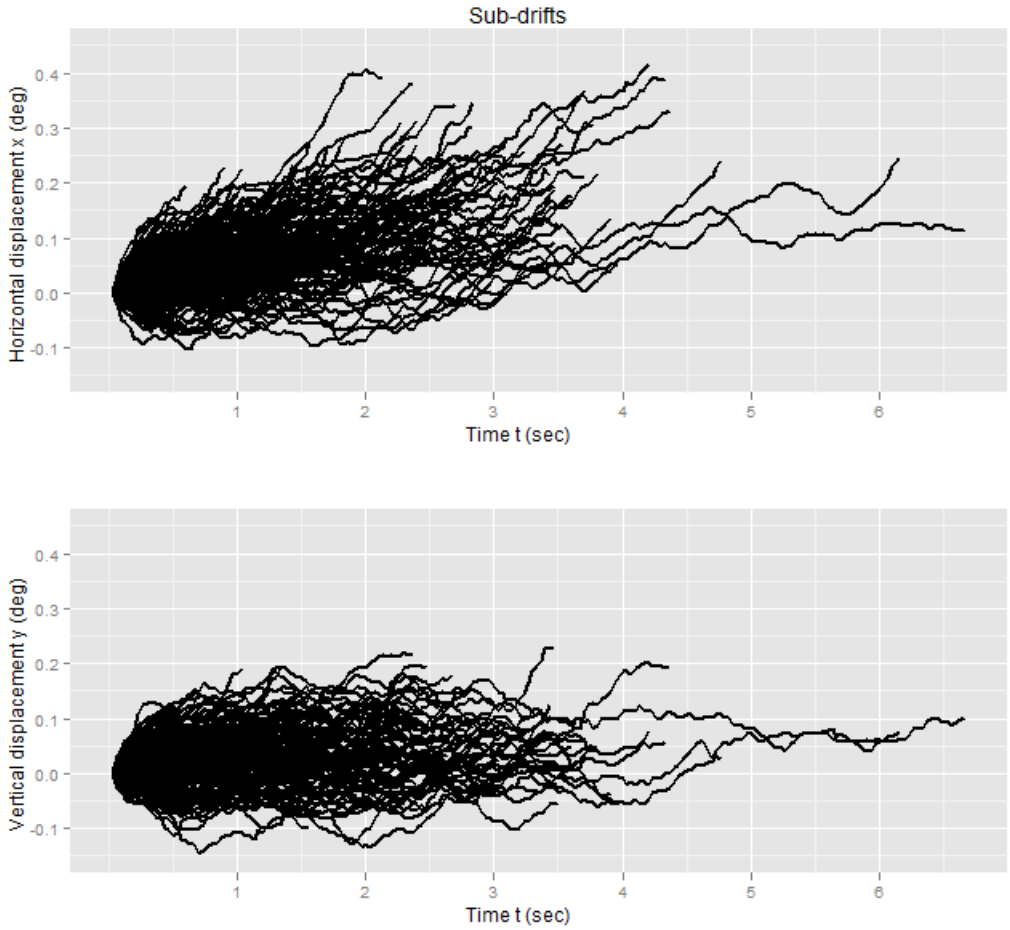

Fig. 35-1. Sub-drifts' displacements vs. time (following microsaccades) in horizontal and vertical directions for the nonamblyopic eye (see Methods).

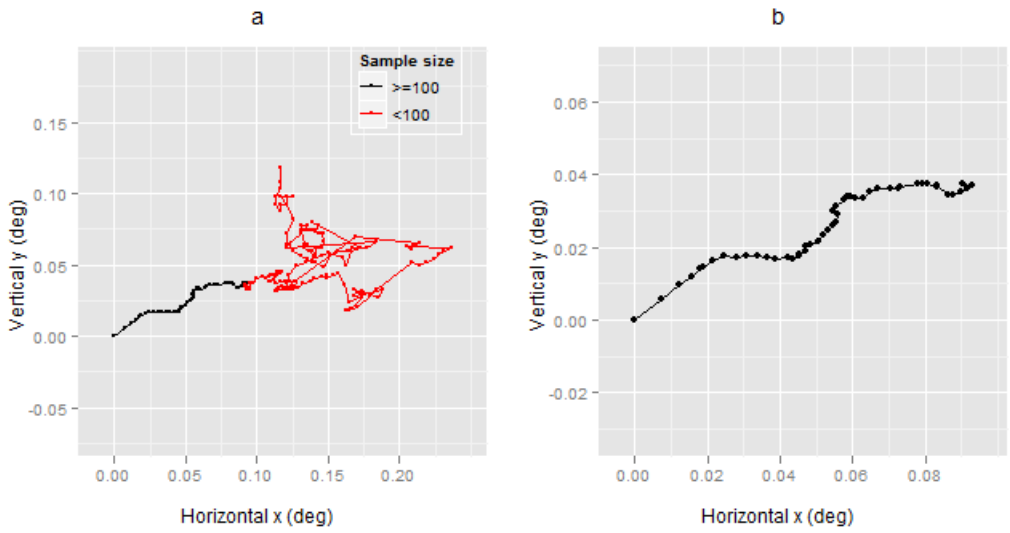

Fig. 35-2. Average trajectory of sub-drifts of a) any sample size or of b) only large sample size (i.e. greater than 100), for the nonamblyopic eye. Black and red traces denote sample sizes greater than or less than 100 respectively. The trajectory starts at **0** since the position of the first point is subtracted from all points (see Methods).

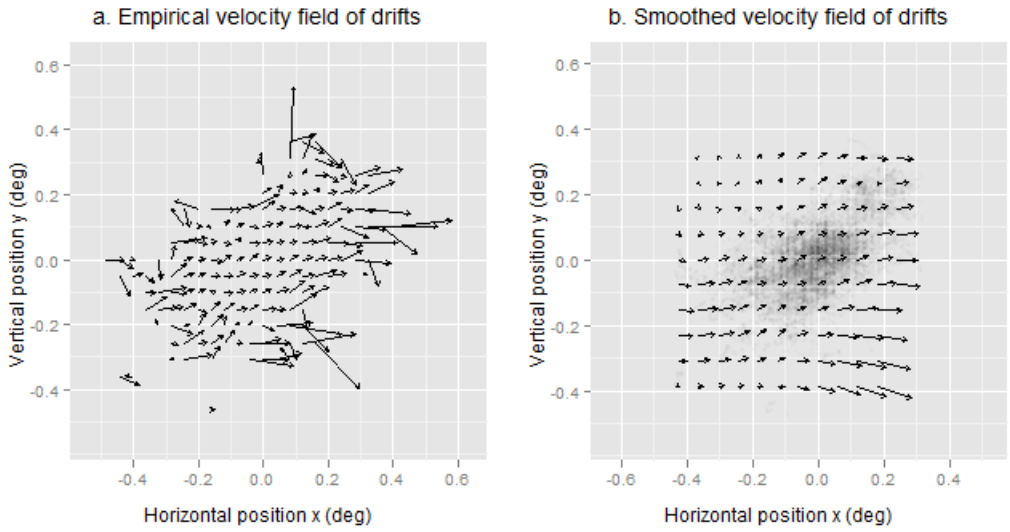

Fig. 36. a) Empirical and b) smoothed velocity fields of the drift for the nonamblyopic eye. Each arrow represents the averaged velocity of drifts in a small bin. The beginning position of each arrow is absolute, whereas the end position (i.e. arrow head) and the length of the arrow may be uniformly scaled. The smoothed velocities are predicted by the semi-parametric spline smoothing of degree 4. Eye positions of original data are scattered as semi-transparent points in the smoothed velocity field. The nonamblyopic eye's drift velocity field shows a rightward bias.

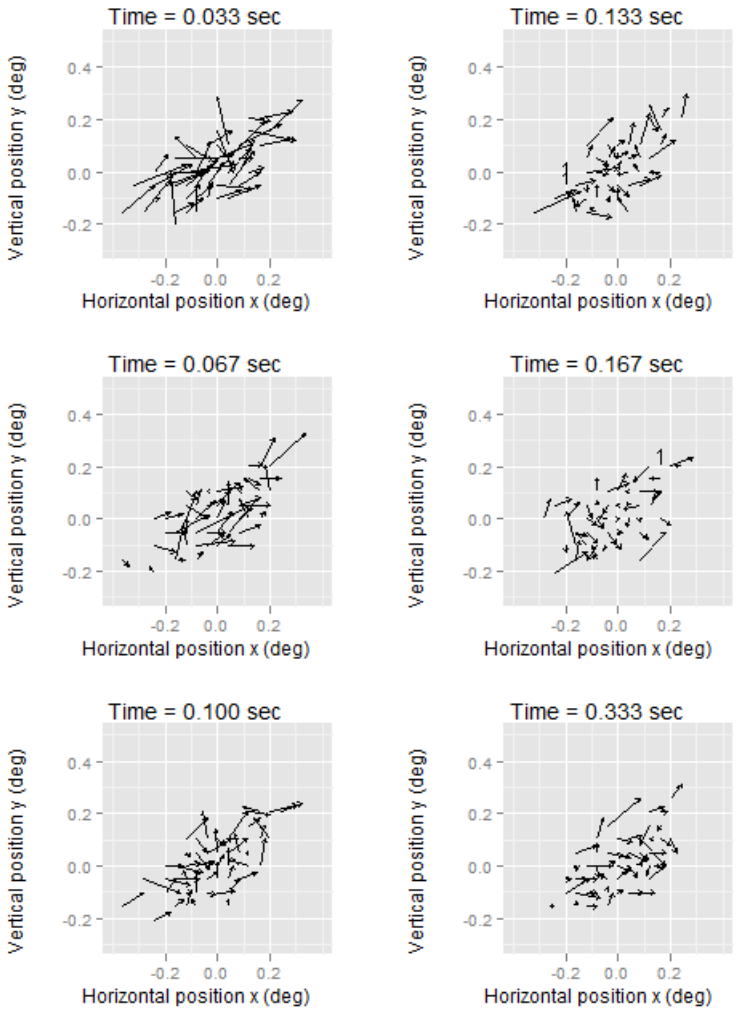

Fig. 37-1. Drift's empirical velocity fields at different times (following a microsaccade) for the nonamblyopic eye. Each arrow represents the averaged velocity of drifts in a bin with small widths. The beginning position of each arrow is absolute, whereas the end position (i.e. arrow head) and the length of the arrow may be uniformly scaled.

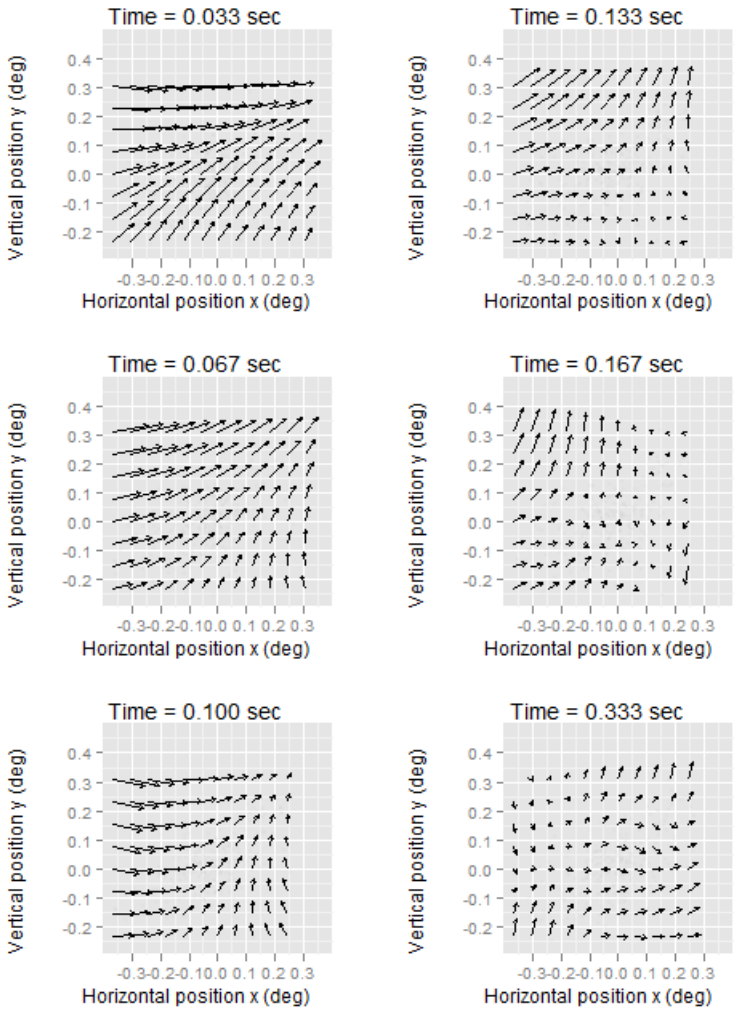

Fig. 37-2. Drift's smoothed velocity fields at different times (following a microsaccade) for the nonamblyopic eye. The smoothed velocities are predicted by the semi-parametric spline smoothing of degree 4.

The drift velocity field averaged over time (Fig. 36) demonstrates a clear rightward movement. And Fig. 37 shows that the fixation drifts fast in the upper right direction systematically at the beginning, but the movement soon slows down with increased randomness in orientation. The fitted potential functions at several different times illustrate the change of drift pattern with time (Fig. 38). In particular, within 0.1 sec following a microsaccade, the potential functions of drift are tilted from the lower left quadrant to the upper right quadrant, whereas at the lag of 0.867 sec the potential function is almost flat, especially in the y axis. Moreover, the coefficient of the horizontal linear term in the potential function (i.e. β_1) is the only one that remains statistically significant, consistent with the rightward drift found by previous results.

Model: $V(x,y) = \beta_0 + \beta_1 x + \beta_2 x^2 + \beta_3 y + \beta_4 y^2 + \beta_5 xy$

Time =1

Coefficients	Estimate	Std. Error	t value	Pr(>|t|)
β_1	0.21655	0.02145	10.094	< 2e-16 ***
β_2	0.16876	0.02107	8.009	8.88e-15 ***
β_3	-0.07120	0.08595	-0.828	0.4079
β_4	-0.18769	0.10172	-1.845	0.0656 .
β_5	0.20135	0.14250	1.413	0.1583

Signif. codes: 0 '***' 0.001 '**' 0.01 '*' 0.05 '.' 0.1 ' ' 1

Multiple R^2	0.2811
Adjusted R^2	0.2736

Time =2

Coefficients	Estimate	Std. Error	t value	Pr(>|t|)
β_1	0.13916	0.01695	8.211	2.12e-15 ***
β_2	0.11916	0.01674	7.117	4.14e-12 ***
β_3	-0.14288	0.06927	-2.063	0.0397 *
β_4	-0.01371	0.08621	-0.159	0.8737
β_5	0.20055	0.11846	1.693	0.0911 .

Signif. codes: 0 '***' 0.001 '**' 0.01 '*' 0.05 '.' 0.1 ' ' 1

Multiple R^2	0.2220
Adjusted R^2	0.2138

Time =3

Coefficients	Estimate	Std. Error	t value	Pr(>|t|)
β_1	0.08619	0.01549	5.565	4.41e-08 ***
β_2	0.08205	0.01532	5.355	1.34e-07 ***
β_3	-0.25397	0.06488	-3.915	0.000104 ***
β_4	-0.06741	0.07867	-0.857	0.391995
β_5	0.28867	0.10982	2.629	0.008856 **

Signif. codes: 0 '***' 0.001 '**' 0.01 '*' 0.05 '.' 0.1 ' ' 1

Multiple R^2	0.1548
Adjusted R^2	0.1457

Time =4

Coefficients	Estimate	Std. Error	t value	Pr(>|t|)
β_1	0.06371	0.01550	4.109	4.69e-05 ***
β_2	0.06910	0.01537	4.497	8.71e-06 ***
β_3	-0.16239	0.06637	-2.447	0.0148 *

β_4	0.14601	0.07913	1.845	0.0656 .
β_5	0.10763	0.11194	0.962	0.3368
			Signif. codes:	0 '***' 0.001 '**' 0.01 '*' 0.05 '.' 0.1 ' ' 1
Multiple R^2	0.1044			
Adjusted R^2	0.0949			

Time =5

Coefficients	Estimate	Std. Error	t value	Pr(>|t|)
β_1	0.020346	0.016066	1.266	0.2060
β_2	0.006629	0.015944	0.416	0.6778
β_3	-0.121777	0.069526	-1.752	0.0805 .
β_4	0.054335	0.080805	0.672	0.5016
β_5	-0.102726	0.116009	-0.885	0.3763
			Signif. codes:	0 '***' 0.001 '**' 0.01 '*' 0.05 '.' 0.1 ' ' 1
Multiple R^2	0.0203			
Adjusted R^2	0.0098			

Time =6

Coefficients	Estimate	Std. Error	t value	Pr(>|t|)
β_1	0.0828949	0.0130803	6.337	5.61e-10 ***
β_2	0.0002463	0.0130454	0.019	0.985
β_3	0.0510900	0.0586450	0.871	0.384
β_4	-0.0385469	0.0672564	-0.573	0.567
β_5	-0.0822899	0.0965852	-0.852	0.395
			Signif. codes:	0 '***' 0.001 '**' 0.01 '*' 0.05 '.' 0.1 ' ' 1
Multiple R^2	0.0833			
Adjusted R^2	0.0733			

Table 9. Summary of the drift potential function regressions at different times (following a microsaccade) for the nonamblyopic eye.

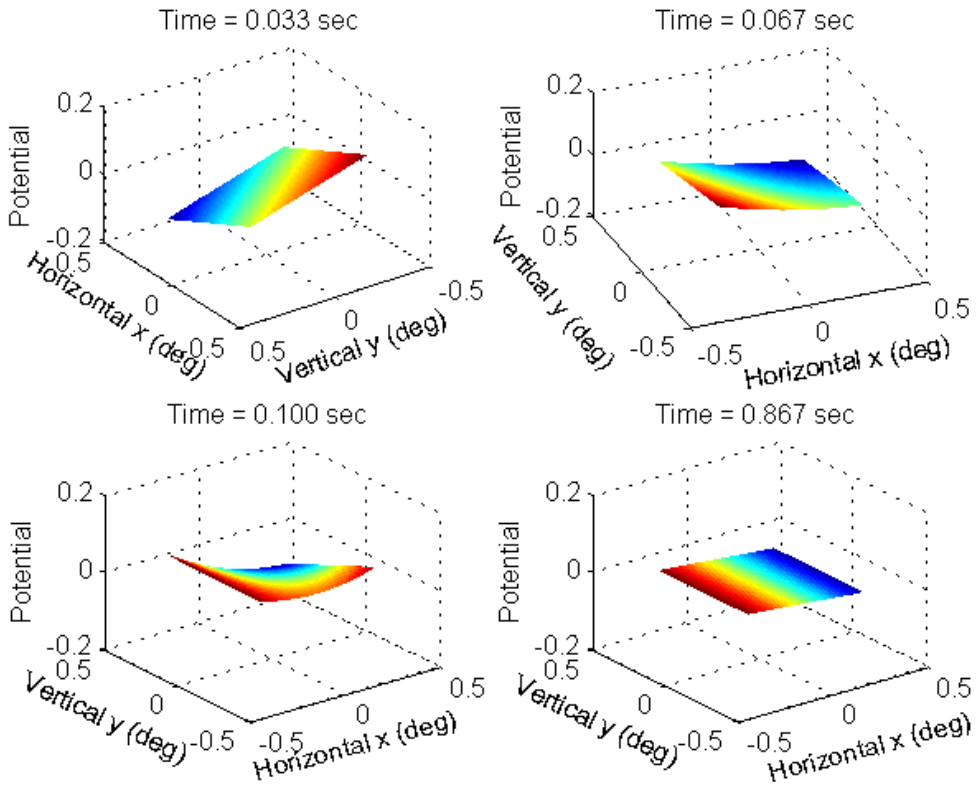

Fig. 38. Reversed potential functions of the drift at different times following a microsaccade for the nonamblyopic eye. $V(x, y, t = 0.033) = 0.22x + 0.17y$; $V(x, y, t = 0.067) = 0.14x + 0.12y - 0.14x^2$; $V(x, y, t = 0.100) = 0.09x + 0.08y - 0.25x^2 + 0.29xy$; $V(x, y, t = 0.833) = 0.05x + 0.05y$.

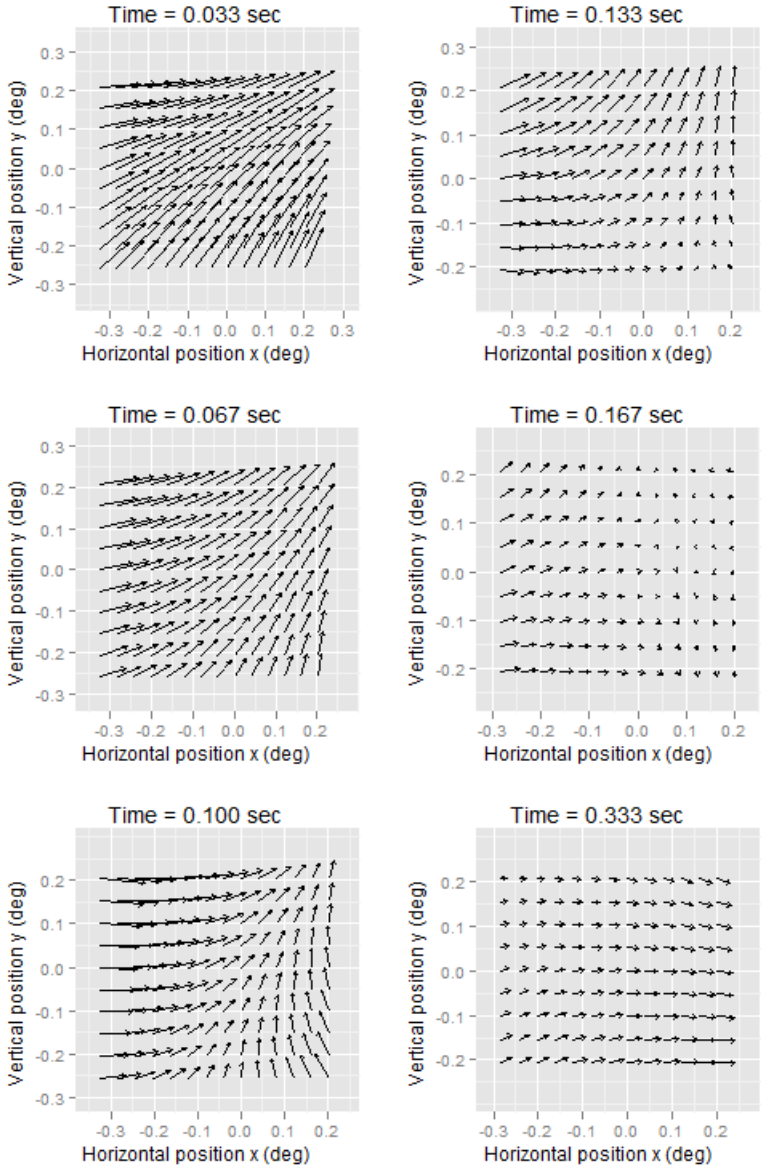

Fig. 39-1. Drift velocity fields at different times following a microsaccade predicted by fitted quadratic potential functions (Fig. 38) for the nonamblyopic eye. The full model including all terms, regardless of statistical significance, is used.

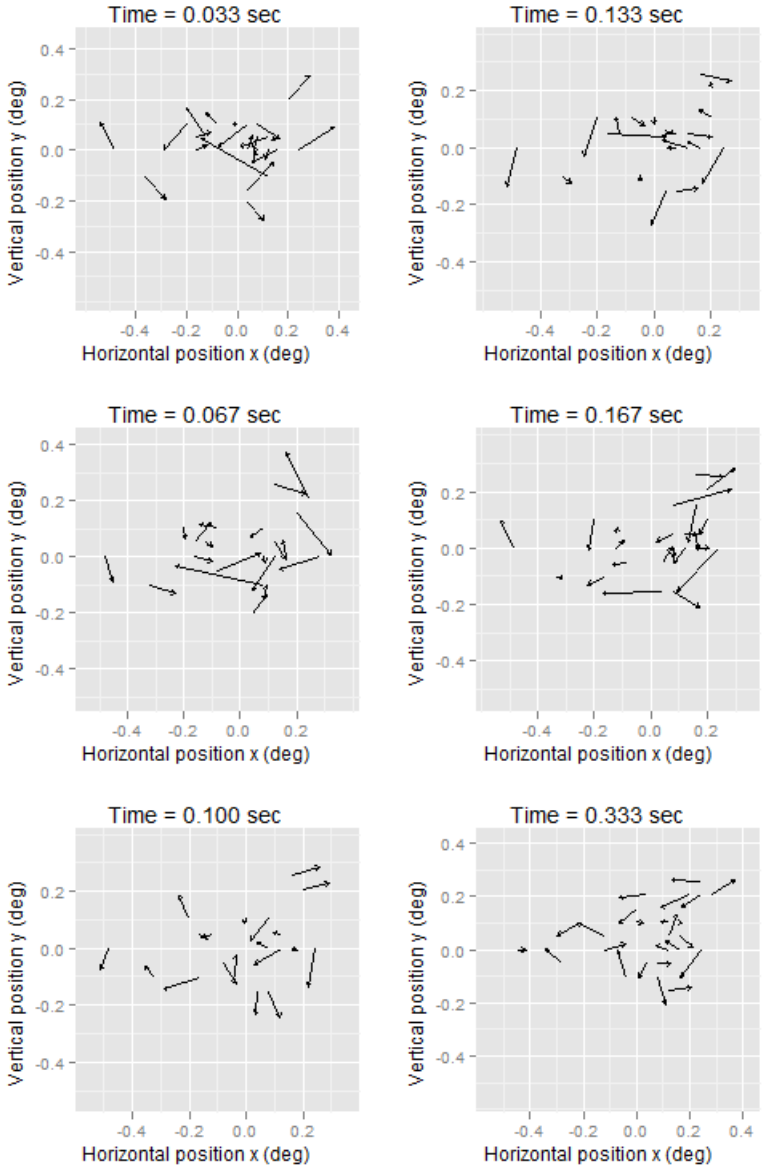

Fig. 39-2. Drift residual velocity field after the fitting of quadratic potential functions (Fig. 38) for the nonamblyopic eye.

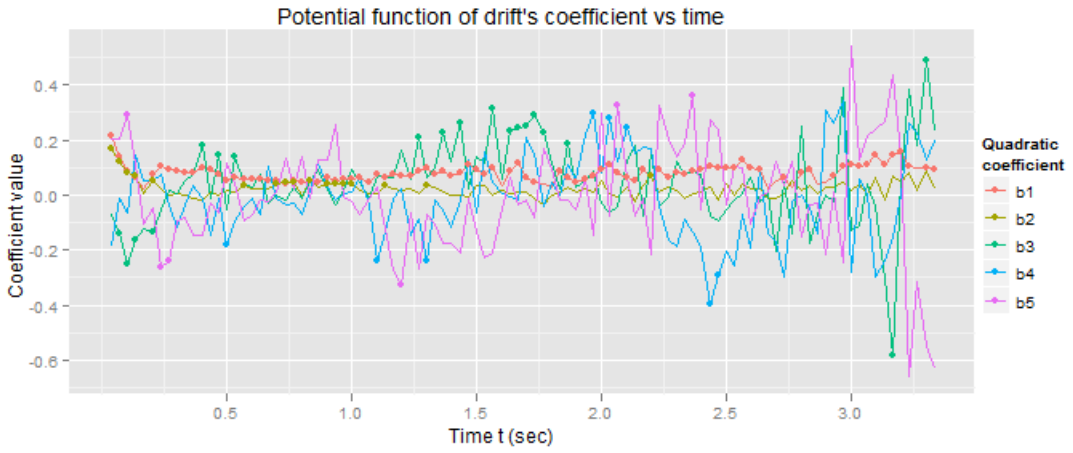

Fig. 40. Coefficients of the drift potential function vs. time (following a microsaccade) for the nonamblyopic eye. Dots denote statistically significant values. β_1 and β_2 represent linear dependence of the potential function on location. β_1 has relatively large values at the beginning and decreases with time and then maintains an approximately constant positive value that's statistically significant. β_2 shows a similar trend but it is only statistically significant for a short period of time. Coefficients of 2nd order do not show any systematic and significant pattern as a function of time.

3.2.3.2 Noise of drifts

The same model (Eq 22, 23) is applied to drift velocity noise as a function of time. And similar results are produced by the nonlinear regression, suggesting the same noise pattern of drifts for both the normal eye and the nonamblyopic eye.

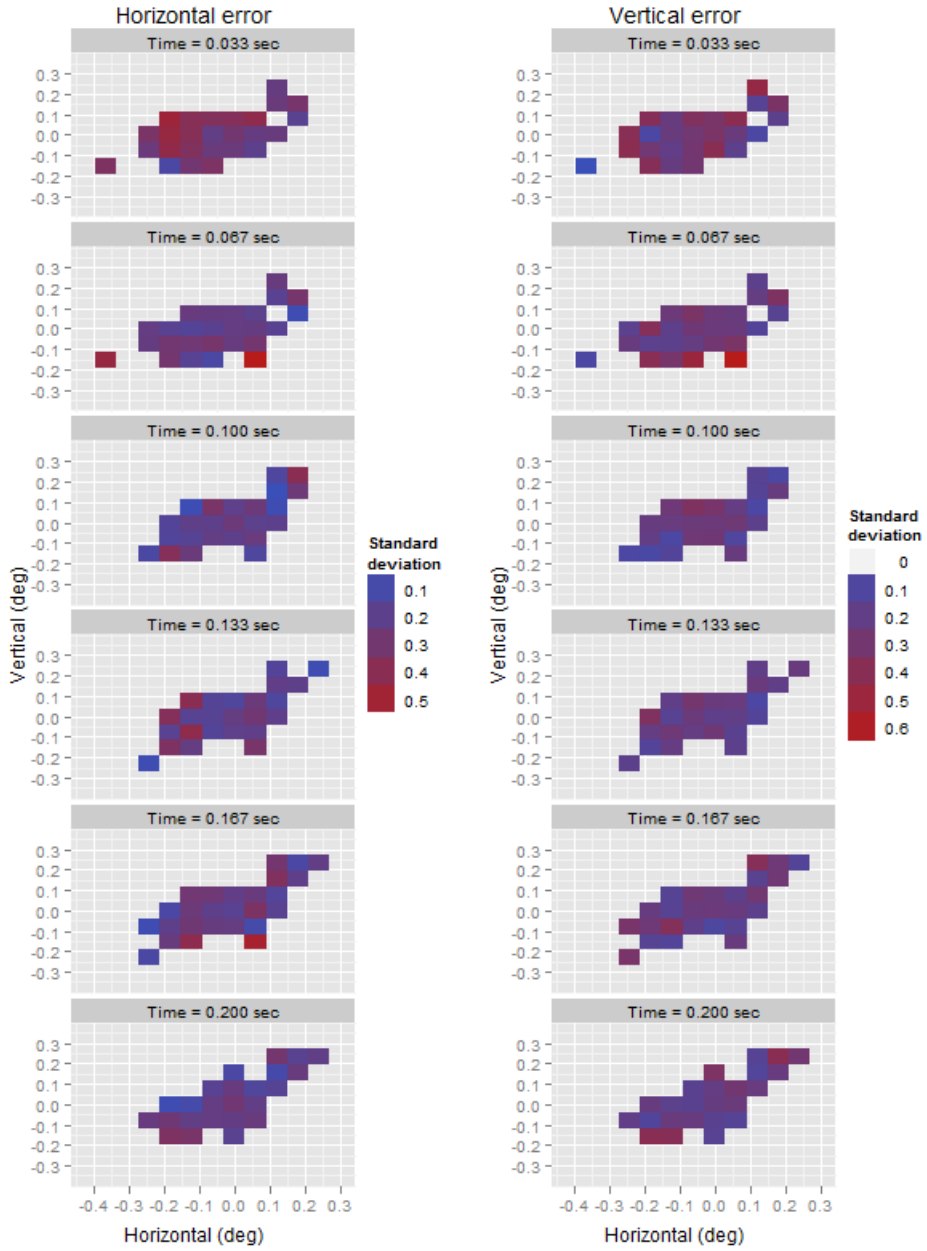

Fig. 41. Drift's a) horizontal and b) vertical velocity deviation vs. location at different times (following a microsaccade) for the nonamblyopic eye. The velocity deviation is estimated directly from the sample standard deviation. At given time (row) and direction (column), the variation of drift velocity deviation over location is relatively small.

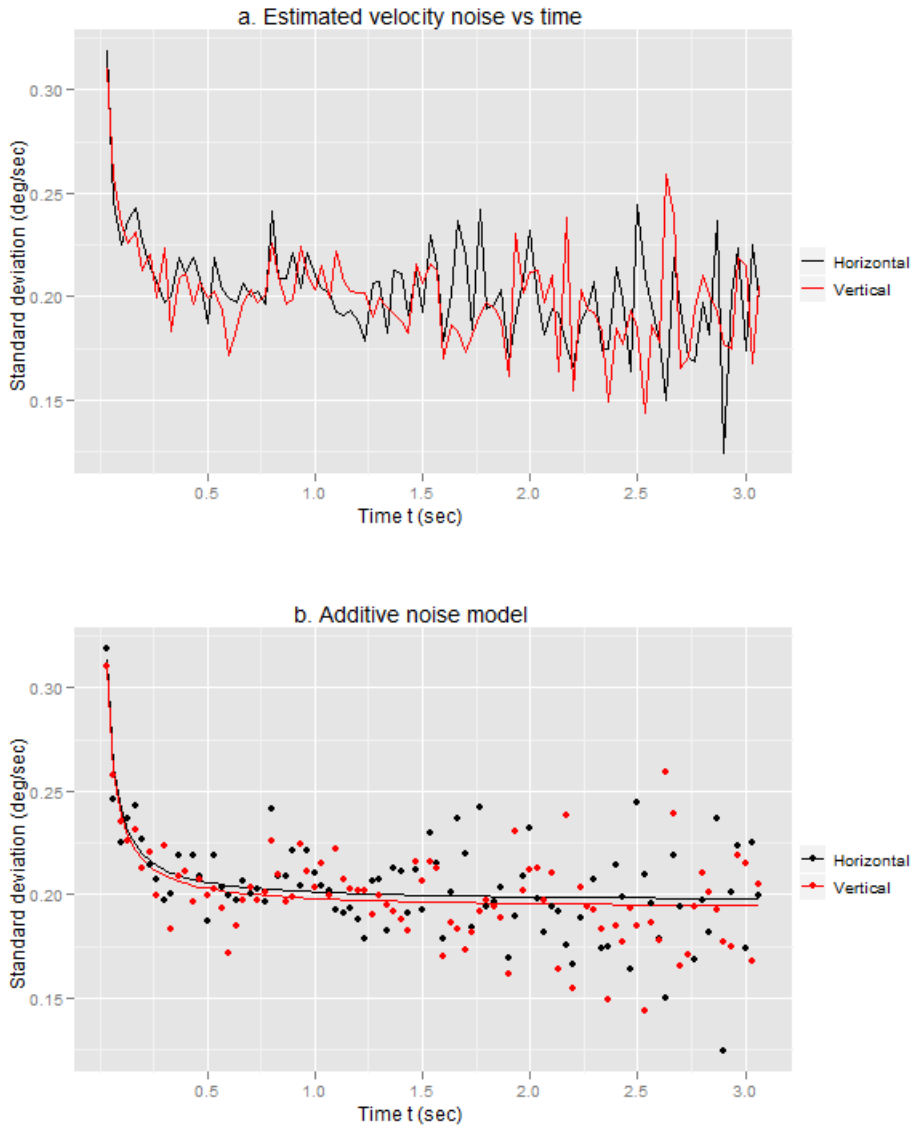

Fig. 42. a) Drift's horizontal (black) and vertical (red) velocity noise magnitude vs. time for the nonamblyopic eye. The noise estimation is based on residuals of semi-parametric spline smoothing of drifts whose sample sizes are greater than 25 at each time point. b) Additive noise models (curves) fitted to sample noise, i.e., drift velocity noise (dots), in horizontal (black) and vertical (red) directions. The fitted models are $\sigma_x(t) = \sqrt{0.039 + 0.060t^{-1.015}}$ and $\sigma_y(t) = \sqrt{0.037 + 0.059t^{-1.001}}$.

Model: $\sigma_x(t) = \sqrt{\beta_0 + \beta_1 t^{\beta_2}}$

Coefficients	Estimate	Std. Error	t value	Pr(>|t|)
β_0	0.038657	0.001429	27.054	< 2e-16 ***
β_1	0.059695	0.007308	8.168	1.96e-12 ***

β_2	-1.014524	0.199195	5.093	1.95e-06 ***
			Signif. codes:	0 '***' 0.001 '**' 0.01 '*' 0.05 '.' 0.1 ' ' 1

Model: $\sigma_y(t) = \sqrt{\beta_0 + \beta_1 t^{\beta_2}}$

Coefficients	Estimate	Std. Error	t value	Pr(>|t|)
β_0	0.037345	0.001396	26.743	< 2e-16 ***
β_1	0.058680	0.006995	8.389	6.88e-13 ***
β_2	-1.000941	0.191755	5.220	1.16e-06 ***
			Signif. codes:	0 '***' 0.001 '**' 0.01 '*' 0.05 '.' 0.1 ' ' 1

Table 10. Summary of nonlinear additive noise model regression in horizontal and vertical directions of the nonamblyopic eye.

3.3 Amblyopic eye

3.3.1 Overview

The 20-second sample trace of the strabismic amblyopic eye's fixational eye movement demonstrates the large fixation eccentricity and the high degree of instability during fixation for the amblyopic eye that is not seen in either the normal eye of DR or the nonamblyopic eye of the same amblyopic subject SF (Fig. 43). The average fixation of the amblyopic eye is located 3.8 deg nasal and 2.5 deg above the fovea. Intrusive saccades are frequent, and jerk nystagmus is also present. The amblyopic eye moves at speed up to 170.92 deg/sec, with $MAD(\omega_{AE})$ = 0.33 deg/sec and $median(\omega_{AE})$ = 0.46 deg/sec (Fig. 44-1). The same threshold speed obtained from the fellow nonamblyopic eye for microsaccades detection (i.e. 1.044 deg/sec) was applied to the amblyopic eye's fixational eye movement. Fig. 44-1 shows that the speed distribution for the amblyopic eye is grossly shifted to the right, not only for microsaccades, but also for drifts, which are differentiated by the threshold 1.044 deg/sec. This is consistent with previous findings of abnormally large drifts in strabismic amblyopia (Ciuffreda et al., 1979a, 1980). Note that although the saccadic movement may be too large (i.e. several degrees in magnitude) to be called *microsaccade* for a normal observer, for simplicity we do not change the notation in this article and one may think of it as a *pathological microsaccade*.

As we would expect from the sample traces and the summary statistics, Fig. 44 shows that microsaccades are characterized by a wide distribution of velocities with a somewhat longer tail at the lower left quadrant, whereas the velocity distribution of drifts doesn't seem to be much different from those of the normal and nonamblyopic eyes.

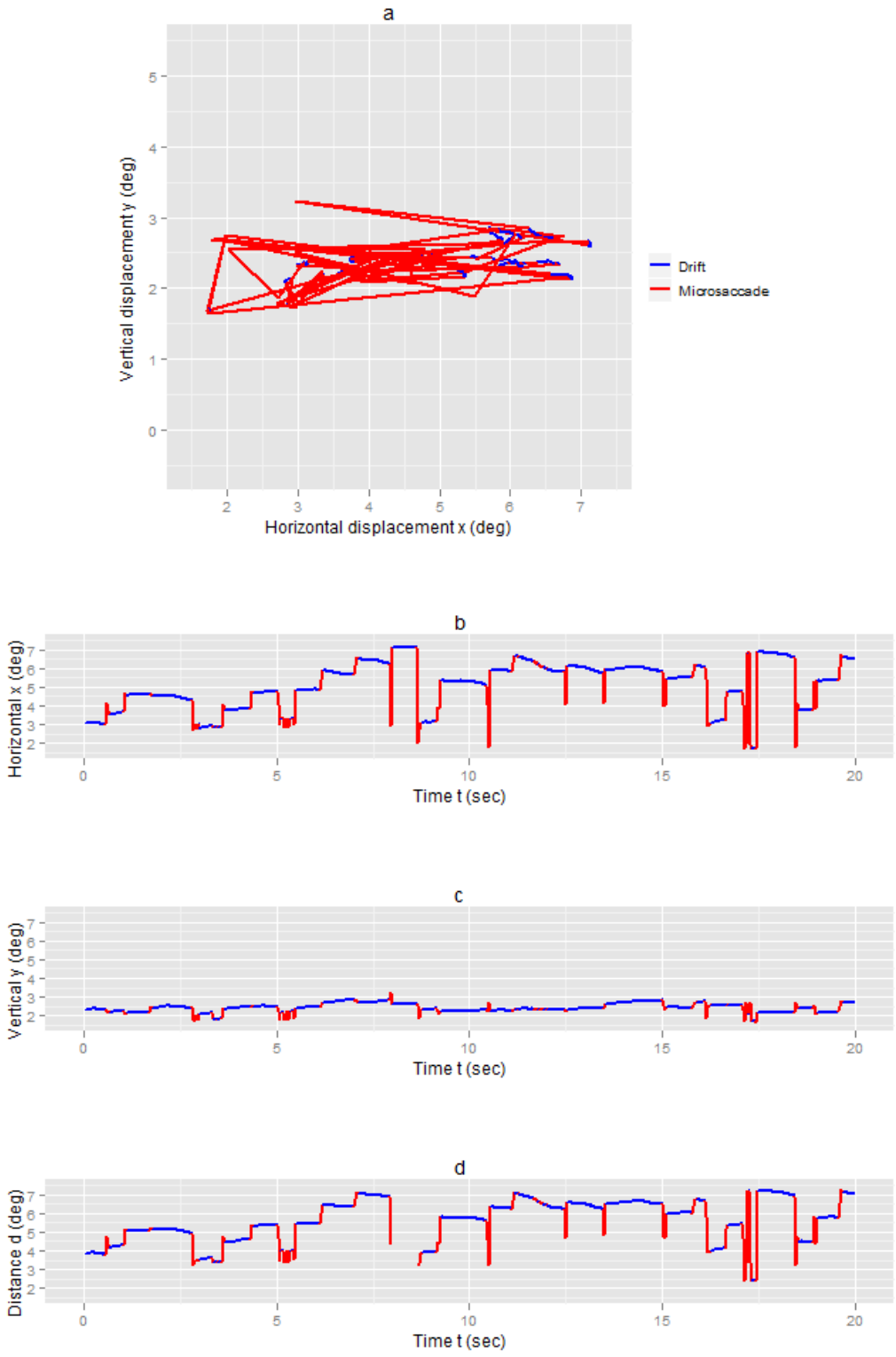

Fig. 43. A 20-second fixational eye movement sample from the amblyopic eye of the strabismic amblyopic subject SF. a) Two-dim trajectory. b) Horizontal displacement x vs. time t. c) Vertical displacement y vs.

time t. d) Euclidian distance d from the fixation vs. time t. Blue and red traces are drifts and microsaccades respectively.

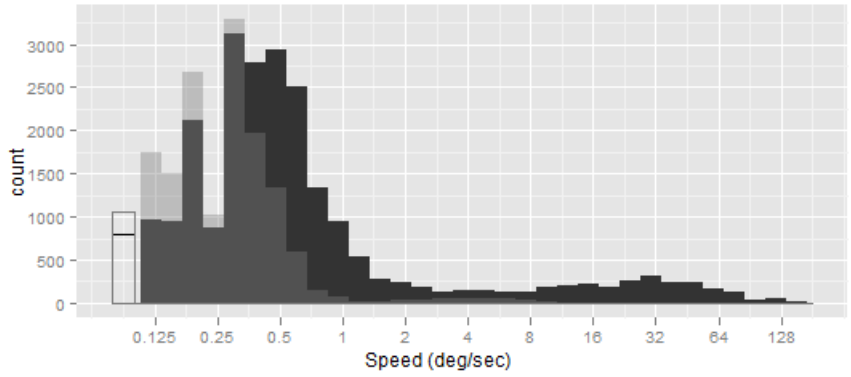

Fig. 44-1. Empirical distribution of the fixational eye movement speed magnitude ω (deg/sec) for the amblyopic eye (black) on a logarithmic axis. The unfilled black edged bar on the left represents the number of data points with zero speed. The same speed histogram for the nonamblyopic eye is superimposed (transparent grey). $Median\ (\omega)$ = 0.46 deg/sec, $MAD\ (\omega)$ = 0.33 deg/sec, $\min(\omega)$ = 0 deg/sec, $\max(\omega)$ = 170.92 deg/sec.

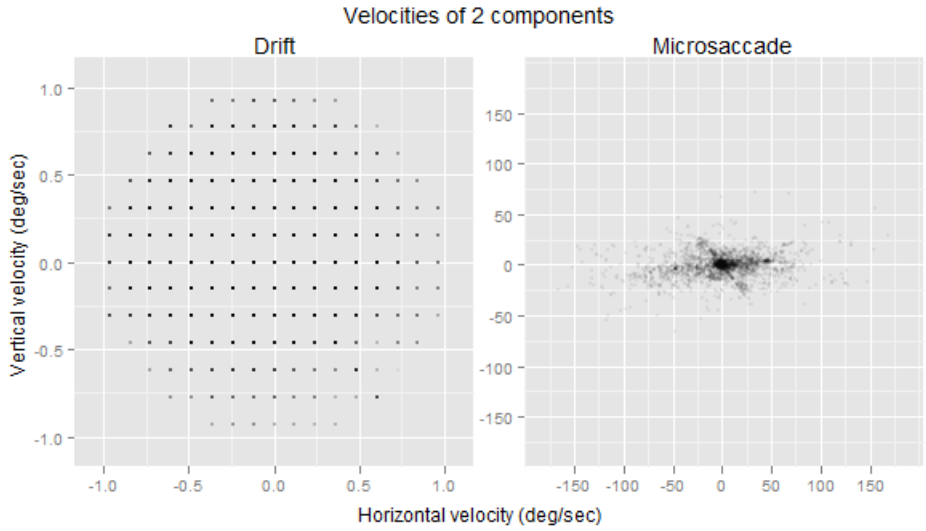

Fig. 44-2. Two-dim empirical distributions of drifts' and microsaccades' velocities for the amblyopic eye. The threshold speed for detecting microsaccades is set at 1.044 deg/sec.

During fixation, the strabismic amblyopic eye is not only eccentrically fixated, but also very poor at holding the fixation. Consequently, Fig. 45 shows a wide spread of eye positions loosely centered in the periphery. (*Note that an almost straight line of eye positions that are closest to the fovea and left of the main body of points is from one recording using a small cross fixation target only and will be excluded from data analyses*). From Fig. 45, we observe that

microsaccades tend to be attracted to different locations and form several clusters. Based on these clusters formed by microsaccades, all eye positions (including both microsaccades and drifts) are classified into 3 categories, as shown in Fig. 46, and we will refer to the 3 groups as state 0, state 1 and state 2, which will be useful for further analyses in the following section.

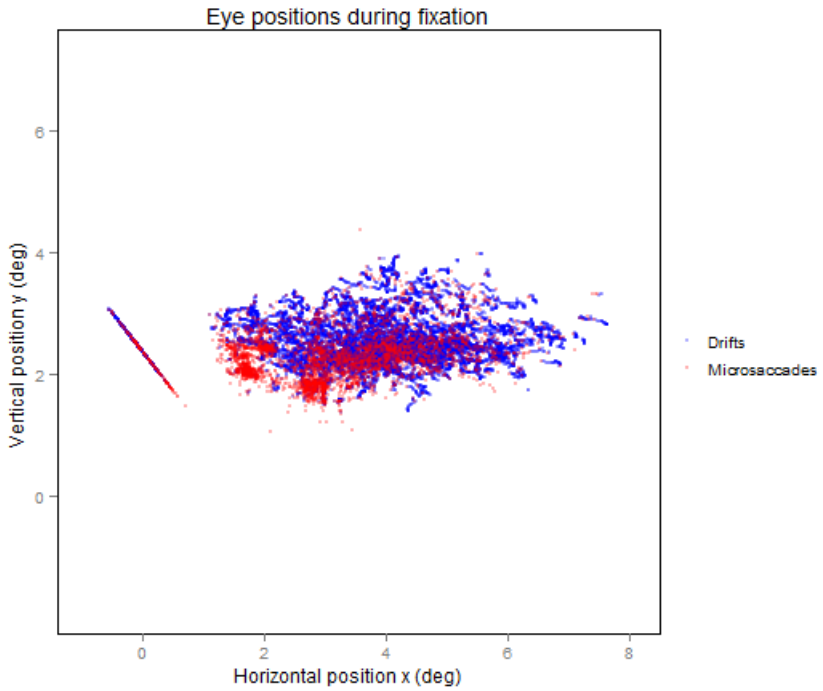

Fig. 45. Eye positions for drifts (blue) and microsaccades (red) during the amblyopic eye's fixation. The fixation area of the amblyopic eye is very wide compared to that of the normal or the nonamblyopic eye. The line of positions on the left of the main body of eye positions is from one recording only (20 sec) using a small cross as the fixation target.

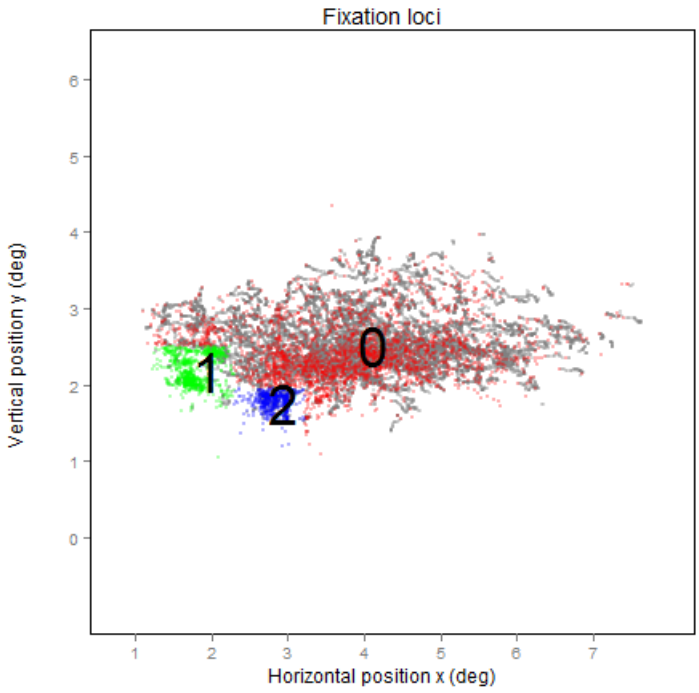

Fig. 46. Multiple loci (i.e. states) of fixation for the nonamblyopic eye. Red, blue, and green dots represent microsaccades at states 0, 1, and 2 (black numeric labels). Semi-transparent grey dots represent drifts. Drifts are also classified to these states based on location. The classification is done manually by visual assessment.

3.3.2 Microsaccades

3.3.2.1 Chain of microsaccades

The strabismic amblyopic eye positions spread over a large area several degrees wide. Since drifts are slow in speed and short in time (i.e. inter-microsaccade intervals are relatively short due to the high frequency of microsaccades), it must be microsaccades that almost exclusively contribute to the abnormally high mobility of the amblyopic eye during fixation. One microsaccade can move the fixation several degrees towards or away from the target. Clusters relatively close to the fovea are formed by microsaccades, as if the gaze were attracted to these hot spots in an attempt to achieve better acuity. In particular, we find that the distinctness of these hot spots depend on task – they are more notable for letter identification task than say, when the big cross fixation target was used, which perhaps indicates the effort made by the amblyopic eye for fixation tasks of different levels of difficulty (discussed below).

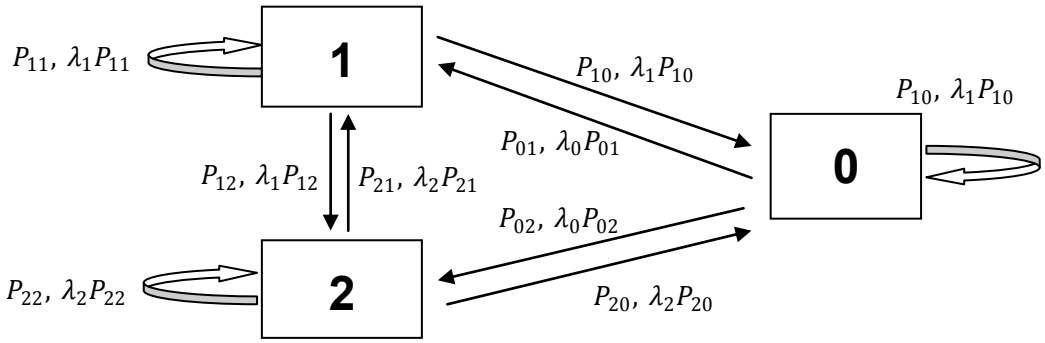

Fig. 47. Illustration of fixation states and the transition probabilities and rates of microsaccades for the amblyopic eye.

We developed a chain model of microsaccade in an attempt to characterize the drastic fixational movement of the amblyopic eye that lacks any smoothness. As introduced at the end of the previous section, each data point of the eye trace is classified to be in one of three states (0, 1, and 2). State 0 can be considered as the "resting" state that has the largest area, and states 1 & 2 correspond to two small areas that are relatively close to the fovea. During fixation, the amblyopic eye stays at a state (i.e. drifts at the same state) for some time, and then a microsaccade occurs and moves the eye position from one state to another, or to a different location at the same state, with certain probability (or rate). This process is sketched in Fig. 47, and can be characterized by a transition probability matrix or a transition rate matrix,

$$\begin{matrix} 0 \\ 1 \\ 2 \end{matrix} \begin{pmatrix} P_{00} & P_{01} & P_{02} \\ P_{10} & P_{11} & P_{12} \\ P_{20} & P_{21} & P_{22} \end{pmatrix} \begin{matrix} \boldsymbol{\pi_0} \\ \boldsymbol{\pi_1}, \\ \boldsymbol{\pi_2} \end{matrix} \qquad \begin{pmatrix} \lambda_0 P_{00} & \lambda_0 P_{01} & \lambda_0 P_{02} \\ \lambda_1 P_{10} & \lambda_1 P_{11} & \lambda_1 P_{12} \\ \lambda_2 P_{20} & \lambda_2 P_{21} & \lambda_2 P_{22} \end{pmatrix} \begin{matrix} \boldsymbol{\lambda_0} \\ \boldsymbol{\lambda_1} \\ \boldsymbol{\lambda_2} \end{matrix} \tag{34}$$

where $P_{ij} = P(arriving\ at\ state\ j \mid leaving\ state\ i)$, λ_i is the rate of the occurrence of microsaccades at state i, and π_i is the stationary distribution (density) of microsaccades at state i.

Target	State	Transition probabilities (P_{ij}) **Stationary distribution ($\boldsymbol{\pi_i}$)**	Transition rates ($\lambda_i P_{ij}$) **Overall rates ($\boldsymbol{\lambda_i}$)**
Total	0	$\begin{pmatrix} 0.85 & 0.09 & 0.06 \end{pmatrix}$ **0.64**	$\begin{pmatrix} 3.39 & 0.37 & 0.23 \end{pmatrix}$ **3.99**
	1	$\begin{pmatrix} 0.25 & 0.61 & 0.14 \end{pmatrix}$ **0.22**	$\begin{pmatrix} 5.05 & 12.43 & 2.87 \end{pmatrix}$ **20.34**
	2	$\begin{pmatrix} 0.28 & 0.18 & 0.53 \end{pmatrix}$ **0.15**	$\begin{pmatrix} 4.14 & 2.68 & 7.76 \end{pmatrix}$ **14.57**
Large cross	0	$\begin{pmatrix} 0.91 & 0.06 & 0.03 \end{pmatrix}$ **0.84**	$\begin{pmatrix} 3.40 & 0.23 & 0.10 \end{pmatrix}$ **3.72**
	1	$\begin{pmatrix} 0.48 & 0.50 & 0.02 \end{pmatrix}$ **0.12**	$\begin{pmatrix} 12.35 & 12.94 & 0.59 \end{pmatrix}$ **25.89**
	2	$\begin{pmatrix} 0.50 & 0.21 & 0.29 \end{pmatrix}$ **0.04**	$\begin{pmatrix} 6.77 & 2.90 & 3.87 \end{pmatrix}$ **13.55**

Medium cross	0	$\begin{pmatrix} 0.95 & 0.03 & 0.02 \\ 0.28 & 0.64 & 0.08 \\ 0.33 & 0.07 & 0.60 \end{pmatrix}$	$\mathbf{0.88}$ $\mathbf{0.07}$ $\mathbf{0.04}$	$\begin{pmatrix} 3.06 & 0.10 & 0.05 \\ 4.67 & 10.67 & 1.33 \\ 7.89 & 1.58 & 14.21 \end{pmatrix}$	$\mathbf{3.22}$ $\mathbf{16.67}$ $\mathbf{23.68}$
	1				
	2				
Small cross	0	$\begin{pmatrix} 0.84 & 0.10 & 0.06 \\ 0.38 & 0.49 & 0.13 \\ 0.47 & 0.19 & 0.35 \end{pmatrix}$	$\mathbf{0.73}$ $\mathbf{0.17}$ $\mathbf{0.10}$	$\begin{pmatrix} 2.47 & 0.31 & 0.17 \\ 2.11 & 2.67 & 0.70 \\ 4.65 & 1.86 & 3.49 \end{pmatrix}$	$\mathbf{2.95}$ $\mathbf{5.48}$ $\mathbf{10.00}$
	1				
	2				
Large E	0	$\begin{pmatrix} 0.82 & 0.08 & 0.11 \\ 0.27 & 0.57 & 0.16 \\ 0.29 & 0.07 & 0.64 \end{pmatrix}$	$\mathbf{0.60}$ $\mathbf{0.15}$ $\mathbf{0.25}$	$\begin{pmatrix} 3.58 & 0.34 & 0.47 \\ 7.23 & 14.92 & 4.15 \\ 3.56 & 0.85 & 7.89 \end{pmatrix}$	$\mathbf{4.39}$ $\mathbf{26.31}$ $\mathbf{12.31}$
	1				
	2				
Medium E	0	$\begin{pmatrix} 0.83 & 0.13 & 0.04 \\ 0.20 & 0.65 & 0.15 \\ 0.23 & 0.33 & 0.44 \end{pmatrix}$	$\mathbf{0.55}$ $\mathbf{0.31}$ $\mathbf{0.13}$	$\begin{pmatrix} 3.87 & 0.60 & 0.20 \\ 5.85 & 18.76 & 4.32 \\ 4.67 & 6.74 & 9.08 \end{pmatrix}$	$\mathbf{4.67}$ $\mathbf{28.93}$ $\mathbf{20.49}$
	1				
	2				

Table 11. Transition probabilities, transition rates, stationary distributions of microsaccades, and overall rates of microsaccades at states 0, 1, and 2.

The transition probabilities and rates etc. for different fixation targets/tasks are summarized in table 11. For cross fixation targets, especially those of bigger sizes (i.e. big and medium crosses), more than 70% ~ 80% of microsaccades are at the rest state (i.e. state 0), whereas for letter identification tasks, only 60% or less are at the rest state (i.e. state 0) and the other 40% or so of microsaccades are densely distributed in areas closer to the fovea (i.e. state 1 and 2).

The transition probability matrices show that most microsaccades move within the same state. The second largest proportion of microsaccades jump from the near-fovea states (i.e. 1 & 2) back to state 0, and a significant amount of the rest jump between states 1 and 2.

A natural question is that for letter identification tasks, whether the higher percentage of microsaccades in states 1 & 2 results from more accurate and possibly more stable fixation (i.e. the amblyopic eye holds the fixation at these near-fovea areas for longer periods of time), or just from more short visits to and from these states through microsaccades. Through examination of the microsaccade rates for different fixation targets this question can be easily answered. Basically, the rate would be the same or lower for letter identification compared to the cross target viewing task if the fixation is truly more accurate and better, and higher in the opposite case. Compared to the large or medium fixation cross targets, the tumbling E identification tasks have higher transition rates for all 3 states, suggesting that more frequent microsaccades bring the fixation closer to the fovea but shortly the next train of microsaccades occur, therefore the fixation was not held at any location. The long-range jumps to and from different states may represent intrusive saccades and jerk nystagmus observed by us and others (Ciuffreda et al., 1979a, 1979b; Martinez-Conde, 2006). *Since the tumbling E changes direction randomly, it will be interesting to correlate the eye movement with the direction switches of the stimuli. We will present the analysis elsewhere.* Interestingly, the small cross fixation target produces the most stable fixation of the amblyopic eye in terms of microsaccade rate. In the

experiments, the small cross is 6 min arc in size, which is slightly larger than the minimum angle of resolution (MAR) of the subject SF (4 ~ 5 min arc), hence the subject cannot resolve the details of the small cross. Perhaps it is this "effortless" viewing of a visible but small enough "blob" that somehow stabilized the amblyopic eye to some extent.

3.3.2.2 Random point process of microsaccades

Unlike that for the normal or nonamblyopic eye, the distribution of microsaccades' intervals for the amblyopic eye has the highest density at the shortest interval (Fig. 48). The *log-log* plot shows that although slightly less steep over shorter intervals, frequency decreases monotonically with inter-microsaccade interval length. Recall that for the normal eye, the histogram of intervals peaks at 0.33 sec for the normal eye and 0.867 sec for the nonamblyopic eye. The "refractory period" following a microsaccade present in both normal and nonamblyopic eyes is missing in the amblyopic eye, suggesting the normal microsaccade inhibition defect in the amblyopic eye.

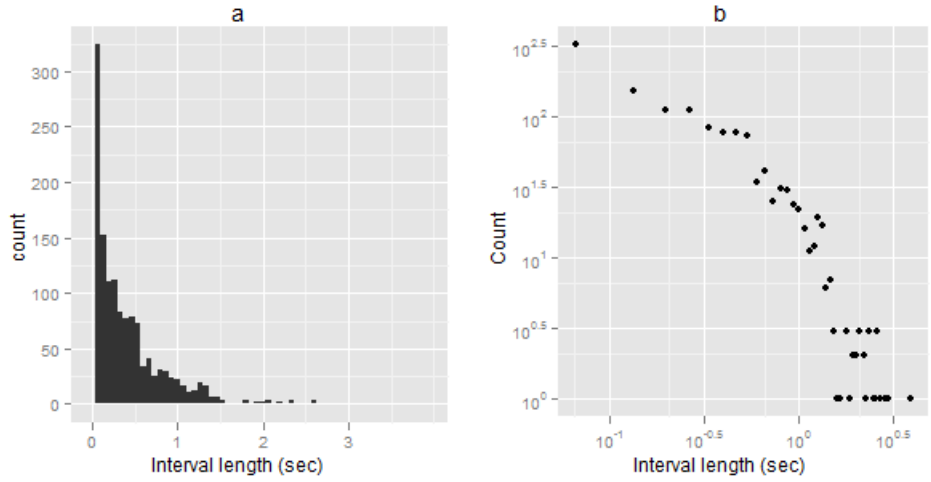

Fig. 48. a) Histogram of inter-microsaccade interval length for the amblyopic eye. The peak of the histogram is near 0. The number of intervals decreases approximately exponentially as the interval length increases. b) *Log-log* plot of a). *Log* frequency decreases monotonically with *log* interval length.

3.3.2.3 Potential function of microsaccades at state 0

As mentioned above, state 0 can be regarded as the resting state during fixation for the amblyopic eye. Indeed, the smoothed microsaccade velocity field and the fitted potential function on state 0 show similar shapes to the normal and nonamblyopic eyes (Fig. 49, 50) except that it is much steeper horizontally than it is vertically. Note that the large values of the linear coefficients (β_1 and β_2) reflect the large fixation eccentricity of the amblyopic eye, i.e. the minimum of the reversed potential function is far from the fovea (0,0).

Model: $V(x,y) = \beta_0 + \beta_1 x + \beta_2 x^2 + \beta_3 y + \beta_4 y^2 + \beta_5 xy$

Coefficients	Estimate	Std. Error	t value	Pr(>|t|)
β_1	39.0794	1.5851	24.655	< 2e-16 ***
β_2	10.4690	2.5109	4.169	3.11e-05 ***
β_3	-4.6507	0.1718	-27.066	< 2e-16 ***
β_4	-1.9382	0.4525	-4.283	1.88e-05 ***
β_5	-0.2489	0.3221	-0.773	0.44

Signif. codes: 0 '***' 0.001 '**' 0.01 '*' 0.05 '.' 0.1 ' ' 1

Multiple R^2	0.1497
Adjusted R^2	0.1488

Table 12. Summary of microsaccade's (state 0) potential function regression for the amblyopic eye.

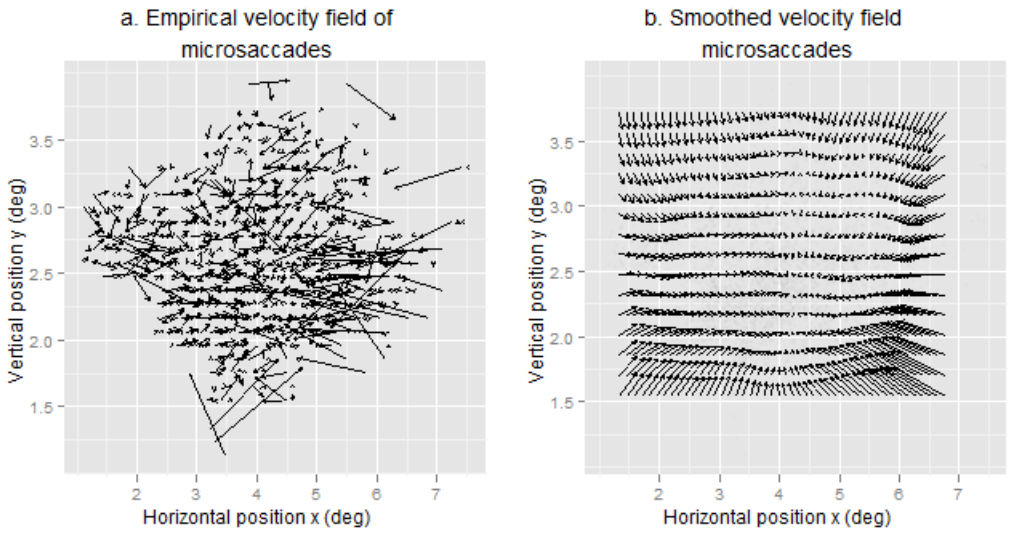

Fig. 49. a) Empirical and b) smoothed velocity fields of microsaccades of the amblyopic eye. Each arrow represents the averaged velocity of microsaccades in a small bin. The beginning position of each arrow is absolute, whereas the end position (i.e. arrow head) and the length of the arrow may be scaled. The smoothed velocities are predicted by the semi-parametric spline smoothing of degree 4.

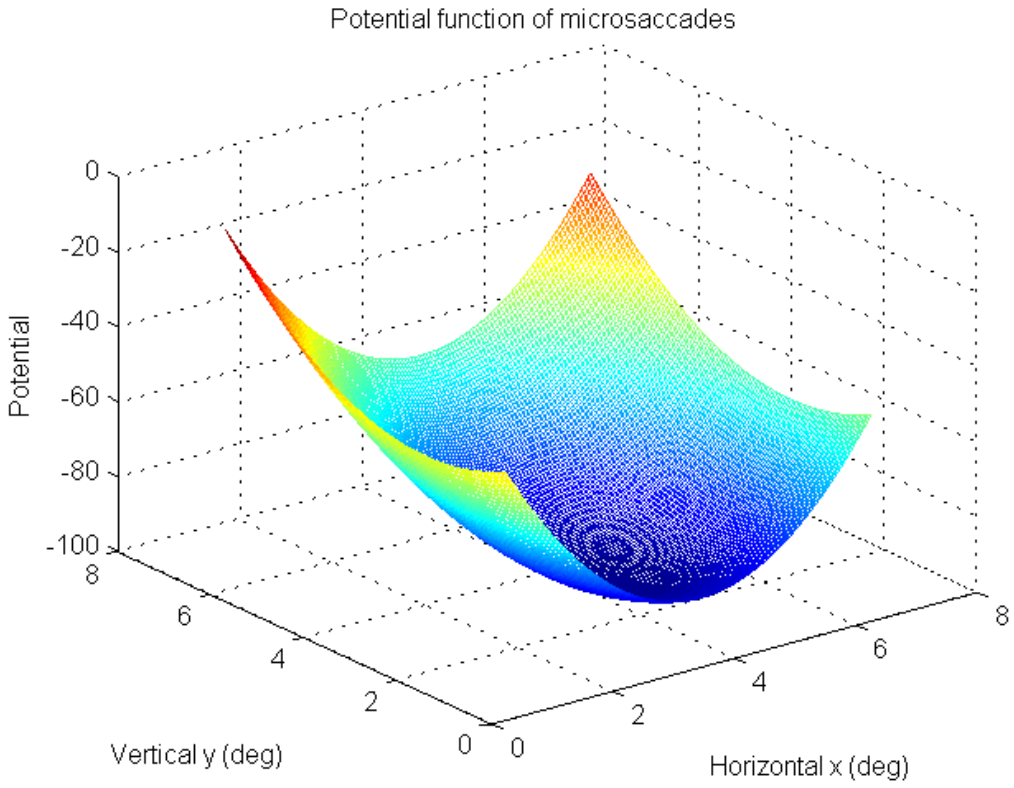

Fig. 50. Reversed potential function for microsaccades for the amblyopic eye, $V(x,y) = 39.08.01x + 10.47y - 4.65x^2 - 1.94y^2 - 0.25xy$.

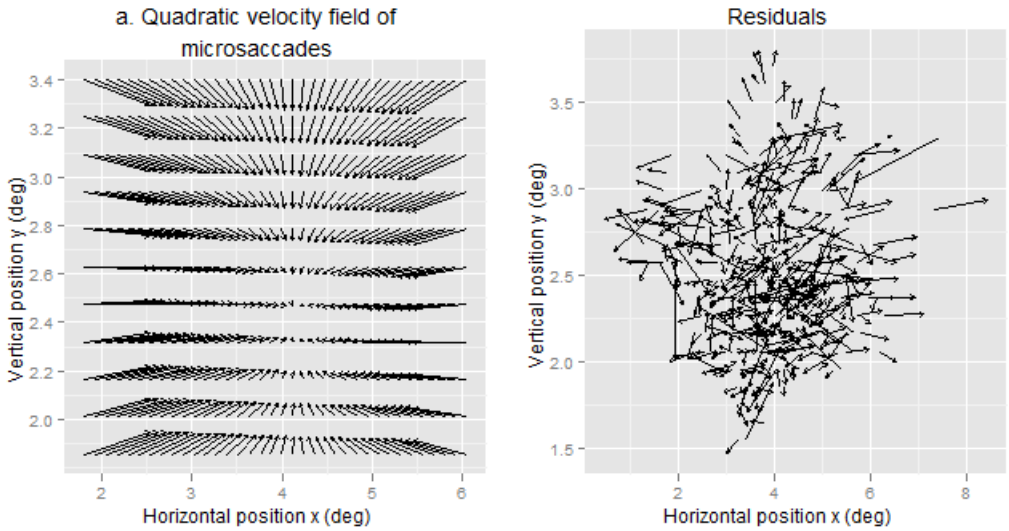

Fig. 51. a) Microsaccades' velocity field predicted by the fitted quadratic potential function for the amblyopic eye, and b) the corresponding residual velocity field. The full model including all terms, regardless of statistical significance, is used.

Similar to the normal and nonamblyopic eyes, the noise of microsaccade velocity for the amblyopic eye measured empirically from sample standard deviations doesn't vary much over location compared to the wide distribution of microsaccade speed that ranges from 1.044 deg/sec to 170.09 deg/sec. The velocity noise estimated through fitted residuals of the potential function are: $\hat{\sigma}_x = \sqrt{\frac{RSS_x}{df}} =$ 23.55 deg/sec, $\hat{\sigma}_y = \sqrt{\frac{RSS_y}{df}} =$ 5.69 deg/sec.

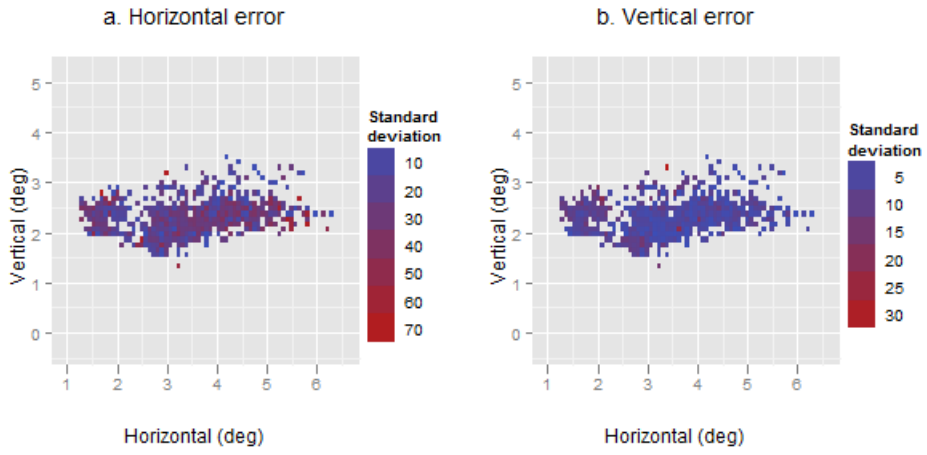

Fig. 52. Microsaccade's a) horizontal and b) vertical velocity deviation vs. location for the amblyopic eye. The velocity deviation is estimated directly from the standard deviations of microsaccades.

3.3.3 Drifts

3.3.3.1 Potential functions of drifts

We have checked that the distribution of either horizontal or vertical velocity can be nicely approximated by a Gaussian distribution (Appendix 3A).

Following a microsaccade, the amblyopic eye position drifts upward and leftward (i.e. temporalward). The average sub-drift is fairly straight with a small variation near the origin. Since the fovea is located below and left of the average fixation center, drift decreases the horizontal displacement but increases the vertical displacement of the eye position on average. This result is an exception of previous findings that nasal drifts occurred more often in the strabismic amblyopic eye. Fig. 53 depicts the trend of the average drift velocity of an entire frame over time, but bears no information regarding the relation between drift velocity and location, which can be characterized by the potential function as we have seen before.

Potential functions of quadratic polynomials for the amblyopic eye are fitted to drifts in the same way as for the normal and nonamblyopic eyes. Aside from a bias potential function characterizing an upward and leftward movement (Fig. 53 ~ 59), the drift potential function for the amblyopic eye also depends on time, similar to the normal and nonamblyopic eyes. Immediately following a microsaccade, the drift is directed towards some point of attraction (Fig. 60). However, such attraction locations are not near the average fixation center and the velocity's quadratic dependence on location is fairly weak (i.e. $R^2 < 0.1$), suggesting existence of strong bias and possibly high degree of randomness in early sub-drifts. Points of attraction, although weak, disappear with time.

Interestingly, the approximately constant variance over location for each time point, as well as its relation with time which can be characterized by an additive noise model, is not much different from those of the normal and the nonamblyopic eyes (Fig. 61, 62), which suggests that the randomness (noise) of drifts that cannot be characterized by the potential function is probably not sensory noise that would be related to the poor vision of the amblyopic eye.

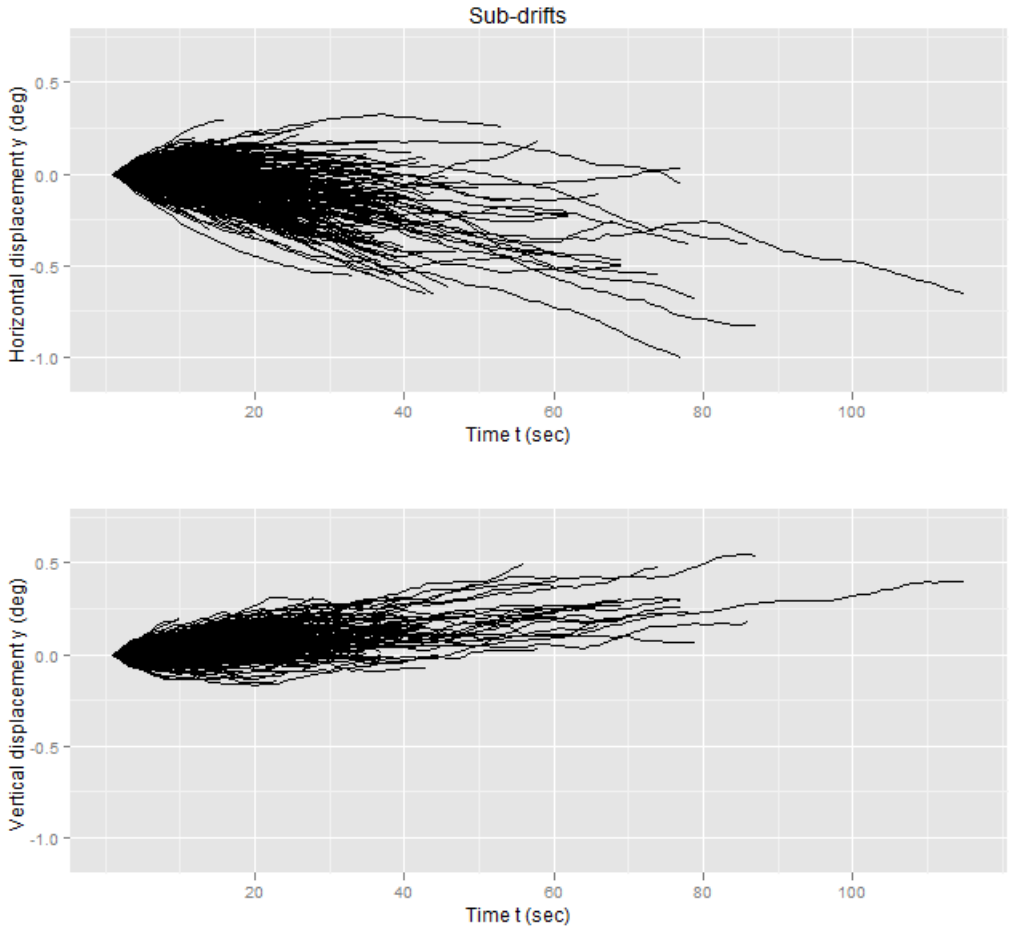

Fig. 53-1. Sub-drifts' displacements vs. time (following microsaccades) in horizontal and vertical directions for the amblyopic eye (see Methods).

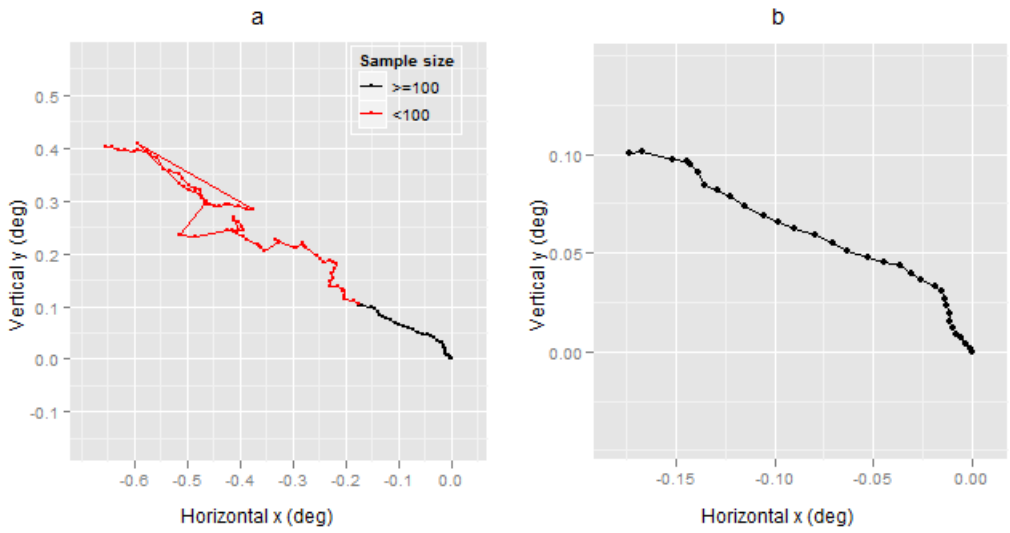

Fig. 53-2. Average trajectory of sub-drifts of a) any sample size or of b) only large sample size (i.e. greater than 100), for the amblyopic eye. Black and red traces denote sample sizes greater than or less than 100 respectively. The trajectory starts at **0** since the position of the first point is subtracted from all points (see Methods).

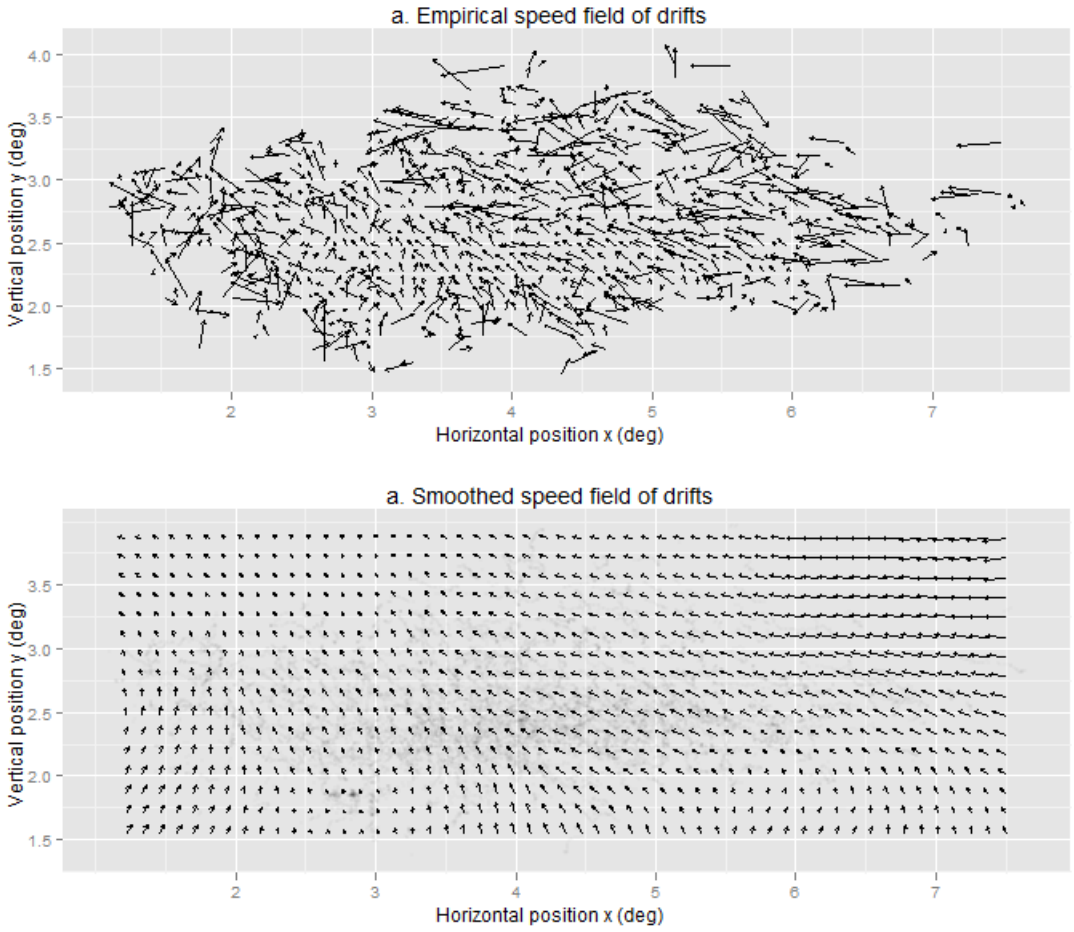

Fig. 54. a) Empirical and b) smoothed velocity fields of the drift for the amblyopic eye. Each arrow represents the averaged velocity of drifts in a small bin. The beginning position of each arrow is absolute, whereas the end position (i.e. arrow head) and the length of the arrow may be uniformly scaled. The smoothed velocities are predicted by the semi-parametric spline smoothing of degree 4. Eye positions of original data are scattered as semi-transparent points in the smoothed velocity field.

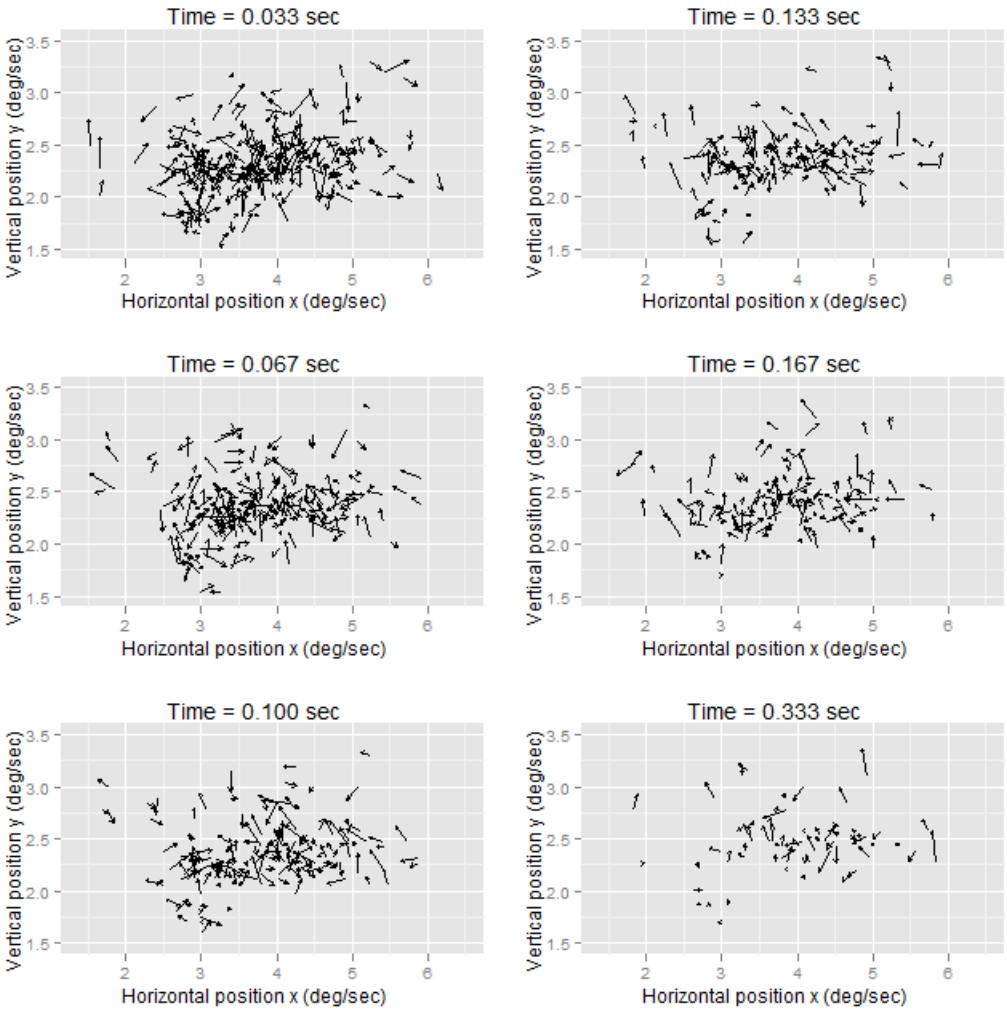

Fig. 55-1. Drift's empirical velocity fields at different times (following a microsaccade) for the amblyopic eye. Each arrow represents the averaged velocity of drifts in a bin with small widths. The beginning position of each arrow is absolute, whereas the end position (i.e. arrow head) and the length of the arrow may be uniformly scaled.

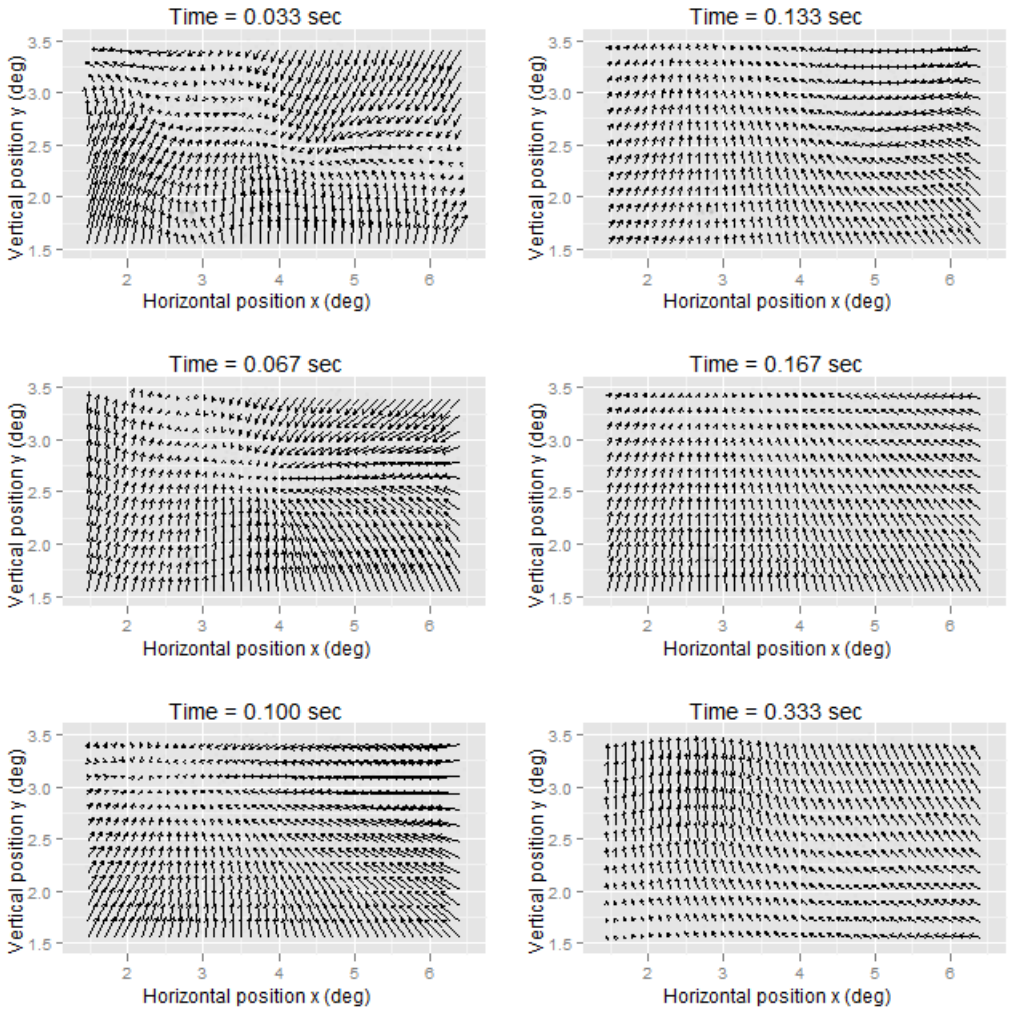

Fig. 55-2. Drift's smoothed velocity fields at different times (following a microsaccade) for the amblyopic eye. The smoothed velocities are predicted by the semi-parametric spline smoothing of degree 4.

Model: $V(x,y) = \beta_0 + \beta_1 x + \beta_2 x^2 + \beta_3 y + \beta_4 y^2 + \beta_5 xy$

Time =1

Coefficients	Estimate	Std. Error	t value	Pr(>|t|)
β_1	0.221854	0.042198	5.257	1.57e-07 ***
β_2	0.554378	0.065480	8.466	< 2e-16 ***
β_3	-0.019861	0.004771	-4.163	3.23e-05 ***
β_4	-0.073197	0.013168	-5.559	2.96e-08 ***
β_5	-0.038937	0.009173	-4.245	2.26e-05 ***

Signif. codes: 0 '***' 0.001 '**' 0.01 '*' 0.05 '.' 0.1 ' ' 1

Multiple R^2 0.0382

Adjusted R^2	0.0365			

Time =2

Coefficients	Estimate	Std. Error	t value	Pr(>|t|)
β_1	0.253730	0.042013	6.039	1.79e-09 ***
β_2	0.580422	0.065521	8.859	< 2e-16 ***
β_3	-0.035805	0.004664	-7.677	2.35e-14 ***
β_4	-0.088385	0.012758	-6.928	5.47e-12 ***
β_5	-0.018148	0.008900	-2.039	0.0416 *
			Signif. codes:	0 '***' 0.001 '**' 0.01 '*' 0.05 '.' 0.1 ' ' 1
Multiple R^2	0.0859			
Adjusted R^2	0.0840			

Time =3

Coefficients	Estimate	Std. Error	t value	Pr(>|t|)
β_1	0.253706	0.040013	6.341	2.78e-10 ***
β_2	0.415922	0.063413	6.559	6.75e-11 ***
β_3	-0.040973	0.004414	-9.283	< 2e-16 ***
β_4	-0.059339	0.012223	-4.855	1.29e-06 ***
β_5	-0.011508	0.008421	-1.367	0.172
			Signif. codes:	0 '***' 0.001 '**' 0.01 '*' 0.05 '.' 0.1 ' ' 1
Multiple R^2	0.1111			
Adjusted R^2	0.1090			

Time =20

Coefficients	Estimate	Std. Error	t value	Pr(>|t|)
β_1	-0.169348	0.069799	-2.426	0.0156 *
β_2	0.104208	0.129587	0.804	0.4217
β_3	-0.010784	0.007079	-1.523	0.1283
β_4	-0.004014	0.022085	-0.182	0.8559
β_5	0.005792	0.013484	0.430	0.6677
			Signif. codes:	0 '***' 0.001 '**' 0.01 '*' 0.05 '.' 0.1 ' ' 1
Multiple R^2	0.3362			
Adjusted R^2	0.3299			

Table 13. Summary of the drift potential function regressions at different times (following a microsaccade) for the amblyopic eye.

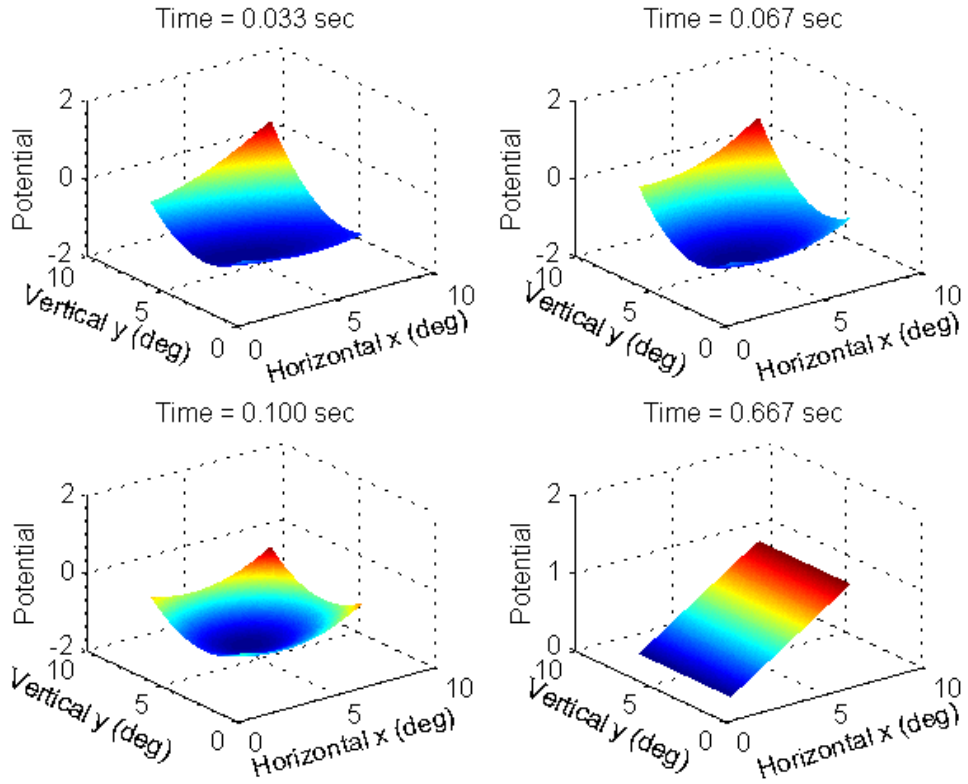

Fig. 57. Reversed potential functions of the drift at different times following a microsaccade for the amblyopic eye. $V(x, y, t = 0.033) = 0.22x + 0.55y - 0.02x^2 - 0.07y^2 - 0.04xy$; $V(x, y, t = 0.067) = 0.25x + 0.58y - 0.04x^2 - 0.09y^2 - 0.02xy$; $V(x, y, t = 0.100) = 0.25x + 0.42y - 0.04x^2 - 0.06y^2$; $V(x, y, t = 0.667 = 0.17x$.

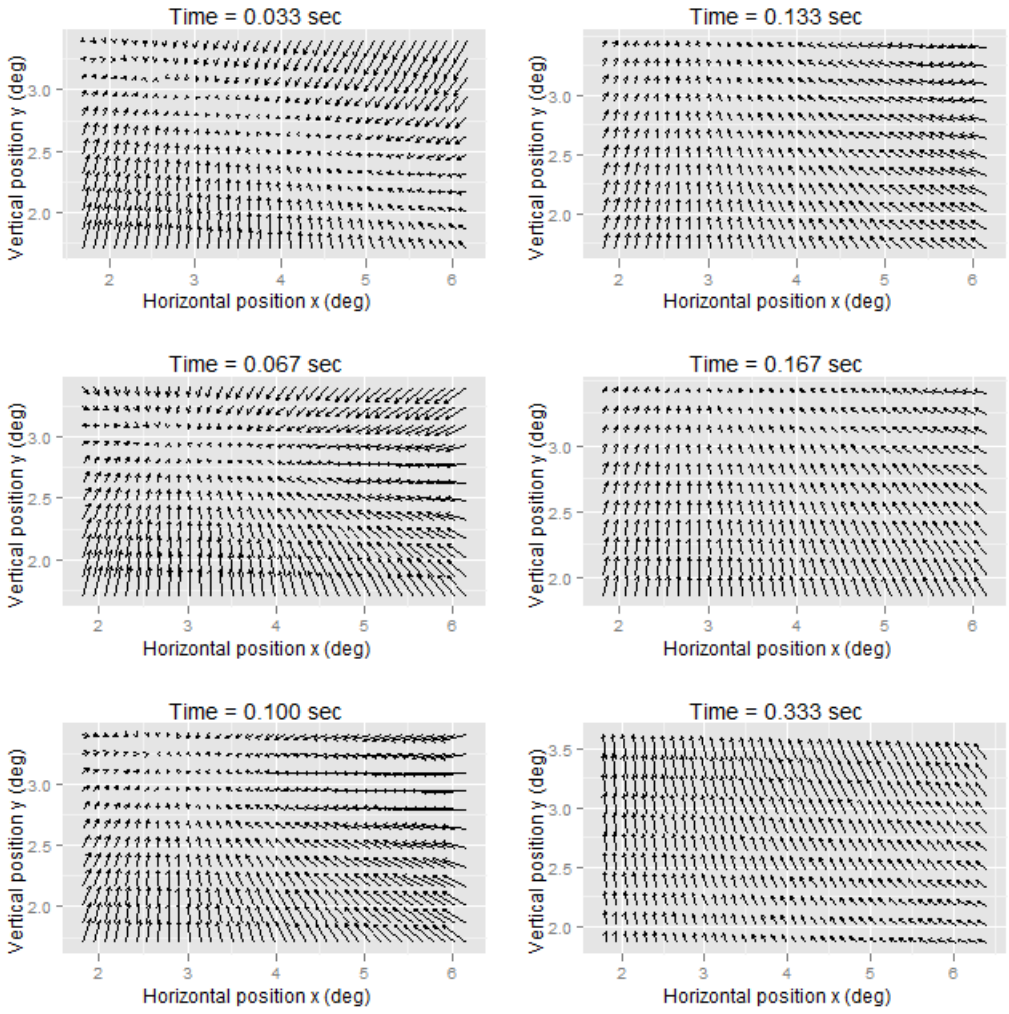

Fig. 58-1. Drift velocity fields at different times following a microsaccade predicted by fitted quadratic potential functions (Fig. 57) for the amblyopic eye. The full model including all terms, regardless of statistical significance, is used.

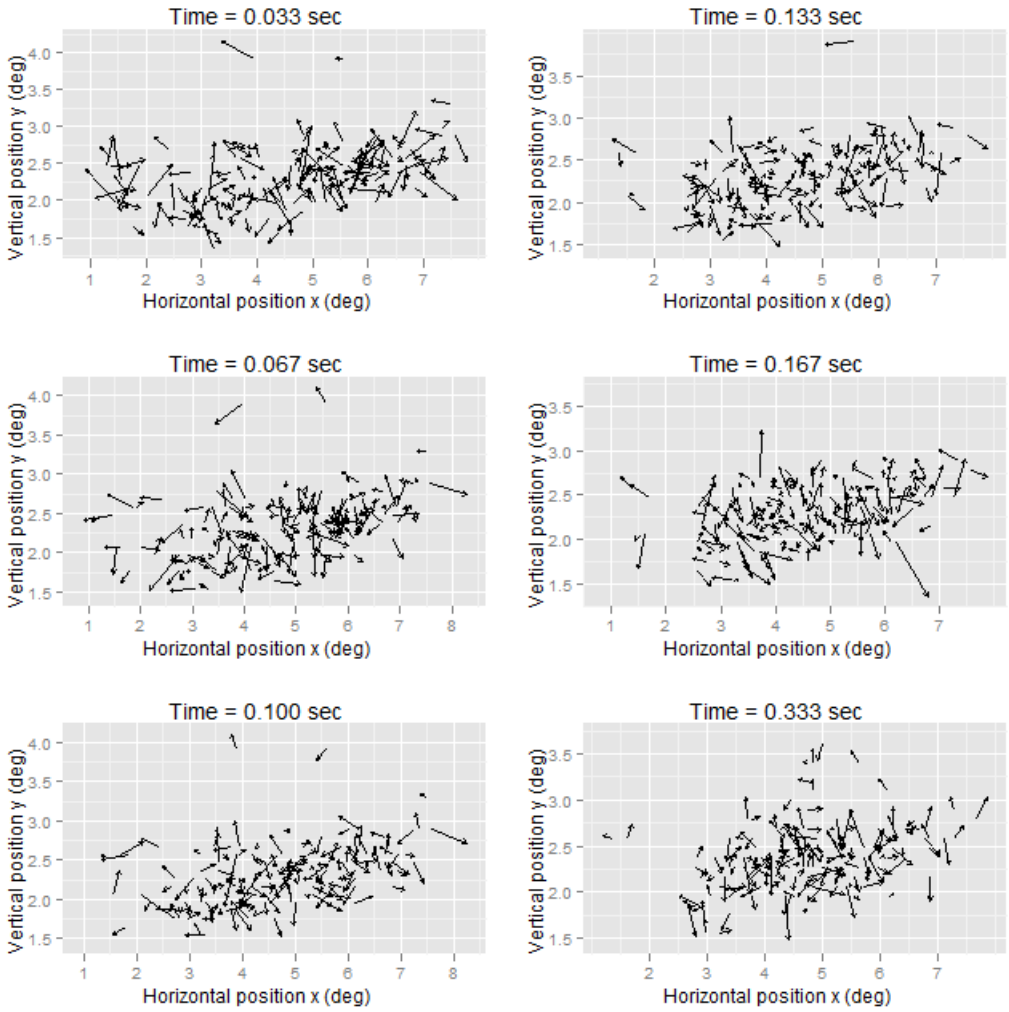

Fig. 58-2. Drift residual velocity field after the fitting of quadratic potential functions (Fig. 57) for the amblyopic eye.

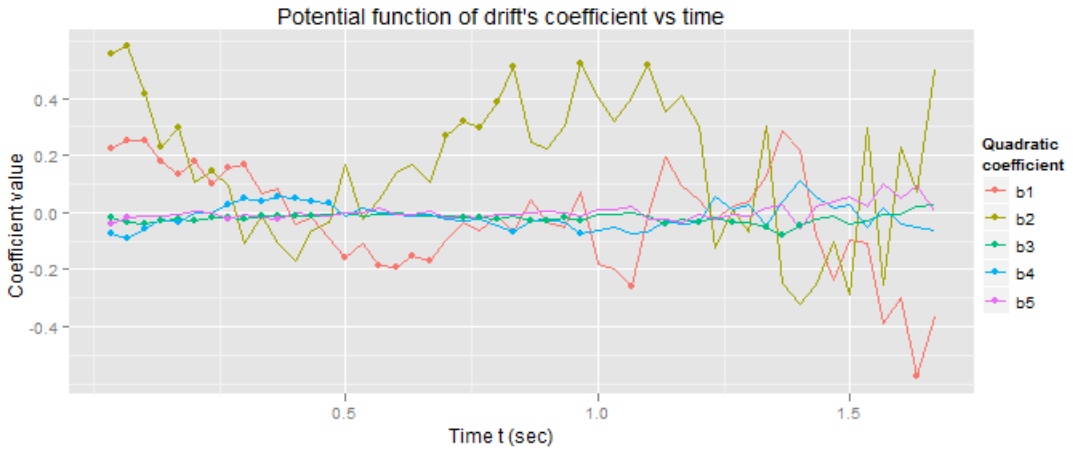

Fig. 59. Coefficients of the drift potential function vs. time (following a microsaccade) for the amblyopic eye. Dots denote statistically significant values. Coefficients of linear terms, β_1 and β_2, have relatively large values that are statistically significant near the beginning, and then lose the significance as time increases. Coefficients of the 2nd order are small compared to those of the 1st order (i.e. linear terms).

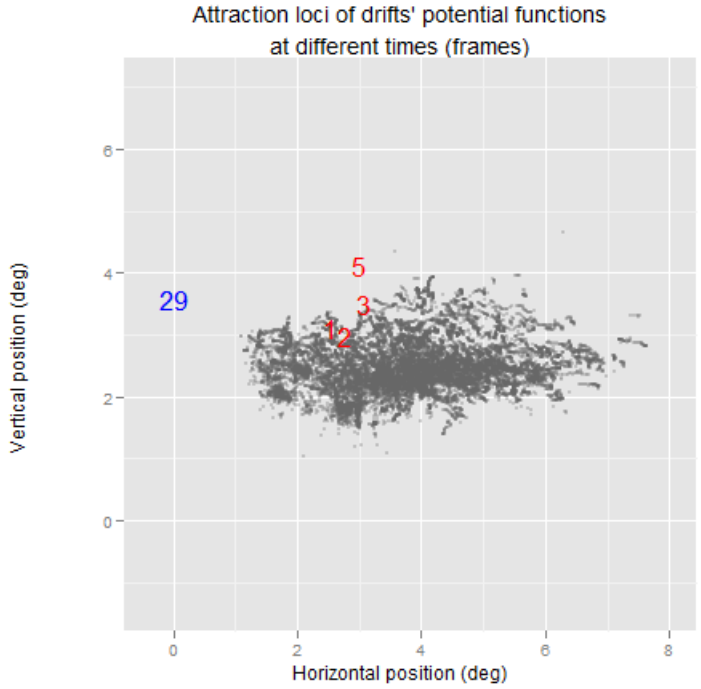

Fig. 60. Drift's loci of attraction predicted by fitted potential functions at different times for the amblyopic eye. Red and blue text 1, 2, 3, 5 and 29 represents all existing attraction points that are of the specified frames, i.e., 0.033 sec, 0.067 sec, 0.1 sec, 0.167 sec, and 0.967 sec following a microsaccade respectively. The attraction points are superimposed on the eye positions (grey dots).

3.3.3.2 Noise of drifts

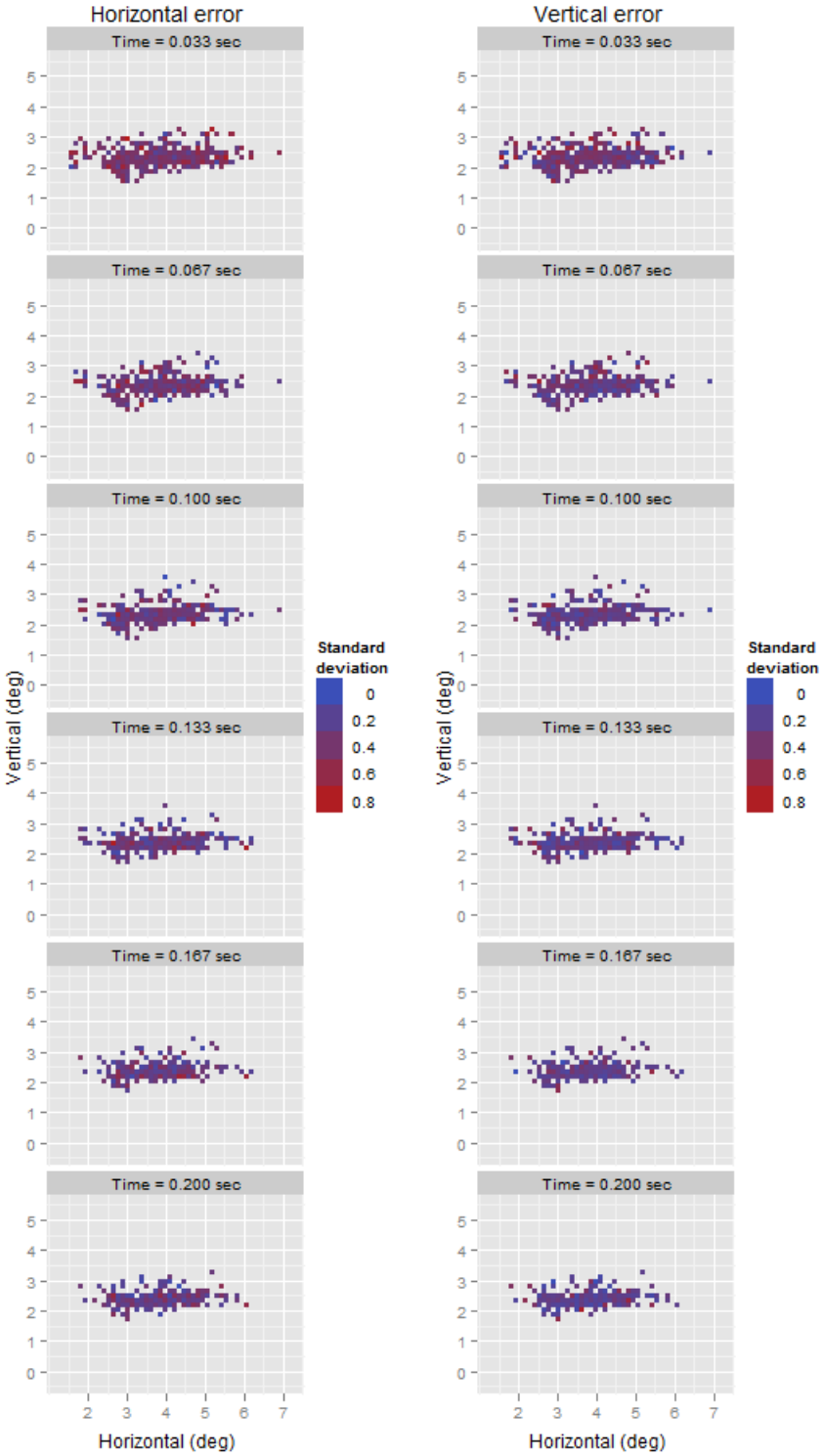

Fig. 61. Drift's a) horizontal and b) vertical velocity deviation vs. location at different times (following a microsaccade) for the amblyopic eye. The velocity deviation is estimated directly from sample standard

deviations. At given time (row) and direction (column), the variation of drift velocity noise magnitude over location is relatively small.

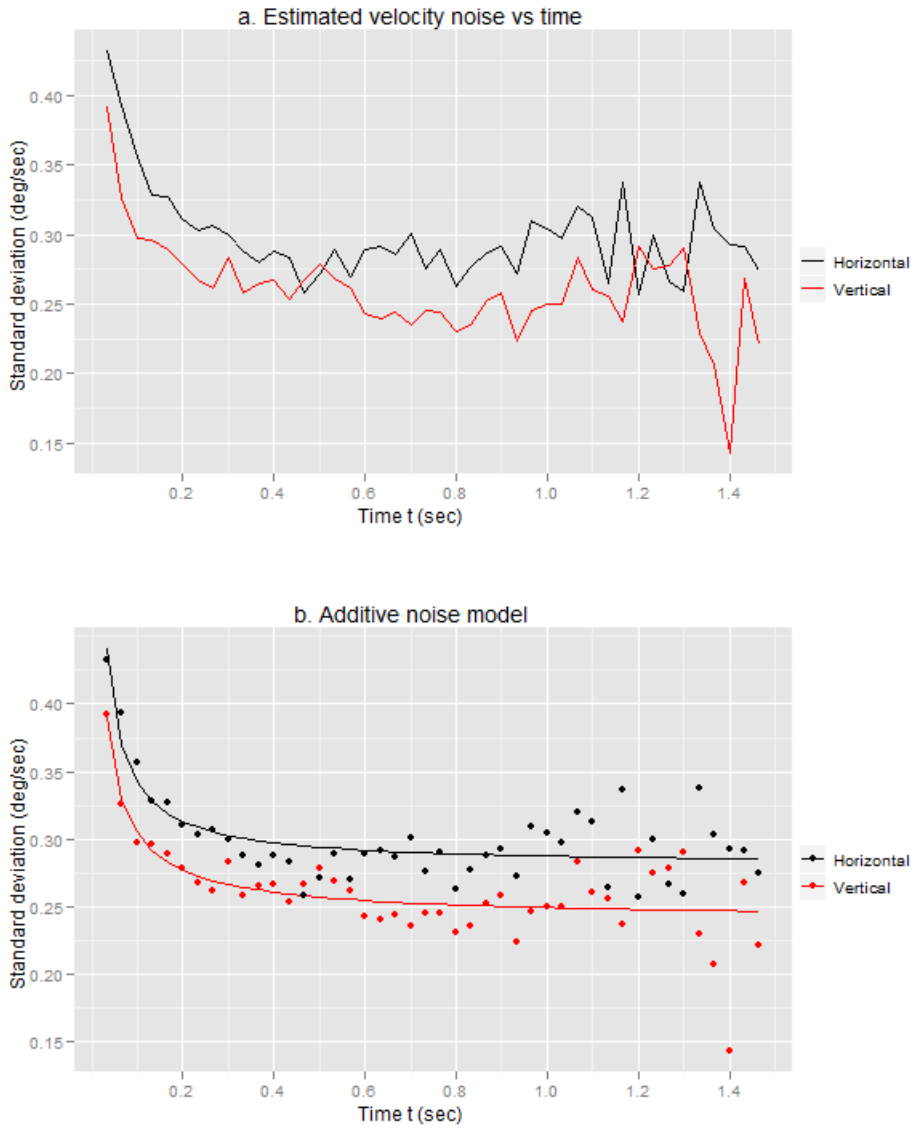

Fig. 62. a) Drift's horizontal (black) and vertical (red) velocity noise magnitude vs. time for the amblyopic eye. The noise estimation is based on residuals of semi-parametric spline smoothing of drifts whose sample sizes are greater than 25 at each time point. b) Additive noise models (curves) fitted to sample noise, i.e., drift velocity noise (dots), in horizontal (black) and vertical (red) directions. The fitted models are $\sigma_x(t) = \sqrt{0.079 + 0.116t^{-1.005}}$ and $\sigma_y(t) = \sqrt{0.057 + 0.095t^{-0.887}}$.

Model: $\sigma_x(t) = \sqrt{\beta_0 + \beta_1 t^{\beta_2}}$

Coefficients	Estimate	Std. Error	t value	Pr(>|t|)
β_0	0.078783	0.004015	19.620	< 2e-16 ***
β_1	0.116013	0.011294	10.272	6.64e-13 ***
β_2	-1.004655	0.196018	5.125	7.49e-06 ***
			Signif. codes:	0 '***' 0.001 '**' 0.01 '*' 0.05 '.' 0.1 ' ' 1

Model: $\sigma_y(t) = \sqrt{\beta_0 + \beta_1 t^{\beta_2}}$

Coefficients	Estimate	Std. Error	t value	Pr(>|t|)
β_0	0.057462	0.004567	12.583	1.15e-15 ***
β_1	0.094804	0.010342	9.167	1.77e-11 ***
β_2	0.886665	0.206437	4.295	0.000104 ***
			Signif. codes:	0 '***' 0.001 '**' 0.01 '*' 0.05 '.' 0.1 ' ' 1

Table 14. Summary of nonlinear additive noise model regressions in horizontal and vertical directions of the amblyopic eye.

4 Discussion and summary

4.1 Normal fixational eye movements

Although fixational eye movements are random on small scales of time and space, they are clearly not random on visible scales under normal conditions, i.e. they are strictly centered on the fixation locus with very small variation, no matter how long the fixating time is. The oculomotor mechanisms of fixation maintenance by the miniature eye movement have a long history of investigation. At first, it was hypothesized that drifts are random and produce inaccuracies of fixation whereas microsaccades can correct these errors by returning the eye position towards the fixation location (i.e. fovea) (Cornsweet, 1956). However, this speculation was challenged by others who had found inconsistent or even contradictory results. A number of studies claimed that microsaccades are both error producing and error correcting (Kowler & Steinman, 1979, 1980; Nachmias, 1959, 1961).

By comparing distributions of the beginning and end positions of error-correcting and error-producing microsaccades respectively, we find that on average microsaccades correct for fixation inaccuracy and therefore are important in fixation maintenance. The potential function of microsaccade is symmetrically centered at the fixation location and can be approximated by a quadratic surface, which predicts that microsaccades are more likely to move faster and in the "correct" direction (i.e. towards the target) at relatively large fixation displacements, where the rate of the occurrence of microsaccades is also higher.

It has been proposed that drifts may also contribute to correcting fixation errors through slow control (Kowler & Steinman, 1979; Steinman et al., 1967; Steinman et al., 1973). Drift potential functions at different times show that there exists a velocity bias which seems to be

intrinsic to the drift. In other words, the base component of a drift can be approximated by a simple two-dimensional Brownian motion with constant two-dimensional rate (i.e. bias). The direction and magnitude of the bias are probably different for different individuals. But Brownian motion is not all about a drift. Following a microsaccade, initially, the drift potential function has a global maximum (i.e. point of attraction) similar to that of microsaccades. But this centric organization with attraction of drift velocity disappears within a few hundred mini-seconds and then the random motion with bias becomes dominant. It is as if at first drift is driven by some feedback mechanism that detects and corrects fixation errors, but soon the sensitivity is lost, possibly due to adaptation. Then, fixation drifts randomly (with bias) until the occurrence of another microsaccade, which refreshes the "memory" and re-sensitizes the error correcting mechanism for drifts. It seems plausible that microsaccades contribute to the maintenance of accurate fixation not only by directly returning the deviated fixation to the target, but also by ending the random phase of a drift and triggering its error-correcting potential. Since there is evidence that drift alone can maintain stable fixation through slow control, some people have raised doubt as to whether microsaccades have any significant and indispensible role in fixation other than mere "busy work" (Kowler & Steinman, 1979, 1980). It is true that when we aim at a tiny object or focus on a target, fixation is more stable even though microsaccades are less frequent, but a great amount of attention is paid which requires a lot of effort. Such fixation process is tiring, and little attention is allocated to the surroundings. This certainly is not optimal under many other conditions.

Microsaccades are synchronized binocularly. While drifts are not correlated between the two eyes, directions and amplitudes of microsaccades are, and it has been reported that microsaccades can reduce binocular disparity (Engbert & Kliegl, 2004). Binocular fixational eye movements are not the topic of the current study since all our data were recorded monocularly. However, both eyes of the strabismic amblyopic patient strongly suggest that the direction and magnitude of microsaccade for the nonamblyopic eye are correlated with those of abnormally large "microsaccade" for the amblyopic eye. Since the rates of the occurrence of microsaccades are quite different between the nonamblyopic and the amblyopic eyes, there must be only a small percentage of microsaccades that are synchronized between the two eyes. Therefore, under certain circumstances (e.g. pathological conditions), microsaccades of the two eyes can be desynchronized.

There is neurophysiological evidence that microsaccades during fixation and saccades during free viewing are generated by the same neural mechanism and only differ in voluntariness and in scale (Hafed, Goffart, & Krauzlis, 2009). Neural activity in response to microsaccades have been found in every visual area examined (Martinez-Conde, Macknik, & Hubel, 2002; Martinez-Conde et al., 2004). Psychophysical studies suggest that microsaccades may serve as a near perfect indicator of covert spatial attention in addition to preventing visual perceptual fading (Engbert & Kliegl, 2003; Hafed & Clark, 2002; Rolfs, 2009). It seems that microsaccades keep the visual system in a "warm-up" state so that it can readily respond to

anything interesting in the visual environment. Further investigation is required to link the motion characteristics of microsaccades to its physiological functions.

4.2 Pathological fixational eye movements in strabismic amblyopia

When the image of an object of interest falls in the periphery of the retina, normally a reflex of eye movement that shifts the image to the fovea is elicited. For strabismic amblyopes with eccentric fixation, however, foveal vision is suppressed and the preferred retinal locus is in the parafovea. Eccentric fixation can be understood as a kind of motor adaptation due to impaired foveal acuity. Subject SF has very unstable and largely eccentric fixation. The scatter of the amblyopic eye's positions during fixation shows that his fovea has been completely missed. In fact, the shortest distance between his fovea and the target image on the retina is about 2 degrees. Fixation of the amblyopic eye is not just eccentric, but also very imprecise and unstable. The amblyopic eye wanders within an area several degrees wide when the subject is trying to fixate at a target. This may be at least partly due to the large size of the receptive field and the poor visual acuity / sensitivity in the periphery, but is also because of the abnormally ample microsaccades with extremely large amplitudes, including saccadic intrusions and jerk nystagmus. Subject SF has nasal eccentric fixation with dominantly horizontal microsaccades, which seems to be typical in strabismic amblyopia. However, the increased temporalward drifts in SF's amblyopic eye is different from more common findings of nasalward drifts in strabismic amblyopia. The nasalward microsaccades in the fellow nonamblyopic eye are also opposite to what have been reported for nonamblyopic eyes. The non-typical movement direction in the two eyes makes the binocular eye movement conjugate to some degree, consistent with earlier results.

An interesting finding is that strabismic amblyopic eye's fixational eye movement depends on tasks. Tasks that require more attention and effort can induce movements directed towards the target, resulting in some other fixation loci that are closer to the fovea. These "better" fixation loci are often transient in the sense that fixations at these locations are unstable and composed of mostly short visits made by saccadic eye movements. This result is consistent with previous finding that microsaccadic pattern and the fixation locus in strabismic amblyopia is task dependent (Siepmann et al., 2006). We also noted that the best fixation was achieved using a small cross fixation target whose size is about the subject's minimal angle of resolution (MAR), and therefore the target's visibility is good enough but its details can't be resolved. It suggests that viewing efforts – either identifying a letter or aimlessly seeking for details of an object may increase instability in fixation for strabismic amblyopes, and that a non-challenging, visible but featureless object may be a desirable fixation target for strabismic amblyopes.

Normally there exists a "refractory period" after the offset of a microsaccade during which the probability of the occurrence of another microsaccade is small. After this period microsaccades occur with roughly constant probability within any small time interval at given location. The latency after a microsaccade is similar to the refractory period observed in neural

spike train histograms, which is not surprising at all due to a number of factors that can delay the occurrence of a new microsaccade, including the neuromuscular signal transduction process that are involved in the elicitation of a microsaccade. In the strabismic amblyopic eye examined, however, this inhibition was missing, i.e., there are trains of microsaccades with very short separations or no separation at all. Whether this defect has a peripheral or a cortical origin is not clear as for now. And it requires further study to confirm whether this is generally true for strabismic and / or amblyopic observers.

Using stochastic modeling and potential function approach, we quantitatively characterized fixational eye movement components for a normal observer as well as both nonamblyopic and amblyopic eyes of a strabismic amblyopic patient. Studies regarding the physiological roles of fixational eye movements will be an interesting direction in the future.

5 Appendix

5.1 Normal eye

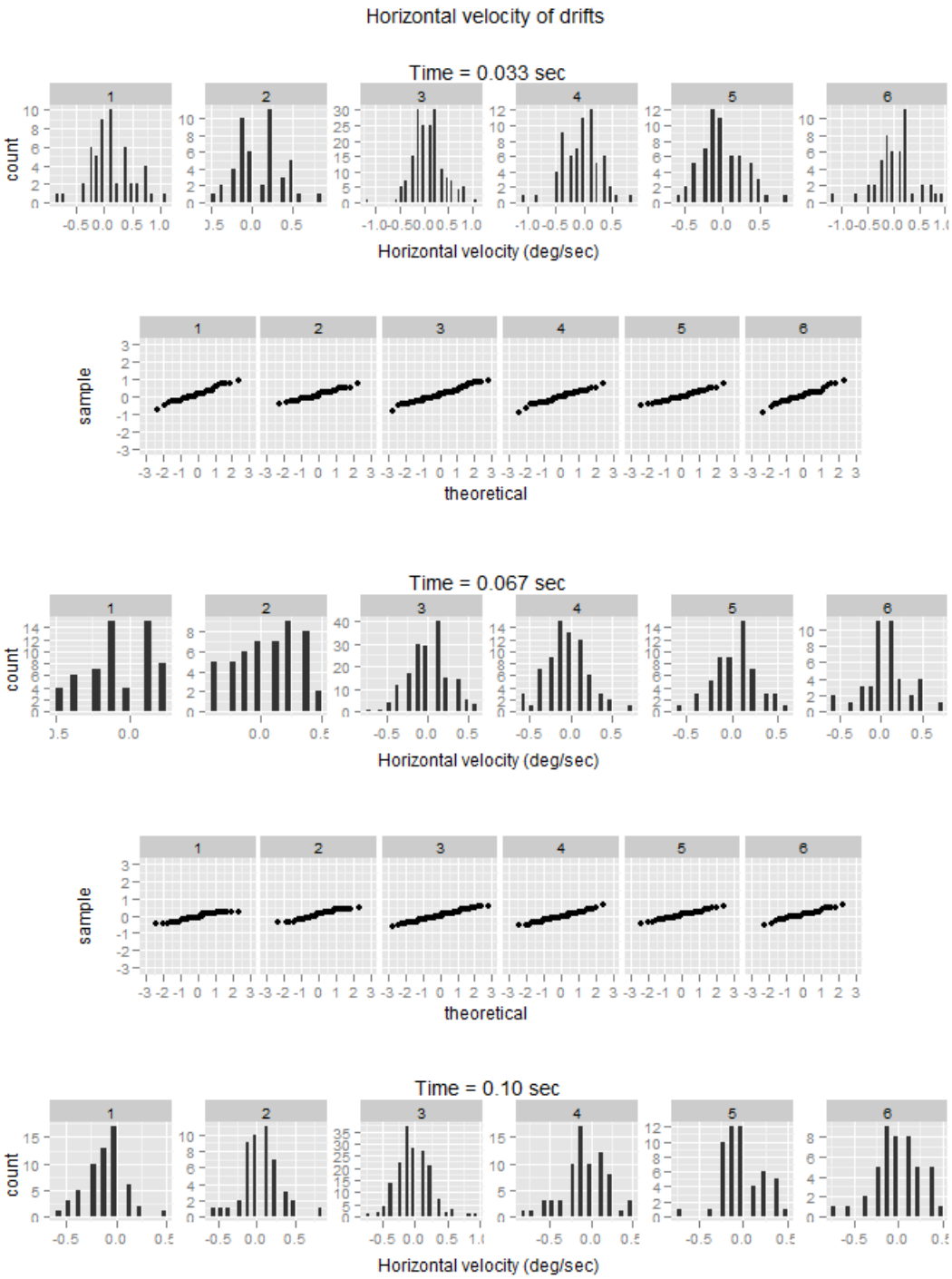

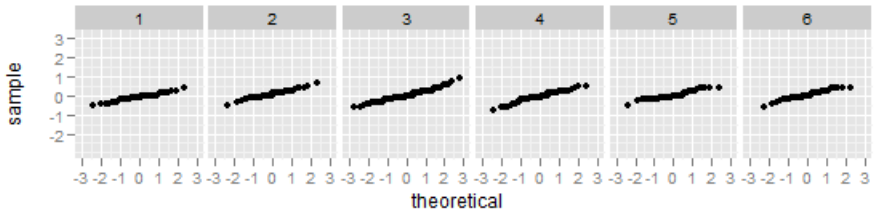

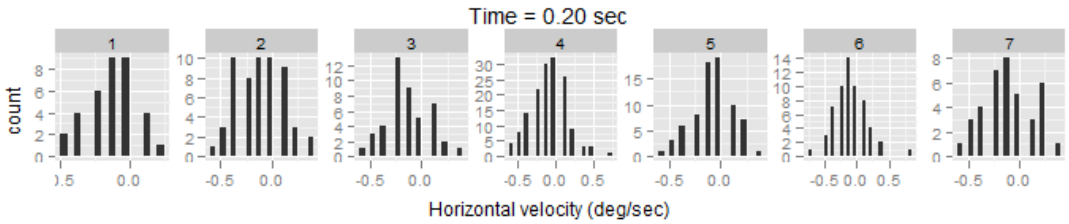

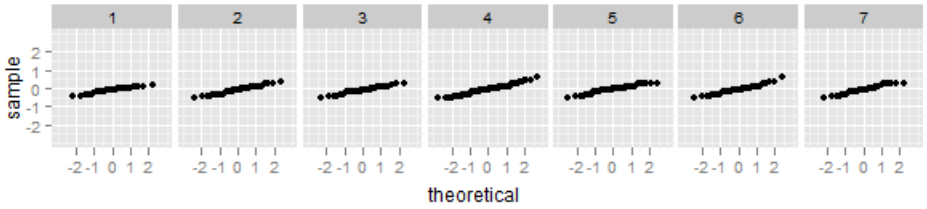

Vertical velocity of drifts

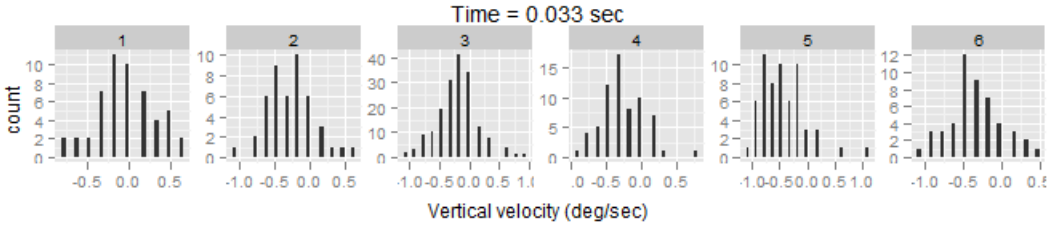

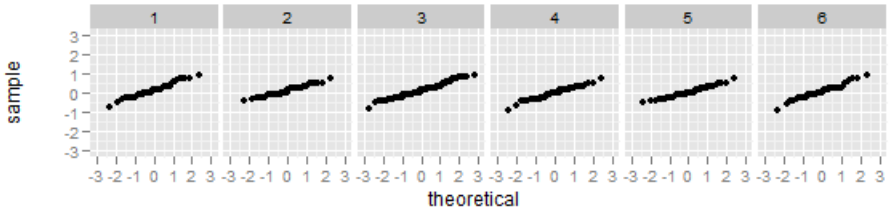

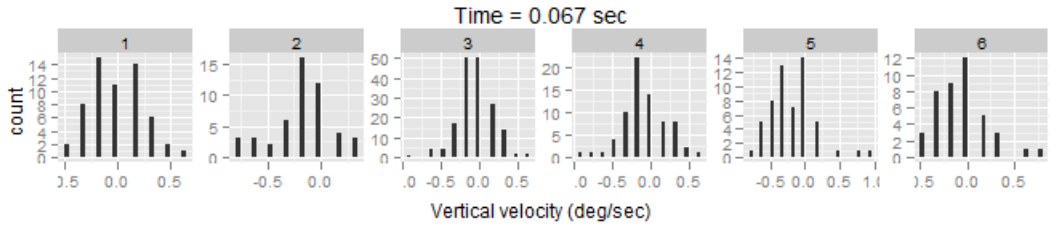
Time = 0.067 sec
1
2
3
4
5
6
count
Vertical velocity (deg/sec)

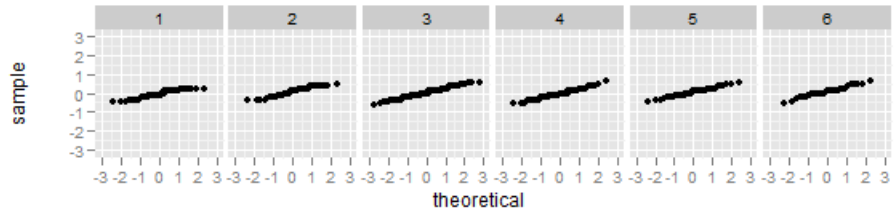
1
2
3
4
5
6
sample
theoretical

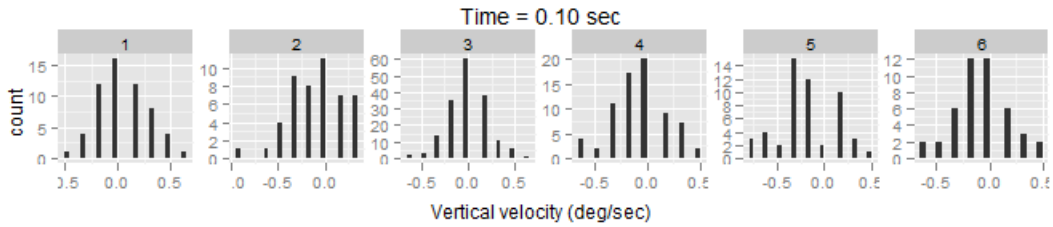
Time = 0.10 sec
1
2
3
4
5
6
count
Vertical velocity (deg/sec)

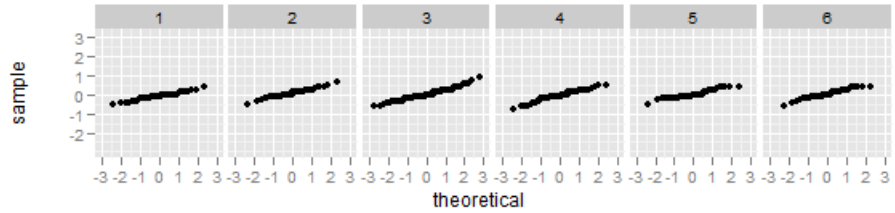
1
2
3
4
5
6
sample
theoretical

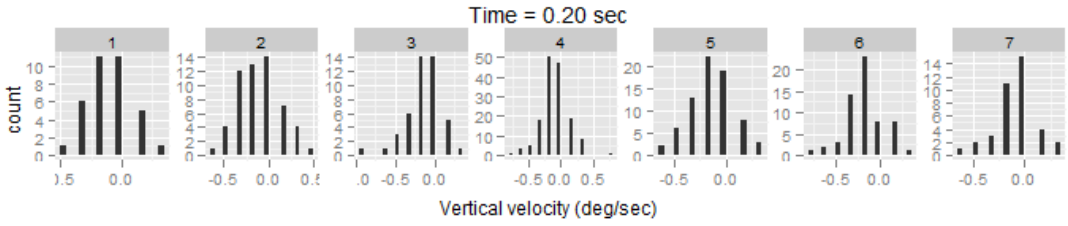
Time = 0.20 sec
1
2
3
4
5
6
7
count
Vertical velocity (deg/sec)

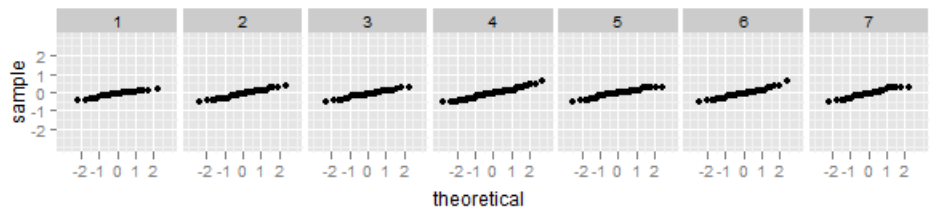
1
2
3
4
5
6
7
sample
theoretical

A. Histograms of horizontal and vertical velocities binned over location and time (following a microsaccade), and corresponding quantile-quantile plots for the normal eye. All are approximately normally distributed.

5.2 Nonamblyopic eye

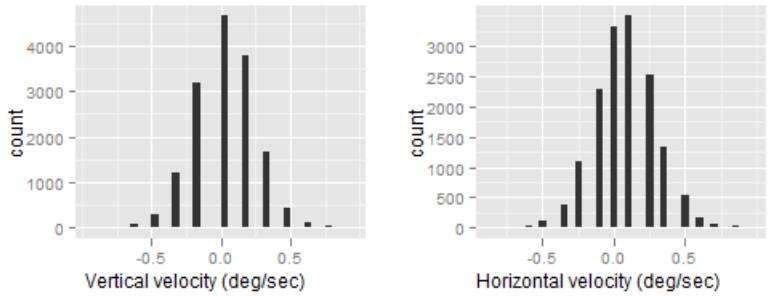

A. Histograms of horizontal and vertical velocities binned over location for the nonamblyopic eye. Both are approximately normally distributed.

5.3 Amblyopic eye

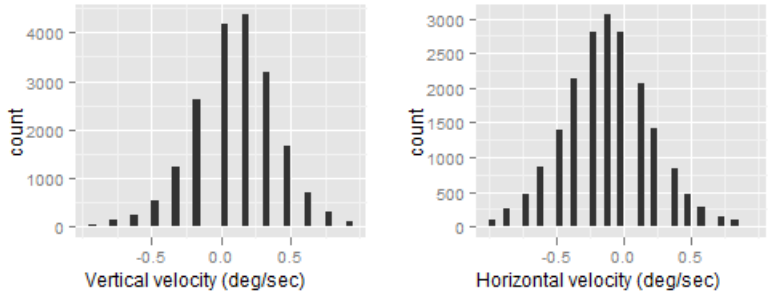

A. Histograms of horizontal and vertical velocities binned over location for the amblyopic eye. Both are approximately normally distributed.

SUMMARY

We have come to conclusions in support of the established hypothesis that strabismic amblyopia is like normal peripheral vision especially in spatial properties (Ciuffreda et al., 1991; Levi, 1991; Levi & Carkeet, 1993), through different approaches – from letter identification to estimation of basic mechanisms for simple image feature detection. The fixational eye movement as an important physical foundation for vision is also abnormal in strabismic amblyopia, although understanding its physiological significance requires further studies.

Letter acuity is the most common clinical evaluation of visual functions. Flanked or unflanked letter stimuli were used to measure acuity with or without spatial interaction (e.g. crowding), respectively, in the present study. If strabismic amblyopia can be modeled as the normal peripheral vision, and non-strabismic (i.e. anisometropic) amblyopia the blurred normal fovea, then for each pair of conditions both the visual resolution and the spatial interaction should be the same. We found that, indeed, the quantitative relationship between flanked and unflanked acuities is similar in strabismic amblyopia and the normal periphery, as well as in non-strabismic amblyopia and the normal fovea with optical blur, respectively. A model was developed which summarizes the legibility limits under different conditions. At fixation for normal (with optical blur) and non-strabismic amblyopic eyes, there is no crowding: legibility of a flanked letter is limited by overlap masking or acuity, depending on the letter spacing. In the normal periphery and strabismic amblyopia, legibility is limited by crowding unless the letter spacing is very loose. Equivalent blur and equivalent eccentricity defined based on the ratio of flanked to unflanked acuities (i.e. equivalent to the crowding-acuity ratio) show that the former does not differ between the two subtypes of amblyopia, whereas the latter is much greater in strabismic amblyopia than in non-strabismic amblyopia. Among our 18 amblyopes, we find near-perfect agreement of three diagnostic indicators: history of strabismus, absence of stereopsis, and a high crowding-acuity ratio. These results support the hypothesis that strabismic amblyopia is like the normal peripheral vision, but non-strabismic amblyopia is like the blurred fovea. The implication for screening is that both unflanked and flanked letter acuities should be measured, and the letter-to-letter spacing for the flanked stimuli should be tight.

Since the letter stimuli employed in the above study were different from those for clinical letter charts in contrast (medium vs. high), polarity (bright vs. dark), and duration (short vs. infinite), we systematically investigated the significance of these factors in normal visual acuities. We found that the effects of optical blur on flanked and unflanked acuities are independent of stimulus, and therefore reliably represent overlap masking; duration has similar effects on all tested conditions, i.e., flanked and unflanked stimuli, in the fovea and the periphery; contrast is most important for unflanked acuity in the fovea, followed by unflanked acuity at 5 deg and flanked acuity in the fovea, and it has almost no effect on flanked acuity at 5

deg. We also found that for letters with high contrast but not those with low contrast, acuity is independent of pupil size.

Whether or not crowding exists in the normal fovea is still controversial. By using print-like letter stimuli with very high contrast, we demonstrated crowding in the normal fovea, with the critical spacing 0.09 ~ 0.1 deg independent of stimulus conditions such as contrast or polarity. This result is consistent with those reported on foveal flanking effect using simple stimuli / tasks such as Vernier acuity (Latham & Whitaker, 1996; Levi et al., 1985; Toet & Levi, 1992). Perhaps the reason that some previous studies failed to find crowding in the fovea is because the stimuli used in those studies were not small enough to allow crowding to occur in the normal fovea (Levi, Klein et al., 2002; Pelli et al., 2004); see Levi (2008) for a discussion on foveal crowding.

Next, using the method of classification images, we estimated the spatiotemporal mechanisms for detecting a luminance increment and the spatiotemporal interactions of discriminating an orientation feature subject to crowding in both normal and amblyopic eyes. The normal template for luminance discrimination has an inhibition – summation – inhibition structure in space, and a summation – inhibition time course. The normal peripheral spatiotemporal interaction is characterized by strong perceptual assimilation (i.e. crowding) near the target and relatively weak perceptual repulsion farther from the target. Simultaneous, forward, and backward assimilation effects (i.e. crowding) are all present but affected by different cues, and interestingly the simultaneous assimilation effect is relatively less strong. We noted that the center /surround organization here may be a general spatial template for both lower level and higher level visual processing for a wide variety of visual tasks, including luminance discrimination, Vernier acuity position bias, phase capture for cluttered Gabor patches, orientation discrimination, and so on (Badcock & Westheimer, 1985; Levi et al., 2003; Wilson, 1978). We hypothesized that feature pooling that causes crowding (i.e. assimilation) may represent the centroid of the feature identification process, whereas the "anti-crowding" (i.e. repulsion) uncovered by the classification image in the present study perhaps represents the surrounding subtractive mechanism. The temporal profile for luminance discrimination has well defined summation and inhibition zones, which differs from the pure-summation result of an earlier similar study, probably because the high temporal uncertainty associated with the earlier study was eliminated in our study by using a discrimination (instead of detection) task (Neri & Heeger, 2002). The normal summation – inhibition asymmetric temporal profile resembles the widely assumed temporal impulse function, but differs from the classic two – pulse, three – pulse, or flicker sensitivity time course that is symmetric (Bergen & Wilson, 1985; Kelly, 1971a; Rashbass, 1970; Watson & Nachmias, 1977). Possible reasons that can account for this difference include, first, the stimuli were suprathreshold in the present study but near-threshold in earlier studies; second, the presence of spatiotemporal noise in the present study may have affected the perception, especially considering that the classic studies were done exclusively in the temporal domain. Furthermore, the temporal template estimated by the classification image

method may be related to backward masking (Breitmeyer & Ogmen, 2000).

The amblyopic spatiotemporal mechanism for luminance discrimination lacks inhibition, especially the temporal inhibition. Neither increasing the signal-to-noise ratio of the stimuli for the amblyopic eye or decreasing the signal-to-noise ratio of the stimuli for the normal eye or blurring the stimuli spatiotemporally affected the template significantly. However, by decreasing the fundamental frequency of the stimuli the normal template was successfully restored in the amblyopic eye, suggesting that the amblyopic mechanism for luminance discrimination is shifted towards lower spatial frequencies, consistent with previous reports (Bradley & Freeman, 1985; Levi & Harwerth, 1977; Manny & Levi, 1982a, 1982b). The normal peripheral template appears similar to the amblyopic template in the lack of inhibition. Lowering the fundamental frequency of the stimuli restored the spatial inhibition components but not the temporal inhibition component of the template. Moreover, the spatiotemporal interaction map for orientation discrimination is not substantially different between normal and amblyopic eyes except that in general orientation assimilation (i.e. crowding) is more widely distributed around and after the target presentation. Therefore the spatial mechanism for simple image feature detection is similar in amblyopia and normal peripheral vision, but the temporal mechanism may be different.

Lastly, we applied novel techniques and analytical methods to the quantitative modeling of fixational eye movements in both normal and amblyopic eyes. An adaptive optics scanning laser ophthalmoscope (AOSLO) was used to record fixational eye movements, allowing direct viewing of retinal movements and fixation locations (Poonja et al., 2005; Roorda, Romero-Borja, Donnelly III, & Queener, 2002). Although fixational eye movements appear random on small spatiotemporal scales, they are clearly non-random on visible scales under normal conditions, i.e. they are centered on the target with very small variation, no matter how long the fixating time is. A stochastic model with the potential function approach assumed of a quadratic polynomial form was applied to capture both the randomness and the determinacy of microsaccades and drifts of fixational eye movements (Brillinger, 2007a). The fitted potential function depicts the direction and speed of the movement in a natural way. The rate of the occurrence of microsaccades was approximated by a Poisson point process. Our results confirm that microsaccades, on average, correct for fixation inaccuracy. They occur more frequently and tend to move faster towards the target at relatively large displacements, as predicted by the microsaccade rate map and the quadratic potential function. Drift is characterized by a Brownian motion with constant rate over time plus an error-correcting component initially following a microsaccade. Therefore drifts seem to be error correcting at the beginning but soon lose the fixation attraction and become random, which will eventually produce fixation errors, until being intercepted by the next microsaccade. Fixational eye movements are more erratic and eccentric in the strabismic amblyopic eye (Ciuffreda et al., 1979a, 1979b; Schor & Hallmark, 1978). Intrusive saccades with large amplitudes and high speeds occur frequently. The strabismic amblyopic fixation pattern on multiple loci is task dependent, with less eccentric

but unstable fixation induced by challenging tasks (e.g. tumbling E identification), and relatively stable fixation by small highly visible static targets, consistent with previous findings (Siepmann et al., 2006). Understanding the relationship between the oculomotor mechanism and the physiological roles of normal and pathological fixational eye movements requires further investigation.

REFERENCES

Ahumada, A. J., Jr. (1996). Perceptual classification images from Vernier acuity masked by noise. *Perception, 26*(18), 1831?1840.

Ahumada, A. J., Jr. (2002). Classification image weights and internal noise level estimation. *J Vis, 2*(1), 121-131.

Ahumada, A. J., Jr., & lovell, J. (1971). Stimulus features in signal detection. *J. Acoust. Soc. Am., 49*(6B), 1751-1756.

Albrecht, D. G., Geisler, W. S., Frazor, R. A., & Crane, A. M. (2002). Visual cortex neurons of monkeys and cats: temporal dynamics of the contrast response function. *J Neurophysiol, 88*(2), 888-913.

Artal, P., Marcos, S., Iglesias, I., & Green, D. G. (1996). Optical modulation transfer and contrast sensitivity with decentered small pupils in the human eye. *Vision Res, 36*(22), 3575-3586.

Atkinson, J. (1991). *Review of human visual development: crowding and dyslexia*. London: MacMillan Press.

Atkinson, J., Anker, S., Evans, C., Hall, R., & Pimm-Smith, E. (1988). Visual acuity testing of young children with the Cambridge Crowding Cards at 3 and 6 m. *Acta Ophthalmol (Copenh), 66*(5), 505-508.

Atkinson, J., Pimm-Smith, E., Evans, C., Harding, G., & Braddick, O. (1986). Visual crowding in young children. *Doc Ophthalmol Proc Ser, 45*, 201-213.

Badcock, D. R., & Westheimer, G. (1985). Spatial location and hyperacuity: the centre/surround localization contribution function has two substrates. *Vision research, 25*(9), 1259.

Balas, B. J., Nakano, L., & Rosenholtz, R. (2009). A summary-statistic representation in peripheral vision explains visual crowding. *Journal of vision, 9*, 12-13.

Barlow, H. B. (1952). Eye movements during fixation. *J Physiol, 116*(3), 290-306.

Baron, W. S., & Westheimer, G. (1973). Visual acuity as a function of exposure duration. *J Opt Soc Am, 63*(2), 212-219.

Beard, B. L., & Ahumada, A. J., Jr. (1998). *Technique to extract relevant image features for visual tasks*.

Bedell, H. E., & Flom, M. C. (1981). Monocular spatial distortion in strabismic amblyopia. *Invest Ophthalmol Vis Sci, 20*(2), 263-268.

Bedell, H. E., & Flom, M. C. (1985). Bilateral oculomotor abnormalities in strabismic amblyopes: evidence for a common central mechanism. *Doc Ophthalmol, 59*(4), 309-321.

Bergen, J. R., & Wilson, H. R. (1985). Prediction of flicker sensitivities from temporal three-pulse data. *Vision Res, 25*(4), 577-582.

Bonneh, Y. S., Sagi, D., & Polat, U. (2004). Local and non-local deficits in amblyopia: acuity and spatial interactions. *Vision Res, 44*(27), 3099-3110.

Bouma, H. (1970). Interaction effects in parafoveal letter recognition. *Nature, 226*(5241), 177-178.

Boyce, P. R. (1967). Monocular fixation in human eye movement. *Proc R Soc Lond B Biol Sci, 167*(8), 293-315.

Bradley, A., & Freeman, R. D. (1985). Temporal sensitivity in amblyopia: an explanation of conflicting reports. *Vision Res, 25*(1), 39-46.

Brainard, D. H. (1997). The Psychophysics Toolbox. *Spat Vis, 10*(4), 433-436.

Breitmeyer, B. G., & Ogmen, H. (2000). Recent models and findings in visual backward masking: a comparison, review, and update. *Percept Psychophys, 62*(8), 1572-1595.

Brillinger, D. R. (2007a). Learning a potential function from a trajectory. *IEEE Signal Processing Letters, 14*(11),

867.

Brillinger, D. R. (2007b). A potential function approach to the flow of play in soccer. *J. Quant. Anal. Sports, 3*(1).

Brillinger, D. R., Preisler, H. K., Ager, A. A., & Kie, J. G. (2001). The use of potential functions in modelling animal movement. *Data analysis from statistical foundations: a festschrift in honour of the 75th birthday of DAS Fraser*, 369.

Brillinger, D. R., Preisler, H. K., Ager, A. A., Kie, J. G., & Stewart, B. S. (2001). Modelling movements of free-ranging animals. *Univ. Calif. Berkeley Statistics Technical Report, 610*.

Bussgang, J. J. (1952). Crosscorrelation functions of amplitude-distorted Gaussian signals. *MIT Res Lab Elec Tech Rep, 216*, 1-14.

Campbell, F. W., & Gubisch, R. W. (1966). Optical quality of the human eye. *J Physiol, 186*(3), 558-578.

Chung, S. T. L. (2007). Learning to identify crowded letters: does it improve reading speed? *Vision Res, 47*(25), 3150-3159.

Chung, S. T. L., Levi, D. M., & Legge, G. E. (2001). Spatial-frequency and contrast properties of crowding. *Vision Res, 41*(14), 1833-1850.

Ciuffreda, K. J. (1979). Jerk nystagmus: some new findings. *Am J Optom Physiol Opt, 56*(8), 521-530.

Ciuffreda, K. J., Kenyon, R. V., & Stark, L. (1979a). Fixational eye movements in amblyopia and strabismus. *J Am Optom Assoc, 50*(11), 1251-1258.

Ciuffreda, K. J., Kenyon, R. V., & Stark, L. (1979b). Saccadic intrusions in strabismus. *Arch Ophthalmol, 97*(9), 1673-1679.

Ciuffreda, K. J., Kenyon, R. V., & Stark, L. (1980). Increased drift in amblyopic eyes. *Br J Ophthalmol, 64*(1), 7-14.

Ciuffreda, K. J., Levi, D. M., & Selenow, A. (1991). *Amblyopia: Basic and Clinical Aspects*: Boston: Butterworth-Heinemann.

Cornsweet, T. N. (1956). Determination of the stimuli for involuntary drifts and saccadic eye movements. *J Opt Soc Am, 46*(11), 987-993.

Darwin, R. W. (1786). New experiments on the ocular spectra of light and colours. *Philosophical Transactions of the Royal Society, 76*, 313-348.

de Boer, E. (1967). Correlation studies applied to the frequency resolution of the cochlea. *J Aud Res, 7*, 209-217.

de Boer, R., & Kuyper, P. (1968). Triggered correlation. *IEEE Trans Biomed Eng, 15*(3), 169-179.

DeAngelis, G. C., Ohzawa, I., & Freeman, R. D. (1993). Spatiotemporal organization of simple-cell receptive fields in the cat's striate cortex. I. General characteristics and postnatal development. *J Neurophysiol, 69*(4), 1091-1117.

Ditchburn, R. W., & Ginsborg, B. L. (1952). Vision with a stabilized retinal image. *Nature, 170*(4314), 36-37.

Ditchburn, R. W., & Ginsborg, B. L. (1953). Involuntary eye movements during fixation. *J Physiol, 119*(1), 1-17.

Ehrlich, M. I., Reinecke, R. D., & Simons, K. (1983). Preschool vision screening for amblyopia and strabismus. Programs, methods, guidelines, 1983. *Surv Ophthalmol, 28*(3), 145-163.

Ellemberg, D., Hess, R. F., & Arsenault, A. S. (2002). Lateral interactions in amblyopia. *Vision Res, 42*(21), 2471-2478.

Elliott, D. B., Whitaker, D., & Bonette, L. (1990). Differences in the legibility of letters at contrast threshold using the Pelli-Robson chart. *Ophthalmic Physiol Opt, 10*(4), 323-326.

Engbert, R. (2006). Microsaccades: A microcosm for research on oculomotor control, attention, and visual

perception. *Prog Brain Res, 154*, 177-192.

Engbert, R., & Kliegl, R. (2003). Microsaccades uncover the orientation of covert attention. *Vision Res, 43*(9), 1035-1045.

Engbert, R., & Kliegl, R. (2004). Microsaccades keep the eyes' balance during fixation. *Psychol Sci, 15*(6), 431-436.

Felisbert, F. M., Solomon, J. A., & Morgan, M. J. (2005). The role of target salience in crowding. *Perception, 34*(7), 823-833.

Gold, J. M., Murray, R. F., Bennett, P. J., & Sekuler, A. B. (2000). Deriving behavioural receptive fields for visually completed contours. *Curr Biol, 10*(11), 663-666.

Hafed, Z. M., & Clark, J. J. (2002). Microsaccades as an overt measure of covert attention shifts. *Vision Res, 42*(22), 2533-2545.

Hafed, Z. M., Goffart, L., & Krauzlis, R. J. (2009). A neural mechanism for microsaccade generation in the primate superior colliculus. *Science, 323*(5916), 940-943.

Hess, R. F., & Bradley, A. (1980). Contrast perception above threshold is only minimally impaired in human amblyopia. *Nature, 287*(5781), 463-464.

Hess, R. F., & Demanins, R. (1998). Contour integration in anisometropic amblyopia. *Vision Res, 38*(6), 889-894.

Hess, R. F., & Jacobs, R. J. (1979). A preliminary report of acuity and contour interactions across the amblyope's visual field. *Vision Res, 19*(12), 1403-1408.

Higgins, K. E., Daugman, J. G., & Mansfield, R. J. (1982). Amblyopic contrast sensitivity: insensitivity to unsteady fixation. *Invest Ophthalmol Vis Sci, 23*(1), 113-120.

Hubel, D. H., & Wiesel, T. N. (1959). Receptive fields of single neurones in the cat's striate cortex. *J Physiol, 148*, 574-591.

Intriligator, J., & Cavanagh, P. (2001). The spatial resolution of visual attention. *Cognit Psychol, 43*(3), 171-216.

Jones, J. P., & Palmer, L. A. (1987). The two-dimensional spatial structure of simple receptive fields in cat striate cortex. *J Neurophysiol, 58*(6), 1187-1211.

Jurin, J. (1738). *An essay on distinct and indistinct vision.* (Vol. 2). Cambridge.

Kelly, D. H. (1971a). Theory of flicker and transient responses. I. Uniform fields. *J Opt Soc Am, 61*(4), 537-546.

Kelly, D. H. (1971b). Theory of flicker and transient responses. II. Counterphase gratings. *J Opt Soc Am, 61*(5), 632-640.

Kelly, D. H., & Savoie, R. E. (1978). Theory of flicker and transient responses. III. An essential nonlinearity. *J Opt Soc Am, 68*(11), 1481-1490.

Kirwan, C., & O'Keefe, M. (2008). Higher order aberrations in children with amblyopia. *J Pediatr Ophthalmol Strabismus, 45*(2), 92-96.

Korte, W. (1923). Über die Gestaltauffassung im indirekten Sehen *Zeitschrift für Psychologie, 93*, 17-82.

Kowler, E., & Steinman, R. M. (1979). Miniature saccades: eye movements that do not count. *Vision Res, 19*(1), 105-108.

Kowler, E., & Steinman, R. M. (1980). Small saccades serve no useful purpose: reply to a letter by R. W. Ditchburn. *Vision Res, 20*(3), 273-276.

Krauskopf, J., Cornsweet, T. N., & Riggs, L. A. (1960). Analysis of eye movements during monocular and binocular fixation. *J Opt Soc Am, 50*, 572-578.

Kwon, M., Legge, G. E., & Dubbels, B. R. (2007). Developmental changes in the visual span for reading. *Vision*

Res, 47(22), 2889-2900.

Latham, K., & Whitaker, D. (1996). Relative roles of resolution and spatial interference in foveal and peripheral vision. *Ophthalmic Physiol Opt, 16*(1), 49-57.

Levi, D. M. (1991). Spatial vision in amblyopia. In D. Regan (Ed.), *Spatial vision* (pp. 212-238). London: Macmillan Press.

Levi, D. M. (2008). Crowding--an essential bottleneck for object recognition: a mini-review. *Vision Res, 48*(5), 635-654.

Levi, D. M., & Carkeet, A. (1993). Amblyopia: A consequence of abnormal visual development. In K. Simons (Ed.), *Early Visual Development, Normal and Abnormal* (pp. 391-408): Oxford University Press.

Levi, D. M., & Carney, T. (2009). Crowding in Peripheral Vision: Why Bigger Is Better. *Curr Biol*.

Levi, D. M., Hariharan, S., & Klein, S. A. (2002a). Suppressive and facilitatory spatial interactions in amblyopic vision. *Vision Res, 42*(11), 1379-1394.

Levi, D. M., Hariharan, S., & Klein, S. A. (2002b). Suppressive and facilitatory spatial interactions in peripheral vision: peripheral crowding is neither size invariant nor simple contrast masking. *J Vis, 2*(2), 167-177.

Levi, D. M., & Harwerth, R. S. (1977). Spatio-temporal interactions in anisometropic and strabismic amblyopia. *Invest Ophthalmol Vis Sci, 16*(1), 90-95.

Levi, D. M., & Klein, S. (1982). Hyperacuity and amblyopia. *Nature, 298*(5871), 268-270.

Levi, D. M., & Klein, S. A. (1985). Vernier acuity, crowding and amblyopia. *Vision Res, 25*(7), 979-991.

Levi, D. M., & Klein, S. A. (1990a). Equivalent intrinsic blur in amblyopia. *Vision Res, 30*(12), 1995-2022.

Levi, D. M., & Klein, S. A. (1990b). Equivalent intrinsic blur in spatial vision. *Vision Res, 30*(12), 1971-1993.

Levi, D. M., & Klein, S. A. (2002). Classification images for detection and position discrimination in the fovea and parafovea. *J Vis, 2*(1), 46-65.

Levi, D. M., & Klein, S. A. (2003). Noise provides some new signals about the spatial vision of amblyopes. *J Neurosci, 23*(7), 2522-2526.

Levi, D. M., Klein, S. A., & Aitsebaomo, A. P. (1985). Vernier acuity, crowding and cortical magnification. *Vision Res, 25*(7), 963-977.

Levi, D. M., Klein, S. A., & Chen, I. (2008). What limits performance in the amblyopic visual system: seeing signals in noise with an amblyopic brain. *J Vis, 8*(4), 1 1-23.

Levi, D. M., Klein, S. A., & Hariharan, S. (2002). Suppressive and facilitatory spatial interactions in foveal vision: foveal crowding is simple contrast masking. *J Vis, 2*(2), 140-166.

Levi, D. M., Li, R. W., & Klein, S. A. (2003). "Phase capture" in the perception of interpolated shape: cue combination and the influence function. *Vision research, 43*(21), 2233-2243.

Levi, D. M., Song, S., & Pelli, D. G. (2007). Amblyopic reading is crowded. *J Vis, 7*(2), 21 21-17.

Levi, D. M., Yu, C., Kuai, S. G., & Rislove, E. (2007). Global contour processing in amblyopia. *Vision Res, 47*(4), 512-524.

Li, R. W., Klein, S. A., & Levi, D. M. (2008). Prolonged perceptual learning of positional acuity in adult amblyopia: perceptual template retuning dynamics. *J Neurosci, 28*(52), 14223-14229.

Liang, J., Williams, D. R., & Miller, D. T. (1997). Supernormal vision and high-resolution retinal imaging through adaptive optics. *J Opt Soc Am A Opt Image Sci Vis, 14*(11), 2884-2892.

Manny, R. E., & Levi, D. M. (1982a). Psychophysical investigations of the temporal modulation sensitivity function in amblyopia: spatiotemporal interactions. *Invest Ophthalmol Vis Sci, 22*(4), 525-534.

Manny, R. E., & Levi, D. M. (1982b). Psychophysical investigations of the temporal modulation sensitivity function in amblyopia: uniform field flicker. *Invest Ophthalmol Vis Sci, 22*(4), 515-524.

Martinez-Conde, S. (2006). Fixational eye movements in normal and pathological vision. *Prog Brain Res, 154*, 151-176.

Martinez-Conde, S., Macknik, S. L., & Hubel, D. H. (2002). The function of bursts of spikes during visual fixation in the awake primate lateral geniculate nucleus and primary visual cortex. *Proc Natl Acad Sci U S A, 99*(21), 13920-13925.

Martinez-Conde, S., Macknik, S. L., & Hubel, D. H. (2004). The role of fixational eye movements in visual perception. *Nat Rev Neurosci, 5*(3), 229-240.

McKee, S. P., Levi, D. M., & Movshon, J. A. (2003). The pattern of visual deficits in amblyopia. *J Vis, 3*(5), 380-405.

Morad, Y., Werker, E., & Nemet, P. (1999). Visual acuity tests using chart, line, and single optotype in healthy and amblyopic children. *J AAPOS: the official publication of the American Association for Pediatric Ophthalmology and Strabismus, 3*(2), 94-97.

Nachmias, J. (1959). Two-dimensional motion of the retinal image during monocular fixation. *J Opt Soc Am, 49*, 901-908.

Nachmias, J. (1961). Determiners of the drift of the eye during monocular fixation. *J Opt Soc Am, 51*, 761-766.

Nandy, A. S., & Tjan, B. S. (2007). The nature of letter crowding as revealed by first- and second-order classification images. *J Vis, 7*(2), 5 1-26.

Neri, P., & Heeger, D. J. (2002). Spatiotemporal mechanisms for detecting and identifying image features in human vision. *Nat Neurosci, 5*(8), 812-816.

Neri, P., & Levi, D. M. (2006). Receptive versus perceptive fields from the reverse-correlation viewpoint. *Vision Res, 46*(16), 2465-2474.

Neri, P., Parker, A. J., & Blakemore, C. (1999). Probing the human stereoscopic system with reverse correlation. *Nature, 401*(6754), 695-698.

Ohzawa, I., DeAngelis, G. C., & Freeman, R. D. (1997). Encoding of binocular disparity by complex cells in the cat's visual cortex. *J Neurophysiol, 77*(6), 2879-2909.

Parkes, L., Lund, J., Angelucci, A., Solomon, J. A., & Morgan, M. (2001). Compulsory averaging of crowded orientation signals in human vision. *Nat Neurosci, 4*(7), 739-744.

Pelli, D. G. (1997). The VideoToolbox software for visual psychophysics: transforming numbers into movies. *Spat Vis, 10*(4), 437-442.

Pelli, D. G., Palomares, M., & Majaj, N. J. (2004). Crowding is unlike ordinary masking: distinguishing feature integration from detection. *J Vis, 4*(12), 1136-1169.

Pelli, D. G., & Tillman, K. A. (2008). The uncrowded window of object recognition. *Nat Neurosci, 11*(10), 1129-1135.

Pelli, D. G., Tillman, K. A., Freeman, J., Su, M., Berger, T. D., & Majaj, N. J. (2007). Crowding and eccentricity determine reading rate. *J Vis, 7*(2), 20 21-36.

Polat, U., Bonneh, Y., Ma-Naim, T., Belkin, M., & Sagi, D. (2005). Spatial interactions in amblyopia: effects of stimulus parameters and amblyopia type. *Vision Res, 45*(11), 1471-1479.

Poonja, S., Patel, S., Henry, L., & Roorda, A. (2005). Dynamic visual stimulus presentation in an adaptive optics scanning laser ophthalmoscope. *J Refract Surg, 21*(5), S575-580.

Putnam, N., Hofer, H., Doble, N., Chen, L., Carroll, J., & Williams, D. (2005). The locus of fixation and the foveal cone mosaic. *J. Vision, 5*, 632-639.

Rashbass, C. (1970). The visibility of transient changes of luminance. *J Physiol, 210*(1), 165-186.

Riggs, L. A., & Ratliff, F. (1952). The effects of counteracting the normal movements of the eye. *J. Opt. Soc. Am., 42*, 872-873.

Ringach, D. L., Hawken, M. J., & Shapley, R. (1997). Dynamics of orientation tuning in macaque primary visual cortex. *Nature, 387*(6630), 281-284.

Ringach, D. L., & Shapley, R. (2004). Reverse correlation in neurophysiology. *Cognitive Science, 28*(2), 147-166.

Rolfs, M. (2009). Microsaccades: small steps on a long way. *Vision Res, 49*(20), 2415-2441.

Roorda, A., Romero-Borja, F., Donnelly III, W., & Queener, H. (2002). Adaptive optics scanning laser ophthalmoscopy. *Opt Express, 10*(9), 405-412.

Roorda, A., Romero-Borja, F., Donnelly III, W., Queener, H., Hebert, T., & Campbell, M. (2002). Adaptive optics scanning laser ophthalmoscopy. *Opt Express, 10*(9), 405-412.

Schor, C. M., & Flom, M. C. (1975). Eye position control and visual acuity in strabismus amblyopia. *Basic Mechanisms in Ocular Motility and Their Clinical Implications, Lennerstrand G and Bach-y-Rita P, editors. New York*, 555-559.

Schor, C. M., & Hallmark, W. (1978). Slow control of eye position in strabismic amblyopia. *Invest Ophthalmol Vis Sci, 17*(6), 577-581.

Siepmann, K., Reinhard, J., & Herzau, V. (2006). The locus of fixation in strabismic amblyopia changes with increasing effort of recognition as assessed by scanning laser ophthalmoscope. *Acta Ophthalmol Scand, 84*(1), 124-129.

Snellen, H. (1866). *Test-types for the determination of the acuteness of vision* (4th ed.). London: Williams & Norgate.

Snodderly, D. M., & Kurtz, D. (1985). Eye position during fixation tasks: comparison of macaque and human. *Vision Res, 25*(1), 83-98.

Solomon, J. A., Felisberti, F. M., & Morgan, M. J. (2004). Crowding and the tilt illusion: toward a unified account. *J Vis, 4*(6), 500-508.

Steinman, R. M., Cunitz, R. J., Timberlake, G. T., & Herman, M. (1967). Voluntary control of microsaccades during maintained monocular fixation. *Science, 155*(769), 1577-1579.

Steinman, R. M., Haddad, G. M., Skavenski, A. A., & Wyman, D. (1973). Miniature eye movement. *Science, 181*(102), 810-819.

Stevenson, S. B., & Roorda, A. (2005). *Correcting for miniature eye movements in high resolution scanning laser ophthalmoscopy*.

Strasburger, H. (2005). Unfocused spatial attention underlies the crowding effect in indirect form vision. *J Vis, 5*(11), 1024-1037.

Stuart, J. A., & Burian, H. M. (1962). A study of separation difficulty. Its relationship to visual acuity in normal and amblyopic eyes. *Am J Ophthalmol, 53*, 471-477.

Thomas-Decortis, G. (1959). [Angular visual acuity and morphoscopic visual acuity in amblyopia ex anopsia.]. *Bull Soc Belge Ophtalmol, 123*, 488-499.

Tjan, B. S., & Nandy, A. S. (2006). Classification images with uncertainty. *J Vis, 6*(4), 387-413.

Toet, A., & Levi, D. M. (1992). The two-dimensional shape of spatial interaction zones in the parafovea. *Vision*

Res, 32(7), 1349-1357.

Tommila, V. (1972). A new chart for testing line acuity in amblyopia. *Acta Ophthalmol (Copenh), 50*(4), 565-569.

Tripathy, S. P., & Cavanagh, P. (2002). The extent of crowding in peripheral vision does not scale with target size. *Vision Res, 42*(20), 2357-2369.

Vasudevan, R., Phatak, A. V., & Smith, J. D. (1972). A stochastic model for eye movements during fixation on a stationary target. *Kybernetik, 11*(1), 24-31.

Von Helmholtz, H. (1924). Treatise on physiological optics. *The Optical Society of America, 2*.

Watson, A. B. (1986). *Temporal sensitivity* (Vol. 1).

Watson, A. B., & Nachmias, J. (1977). Patterns of temporal interaction in the detection of gratings. *Vision Res, 17*(8), 893-902.

Watson, A. B., & Rosenholtz, R. (1997). A Rorschach test for visual classification strategies. *Invest. Ophthalmol. Visual Sci, 38*.

Watt, R. J., & Hess, R. F. (1987). Spatial information and uncertainty in anisometropic amblyopia. *Vision Res, 27*(4), 661-674.

Watt, R. J., & Morgan, M. J. (1984). Spatial filters and the localization of luminance changes in human vision. *Vision Res, 24*(10), 1387-1397.

Westheimer, G. (2003). Visual acuity with reversed-contrast charts: I. Theoretical and psychophysical investigations. *Optom Vis Sci, 80*(11), 745-748.

Westheimer, G., Chu, P., Huang, W., Tran, T., & Dister, R. (2003). Visual acuity with reversed-contrast charts: II. Clinical investigation. *Optom Vis Sci, 80*(11), 749-752.

Westheimer, G., & Hauske, G. (1975). Temporal and spatial interference with vernier acuity. *Vision Res, 15*, 1137-1141.

Wick, B., & Schor, C. M. (1984). A comparison of the Snellen chart and the S-chart for visual acuity assessment in amblyopia. *J Am Optom Assoc, 55*(5), 359-361.

Wilson, H. R. (1978). Quantitative characterization of two types of line-spread function near the fovea. *Vision Res, 18*(8), 971-981.